



저작자표시-비영리-변경금지 2.0 대한민국

이용자는 아래의 조건을 따르는 경우에 한하여 자유롭게

- 이 저작물을 복제, 배포, 전송, 전시, 공연 및 방송할 수 있습니다.

다음과 같은 조건을 따라야 합니다:



저작자표시. 귀하는 원저작자를 표시하여야 합니다.



비영리. 귀하는 이 저작물을 영리 목적으로 이용할 수 없습니다.



변경금지. 귀하는 이 저작물을 개작, 변형 또는 가공할 수 없습니다.

- 귀하는, 이 저작물의 재이용이나 배포의 경우, 이 저작물에 적용된 이용허락조건을 명확하게 나타내어야 합니다.
- 저작권자로부터 별도의 허가를 받으면 이러한 조건들은 적용되지 않습니다.

저작권법에 따른 이용자의 권리는 위의 내용에 의하여 영향을 받지 않습니다.

이것은 [이용허락규약\(Legal Code\)](#)을 이해하기 쉽게 요약한 것입니다.

[Disclaimer](#)

공학박사 학위논문

**Fabrication and Operation Analysis of  
Membrane-Iridium Oxide Electrodeposited  
Electrode Assembly in Unitized Regenerative  
Proton Exchange Membrane Fuel Cell**

양이온 교환막 일체형 재생 연료전지용  
막-산화 이리듐 도금 전극 접합체 제조 및 운전 분석

2020 년 8 월

서울대학교 대학원

화학생물공학부

에너지환경화학융합기술전공

임 아 연

# **Abstract**

## **Fabrication and Operation Analysis of Membrane-Iridium Oxide Electrodeposited Electrode Assembly in Unitized Regenerative Proton Exchange Membrane Fuel Cell**

Ahyoun Lim

School of Chemical and Biological Engineering

Chemical Convergence for Energy & Environment

The Graduate School

Seoul National University

Hydrogen energy is receiving great attention as alternatives to coal and petroleum since it does not emit greenhouse gases even when burned. To vitalize the hydrogen economy, production of hydrogen and power generation from hydrogen are important. There are some ways of producing hydrogen such as steam reforming, pyrolysis, plasma reforming, biomass gasification, etc., but among them, water electrolysis, producing hydrogen and oxygen from water by

electrolysis, is the most environment-friendly technology. In addition, fuel cell is eco-friendly cell to generate power from hydrogen and oxygen. Unitized regenerative fuel cell (URFC) is a device capable of both operations, i.e. water electrolysis and fuel cell.

For production of effective and durable URFC, highly active catalysts and corrosion-resistant and stable electrodes are required. Since carbon electrodes are easily corroded in oxidative condition of water electrolysis, titanium electrodes are generally reported as oxygen electrode of water electrolysis operation in URFC. Here, iridium oxide ( $\text{IrO}_2$ )-electrodeposited titanium electrodes were used to fabricate URFC electrodes exhibiting stable and high performance with low amount of noble catalysts. The  $\text{IrO}_2$ -electrodeposited electrode not only provides good electrolytic performance with small amount of  $\text{IrO}_2$  ( $< 0.2 \text{ mg cm}^{-2}$ ), but also prevents corrosion of the titanium electrode by coating the surface of the electrode with  $\text{IrO}_2$ . In this dissertation, the problems when the  $\text{IrO}_2$ -electrodeposited titanium electrode is applied in URFC were figured out, and studies were conducted to ameliorate the issues.

In chapter 1, a brief overview of proton exchange membrane based water electrolysis, fuel cell and unitized regenerative fuel cell, and applications of electroplating electrodes in those devices was introduced.

In chapter 2, platinum (Pt) supports were electrodeposited to enhance active surface area of the  $\text{IrO}_2$ -electrodeposited electrode. From sequential electrodeposition, catalysts having hemispheric Pt core- $\text{IrO}_2$  shell structure were

fabricated. Pt supports are not only stable in the oxidative condition during electrodeposition of IrO<sub>2</sub>, but also form strong chemical bonds with the titanium substrate and IrO<sub>2</sub> to form stable catalyst layers. Compared to the electrode formed by catalyst spray coating and the single electrodeposited electrode, performance of current density per mass was 2.1 times that of the electrodeposited electrode without the supports and 56 times that of the spray electrode in electrolysis operation. It was confirmed that decrease of mass transport resistance from hydrophilicity of the electrodeposited electrode, increase of active surface area in the dual electrodeposited electrode, and reduction of ohmic resistance due to conductive Pt supports contribute to superior electrolysis performance of the dual electrodeposited electrode. In addition, it was confirmed that it can be used as a fuel cell electrode by reduction of IrO<sub>2</sub> surface and exhibits high URFC performance even with a low noble metal loading of 0.83 mg<sub>(Pt+Ir)</sub> cm<sup>-2</sup>.

In chapter 3, amphiphilic electrodeposited electrodes were fabricated and applied in URFC. While maintaining hydrophilicity of the electrode from IrO<sub>2</sub> electrodeposition, hydrophobic PDMS polymer brushes were coated at regular intervals to form patterned hydrophilic/hydrophobic channels in the electrode. The oxygen electrode of URFC included electrodeposited IrO<sub>2</sub> catalysts and spray coated Pt catalysts. In the oxygen electrode, the Pt catalyst layer having highly porous structure and hydrophobic property increases mass transport resistance during water electrolysis operation, while the IrO<sub>2</sub> catalysts have hydrophilicity, which negatively affects the mass transport of gas during fuel cell operation,

resulting severe flooding. Accordingly, it was confirmed that the mutually adverse effects were ameliorated, thereby significantly improving the performance in both electrolysis and fuel cell operation when the amphiphilic porous transport layer was applied in URFC.

In chapter 4, the principle and analysis methods of scanning electrochemical microscopy (SECM) were introduced through basic experiments and the effect of the amphiphilic porous transport layer on gas emission was verified using SECM analysis. Topography of the titanium porous transport layer was analyzed by principle of current change of ultramicroelectrode (UME) through distance between the UME and the substrate in the solution containing redox mediators when the constant voltage was applied to the UME. In addition, when the oxygen evolution reaction (OER) occurred in the porous transport layer, oxygen generated in the substrate was detected through an oxygen reduction reaction (ORR) of the UME above the back surface of the porous transport layer. As a result, when UME passed within 20  $\mu\text{m}$  distance on the substrate, more oxygen detection occurred when passing over the pore. However, it was not affected by topography by diffusion at a distance more than 27  $\mu\text{m}$ . In addition, it was confirmed that the amount of detected oxygen along the hydrophobic channel region is significantly higher than the hydrophilic channel region by experiment above 30  $\mu\text{m}$  of the amphiphilic porous transport layer.

In chapter 5, the effects of operation configuration and relative humidity (RH) of providing fuels on fuel cell performance were analyzed when the IrO<sub>2</sub>-

electrodeposited porous transport layer including Pt catalysts, which is the oxygen electrode in electrolysis operation, is introduced in URFC. Since Pt is active catalysts in both ORR and hydrogen oxidation reaction (HOR), the IrO<sub>2</sub>-electrodeposited electrode including Pt can be used as either an oxygen electrode or a hydrogen electrode. When operating the electrode as a hydrogen electrode instead of an oxygen electrode generally reported, it has the following advantages. First, in the aspect of water management, reduction of fuel cell performance from flooding can be solved by using a hydrophobic carbon porous transport layer, which is optimized for fuel cell operation, in the oxygen electrode. Second, Pt/C catalysts having high mass activity from higher electrochemical active surface area compared to Pt black can be used in oxygen electrode where relatively sluggish ORR occurs. Third, it is possible to reduce the amount of Pt catalysts at the electrodeposited electrode when Pt is used as relatively fast HOR catalysts in a hydrogen electrode. Due to the difference in properties of the hydrophilic electrodeposited electrode and the hydrophobic carbon electrode, the effects of RH on the performance of fuel cell are significantly different when the electrodeposited electrode is used as an oxygen electrode and when it is used as a hydrogen electrode. As a result of comparison between estimated water distribution in the electrode and the results of operation according to the RH, lower ohmic resistance and higher performance was observed as anode water content increases. In this study, high water electrolysis and fuel cell performance were achieved with low noble catalysts loading of 0.65 mg<sub>(Pt+Ir)</sub> cm<sup>-2</sup> by control

of operation configuration and relative humidity.

Chapter 6 demonstrated research about analysis of the effects of electrode fabrication and operation methods to improve performance of anion exchange membrane water electrolysis (AEMWE). AEMWE has advantages of in terms of cost compared to proton exchange membrane water electrolysis due to the use of non-noble metal catalysts and cheaper membranes as water electrolysis occurs in an alkaline environment, but its reported performances are low. Except for the materials, the performance of AEMWE was optimized by analysis of the influence of pressing in membrane-electrode assembly, torque of cell assembly, pre-feeding electrolyte and operation temperature.

**Keywords:** unitized regenerative fuel cells, polymer exchange membrane water electrolysis, electrodeposition, scanning electrochemical microscopy

**Student Number:** 2015-21029

# Contents

<b>Abstract.....</b>	<b>i</b>
<b>Contents .....</b>	<b>vii</b>
<b>List of Tables.....</b>	<b>xi</b>
<b>List of Figures.....</b>	<b>xiii</b>
<b>Chapter 1. Introduction.....</b>	<b>1</b>
1.1. General Introduction to Polymer Electrolyte Membrane based Water Electrolysis and Fuel Cells .....	1
1.2. General Introduction to Unitized Regenerative Proton Exchange Membrane Fuel Cells (UR-PEMFC).....	9
1.3. Applications of Electrodeposition in Proton Exchange Membrane based Water Electrolysis and Fuel Cells .....	15
1.4. Aim of This Thesis .....	18
1.5. References .....	21

**Chapter 2. Low-loading IrO<sub>2</sub> Supported on Pt for Catalysis of PEM Water Electrolysis and Regenerative Fuel Cells.. 31**

2.1. Introduction ..... 31

2.2. Experimental Section ..... 35

2.3. Results and Discussion ..... 38

2.4. Conclusions ..... 73

2.5. References ..... 74

**Chapter 3. Through-Plane Amphiphilic Channel Formation on Porous Transport Layer for Highly Effective Unitized Regenerative Fuel Cell (URFC)..... 83**

3.1. Introduction ..... 83

3.2. Experimental Section ..... 85

3.3. Results and Discussion ..... 89

3.4. Conclusions ..... 107

3.5. References ..... 108

**Chapter 4. Scanning Electrochemical Microscopy (SECM)..... 112**

4.1. Introduction .....	112
4.2. Experimental Section .....	113
4.3. Results and Discussion .....	116
4.4. Conclusions .....	138
4.5. References .....	139

**Chapter 5. Highly Efficient Operation of Unitized Regenerative Fuel Cell with Amphiphilic Membrane-Electrode Assembly .....** **141**

5.1. Introduction .....	141
5.2. Experimental Section .....	147
5.3. Results and Discussion .....	149
5.4. Conclusions .....	170
5.5. References .....	171

**Chapter 6. A Study on Electrode Fabrication and Operation Variables Affecting the Performance of Anion Exchange Membrane Water Electrolysis .....** **180**

6.1. Introduction .....	180
-------------------------	-----

6.2. Experimental Section .....	186
6.3. Results and Discussion .....	188
6.4. Conclusions .....	210
6.5. References .....	211
<b>Chapter 7. Conclusions.....</b>	<b>218</b>
7.1. Summary .....	218
7.2. Perspectives .....	222
7.3. References .....	227
<b>국문 초록 .....</b>	<b>231</b>
<b>Appendix. Publication List.....</b>	<b>236</b>

# List of Tables

<b>Table 1.1.</b> Operation principles, advantages and disadvantages of PEMWE and AEMWE. ....	3
<b>Table 1.2.</b> Operation principles, advantages and disadvantages of PEMFC and AEMFC.....	6
<b>Table 1.3.</b> Comparison of specific energy of URFC with other rechargeable batteries.....	11
<b>Table 1.4.</b> Previous reported round trip efficiency of UR-PEMFC with types of membrane, amount of catalysts loading and operation temperature.....	13
<b>Table 1.5.</b> Overview of Pt or IrO <sub>2</sub> electrodeposition in PEMFC or PEMWE. ..	17
<b>Table 2.1.</b> PEMWE current density at 1.9 V, PEMWE current density at 0.5 V, amount of catalysts on the oxygen electrode with different electrodeposition time of Pt from 0 to 10 min. The catalyst loading was determined by ICP-OES. ....	47
<b>Table 2.2.</b> Resistance of bare Ti, e-IrO <sub>2</sub> , e-Pt and sequential e-Pt@IrO <sub>2</sub> obtained from 4-probe measurement using FIB-Quanta 3D. Resistivity was estimated with the assumption of cross-section area 400 μm <sup>2</sup> and probe distance 10 μm. ....	62
<b>Table 2.3.</b> Literature review of round trip efficiency (RT) at 0.2 A cm <sup>-2</sup> and 0.4 A cm <sup>-2</sup> of UR-PEMFC including the catalyst loading. URFC reports shown in the table are based on non-carbon PTL for the oxygen electrode in water electrolysis. (m <sub>O</sub> : noble-catalyst loading of oxygen electrode in fuel cell, m <sub>H</sub> : noble-catalyst loading of hydrogen electrode in fuel cell, m <sub>tot</sub> is the sum of m <sub>O</sub> and m <sub>H</sub> ) .....	68

**Table 5.1.** Definition of abbreviations in manuscripts..... 146

**Table 6.1.** AEMWE current density at 1.8 V with different variables employed in the cell fabrication and operation. The electrolysis current was obtained at 50<sup>th</sup> cycle in voltage cycle operation from 1.5 to 2.2 V except the measurements at different operation temperatures. For the temperature controlled operations, current density at 1.8 V was averaged during 60 min of chronoamperometry. 189

# List of Figures

<b>Figure 1.1.</b> Schematic structure and operation of URFC. ....	12
<b>Figure 1.2.</b> Schematic summary of the main thesis.....	20
<b>Figure 2.1.</b> Schematic procedure of fabrication of e-Pt@IrO <sub>2</sub> and e-IrO <sub>2</sub> . ....	40
<b>Figure 2.2.</b> Electrochemical analysis in iridium oxide electrodeposition. (a) Cyclic voltammetry in precursor solution (pH 10.5) of Iridium oxide electrodeposition using rotating disk electrode without rpm at 5 mV s <sup>-1</sup> and its average current density vs. potential. (b) Enlarged image of (a). ....	41
<b>Figure 2.3.</b> SEM and TEM Image of e-IrO <sub>2</sub> and e-Pt@IrO <sub>2</sub> . (a) Top and (b) cross-section FIB-SEM images of e-IrO <sub>2</sub> on each fiber in Ti felt. (c) STEM image of sequential e-Pt@IrO <sub>2</sub> (inserted; HAADF-STEM TEM image). (d) Top and (e) cross-section FIB-SEM images of sequential e-Pt@IrO <sub>2</sub> . Surface Pt coatings were done for surface protection during straight cutting using ion-beam. (f) Quantitative EDX elemental maps image of sequential e-Pt@IrO <sub>2</sub> (red:Ir, sky blue: Ti, green: Pt).....	42
<b>Figure 2.4.</b> Image of Pt electrodeposited electrodes. SEM images of e-Pt/Ti. Pt deposition time was varied from 0.5 min to 10 min from top-left to bottom-right (scale bar in inserted figures: 1 μm).....	43
<b>Figure 2.5.</b> Particle size distribution of electrodeposited Pt (5 min). ....	46
<b>Figure 2.6.</b> Elemental distribution observed in the cross-section of e-Pt@IrO <sub>2</sub> electrode. EDS mapping of cross-section of the sequential e-Pt@IrO <sub>2</sub> (0.16 mg <sub>Ir</sub>	

cm<sup>-2</sup>, 0.28 mg<sub>Pt</sub> cm<sup>-2</sup>)/Ti (scale bar in figures: 100 μm). ..... 48

**Figure 2.7.** Hydrophobicity/hydrophilicity property of the electrodes. Water contact angle of (a) C PTL (10 BC), (b) Ti PTL, (c) IrO<sub>2</sub> electrodeposited Ti PTL and (d) sprayed IrO<sub>2</sub> on Ti PTL. .... 49

**Figure 2.8.** Elemental distribution observed in the top-surface of e-Pt@IrO<sub>2</sub> electrode. EDS mapping of surface of the sequential e-Pt@IrO<sub>2</sub> (0.16 mg<sub>Ir</sub> cm<sup>-2</sup>, 0.28 mg<sub>Pt</sub> cm<sup>-2</sup>)/Ti (scale bar in figures: 2 μm). ..... 50

**Figure 2.9.** URFC Performance with different catalyst amounts of e-Pt@IrO<sub>2</sub>. The e-Pt@IrO<sub>2</sub> was used as oxygen electrode in both WE and FC and FC performance was measured after reduction of IrO<sub>2</sub> surface to Ir. (a) IV curve of URFC (Pt deposition time controlled from 0.5 min to 10 min). (b) Current density at 1.9 V (WE mode) and 0.5 V (FC mode) with the different amount of electrodeposited e-Pt@IrO<sub>2</sub>. ..... 51

**Figure 2.10.** Surface element characterization of e-IrO<sub>2</sub> and e-Pt@IrO<sub>2</sub> by XPS. (a) Pt (4f<sub>5/2</sub> and 4f<sub>7/2</sub>) and (b) Ir (4f<sub>5/2</sub> and 4f<sub>7/2</sub>) peaks of e-Pt (black) and e-Pt@IrO<sub>2</sub> (red) in XPS. .... 52

**Figure 2.11.** Comparison of IrO<sub>2</sub> nanoparticles on Ti PTL fabricated by spray and electrodeposition method. (a) TEM images of commercial IrO<sub>2</sub> nanoparticles used in s-IrO<sub>2</sub>. (b) Cross-section SEM images of s-IrO<sub>2</sub> (3.5 mg<sub>Ir</sub> cm<sup>-2</sup>) showing Ti and IrO<sub>2</sub> nanoparticle (yellow dots) distribution from EDS mapping. (c) TEM images of IrO<sub>2</sub> nanoparticles from e-IrO<sub>2</sub>. (d) Cross-section SEM images of e-IrO<sub>2</sub> (0.15 mg<sub>Ir</sub> cm<sup>-2</sup>) showing Ti and IrO<sub>2</sub> nanoparticle (yellow dots) distribution from EDS

mapping. .... 55

**Figure 2.12.** Comparison of IV performance of UR-PEMFC, porosity of the electrodes and round trip efficiency. (a) IV curve of PEMWE operation. (closed symbol: electrodeposited-catalysts electrode, open symbol: spray-catalysts electrode, red: Ir oxide and Pt, blue: only Ir oxide) (b) Pore distribution of electrodes measured by mercury porosimetry in 0.5 – 4  $\mu\text{m}$  range (inserted; 0.5 - 100  $\mu\text{m}$  range). (c) IV curve of PEMFC operation ( $T_{\text{cell}}$ : 80°C). In the device using e-Pt@IrO<sub>2</sub> or reduced e-Pt@IrO<sub>2</sub> operates as the FC oxygen electrode (cathode). H<sub>2</sub> and O<sub>2</sub> temperature was at 70°C (black dash and blue dot line). When reduced e-Pt@IrO<sub>2</sub> is used as the FC hydrogen electrode (anode), H<sub>2</sub> and O<sub>2</sub> temperature was held at 70 and 80°C, respectively (red solid line). (d) Round trip efficiency at 0.4 A cm<sup>-2</sup> versus total noble-catalysts loading in single cell..... 56

**Figure 2.13.** Potentiostatic Electrochemical Impedance Spectroscopy (PEIS) at 2.0 V<sub>cell</sub> in water electrolysis for different electrodes. (a) Equivalent circuit for Impedance fitting analysis. PEIS data (black) and fitting results (red) of (b) e-Pt@IrO<sub>2</sub> (0.16 mg<sub>Ir</sub> cm<sup>-2</sup>), (c) e-IrO<sub>2</sub> (0.15 mg<sub>Ir</sub> cm<sup>-2</sup>) and (d) s-IrO<sub>2</sub> (3.5 mg<sub>Ir</sub> cm<sup>-2</sup>)..... 58

**Figure 2.14.** XPS of Ir detected in e-Pt@IrO<sub>2</sub>. XPS (a) before and (b) after electrochemical reduction process. .... 60

**Figure 2.15.** CVs of e-Pt@IrO<sub>2</sub> and Ir electrode ranged from 0.05 to 0.6 V (vs. pseudo RHE). CVs of e-Pt@IrO<sub>2</sub> electrode before and after electrochemical reduction process (black and red) including commercial metallic Ir electrode

sprayed on Ti PTL. (a) Comparison of CVs before and after electrochemical reduction process at e-Pt@IrO<sub>2</sub> and metallic Ir electrode and (b) e-IrO<sub>2</sub> electrode.

..... 61

**Figure 2.16.** SEM image of 4-probe resistivity measurement in FIB-Quanta 3D.

(a) Bare Ti, (b) e-IrO<sub>2</sub> /Ti, (c) e-Pt/Ti and (d) sequential e-Pt@IrO<sub>2</sub>/Ti (scale bar: 10 μm). ..... 63

**Figure 2.17.** IV of FC mode of URFC with controlled temperature of the oxygen electrode (cathode, e-Pt@IrO<sub>2</sub> electrode). T<sub>ca</sub> indicates temperature of O<sub>2</sub> gas feeding to cathode. The temperature of fuel in the hydrogen electrode (anode, Pt/C electrode) was controlled to 70 °C. .... 67

**Figure 2.18.** Long-term operation of URFC (e-Pt@IrO<sub>2</sub> as anode and Pt/C as cathode of URFC, T<sub>H<sub>2</sub></sub>: 70°C, T<sub>O<sub>2</sub></sub>: 80°C T<sub>cell</sub>: 80°C). (a) Cell voltage at 0.4 A cm<sup>-2</sup> and (b) high frequency resistance measured at 5 kHz in EIS during long-term operation. .... 70

**Figure 2.19.** SEM images of surface of (a) Ti PTL and (b) membrane detached from MEA after long term tests of ED-Pt@IrO<sub>2</sub>. .... 71

**Figure 3.1.** Schematic illustration of fabrication procedure of amphiphilic porous transport layers (PTLs). ..... 88

**Figure 3.2.** Optical microscope images of shadow masks of (a) LP (width: 125 μm, space: 125 μm, pitch: 250 μm) and (b) SP (width: 30 μm, space: 45 μm, pitch: 75 μm). .... 92

**Figure 3.3.** Optical microscope images and photographs of (a) Ref, (b) NP, (c)

SP and (d) LP after dropping water. (e) The enlarged photograph of LP. (Blue indicates the region of hydrophilic channels and red indicates the region of hydrophobic channels.)..... 93

**Figure 3.4.** (a) FE-SEM images of bare Ti and PDMS brush treated Ti. (b) FE-SEM images during 4-probe measurements of bare Ti and PDMS brush treated Ti including nanomanipulators. The inserted values in images are measured conductivity..... 95

**Figure 3.5.** (a) Surface characterization by XPS of e-IrO<sub>2</sub> side of PDMS treated e-IrO<sub>2</sub>/Ti (NP), bare Ti and PDMS coated side of NP. (b) NEXAFS C K-edge spectra of bare Ti, e-IrO<sub>2</sub>/Ti (Ref), NP (PDMS coated side) and PDMS polymer brush..... 97

**Figure 3.6.** Comparison of IV performance and power density between Ref, NP, SP and LP in FC mode at (a) RH 65 and (b) RH 100. (c) Comparison of current density at 0.6 V at RH 65 and RH 100. Ref refers to e-IrO<sub>2</sub>/Ti, NP refers to PDMS coated e-IrO<sub>2</sub>/Ti without patterns, and SP and LP refers to PDMS coated e-IrO<sub>2</sub>/Ti with small and large patterns. .... 100

**Figure 3.7.** Comparison of (a) IV performance and (b) Nyquist plot of galvanostatic impedance spectroscopy (GEIS) at 2 A cm<sup>-2</sup> between Ref, NP, SP and LP in EC mode. (c) Comparison of overvoltage from mass transport resistance at 2 A cm<sup>-2</sup> and current density at 1.8 V between Ref, NP, SP and LP. .... 101

**Figure 3.8.** (a) URFC performance and round trip efficiency (RT) at 0.5 A cm<sup>-2</sup>

of PTLs (Ref, NP, SP and LP). (b) Comparison of RT at  $0.5 \text{ A cm}^{-2}$  versus total catalyst loading in URFC single cell with previous researches. The data of previous studies in the graph are limited to the case of using non-carbon PTLs in the oxygen electrode of URFC..... 103

**Figure 3.9.** Long-term URFC operation of LP at  $0.5 \text{ A cm}^{-2}$  (FC:  $\text{H}_2/\text{O}_2$ , RH 65).

During long-term operation, high frequency resistance at 50 kHz in GEIS (@  $0.5 \text{ A cm}^{-2}$ ) was measured every 2 minutes..... 105

**Figure 3.10.** Cyclic voltammetry from 0.05 to 1.1 V (vs. pseudo RHE) of LP before and after the 160 h long term test. Fully humidified  $\text{H}_2$  gas was purged to Pt/C catalysts on the C PTL, which acted as a pseudo reference. Fully humidified  $\text{N}_2$  gas was purged to the large patterned e- $\text{IrO}_2/\text{Ti}$  PTL including Pt black catalysts..... 106

**Figure 4.1.** Structure illustration of the SECM. .... 114

**Figure 4.2.** Cyclic voltammetry of (a) 5 mm glassy carbon disk electrode and (b) 25  $\mu\text{m}$  ultramicroelectrode (UME) in ferricyanide/ferrocyanide redox couple solution through the scan rate from  $5 \text{ mV s}^{-1}$  to  $100 \text{ mV s}^{-1}$ . .... 118

**Figure 4.3.** Setting of basic experiments including feedback modes. (a) The photo of the substrate and (b) the schematic diagram of the test system with the UME in SECM used in basic experiments. (c) The schematic illustration of a negative feedback mode of the UME on insulator. (d) Decrease of the tip current as approach of the UME tip to the insulating substrate. (g) The schematic illustration of a positive feedback mode of the UME on conductor. (h) Increase of the tip

current as approach of the UME tip to the conductive substrate. ....	119
<b>Figure 4.4.</b> Leveling of the substrate in ferricyanide/ferrocyanide redox couple solution with approach curves. (a) Schematic method of leveling by controlling the height of the substrate. Approach curves at three points (UNE tip: $-0.25 V_{Ag/AgCl}$ ) (b) before and (c) after leveling. ....	122
<b>Figure 4.5.</b> Schematic diagram of setting of Ti substrates for line mapping, area mapping, etc. in SECM. Inserted SEM image is the Ti porous transport layer used in the experiments. ....	124
<b>Figure 4.6.</b> Experimental and simulated approach curves. $h$ is the ratio of radius of substrate to that of UME tip. ( $L=d/a$ , $d$ : distance between the tip and the substrate, $a$ : radius of the UME tip). ....	125
<b>Figure 4.7.</b> (a) Theoretical approach curves on the conductive substrate and the insulating substrate for some $RG$ values, e.g. 10, 8, 5. The theoretical values are obtained from ref. [4]. (b) The example of fitting of the approach curve on the Kapton tape (the insulating substrate). ....	126
<b>Figure 4.8.</b> (a) Schematic example of line-mapping of Ti PTL using SECM in $[Fe(CN)_6]^{4-} / [Fe(CN)_6]^{3-}$ redox couple solution. Line mapping of Ti PTL (b) without and (b) with surface polymer coating in two cases, i.e. Ti substrate at OCV and $0.6 V_{Ag/AgCl}$ . ....	128
<b>Figure 4.9.</b> Area mapping of Ti porous transport layer without polymer coating ( $500 \mu m \times 500 \mu m$ ) using SECM. (Pt tip: $-0.25 V_{Ag/AgCl}$ , Ti substrate: $0.6 V_{Ag/AgCl}$ ) ....	129

**Figure 4.10.** (a) Schematic illustration of line scan of the OER-ORR (SG-TC) mode of a UME on the back side of the iridium oxide electrodeposited Ti PTL without polymer coating. (b) Comparison of normalized collection efficiency (C.E) of line scans of the OER-ORR (SG-TC) mode on the back side of the iridium oxide electrodeposited Ti PTL through the distance of the UME tip on the substrate and  $i_T/i_{T,\infty}$  of the positive feedback mode in line scan using  $[\text{Fe}(\text{CN})_6]^{4-}/[\text{Fe}(\text{CN})_6]^{3-}$  redox solution. Potentials of the substrate and the tip were 1.15 and 0  $V_{\text{Ag}/\text{AgCl}}$  in the OER-ORR (SG-TC) mode and 0.6 and -0.25 0  $V_{\text{Ag}/\text{AgCl}}$  in the positive feedback mode..... 131

**Figure 4.11.** (a) Schematic illustration of line scan of the OER-ORR (SG-TC) mode of a UME on the back side of hydrophobic polymer patterned Ti PTL. (b) Generated  $\text{O}_2$  and detected  $\text{O}_2$  through line scan on the back side of the hydrophobic polymer patterned Ti PTL. Potentials of the substrate and the tip were 1.15  $V_{\text{Ag}/\text{AgCl}}$  and 0  $V_{\text{Ag}/\text{AgCl}}$  in the OER-ORR (SG-TC) mode..... 134

**Figure 4.12.** The example of current density through time on (a) the substrate and (b) the tip from OER and ORR (at 625  $\mu\text{m}$ ). The inserted figure in (b) is the magnified graph in the region of 27.5 to 45.0 second..... 136

**Figure 4.13.** (a) Detected amount of oxygen estimated by UME tip current on each position of the backside of patterned Ti PTL at 40 sec ( $d=30 \mu\text{m}$ ). (b) Line-mapping of the region of points detection in  $[\text{Fe}(\text{CN})_6]^{4-}/[\text{Fe}(\text{CN})_6]^{3-}$  redox couple solution at  $d=20 \mu\text{m}$ . ..... 137

**Figure 5.1.** Schematic illustration of two operation configurations in unitized

regenerative fuel cell (URFC). (a) hydrogen and oxygen electrode configuration (HOEC) and (b) reduction and oxidation electrode configuration (ROEC).....	145
<b>Figure 5.2.</b> SEM and EDS mapping of top surface of e-IrO <sub>2</sub> /Ti (0.15 mg <sub>Ir</sub> cm <sup>-2</sup> ).....	151
<b>Figure 5.3.</b> SEM and EDS mapping of top surface of s-IrO <sub>2</sub> /Ti (0.15 mg <sub>Ir</sub> cm <sup>-2</sup> ).....	152
<b>Figure 5.4.</b> Overlapping SEM and EDS images of cross-section of (a) e-IrO <sub>2</sub> /Ti and (b) s-IrO <sub>2</sub> /Ti (inserted bar: 50 μm). ....	153
<b>Figure 5.5.</b> Water contact angle of pristine C PTL, IrO <sub>2</sub> spray coated C PTL, pristine Ti PTL, IrO <sub>2</sub> spray coated Ti PTL and IrO <sub>2</sub> electrodeposited Ti PTL. ....	154
<b>Figure 5.6.</b> Schematic illustration of water distribution inside of membrane electrode assembly (MEA) during operation of fuel cell.....	156
<b>Figure 5.7.</b> Estimated (a) membrane water flux (MWF), (b) cathode water out-flux (CWF) and (c) anode water out-flux (AWF) versus current density according to conditions of gas humidification.....	159
<b>Figure 5.8.</b> IV performance and current density at 0.6 V through control of relative humidity (RH) in (a) ROEC and (b) HOEC operation. In RH A/B, A and B indicate RH value of anode and cathode, respectively. ....	162
<b>Figure 5.9.</b> Comparison of ohmic resistance (R <sub>ohm</sub> ) and estimated water out-flux based on current density and impedance measurements at 0.6 V of FC. (a) Ohmic resistance and estimated anode water out-flux (AWF) according to RH conditions	

in ROEC operation. (b) Ohmic resistance and estimated total water out-flux (TWF) according to RH conditions in HOEC operation. .... 163

**Figure 5.10.** Comparison of charge transfer resistance ( $R_{ct}$ ) and estimated cathode water out-flux (CWF) according to RH conditions based on current density and impedance measurements at 0.6 V of FC in (a) ROEC and (b) HOEC operation. .... 164

**Figure 5.11.** Comparison of IV performance of FC according to the amount of Pt black catalysts (0.6, 0.2 and 0.1  $\text{mg cm}^{-2}$ ) in (a) ROEC (RH100(Ca.)/RH100(An.)) and (b) HOEC RH100(Ca.)/RH65(An.) operation ..... 166

**Figure 5.12.** Comparison of (a) IV performance of URFC in ROEC according to the amount of Pt black catalysts (0.6, 0.2 and 0.1  $\text{mg cm}^{-2}$ ) and (b) Round trip efficiency at 0.4  $\text{A cm}^{-2}$  versus reciprocal values of catalyst loading..... 168

**Figure 5.13.** Long-term operation of URFC at 0.4  $\text{A cm}^{-2}$  during 80 h (ROEC: Pt(CCM),e-IrO<sub>2</sub>/Ti electrode as anode and Pt/C(CCM) C electrode as cathode of URFC). Cell temperature of both FC (RH 65) and EC is 80°C. Amount of Pt black catalysts loading is 0.1  $\text{mg cm}^{-2}$ . .... 169

**Figure 6.1.** Schematic procedure of fabrication and operation of the anion exchange membrane water electrolysis cell..... 183

**Figure 6.2.** Performance summary of AEMWE cells with different fabrication and operation variables. The displayed performance is the current density at 1.8 V measured at 50<sup>th</sup> cycle in voltage cycle operation from 1.5 to 2.2 V. However, for the temperature controlled operation, current density at 1.8 V was averaged

during 60 min of chronoamperometry. Factors of the AEMWE fabrication and operation are summarized in Table 1. .... 190

**Figure 6.3.** (a) Current-voltage relationship, (b) Nyquist plot, and (c) SEM images of the anode catalyst layer surface of AEMWE cells with different press time used in the electrode fabrication (0, 1, and 3 min.). PEIS was measured at 500<sup>th</sup> cycle at 1.8 V. .... 192

**Figure 6.4.** (a) Primary pore and (b) secondary pore distribution of cathode with different press time used in the electrode fabrication (0, 1, and 3 min.). The pore distribution is measured by mercury porosimetry. .... 195

**Figure 6.5.** SEM images of the cathode catalyst layer surface of AEMWE cells with different press time used in the electrode fabrication (0, 1, and 3 min.). 197

**Figure 6.6.** (a) Primary pore and (b) secondary pore distribution of anode electrodes with different press time used in the electrode fabrication (0, 1, and 3 min.). The pore distribution is measured by mercury porosimetry. .... 197

**Figure 6.7.** (a) The picture of gasket with contamination after the operation in the case of 3 Nm cell assembly. The results of pressure-film after application of (b) 3Nm, (c) 4Nm, (d) 5 Nm assemble torque on the cell. .... 198

**Figure 6.8.** Linear sweep voltammetry with different torque of cell assembly. .... 198

**Figure 6.9.** (a) Ohmic resistance change in the continuous solution feed of 0.5 M KOH electrolyte solution to AEMWE single cell. CVs at (b) 50<sup>th</sup> and (c) 500<sup>th</sup> cycle with and without 24 h of electrolyte pre-feed to AEMWE cell. The ohmic

resistance was measured in EIS at open circuit voltage. CVs were measured at a scan rate of 20 mV/s. ....	201
<b>Figure 6.10.</b> (a) Linear sweep voltammetry and (b) ohmic resistance with different solution. ....	202
<b>Figure 6.11.</b> Calculated open circuit voltage of water electrolysis versus temperature from 0 to 100 °C. ....	203
<b>Figure 6.12.</b> (a) Chronoamperograms and (b) EIS Nyquist plots of the AEMWE cell operated at different temperatures from 50 to 90 °C. The chronoamperometry and EIS was performed at the identical overvoltage of 0.59 V at different operational temperatures. ....	206
<b>Figure 6.13.</b> Conductivity of electrolysis cell based on ohmic resistance measured by impedance spectroscopy during cell-operation. (Assume ion transport resistance in the membrane dominates the ohmic resistance during the operation of the electrolysis cell.) ....	207
<b>Figure 6.14.</b> Chronoamperometry of 90 °C operation at 1.8 V (w/o pressing, 4 Nm torque of cell assembly, 24 h 0.5 M KOH prefeed) for 1 hour. ....	208
<b>Figure 6.15.</b> Comparison of AEMWE performance with other research. ....	209
<b>Figure 7.1.</b> Schematic example fields of applications of URFC systems. ....	225
<b>Figure 7.2.</b> A schematic example of power curve of renewable energy supply and electrical demand through time. ....	226

# **Chapter 1. Introduction**

## **1.1. General Introduction to Polymer Electrolyte Membrane Based Water Electrolysis and Fuel Cells**

### **1.1.1. Hydrogen Generation by Polymer Exchange Membrane Water Electrolysis**

As greenhouse gas emissions expedite the global warming and climate change, hydrogen takes center stage of ideal alternative fuel in future since it is environmentally clean, i.e. no carbon emission, and has high energy density, i.e. 33.3 kWh kg<sup>-1</sup> for pressurized hydrogen at 200 bar or liquid hydrogen [1]. However, hydrogen is the lightest molecule, which is not abundant in nature in the form of H<sub>2</sub>. To produce hydrogen, there are many different technologies such as hydrocarbon steam reforming, pyrolysis, plasma reforming, biomass gasification, ammonia reforming and water electrolysis, etc [2]. Steam reforming is an already commercialized main technology used in large scale hydrogen production in industry due to its high thermal efficiency (>85%) and low cost of production. However, there is still the issue of low level production of carbon dioxide [2]. Ammonia reforming is attractive to produce hydrogen without carbon emission, because ammonia is abundant and the pipeline systems are already established. Nevertheless, the usual ammonia production technology, i.e. Harbor-Bosch process, induces significant

production of carbon dioxide in the process during ammonia synthesis reaction at low temperature (400-500 °C) and high pressure (150-200 atm), e.g.  $\sim 2 \text{ ton}_{\text{CO}_2} \text{ ton}_{\text{NH}_3}^{-1}$ . [3, 4]. If alternative ways of this technology are not developed, hydrogen production from ammonia reforming is not available. In addition, even if such a new technology is discovered, it would be more desirable to use ammonia as fuel rather than the source of hydrogen production since ammonia itself has high energy density (4.3 KWh L<sup>-1</sup>) with moderate condition for liquefied storage (-33 °C at 1 atm or 10 atm at ambient temperature) [5, 6].

Water electrolysis has substantial potential of zero carbon footprint if renewable energy is utilized as applied electricity in process. Conventional water electrolysis is alkaline water electrolysis (AWE), which consists of anode, cathode and diaphragm separators in between to separate produced gases, conduct ions, block the contact of anode and cathode in alkaline liquid electrolyte. To reduce voltage loss from ionic conduction, highly conductive electrolytes, e.g. pH 13-14 of KOH or NaOH solution, are used in AWE. However, it has limitations in current density ( $< 0.4 \text{ A cm}^{-2} @ 2 \text{ V}$ ) and energy efficiency (70-80%) [7, 8]. In polymer electrolyte membrane based water electrolysis, polymer membrane embedded ionizable functional groups supersedes the diaphragm. Since functional groups are covalently bonded to the polymer and captured the conductive ions in water, i.e. OH<sup>-</sup> or H<sup>+</sup>, high ionic conductivity is achievable even in provision of pure water to the cell [9]. In addition, it has advantages of high energy density (80-90 %), fast-start up, compact system, high purity of produced gas and availability to pressurized operation up to 700 bar [8, 10].

Depending on the kind of conductive ions in membrane, polymer electrolyte membrane based water electrolysis can be divided in proton exchange membrane water electrolysis (PEMWE) and anion exchange membrane water electrolysis

**Table 1.1.** Operation principles, advantages and disadvantages of PEMWE and AEMWE.

	PEMWE	AEMWE
<b>Scheme of Operation Principle</b>	<p>[Cathode] [Membrane] [Anode]</p>	<p>[Cathode] [Membrane] [Anode]</p>
<b>Electrochemical Reaction</b>	<p>Anode : <math>\text{H}_2\text{O} \rightarrow \frac{1}{2} \text{O}_2 + 2 \text{H}^+ + 2 \text{e}^-</math></p> <p>Cathode : <math>2 \text{H}^+ + 2 \text{e}^- \rightarrow \text{H}_2</math></p> <p>Overall : <math>\text{H}_2\text{O} \rightarrow \text{H}_2 + \frac{1}{2} \text{O}_2</math></p>	<p>Anode : <math>2 \text{OH}^- \rightarrow \frac{1}{2} \text{O}_2 + \text{H}_2\text{O} + 2 \text{e}^-</math></p> <p>Cathode : <math>2 \text{H}_2\text{O} + 2 \text{e}^- \rightarrow \text{H}_2 + 2 \text{OH}^-</math></p> <p>Overall : <math>\text{H}_2\text{O} \rightarrow \text{H}_2 + \frac{1}{2} \text{O}_2</math></p>
<b>Advantages</b>	<ul style="list-style-type: none"> <li>High current density (<math>&gt; 2 \text{ A cm}^{-2}</math>).</li> <li>High energy efficiency.</li> </ul>	<ul style="list-style-type: none"> <li>The use of less expensive, non-PGM electrocatalysts.</li> <li>The use of less expensive polymer electrolyte membrane.</li> </ul>
<b>Disadvantages</b>	<ul style="list-style-type: none"> <li>Use of expensive noble electrocatalysts due to harsh acid condition.</li> <li>Use of expensive polymer membrane, e.g. perfluorosulfonic acid polymer.</li> </ul>	<ul style="list-style-type: none"> <li>Low thermal stability of the membrane.</li> <li>Low energy efficiency compared to PEMWE.</li> </ul>

(AEMWE). The basic operation principle and advantages/disadvantages are shown in Table 1.1. The basic core structure is composed of membrane and porous electrodes with catalysts in between, called membrane electrode assembly (MEA). Influx of water to the catalysts in the electrode first, and then electrochemical reactions i.e. oxidation reaction of oxygen evolution (OER) at anode and hydrogen evolution reaction (HER) at cathode, are occurred. Then, produced gas ( $O_2 / H_2$ ) are passed through porous electrode, called porous transport layer (PTL). Highly conductive ( $0.1 \pm 0.02 \text{ S cm}^{-1}$ ) and chemically and mechanically stable membrane and fast kinetics from catalysts contribute to high performance of PEMWE ( $> 2 \text{ A cm}^{-2}$  @  $2 \text{ V}$ ). For instance, solid polysulfonated membranes, e.g. Nafion<sup>®</sup>, pumafem<sup>®</sup>, are commonly used in industry. Due to harsh acid condition, highly active noble catalysts, e.g.  $IrO_2/RuO_2$  as OER catalysts, Pt/Pd as HER catalysts, are normally reported in PEMWE single cells [8]. Substantial researches were done in PEMWE field and it has approached the stage of commercialization with high energy density and stability. However, continuous research is still required to reduce the costs of materials used in PEMWE with maintaining high efficiency and stability to expand the share of market.

On the other hand, AEMWE has a lot of potential to be developed. It supplements the limitation of porous diaphragm in conventional AWE, e.g. gas crossover issue, and combines advantages of PEM electrolysis, e.g. availability of pressurized system, operating under pure water, improved purity of produced gas. Additionally, it maintains alkaline condition, which leads applicability of non-noble metal nanoparticles [11], e.g. Ni- and Co- based metal oxides [12, 13] as electrocatalysts, and less expensive membrane, which has advantages in the aspect of cost. Many researches focused on materials [11, 14-16], but the state of device research is not

mature as material research in AEMWE, less than  $0.5 \text{ A cm}^{-2}$  at  $1.8 \text{ V}$  [17-19]. However, some of high performance AEMWE has reported recently. Fortin et al. reported  $2 \text{ A cm}^{-2}$  @  $1.82 \text{ V}$  using Aemion<sup>®</sup> AEM [20]. Liu et al. demonstrated  $1.63 \text{ V}$  @  $1 \text{ A cm}^{-2}$  with noble catalysts and  $1.90 \text{ V}$  @  $1 \text{ A cm}^{-2}$  with non-noble catalysts by using Sustainion<sup>®</sup> membranes, but if the cell operates without using noble-metals, it is still lower current density ( $< 2 \text{ A cm}^{-2}$  @  $2 \text{ V}$ ) compared to PEMWE [21]. Recent researches reveal great potential of AEMWE in performance. If the stability of the membrane and the activity of non-noble catalysts in the cell are enhanced, commercialization of AEMWE like PEMWE is in the near future.

### **1.1.2. Electrical Power Generation from Polymer Exchange Membrane Fuel Cell**

Fuel cell (FC) is one of the most promising alternative power device without producing any greenhouse gases. Depending on operation temperature and electrolytes, it is classified to low-temperature PEMFC ( $60\text{-}80 \text{ }^\circ\text{C}$ ), low-temperature AEMFC ( $60\text{-}80 \text{ }^\circ\text{C}$ ), high-temperature PEMFC ( $110\text{-}180 \text{ }^\circ\text{C}$ ), solid oxide FC (SOFC,  $800\text{-}1000 \text{ }^\circ\text{C}$ ), molten carbonate FC (MCFC,  $600\text{-}700 \text{ }^\circ\text{C}$ ), phosphoric acid FC (PAFC,  $160\text{-}220 \text{ }^\circ\text{C}$ ), direct methanol FC (DMFC, ambient- $110 \text{ }^\circ\text{C}$ ), microbial fuel cell (MFC,  $20\text{-}60 \text{ }^\circ\text{C}$ ), etc. [22]. Among fuel cells, PEMFC is the most mature state, which is in commercialization in many areas, such as backup power supply and transportations. Operating principle is opposite of electrolysis; hydrogen and air/oxygen is supplied to the cell and water is produced with generation of power, i.e. hydrogen oxidation reaction (HOR) at anode and oxygen reduction reaction (ORR)

**Table 1.2.** Operation principles, advantages and disadvantages of PEMFC and AEMFC.

	PEMFC	AEMFC
<b>Scheme of Operation Principle</b>	<p>[Cathode] [Membrane] [Anode]</p>	<p>[Cathode] [Membrane] [Anode]</p>
<b>Electrochemical Reaction</b>	<p>Anode : <math>\text{H}_2 \rightarrow 2 \text{H}^+ + 2 \text{e}^-</math></p> <p>Cathode : <math>\frac{1}{2} \text{O}_2 + 2 \text{H}^+ + 2 \text{e}^- \rightarrow \text{H}_2\text{O}</math></p> <p>Overall : <math>\text{H}_2 + \frac{1}{2} \text{O}_2 \rightarrow \text{H}_2\text{O}</math></p>	<p>Anode : <math>\text{H}_2 + 2 \text{OH}^- \rightarrow 2 \text{H}_2\text{O} + 2 \text{e}^-</math></p> <p>Cathode : <math>\frac{1}{2} \text{O}_2 + \text{H}_2\text{O} + 2 \text{e}^- \rightarrow 2 \text{OH}^-</math></p> <p>Overall : <math>\text{H}_2 + \frac{1}{2} \text{O}_2 \rightarrow \text{H}_2\text{O}</math></p>
<b>Advantages</b>	<ul style="list-style-type: none"> <li>High power density from higher catalytic activity and higher ionic conductivity.</li> <li>Higher thermal and chemical stability of membrane.</li> </ul>	<ul style="list-style-type: none"> <li>The use of less expensive, non-PGM electrocatalysts.</li> <li>The use of less expensive polymer electrolyte membrane.</li> <li>The availability to wider fuel choice, not only pure hydrogen.</li> <li>The availability of use more concentrated fuels.</li> </ul>
<b>Disadvantages</b>	<ul style="list-style-type: none"> <li>Material costs issue from noble catalysts and membrane.</li> </ul>	<ul style="list-style-type: none"> <li>Lower power density compared to PEMFC.</li> </ul>

at cathode. ORR has much sluggish kinetics and requires large overpotential compared to HOR. Low-temperature polymer membrane based FC also divided by PEMFC and AEMFC according to the conducting ions during operation, i.e.  $H^+$  for PEMFC,  $OH^-$  for AEMFC, which has similar advantages/disadvantages as explained in electrolysis, e.g. high power density but the cost issue of materials from noble metal catalysts and expensive membrane in PEMFC (Table 1.2).

In the aspect of electrocatalysts of PEMFC, Pt is unanimously considered the most active HOR, ORR catalyst in PEMFC, which is, unfortunately, a rare noble metal. According to DOE 2020, the target amount of Pt is  $0.025 \text{ mg cm}^{-2}$  and  $<0.1 \text{ mg cm}^{-2}$  for HOR and ORR in PEMFC. Pt in ORR is much hard to satisfy the target loading since ORR is much sluggish electrochemical reaction compared to HOR. Therefore, tremendous researches have tried to develop the ORR catalysts to reduce the dosage of Pt in PEMFC. Pt/C is the most commercialized catalysts but various approaches have been studied to raise its mass activity (normalized by mass) and specific activity (normalized by surface area) [23-25], e.g. carbon support [26], Pt nanostructure [27], alloying [28-30], core-shell structure [31], non-noble metal [32] and single-atom catalysts (SACs) [33]. For instance, Stamenkovic and Markovic et al. demonstrated  $Pt_3Ni$  (111) reveals 90 times activity of Pt/C in 2007 [28]. They established a volcano-type relationship with d-band center of Pt alloy ( $Pt_3-X$ , X: Ti, V, Fe, Co, Ni) with ORR activity by DFT calculation [34]. However, transition metal alloyed Pt catalysts are thermodynamically unstable and tend to dissolve in acidic condition, i.e. dealloying [35]. Later, Li et al. reported jagged Pt nanowires transformed from PtNi nanowires (J-PtNWs/C) having 33 times and 52 times higher specific and mass activity compared to Pt/C with more than 4 times higher stability (calculated by loss of electrochemical surface area) in 2016 [27]. Non-noble metal electrocatalysts, i.e.

M-N-C catalysts, are ideal solution in the cost aspect, but regretfully its intrinsic activity is at least 10 times less than Pt. Recently, SACs are getting attention from researchers because this kind of structure maximizes the catalyst mass activity with 100 % atom utilization. However, even though its mass activity is superior, it is not certain that SACs will show effective activity per electrode area in device scale of PEMFC. State of art SACs did not reach the DOE target yet and still in-depth research is required to verify its potential in PEMFC application [25].

In addition to the catalyst research, water management is a critical and sensitive issue in PEMFC. MEA generally composed of a catalyst coated membrane (CCM) sandwiched between two porous substrates. This porous substrate is gas diffusion layers (GDLs) since reactant gas is diffused through GDL to the catalyst layer, which is usually called as PTL in PEMWE. GDLs should satisfy several functions such as gas permeability, liquid permeability, electronic conductivity, heat conductivity and mechanical strength. Usually, porous carbon materials are used as GDLs in PEMFC, e.g. carbon cloth and carbon paper [36-38]. Structure of MEA looks simple, but the interrelated and complex phenomena, especially in the aspect of water, happened inside of MEA during FC operation. Arrival of gas reactant to catalyst layers and removal of produced water must occur rapidly in the electrode, especially cathode of PEMFC. If rate of water removal is sluggish compared to rate of water generation, water blocks active sites of catalysts, i.e. water flooding, resulting deterioration of cell performance. In addition, if water removal from catalyst layers to cathode outlet is too fast, membrane dehydration leads reduced ionic conductivity and increased contact resistance between catalyst layers and the membrane, which results in increase of voltage loss from ohmic resistance.

To understand and optimize the water management in PEMFC, numerous

researches were done from fundamental modeling to experimental investigation [39, 40]. In GDL research, four main research approaches were done to solve flooding issue [40]; i) hydrophobic PTFE treatment, ii) GDL materials, iii) microporous layer (MPL) and iv) porosity. For instance, Velayutham et al. experimentally demonstrated that 20-23 wt% of PTFE to GDL is optimized content in the aspect of water management in PEMFC [41]. Many studies reported the positive effect of MPLs on PEMFC [39]. MPL refers to the layer in between GDL and catalysts layer, typically composed of carbon black powder and PTFE. The existence of MPL induces the water diffusion from cathode to anode side and from cathode catalysts layer to outlet of cathode due to increases saturated vapor pressure in MPL from its small pores and hydrophobicity, which fulfills both functions; i) hydration of membrane and ii) alleviation of flooding. Although, many factors have been studied, water management is still the complicate and difficult issue in PEMFC due to numerous variables inside of the cell during operation [42].

## **1.2. General Introduction to Unitized Regenerative Proton Exchange Membrane Fuel Cells (UR-PEMFC)**

As renewable energies from hydro, solar, wind, geothermal etc. are getting high interest and growing with a lot of investment worldwide, more than 30 % of electricity is expected to be provide from renewable sources in 2040 [43]. However, intermittent power generation of renewables restricts direct utilization of electricity to community in application aspect. Secondary batteries or unitized regenerative fuel cell (URFC) are suggested as intermediate device to store and convert the produced

electricity. UR-PEMFC has great potential to utilize due to its high energy density, e.g. more than 5 times higher specific energy compared to battery as in Table 1.3 [44]. However, proton exchange membrane based URFC (UR-PEMFC or PEM-URFC) has several issues compared to rechargeable batteries; i) lower round trip efficiency around 40-50% unlike battery, e.g. Li-ion battery > 95 %, ii) high costs of system, and iii) hydrogen storage [45].

UR-PEMFC is a compact and combined electrochemical device of an electrolysis cell (EC) and a fuel cell (FC), which produces fuel in applying electricity and generates power in supply of fuels. As shown in Figure 1.1, the operating principle is identical with previous PEMWE and PEMFC in EC (or WE) and FC mode of URFC, respectively. The general basic structure of URFC is same with PEMWE and PEMFC; i) end plate fastening the cell, ii) flow field plate including current collector, called bipolar plate (BPP) in other words, which collect the current and flow reactants and products through the flow channel, and iii) MEA composed of PTLs, catalysts and membrane (Figure 1.1). Unlike PEMFC, widespread commercialization of UR-PEMFC is hindered by expensive cell components such as high loading of rare platinum group metals (PGM) as catalysts, fluorinated electrolyte membrane and non-corrosive metal based porous transport layer and flow field plates.

In the aspect of catalysts, oxygen reactions are sluggish compared to hydrogen reactions, and bifunctional oxygen catalyst (BOC) is one of the critical issue in URFC. In fuel cell technologies, carbonaceous catalyst supports such as carbon black, graphene, carbon nanotubes (CNT), mesoporous carbon, carbon nanofiber (CNF), etc. have been heavily studied to maximize the usage of catalyst and Pt/C is

**Table 1.3.** Comparison of specific energy of URFC with other rechargeable batteries. (Adapted from Fred, M. et.al., *Energy & Fuels* 12 (1998) 56-71.)

battery system	theoretical specific energy (Wh/kg)	packaged specific energy (Wh/kg)	comments
H <sub>2</sub> /O <sub>2</sub> URFC	3660	400–1000	URFC with lightweight pressure vessels
Li-SPE/MO <sub>x</sub>	735	220	Li–solid polymer electrolyte/ metal oxide, novel packaging
Ag/Zn	450	200	excess Zn required for high cycle life, low charge rate
Li/LiCoO <sub>2</sub>	735	150	poor cycle life, high capacity fade
Li/AlFeS <sub>2</sub>	515	150	≥ 400 °C thermal management
Na/S	1180	150	~350 °C thermal management
Li/TiS <sub>2</sub>	470	130	~50% DOD for high cycle life (900 cycles)
Li/ion	700	100 (135 <sup>a</sup> )	projection revised Nov 1996
Ni/Zn	305	90	excess Zn required, low specific energy
Ni/MH <sub>x</sub>	470	70 (85 <sup>a</sup> )	MH <sub>x</sub> is metal hydride, projection revised Nov 1996
Ni/H <sub>2</sub>	470	60	low specific energy
Ni/Cd	240	60	low specific energy
Pb/acid	170	50	low specific energy

<sup>a</sup> Projections revised in November 1996 by private communications with B. M. Barnett (A. D. Little, Inc.).

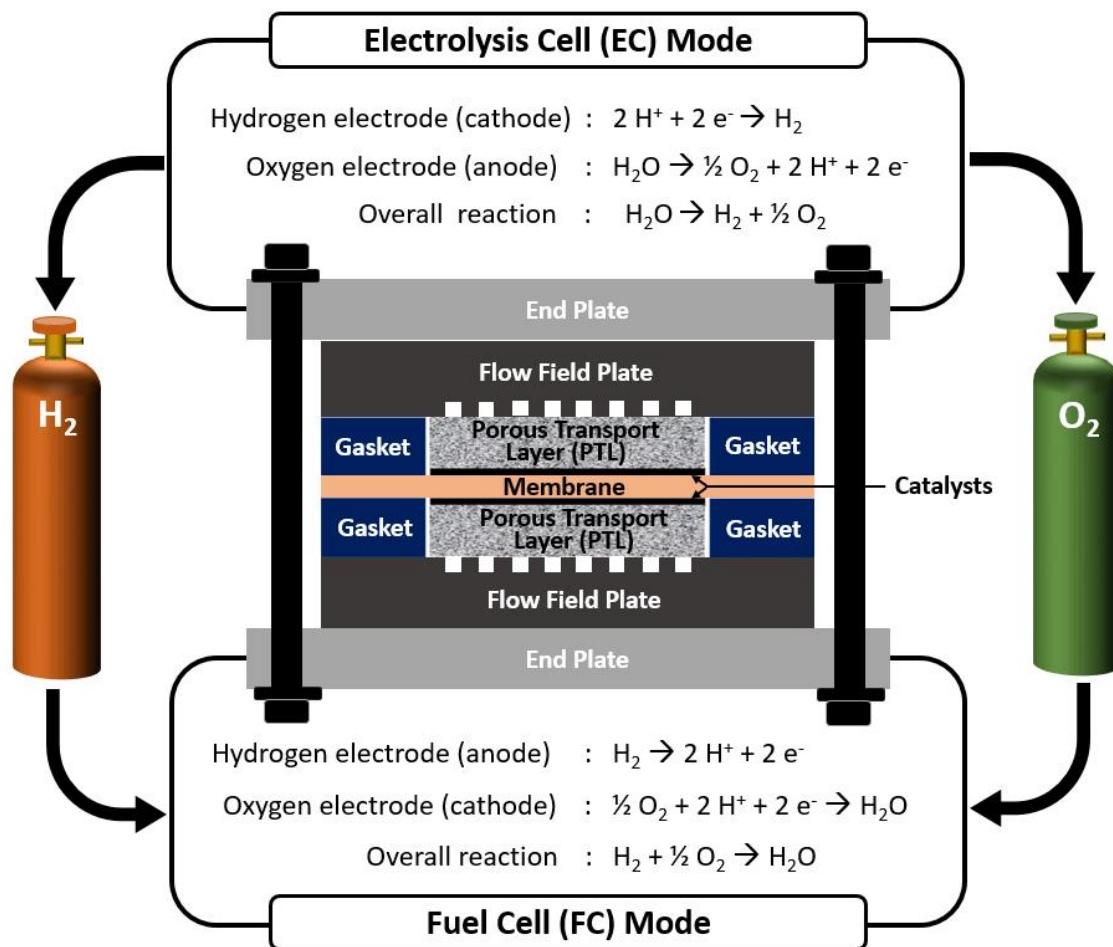


Figure 1.1. Schematic structure and operation of URFC.

**Table 1.4.** Previous reported round trip efficiency of UR-PEMFC with types of membrane, amount of catalysts loading and operation temperature (Adapted from Y. Wang et al., *Renew. Sust. Energ. Rev.* 65 (2016) 961-977.)

References	BHC	Electrolyte	BOC	Temp. (°C)	PPD	Round-trip efficiency
Shao et al. [14]	Pt 0.4 mg cm <sup>-2</sup>	Nafion 115	Pt-IrO <sub>2</sub> (1:1 wt ratio) 0.4 mg cm <sup>-2</sup>	80		40.9% at 400 mA cm <sup>-2</sup>
loroi et al. [46]	Pt 8-10 mg cm <sup>-2</sup>	Nafion 115	Pt-IrO <sub>2</sub> (10-30 mol% IrO <sub>2</sub> ) 8-10 mg cm <sup>-2</sup>	80		49% at 300 mA cm <sup>-2</sup> 42% at 500 mA cm <sup>-2</sup>
loroi et al. [31]	Pt	Nafion 115	IrO <sub>2</sub> /Pt (20 at% IrO <sub>2</sub> )	80		51% at 300 mA cm <sup>-2</sup> 44% at 500 mA cm <sup>-2</sup> ~50% at 200 mA cm <sup>-2</sup>
loroi et al. [47]	Pt 2-4 mg cm <sup>-2</sup>	Nafion 115	Pt-Ir (10 at% Ir) 2-4 mg cm <sup>-2</sup>	80		
Yim et al.[26]	Pt 4 mg cm <sup>-2</sup>	Nafion 1135	Pt-Ir (1:1 wt ratio) 4 mg cm <sup>-2</sup>	60		53% at 200 mA cm <sup>-2</sup> 46% at 500 mA cm <sup>-2</sup>
Yim et al. [27]	Pt 4 mg cm <sup>-2</sup>	Nafion 1135	Pt-Ir (99:1 wt ratio) 4 mg cm <sup>-2</sup>	60		53% at 200 mA cm <sup>-2</sup> 47% at 500 mA cm <sup>-2</sup>
Zhang et al. [15]	Pt/C 0.4 mg <sub>Pt</sub> cm <sup>-2</sup>	Nafion 115	(RuO <sub>2</sub> -IrO <sub>2</sub> )/Pt (25:25:50, wt. ratio) 2 mg cm <sup>-2</sup>	80		50% at 400 mA cm <sup>-2</sup> 43% at 500 mA cm <sup>-2</sup>
Jung et al. [16,17]	Pt 0.5 mg cm <sup>-2</sup>	Nafion 112	Pt-Ir (85 wt% Pt) 4 mg cm <sup>-2</sup>	70-75		49% at 500 mA cm <sup>-2</sup> 41% at 1 A cm <sup>-2</sup>
Zhang et al. [19]	Pt/C 0.2 mg <sub>Pt</sub> cm <sup>-2</sup>	Nafion 212	(Pt/IrO <sub>2</sub> )-Pt (5:95:100, wt. ratio) 1 mg cm <sup>-2</sup>	80	1.16 W cm <sup>-2</sup>	
Huang et al. [18]	Pt 0.5 mg cm <sup>-2</sup>	Nafion 112	(Pt/TiO <sub>2</sub> )-(Ir/TiO <sub>2</sub> ) (Pt/Ir=85/15 wt ratio) 1 mg <sub>Pt</sub> cm <sup>-2</sup>	75	0.93 W cm <sup>-2</sup>	50.3% at 500 mA cm <sup>-2</sup> 42.2% at 1 A cm <sup>-2</sup>
Rivas et al. [25]	Pt/C 0.5-1 mg <sub>Pt</sub> cm <sup>-2</sup>	Nafion 115	Pt <sub>4.5</sub> Ru <sub>4</sub> Ir <sub>0.5</sub> 3-5 mg cm <sup>-2</sup>	80		
Cruz et al. [20]	Pt/C 0.3 mg <sub>Pt</sub> cm <sup>-2</sup>	Nafion 115	Pt/IrO <sub>2</sub> (1:1 wt ratio) 0.5 mg cm <sup>-2</sup>	Room temp.	0.1 W cm <sup>-2</sup>	47% at 50 mA cm <sup>-2</sup> 37% at 100 mA cm <sup>-2</sup> 30% at 200 mA cm <sup>-2</sup>
Huang et al. [36]	Pt 0.5 mg cm <sup>-2</sup>	Nafion 112	Pt/TiO <sub>2</sub>	75	0.94 W cm <sup>-2</sup>	
Pai et al. [44]	Pt 0.25 mg cm <sup>-2</sup>	Nafion 212	Pt/Graphitized carbon 0.25 mg <sub>Pt</sub> cm <sup>-2</sup>		190 mW cm <sup>-2</sup>	37.5% at 100 mA cm <sup>-2</sup>
Cruz et al. [45]	Pt/C 0.4 mg <sub>Pt</sub> cm <sup>-2</sup>	Nafion 115	Pt-IrO <sub>2</sub> (1:1 wt ratio)/ATO 0.5 mg cm <sup>-2</sup>	80		48% at 50 Ag <sup>-1</sup> 43% at 100 A g <sup>-1</sup> 31% at 200 A g <sup>-1</sup>
Chen et al.[51]	Pt/C	Nafion 115	Pt-IrO <sub>2</sub> 2.1 mg <sub>Pt</sub> cm <sup>-2</sup> 0.9 mg <sub>IrO2</sub> cm <sup>-2</sup>	80	474 mW cm <sup>-2</sup>	60.3% at 100 mA cm <sup>-2</sup> 52.1% at 300 mA cm <sup>-2</sup> 44.2% at 500 mA cm <sup>-2</sup> 37.8% at 700 mA cm <sup>-2</sup>
Jung et al. [50]	Pt 4 mg cm <sup>-2</sup>	Nafion 112	Pt-Ir 4 mg cm <sup>-2</sup>	70, 90		
Liu et al. [52]	Pt 0.8 mg cm <sup>-2</sup>	Nafion 115	Pt-IrO <sub>2</sub> 2.2 mg <sub>Pt</sub> cm <sup>-2</sup> 1.7 mg <sub>IrO2</sub> cm <sup>-2</sup>	20,40, 60,80		
Wittstadt et al. [53]	Pt 2 mg cm <sup>-2</sup>	Nafion 117	Pt-Ir (1:1) 2 mg cm <sup>-2</sup>	5, 25, 50, 80		
Chen et al.[54]	Pt/C 0.5 mg cm <sup>-2</sup>	Nafion 1035	Pt-IrO <sub>2</sub> 0.5 mg <sub>Pt</sub> cm <sup>-2</sup> 0.5 mg <sub>IrO2</sub> cm <sup>-2</sup>	80		~60% at 100 mA cm <sup>-2</sup> 42.1% at 800 mA cm <sup>-2</sup>
Altmann et al. [55]	Pt 0.7 mg cm <sup>-2</sup>	Nafion 1135	Pt-IrO <sub>2</sub> 0.73 mg <sub>Pt</sub> cm <sup>-2</sup> 0.73 mg <sub>IrO2</sub> cm <sup>-2</sup>	80-85 95		
Lee et al. [49]	Pt 0.38 mg cm <sup>-2</sup>	Polypyrrole/Nafion composite membrane	Pt 0.38 mg cm <sup>-2</sup>	80		
Pettersson et al. [48]	Pt 3-4 mg cm <sup>-2</sup>	Nafion 115	Pt-Ir 3-4 mg cm <sup>-2</sup>	Room temp.		44% at 50 mA cm <sup>-2</sup> 35% at 100 mA cm <sup>-2</sup>

commercialized [46]. However, severe carbon corrosion ( $\text{CO}_2 + 4\text{H}^+ + 4\text{e}^- \rightleftharpoons \text{C} + 2\text{H}_2\text{O}$ ,  $E^0 = 0.206 \text{ V}_{\text{RHE}}$ ) in high voltage during EC mode, e.g. more than 1.5 V, constrains the usage of carbon materials on the electrode due to stability issue. Lots of studies in UR-PEMFC reported high loading of noble catalysts ( $> 2 \text{ mg cm}^{-2}$  of Pt and Ir) for facilitation of OER and ORR reaction as shown in Table 1.4 [45].

In PTL aspect, carbon-based materials are used in the hydrogen electrode and titanium-based materials, e.g. Ti-mesh, Ti-felt, Ti-powders, are used in the oxygen electrode generally. Ti-based PTLs have high corrosion resistance in EC mode operation, but still has the issue of partial oxidation, resulting high contact resistance [47]. To complement the surface oxidation, Pt coating on Ti PTL was studied [48]. There are few papers related to optimize surface property of Ti PTL in URFC were reported, e.g. PTFE coating [49-51] or MPL composed of Ti particles [52] for water management in the electrode. Ioroi et al. demonstrated PTFE coating enhances performance in the FC mode but adversely affect in the WE mode [51]. However, Hwang et al. argued PTFE coating does not affect WE [50]. The PTL in URFC is required to satisfy not only preferred pathway for gas absorption and water emission in FC mode but also water absorption and gas emission in the WE mode, which is a complicated system. The research focused on PTLs of URFC is still in the early stage.

For widespread commercialization of UR-PEMFC, tremendous researches on cost-efficient cell components, e.g. BOC, BPP, and development of optimized materials based on understanding of the system are still required. In addition, round trip efficiency should be improved to get competitiveness with other energy storage systems in the market.

### **1.3. Applications of Electrodeposition in Proton Exchange Membrane Based Water Electrolysis and Fuel Cells**

In the PEM based electrochemical devices mentioned above, PGM noble electrocatalysts, e.g. Pt for ORR, Ru or Ir for OER, are indispensable due to instability of non-noble catalysts in acid condition. In addition, high loading of noble-catalysts is a serious problem due to its rareness and costs, e.g. 41% of costs from catalysts in fuel cells [53]. To reduce the amount of PGM noble catalysts in fuel cells, tremendous researches on catalysts have been investigated. High mass activity of electrocatalysts was achieved by alloying and modification of nanostructure to hollow, sheet, wire, etc [24, 54, 55]. However, there is still a gap between half-cell results in catalyst studies and single cell applications [56]. Not only catalytic activity, but also ionic conductivity, electric conductivity and mass transport of gas and liquid control the performance in a single cell, which is a highly complicated system compared to a half-cell. Thus, not only catalysts, but also fabrication of catalysts layer on the electrode, e.g. ionomer content, hot press condition, etc., highly influence the performance of the cell [57-61].

Compared to other generalized electrode fabrication methods, e.g. decal, screen printing and spray coating, electrodeposition has some advantages: i) easy to manage the amount of catalysts loading on the substrate by control of deposition time, ii) fast and simple one-pot catalyst synthesis including electrode fabrication, which is easy to scale up to the industrial level, iii) moderate synthesis condition, e.g. room temperature, atmospheric pressure, iv) higher electric connection between catalysts

and v) stable catalyst structure from strong binding due to formation of catalysts layer by electrochemical reaction instead of physical arrangement. Thus, electrodeposition techniques are investigated as novel, facile fabrication methods of catalysts structure to reduce the amount of noble catalysts in the electrodes. There are some researches of Pt or IrO<sub>2</sub> electrodeposition (e-Pt or e-IrO<sub>2</sub>) in electrodes of PEMFC or PEMWE. F-Onana et al. reported e-Pt (0.12 mg cm<sup>-2</sup>) as cathode of PEMFC showing one of the highest mass activity and turnover frequency @ 0.9 V<sub>ir-free</sub> in 2014 [62]. Lee. et al. and Choe. et al. demonstrated e-IrO<sub>2</sub> 0.1-0.4 mg cm<sup>-2</sup> as anode of PEMWE and achieved high mass activity, e.g. 0.5 A cm<sup>-2</sup> @ 1.45 V, 120 °C, 2.5 bar with 0.1 mg<sub>IrO2</sub> cm<sup>-2</sup> [63-67]. Furthermore, coating of noble catalysts creates protective layers, which blocks the partial oxidation of the Ti PTL and enhances stability of the cell [67]. Lee. et al. also reported application of e-IrO<sub>2</sub> on C PTL [68], but e-IrO<sub>2</sub> on C PTL is not stable in long term operation of WE due to carbon corrosion [67]. Additionally, electrodeposition of noble catalysts to three-dimensional macroporous structures was studied to compose highly porous catalyst layers with low loading. For instance, Kim. et al and Park. et al electrodeposited Pt and IrO<sub>2</sub> catalysts to the inverse opal structure and applied to ORR and OER catalysts layer of PEMFC and PEMWE, respectively [69, 70]. This catalyst structure results in enhancement of utilization of catalysts, mass transport and water management, thus high performance with low loading of catalysts. The overview of application of Pt or IrO<sub>2</sub> electrodeposition on PEMFC or PEMWE is summarized in Table 1.5.

**Table 1.5.** Overview of Pt or IrO<sub>2</sub> electrodeposition in PEMFC or PEMWE.

Electro-chemical Device	Electrodeposited catalyst (e-catalysts)	Electrochemical rxn.	Amount of e-catalysts loading / mg cm <sup>-2</sup>	Voltage @ 0.5 A cm <sup>-2</sup> / V	Ref.
PEMFC	Pt	ORR	0.25	0.77	[71]
	Pt	ORR	0.2	0.70	[72]
	Pt (Inverse opal)	ORR	0.12	0.71	[69]
	Pt	HOR, ORR	0.22 (Total)	~0.3	[73]
	Pt	ORR	0.12	0.73	[62]
HT-PEMFC	Pt	HOR	0.05 + Pt/C,	0.63	[74]
	Pt	ORR	0.05 +PtNi/C	0.56	
	Pt	HOR	0.3	0.4	[75]
PEMWE	Pt	HER	0.021	1.58	[63]
	Pt	HER	0.02	1.67	[64]
			0.05	1.64	
			0.07	1.65	
	IrO <sub>2</sub>	OER	0.1	1.51	[65]
	IrO <sub>2</sub>	OER	0.1	1.45	[66]
IrO <sub>2</sub>	OER	0.4	1.50	[67]	
UR-PEMFC	IrO <sub>2</sub> (Inverse opal)	OER	0.02	1.53	[70]
	IrO <sub>2</sub>	OER	0.1	0.71 (FC)	
1.54 (WE)					

## 1.4. Aim of This Thesis

The key research required in URFC is development of cost-effective electrodes with long-term stability. To obtain efficient and durable MEA, issues of material degradation such as carbon corrosion, migration, agglomeration and dissolution of catalysts, and degradation of membrane should be ameliorated. In addition, reduction of PGM catalysts loading and an alternative substance to replace the expensive metallic flow field plate are necessary to reduce the cost of URFC system [10, 45].

In URFC, EC mode operation is more corrosive condition from higher applied cell voltage compared to FC mode operation. Thus, titanium materials instead of carbon are utilized as PTLs of the oxygen electrode in EC mode. In previous research on PEMWE, electrodeposited IrO<sub>2</sub> on Ti PTL (e-IrO<sub>2</sub>/Ti) showed high mass activity and durability due to role of IrO<sub>2</sub> coating as both catalyst and protective layer [67]. However, none of studies about application of e-IrO<sub>2</sub>/Ti in UR-PEMFC has been reported. Due to advantages of e-IrO<sub>2</sub>/Ti, application of noble metal electrodeposited Ti electrode in UR-PEMFC was studied to ameliorate severe issues in UR-PEMFC; high loading of noble catalysts and stability of materials.

The main thesis consists of three aspects; i) hemispheric core-shell electrodeposited catalysts (e-Pt@IrO<sub>2</sub>/Ti), ii) interface engineering of e-IrO<sub>2</sub>/Ti including SECM analysis, and iii) effects of operation condition on UR-PEMFC. First, sequential electrodeposition of supports and catalysts is investigated to enhance conductivity and active surface area of catalysts further from the established previous single electrodeposition (Chapter 2). Second, fabrication of the amphiphilic electrode by patterned-polymer coating on e-IrO<sub>2</sub>/Ti PTL is studied to create highways of gas and water in URFC operation (Chapter 3). Analysis with scanning

electrochemical microscopy (SECM) is additionally tried for understanding tendency of emission of produced bubbles in electrolysis in fabricated electrodes (Chapter 4). Third, the effects of operation configuration and relative humidity on URFC with analysis of water distribution through operation condition are demonstrated (Chapter 5). The main thesis of the research is briefly summarized in Figure 1.2. Through studies, the efficient and stable electrode with low amount of noble catalysts based on the understating the effect of introduction of e-IrO<sub>2</sub> electrode in UR-PEMFC is intended to be achieved.

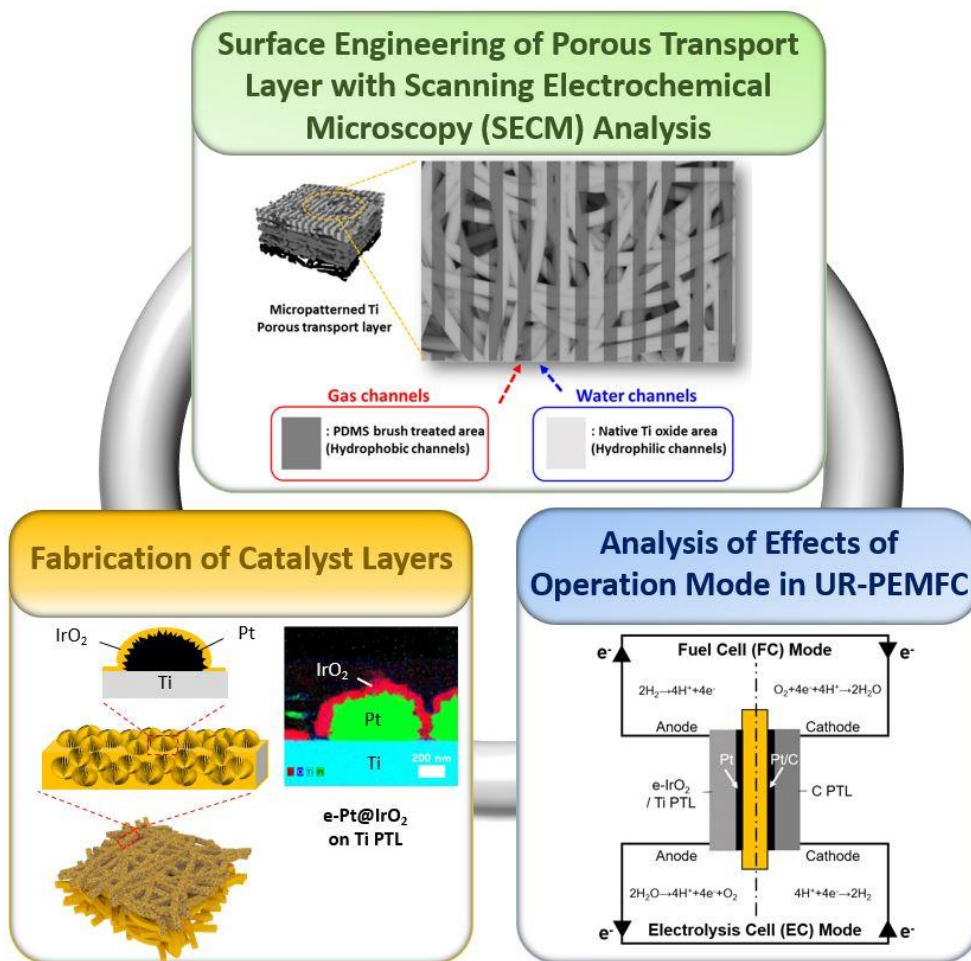


Figure 1.2. Schematic summary of the main thesis.

## 1.5. References

- [1] P. P. Edwards, V. L. Kuznetsov, W.I.F. David, Hydrogen energy, *Phil. Trans. R. Soc. A* 365 (2007) 1043-1056.
- [2] J. D. Holladay, J. Hu, D. L. King, Y. Wang, An overview of hydrogen production technologies, *Catal. Today* 139 (2009) 244-260.
- [3] J. M. Modak, Haber Process for Ammonia synthesis, *Resonance* 7 (2002) 69-77.
- [4] J. Nørskov, J. Chen, Sustainable Ammonia Synthesis, *DOE Roundtable Report, U.S. Department of Energy* (2016).
- [5] G. L. Soloveichik, Liquid fuel cells, *Beilstein J. Nanotechnol.* 5 (2014) 1399-1418.
- [6] J. Wang, L. Yu, L. Hu, G. Chen, H. Xin, X. Feng, Ambient ammonia synthesis via palladium-catalyzed electrohydrogenation of dinitrogen at low overpotential, *Nat. Commun.* 9 (2018) 1795.
- [7] S. Marini, P. Salvi, P. Nelli, R. Pesenti, M. Villa, M. Berrettoni, G. Zangari, Y. Kiros, Advanced alkaline water electrolysis, *Electrochim. Acta* 82 (2012) 384-391.
- [8] S. Shiva Kumar, V. Himabindu, Hydrogen production by PEM water electrolysis – A review, *Mater. Sci. Energ. Technol.* 2 (2019) 442-454.
- [9] M. Schalenbach, G. Tjarks, M. Carmo, W. Lueke, M. Mueller, D. Stolten, Acidic or alkaline? Towards a new perspective on the efficiency of water electrolysis, *J. Electrochem. Soc.* 163 (2016) F3197-F3208.
- [10] U. Babic, M. Suermann, F.N. Büchi, L. Gubler, T.J. Schmidt, Critical review—Identifying critical gaps for polymer electrolyte water electrolysis development,

- J. Electrochem. Soc.* 164 (2017) F387-F399.
- [11] C. Hu, L. Zhang, J. Gong, Recent progress made in the mechanism comprehension and design of electrocatalysts for alkaline water splitting, *Energ. Environ. Sci.* 12 (2019) 2620-2645.
- [12] A. Faid, A. Oyarce Barnett, F. Seland, S. Sunde, Highly active nickel-based catalyst for hydrogen evolution in anion exchange membrane electrolysis, *Catal.* 8 (2018) 614-626.
- [13] M. J. Jang, J. Yang, J. Lee, Y. S. Park, J. Jeong, S. M. Park, J.-Y. Jeong, Y. Yin, M.-H. Seo, S. M. Choi, K. H. Lee, Superior performance and stability of anion exchange membrane water electrolysis: pH-controlled copper cobalt oxide nanoparticles for the oxygen evolution reaction, *J. Mater. Chem. A* 8 (2020) 4290-4299.
- [14] J. S. Kim, B. Kim, H. Kim, K. Kang, Recent progress on multimetal oxide catalysts for the oxygen evolution reaction, *Adv. Energ. Mater.* 8 (2018) 1702774.
- [15] G. Merle, M. Wessling, K. Nijmeijer, Anion exchange membranes for alkaline fuel cells: A review, *J. Membr. Sci.* 377 (2011) 1-35.
- [16] A. Marinkas, I. Strużyńska-Piron, Y. Lee, A. Lim, H. S. Park, J. H. Jang, H.-J. Kim, J. Kim, A. Maljusch, O. Conradi, D. Henkensmeier, Anion-conductive membranes based on 2-mesityl-benzimidazolium functionalised poly(2,6-dimethyl-1,4-phenylene oxide) and their use in alkaline water electrolysis, *Polymer* 145 (2018) 242-251.
- [17] Y. Leng, G. Chen, A. J. Mendoza, T. B. Tighe, M. A. Hickner, C. Y. Wang, Solid-state water electrolysis with an alkaline membrane, *J. Am. Chem. Soc.* 134 (2012) 9054-9057.

- [18] A. Lim, M. K. Cho, S. Y. Lee, H.-J. Kim, S. J. Yoo, Y.-E. Sung, J. H. Jang, H. S. Park, A Review of industrially developed components and operation conditions for anion exchange membrane water electrolysis, *J. Electrochem. Sci. Technol.* 8 (2017) 265-273.
- [19] M. K. Cho, A. Lim, S. Y. Lee, H.-J. Kim, S. J. Yoo, Y.-E. Sung, H. S. Park, J. H. Jang, A review on membranes and catalysts for anion exchange membrane water electrolysis single cells, *J. Electrochem. Sci. Technol.* 8 (2017) 183-196.
- [20] P. Fortin, T. Khoza, X. Cao, S. Y. Martinsen, A. Oyarce Barnett, S. Holdcroft, High-performance alkaline water electrolysis using Aemion™ anion exchange membranes, *J. Power Sources* 451 (2020) 227814.
- [21] Z. Liu, S. D. Sajjad, Y. Gao, J. Kaczur, R. Masel, An alkaline water electrolyzer with sustainion™ membranes: 1 A/cm<sup>2</sup> at 1.9V with base metal catalysts, *ECS Trans.* 77 (2017) 71-73.
- [22] O. Z. Sharaf, M. F. Orhan, An overview of fuel cell technology: Fundamentals and applications, *Renew. Sust. Energ. Rev.* 32 (2014) 810-853.
- [23] S. Sui, X. Wang, X. Zhou, Y. Su, S. Riffat, C.-j. Liu, A comprehensive review of Pt electrocatalysts for the oxygen reduction reaction: Nanostructure, activity, mechanism and carbon support in PEM fuel cells, *J. Mater. Chem. A* 5 (2017) 1808-1825.
- [24] M. Shao, Q. Chang, J.P. Dodelet, R. Chenitz, Recent advances in electrocatalysts for oxygen reduction reaction, *Chem. Rev.* 116 (2016) 3594-3657.
- [25] X. Wang, Z. Li, Y. Qu, T. Yuan, W. Wang, Y. Wu, Y. Li, Review of metal catalysts for oxygen reduction reaction: From nanoscale engineering to atomic design, *Chem.* 5 (2019) 1486-1511.

- [26] P. K. Mohanta, F. Regnet, L. Jorissen, Graphitized carbon: A promising stable cathode catalyst support material for long term PEMFC applications, *Materials* 11 (2018).
- [27] M. Li, Z. Zhao, T. Cheng, A. Fortunelli, C.-Y. Chen, R. Yu, Q. Zhang, L. Gu, B. V. Merinov, Z. Lin, E. Zhu, T. Yu, Q. Jia, J. Guo, L. Zhang, W.A.G. III, Y. Huang, X. Duan, Ultrafine jagged platinum nanowires enable ultrahigh mass activity for the oxygen reduction reaction, *Science* 354 (2016) 1414-1419.
- [28] V. R. Stamenkovic, B. Fowler, B. S. Mun, G. Wang, P. N. Ross, C. A. Lucas, N. M. Marković, Improved oxygen reduction activity on Pt<sub>3</sub>Ni(111) via increased surface site availability, *Science* 315 (2007) 493-497.
- [29] E. Antolini, J.R.C. Salgado, M.J. Giz, E. R. Gonzalez, Effects of geometric and electronic factors on ORR activity of carbon supported Pt–Co electrocatalysts in PEM fuel cells, *Int. J. Hydro. Energ.* 30 (2005) 1213-1220.
- [30] S. Koh, M. F. Toney, P. Strasser, Activity–stability relationships of ordered and disordered alloy phases of Pt<sub>3</sub>Co electrocatalysts for the oxygen reduction reaction (ORR), *Electrochim. Acta* 52 (2007) 2765-2774.
- [31] L. Gan, C. Cui, S. Rudi, P. Strasser, Core–shell and nanoporous particle architectures and their effect on the activity and stability of Pt ORR electrocatalysts, *Top. Catal.* 57 (2013) 236-244.
- [32] Y. He, Q. Tan, L. Lu, J. Sokolowski, G. Wu, Metal-nitrogen-carbon catalysts for oxygen reduction in PEM fuel cells: Self-template synthesis approach to enhancing catalytic activity and stability, *Electrochem. Energ. Rev.* 2 (2019) 231-251.
- [33] J. Liu, M. Jiao, B. Mei, Y. Tong, Y. Li, M. Ruan, P. Song, G. Sun, L. Jiang, Y. Wang, Z. Jiang, L. Gu, Z. Zhou, W. Xu, Carbon-supported divacancy-anchored

- platinum single-atom electrocatalysts with superhigh Pt utilization for the oxygen reduction reaction, *Angew. Chem. Int. Ed.* 58 (2019) 1163-1167.
- [34] V. R. Stamenkovic, B. S. Mun, M. Arenz, K. J. Mayrhofer, C. A. Lucas, G. Wang, P. N. Ross, N. M. Markovic, Trends in electrocatalysis on extended and nanoscale Pt-bimetallic alloy surfaces, *Nat. Mater.* 6 (2007) 241-247.
- [35] J. Greeley, J.K. Nørskov, Electrochemical dissolution of surface alloys in acids: Thermodynamic trends from first-principles calculations, *Electrochim. Acta* 52 (2007) 5829-5836.
- [36] S. Escribano, J.-F. Blachot, J. Ethève, A. Morin, R. Mosdale, Characterization of PEMFCs gas diffusion layers properties, *J. Power Sources* 156 (2006) 8-13.
- [37] H.-K. Lee, J.-H. Park, D.-Y. Kim, T.-H. Lee, A study on the characteristics of the diffusion layer thickness and porosity of the PEMFC, *J. Power Sources* 131 (2004) 200-206.
- [38] W. Chen, F. Jiang, Impact of PTFE content and distribution on liquid–gas flow in PEMFC carbon paper gas distribution layer: 3D lattice Boltzmann simulations, *Int. J. Hydro. Energ.* 41 (2016) 8550-8562.
- [39] F. S. Nanadegani, E. N. Lay, B. Sunden, Effects of an MPL on water and thermal management in a PEMFC, *Int. J. Energ. Res.* 43 (2019) 274-296.
- [40] H. Li, Y. Tang, Z. Wang, Z. Shi, S. Wu, D. Song, J. Zhang, K. Fatih, J. Zhang, H. Wang, Z. Liu, R. Abouatallah, A. Mazza, A review of water flooding issues in the proton exchange membrane fuel cell, *J. Power Sources* 178 (2008) 103-117.
- [41] G. Velayutham, J. Kaushik, N. Rajalakshmi, K. S. Dhathathreyan, Effect of PTFE content in gas diffusion media and microlayer on the performance of PEMFC tested under ambient pressure, *Fuel Cells* 7 (2007) 314-318.

- [42] S. S. Khan, H. Shareef, I. A. Khan, V. Bhattacharjee, K. W. Sultan, Effect of ambient conditions on water management and faults in PEMFC systems: A Review, *IEEE Canadian Conference of Electrical and Computer Engineering (CCECE)* Edmonton, AB, Canada (2019) pp. 1-5.
- [43] T. M. Gür, Review of electrical energy storage technologies, materials and systems: challenges and prospects for large-scale grid storage, *Energ. Environ. Sci.* 11 (2018) 2696-2767.
- [44] F. Mitlitsky, B. Myers, A. H. Weisberg, Regenerative fuel cell systems, *Energ. Fuel.* 12 (1998) 56-71.
- [45] Y. Wang, D.Y.C. Leung, J. Xuan, H. Wang, A review on unitized regenerative fuel cell technologies, part-A: Unitized regenerative proton exchange membrane fuel cells, *Renew. Sust. Energ. Rev.* 65 (2016) 961-977.
- [46] S. Sharma, B.G. Pollet, Support materials for PEMFC and DMFC electrocatalysts—A review, *J. Power Sources* 208 (2012) 96-119.
- [47] T. Hottinen, M. Mikkola, T. Mennola, P. Lund, Titanium sinter as gas diffusion backing in PEMFC, *J. Power Sources* 118 (2003) 183-188.
- [48] C. Rakousky, U. Reimer, K. Wippermann, M. Carmo, W. Lueke, D. Stolten, An analysis of degradation phenomena in polymer electrolyte membrane water electrolysis, *J. Power Sources* 326 (2016) 120-128.
- [49] C. M. Hwang, M. Ishida, H. Ito, T. Maeda, A. Nakano, Y. Hasegawa, N. Yokoi, A. Kato, T. Yoshida, Influence of properties of gas diffusion layers on the performance of polymer electrolyte-based unitized reversible fuel cells, *Int. J. Hydro. Energ.* 36 (2011) 1740-1753.
- [50] C.-M. Hwang, M. Ishida, H. Ito, T. Maeda, A. Nakano, A. Kato, T. Yoshida, Effect of PTFE contents in the gas diffusion layers of polymer electrolyte-based

- unitized reversible fuel cells, *J. Int. Counc. Electr. Eng.* 2 (2012) 171-177.
- [51] T. Ioroi, T. Oku, K. Yasuda, N. Kumagai, Y. Miyazaki, Influence of PTFE coating on gas diffusion backing for unitized regenerative polymer electrolyte fuel cells, *J. Power Sources* 124 (2003) 385-389.
- [52] C. M. Hwang, M. Ishida, H. Ito, T. Maeda, A. Nakano, A. Kato, T. Yoshida, Effect of titanium powder loading in gas diffusion layer of a polymer electrolyte unitized reversible fuel cell, *J. Power Sources* 202 (2012) 108-113.
- [53] S. T. Thompson, B. D. James, J. M. Huya-Kouadio, C. Houchins, D. A. DeSantis, R. Ahluwalia, A. R. Wilson, G. Kleen, D. Papageorgopoulos, Direct hydrogen fuel cell electric vehicle cost analysis: System and high-volume manufacturing description, validation, and outlook, *J. Power Sources* 399 (2018) 304-313.
- [54] N. T. Suen, S. F. Hung, Q. Quan, N. Zhang, Y. J. Xu, H. M. Chen, Electrocatalysis for the oxygen evolution reaction: recent development and future perspectives, *Chem. Soc. Rev.* 46 (2017) 337-365.
- [55] A. Mahata, A. S. Nair, B. Pathak, Recent advancements in Pt-nanostructure-based electrocatalysts for the oxygen reduction reaction, *Catal. Sci. Technol.* 9 (2019) 4835-4863.
- [56] I.E.L. Stephens, J. Rossmeisl, I. Chorkendorff, Toward sustainable fuel cells, *Science* 354 (2016) 1378-1379.
- [57] K.-H. Kim, K.-Y. Lee, H.-J. Kim, E. Cho, S.-Y. Lee, T.-H. Lim, S. P. Yoon, I. C. Hwang, J. H. Jang, The effects of Nafion® ionomer content in PEMFC MEAs prepared by a catalyst-coated membrane (CCM) spraying method, *Int. J. Hydro. Energ.* 35 (2010) 2119-2126.
- [58] A. Suzuki, U. Sen, T. Hattori, R. Miura, R. Nagumo, H. Tsuboi, N. Hatakeyama, A. Endou, H. Takaba, M.C. Williams, A. Miyamoto, Ionomer content in the

- catalyst layer of polymer electrolyte membrane fuel cell (PEMFC): Effects on diffusion and performance, *Int. J. Hydro. Energ.* 36 (2011) 2221-2229.
- [59] W. Xu, K. Scott, The effects of ionomer content on PEM water electrolyser membrane electrode assembly performance, *Int. J. Hydro. Energ.* 35 (2010) 12029-12037.
- [60] M. Bernt, H.A. Gasteiger, Influence of ionomer content in IrO<sub>2</sub>/TiO<sub>2</sub> electrodes on PEM water electrolyzer performance, *J. Electrochem. Soc.* 163 (2016) F3179-F3189.
- [61] M. Yazdanpour, A. Esmacilifar, S. Rowshanzamir, Effects of hot pressing conditions on the performance of Nafion membranes coated by ink-jet printing of Pt/MWCNTs electrocatalyst for PEMFCs, *Int. J. Hydro. Energ.* 37 (2012) 11290-11298.
- [62] F. Fouda-Onana, N. Guillet, A.M. AlMayouf, Modified pulse electrodeposition of Pt nanocatalyst as high-performance electrode for PEMFC, *J. Power Sources* 271 (2014) 401-405.
- [63] H. Kim, S. Choe, H. Park, J. H. Jang, S. H. Ahn, S. K. Kim, An extremely low Pt loading cathode for a highly efficient proton exchange membrane water electrolyzer, *Nanoscale* 9 (2017) 19045-19049.
- [64] H. Park, S. Choe, H. Kim, D.-K. Kim, G. Cho, Y. Park, J. H. Jang, D.-H. Ha, S. H. Ahn, S.-K. Kim, Direct fabrication of gas diffusion cathode by pulse electrodeposition for proton exchange membrane water electrolysis, *Appl. Surf. Sci.* 444 (2018) 303-311.
- [65] B.-S. Lee, S. H. Ahn, H.-Y. Park, I. Choi, S. J. Yoo, H.-J. Kim, D. Henkensmeier, J. Y. Kim, S. Park, S. W. Nam, K.-Y. Lee, J. H. Jang, Development of electrodeposited IrO<sub>2</sub> electrodes as anodes in polymer electrolyte membrane

water electrolysis, *Appl. Catal. B* 179 (2015) 285-291.

- [66] B.-S. Lee, H.-Y. Park, I. Choi, M. K. Cho, H.-J. Kim, S. J. Yoo, D. Henkensmeier, J.Y. Kim, S. W. Nam, S. Park, K.-Y. Lee, J. H. Jang, Polarization characteristics of a low catalyst loading PEM water electrolyzer operating at elevated temperature, *J. Power Sources* 309 (2016) 127-134.
- [67] S. Choe, B.-S. Lee, M. K. Cho, H.-J. Kim, D. Henkensmeier, S. J. Yoo, J. Y. Kim, S. Y. Lee, H. S. Park, J. H. Jang, Electrodeposited IrO<sub>2</sub>/Ti electrodes as durable and cost-effective anodes in high-temperature polymer-membrane-electrolyte water electrolyzers, *Appl. Catal. B* 226 (2018) 289-294.
- [68] B.-S. Lee, H.-Y. Park, M. K. Cho, J. W. Jung, H.-J. Kim, D. Henkensmeier, S. J. Yoo, J. Y. Kim, S. Park, K.-Y. Lee, J. H. Jang, Development of porous Pt/IrO<sub>2</sub>/carbon paper electrocatalysts with enhanced mass transport as oxygen electrodes in unitized regenerative fuel cells, *Electrochem. Comm.* 64 (2016) 14-17.
- [69] O. H. Kim, Y. H. Cho, S. H. Kang, H. Y. Park, M. Kim, J. W. Lim, D. Y. Chung, M. J. Lee, H. Choe, Y. E. Sung, Ordered macroporous platinum electrode and enhanced mass transfer in fuel cells using inverse opal structure, *Nat. Commun.* 4 (2013) 2473-2481.
- [70] J. E. Park, S. Kim, O.-H. Kim, C.-Y. Ahn, M.-J. Kim, S. Y. Kang, T. I. Jeon, J.-G. Shim, D. W. Lee, J. H. Lee, Y.-H. Cho, Y.-E. Sung, Ultra-low loading of IrO<sub>2</sub> with an inverse-opal structure in a polymer-exchange membrane water electrolysis, *Nano Energy* 58 (2019) 158-166.
- [71] H. Kim, B. N. Popov, Development of novel method for preparation of PEMFC electrodes, *Electrochem. Solid St.* 7 (2004) A71-A74.
- [72] J. Choe, D. Kim, J. Shim, I. Lee, Y. Tak, Fabrication of a nanosize-Pt-embedded

- membrane electrode assembly to enhance the utilization of Pt in proton exchange membrane fuel cells, *J. Nanosci. Nanotechnol.* 11 (2011) 7141-7144.
- [73] J. J. Burk, S. K. Buratto, Electrodeposition of Pt nanoparticle catalysts from  $H_2Pt(OH)_6$  and their application in PEM fuel cells, *J. Phys. Chem. C* 117 (2013) 18957-18966.
- [74] D.-K. Kim, H. Kim, H. Park, S. Oh, S. H. Ahn, H.-J. Kim, S.-K. Kim, Performance enhancement of high-temperature polymer electrolyte membrane fuel cells using Pt pulse electrodeposition, *J. Power Sources* 438 (2019) 227022.
- [75] N. Afsham, N. Fallah, B. Nassernejad, M. Javanbakht, Z. Jabbari, Fabrication of gas diffusion electrode via Pt electrodeposition on cathodic oxidized carbon paper as the anode for high-temperature polymer membrane fuel cell in the presence of CO, *Ionics* 25 (2019) 3549-3560.

# **Chapter 2. Low-loading IrO<sub>2</sub> Supported on Pt for Catalysis of PEM Water Electrolysis and Regenerative Fuel Cells**

## **2.1. Introduction**

The development of energy- and economically efficient technologies to store renewable electricity is an impending challenge arising from the urgent need of rapidly deployable renewable energy systems [1]. Devices using different energy carriers, including rechargeable batteries, liquid-organic hydrocarbons, ammonia, and hydrogen, are rigorously studied for scalability, stability, and efficiency required to implement the non-fossil energy infrastructure in present economic systems [2-5]. Hydrogen is a zero-carbon energy vector as it is environmentally produced by electrolyzers (WE) and is converted to water by fuel cells (FC). It possesses a high energy density of 142 MJ kg<sup>-1</sup> or 12.7 MJ m<sup>-3</sup> (HHV). In this context, a unitized regenerative fuel cell (URFC) is potentially well-suited as a clean energy converter in renewable energy systems [6].

URFCs are a combined system of WEs and FCs, which produce hydrogen and oxygen when electricity is available (WE mode) and then generate electricity using the produced hydrogen and oxygen (FC mode). As the production and usage of hydrogen is performed by a single device, URFCs are advantageous for its device

simplicity and cost effectiveness compared to the two separate WE and FC systems [7]. URFCs are classified based on their working temperatures and ion-conducting electrolytes, such as proton exchange membrane-URFCs (UR-PEMFCs or PEM-URFCs), alkaline exchange membrane-URFCs (UR-AFCs), and solid oxide electrolyte-URFC (UR-SOFCs). Among them, UR-PEMFCs are the most mature technology and are used in aerospace and military applications [7, 8].

Widespread commercialization of UR-PEMFCs is hampered by the high cost of cell components, e.g. precious metal catalysts, fluorinated electrolyte membranes, non-corrosive porous transport layers (PTLs), and metal based bipolar plates. Especially, the large amount of noble metal catalysts, up to  $4 \text{ mg cm}^{-2}$  of Pt and Ir, is a substantial cost for state-of-art UR-PEMFC devices that need catalysts to facilitate oxygen reduction and oxygen evolution reactions (ORR and OER). Given the activity and stability of catalysts are unaffected, mass activity of catalysts can be enhanced by using support materials. In fuel cell technologies, carbonaceous catalyst supports, e.g. carbon black, graphene, carbon nanotubes (CNT), carbon nanofiber (CNF), etc., have been heavily used to maximize the catalyst usage [9]. High surface area carbon supports in PEMFCs reduce the use of Pt to the commercialized level, e.g. less than  $0.3 \text{ mg cm}^{-2}$ , by providing (i) a high dispersion of catalysts and higher electrochemical surface area while preventing particle agglomeration [10], (ii) wettability for ion conduction [11], and (iii) sufficient electronic conductivity [12]. However, unlike PEMFCs, amorphous carbon support is an inappropriate material in UR-PEMFCs due to severe carbon corrosion ( $\text{CO}_2 + 4\text{H}^+ + 4\text{e}^- \rightleftharpoons \text{C} + 2 \text{H}_2\text{O}$ ,  $E^0 = 0.206 \text{ V}_{\text{RHE}}$ ) during the OER in WE operation. Due to the absence of suitable commercialized alternatives of carbon support for the OER catalysis, the high loading of unsupported noble catalysts is considered inevitable to secure a sufficient

catalytic surface for the oxygen electrode of the URFC in many reports.

Non-corrosive supporting materials have been studied for utilization as the catalyst support of IrO<sub>2</sub>, the benchmark OER catalyst, instead of carbon materials, e.g. SnO<sub>2</sub> [13], TiO<sub>2</sub> [14], TiC [15], TaC [16], ATO [17] and ITO [18], with limited electric conductivities. IrO<sub>2</sub> nanoparticles were also considered as an appropriate support material of Pt for the ORR of URFCs, which further served as the OER catalyst in the bi-functional electrodes [19, 20]. In this case, IrO<sub>2</sub> provided the physical location for the catalysis, and electrochemical interactions between Ir and Pt were reported to improve the ORR activity of Pt; Ir@Pt core-shell ORR electrocatalysts showed 2.6x higher specific activities compared to commercial Pt/C due to weakening of the Pt-O bond by Pt-Ir interactions [21, 22]. O<sup>-</sup> or OH<sup>-</sup> adsorbed on Ir reduces the OH-coverage on Pt due to electrostatic repulsion between anions, leading to a higher ORR activity [23]. In contrast, bifunctional electrocatalysts using Pt as an IrO<sub>2</sub> support was also studied, in which IrO<sub>2</sub> was chemically formed on Pt black powder [24]. Ioroi *et al.* showed that Pt black with a small surface area (26.1 m<sup>2</sup> g<sup>-1</sup>) could serve as the catalyst support, leading to improved FC and WE performance compared to that using physically mixed Pt and IrO<sub>2</sub> powder catalysts [24, 25]. The Pt support had a sufficient electrical conductivity and electrochemical stability for the OER catalysis using IrO<sub>2</sub>. However, the reported WE performance was insufficient at less than 0.5 A cm<sup>-2</sup> at 1.6 V<sub>Cell</sub>, which was due to the limited surface area of Pt and inefficient distribution of IrO<sub>2</sub> [24].

Electrodeposition (e-) is performed on the active surface, providing both electronic and ionic conductivity in the presence of the chemical precursors, i.e. triple phase boundary [26]. Therefore, the process produces an accurate amount of deposits by manipulating the current flow at the active sites, whereas other physical

coating approaches, e.g. decal, brush printing, screen printing, and spraying, layer the materials on substrates regardless of its electrochemical activity. Studies employing e-Pt catalysts in the anode [27, 28] and cathode [27, 29, 30] of PEMFCs or cathode of PEMWEs [31] demonstrated high mass activity of catalysts. A pulse e-Pt cathode of PEMFC resulted in  $0.1 \text{ A mg}^{-1}$  at  $0.9 \text{ V}_{\text{IR-free}}$  with  $0.12 \text{ mg}_{\text{Pt}} \text{ cm}^{-2}$ , which is 2x higher than that of the sprayed Pt/C of  $0.4 \text{ mg}_{\text{Pt}} \text{ cm}^{-2}$  [29]. e-IrO<sub>2</sub> at the PEMWE anode was reported to exhibit a current density of  $0.97 \text{ A cm}^{-2}$  at  $1.6 \text{ V}_{\text{Cell}}$  and temperature of  $120^\circ\text{C}$  using  $0.4 \text{ mg cm}^{-2}$  of IrO<sub>2</sub>, an amount of IrO<sub>2</sub> that is significantly less than that used in physically coated electrodes for comparable performance [32].

Herein, a highly conductive and active OER electrode, IrO<sub>2</sub> catalyst supported on Pt core (Pt@IrO<sub>2</sub>), is prepared on Ti PTL by sequential electrodeposition of Pt and IrO<sub>2</sub> to maximize the apparent and mass activity of IrO<sub>2</sub> in WE and URFC operations. Hemispheric e-Pt particles with a diameter of approximately  $0.5\text{--}1.5 \mu\text{m}$  are utilized as the support of the nanometer-thick e-IrO<sub>2</sub> catalyst and are fabricated on Ti PTL to preserve the appropriate electrode structure and hydrophilicity. The Pt support enhanced the electrochemical surface area of IrO<sub>2</sub> and significantly reduced the contact resistance between catalysts and the porous Ti substrate. These factors become the primary impetus for maximizing the URFC performance with minimal use of precious metals. The sequential electrodeposition of the Pt@IrO<sub>2</sub> catalyst on the Ti substrate is clearly investigated in order to explain the enhanced URFC single cell performance. This work demonstrates a facile strategy to form a highly-active and cost-effective electrode for WE and URFC. To the best of our knowledge, this is the first trial of a sequential reductive and oxidative electrodeposition of Pt and Ir oxide, respectively, to utilize Pt as the catalyst support of IrO<sub>2</sub>, achieving high

performance in WE and URFCs.

## 2.2. Experimental Section

### 2.2.1. Electrode Preparation

Membrane electrode assembly (MEA, 2.25 cm<sup>2</sup>) was fabricated by a hot pressing process (120°C, 395 psi, 1 min) to prepare a sandwiched structure of proton conducting membranes (NR-212, 50.8 μm, Dupont<sup>TM</sup>) between two electrodes. Pt and IrO<sub>2</sub> were electrodeposited on Ti-felt (250 μm thickness, 60 % porosity, 20 μm fiber diameter, 2 PTL9N-025, Bekaert) to form anode in URFC. Ti mesh (50 mesh, 0.102 mm dia., Alfa-Aesar) and a saturated calomel electrode (SCE) were used as counter and reference electrodes for the electrodeposition. e-Pt was performed in 20 mM chloroplatinic acid hydrate (99.995%, Sigma-Aldrich) dissolved in a 0.5 M sulfuric acid solution with a constant reduction current of 10 mA cm<sup>-2</sup> for different durations (0.5, 1, 2, 5, 8, or 10 min). e-IrO<sub>2</sub> was conducted in the aqueous solution of 0.01 M iridium(IV) chloride hydrate (99.95%, Ir 56.5%, Alfa-Aesar), oxalic acid ((COOH)<sub>2</sub>·2H<sub>2</sub>O: 5 g L<sup>-1</sup>), hydrogen peroxide (35% H<sub>2</sub>O<sub>2</sub>: 10 g L<sup>-1</sup>), and anhydrous potassium carbonate (≥ 99.0%, Sigma-Aldrich). The precursor solution was stirred for 72 h before the deposition. IrO<sub>2</sub> was deposited at 0.7 V<sub>SCE</sub> for 10 min on Ti-felt previously decorated with Pt at room temperature. Ti-felt was cleaned in oxalic-acid before the deposition [32, 33]. The cathode of URFC was prepared by spaying 0.4 mg cm<sup>-2</sup> of Pt/C on carbon paper (10 BC, Sigracet). The catalyst ink slurry contained Pt/C powder (Pt 46.5 wt%, Tanaka K.K) suspended in 5 wt% Nafion solution, deionized water, and isopropyl alcohol and homogenized in an ultrasonic bath (40

kHz), maintaining solution at room temperature by circulation of water in the bath. The conventional IrO<sub>2</sub> electrode was also prepared by spraying commercial Ir oxide (Iridium(IV) oxide, Premion®, 99.99% (metals basis), Ir 84.5% min, Alfa Aesar) with various loading amounts on Ti-felt. The IrO<sub>2</sub> ink composition for spraying was the same as the Pt/C slurry with the exception of the active catalysts.

### **2.2.2. Analysis of Materials and Electrodes**

The surface morphology and distribution of catalyst particles on substrates were examined by field emission scanning electron microscopy (FE-SEM, Teneo Volume Scope) and energy dispersive spectrometer (EDS). X-ray photoelectron spectroscopy (XPS, Thermo VG Scientific, Germany) using a soft X-ray source (Al K $\alpha$ , 1486.6 eV), high-resolution TEM (HRTEM, Talos), and high-angle annular dark-field scanning TEM (HAADF-STEM) were performed on the electrodeposited catalysts. The catalyst composition was analyzed using inductively coupled plasma-optical emission spectroscopy (ICP-OES, iCAP6500 Duo, Thermo). Preconditioning process for ICP-OES analysis of the electrode is as follows: i) Putting sample in mixed solution of the 5 ml HF and 15 ml aqua regia, ii) heating until 150 °C and adding additional 15 ml aqua regia and iii) adding DI-water until 25 ml after heating at 150 °C. Porosity of electrodes were measured by mercury porosimetry (TriStar II 3020, Micromeritics). The mercury is filled on the samples in vacuum and pore distribution is analyzed by measuring volume of pore into which mercury is adsorbed as pressure increase from vacuum. The electric resistivity (or conductivity) of the electrodes, e.g. bare Ti PTL, ED-Pt, ED-IrO<sub>2</sub>, and ED-Pt@IrO<sub>2</sub>, was obtained by four probe measurements on the micrometer scale using a SEM-FIB system (Quanta-

3D; FEI company, Eindhoven, Netherlands) in vacuum containing nanomanipulators (MM3A EM; Kleindiek Nanotechnik GmbH, Reutlingen, Germany) and a semiconductor device analyzer (B1500A; Agilent Technologies, Palo Alto, CA, USA). The electrochemical active surface area (ECSA) of IrO<sub>2</sub> catalysts was estimated from the H-upd peaks at Ir metal surfaces. The oxide surface was first reduced to metallic Ir in repeated cyclic voltammetry (CV) from 0.05 to 0.6 V<sub>Pseudo-RHE</sub> (OR 1.1 V<sub>Pseudo-RHE</sub>) until a steady-state in a single cell MEA was reached. In the measurements, Pt/C electrode was utilized as a pseudo-RHE reference and counter electrode under humidified H<sub>2</sub> gas flow. Then, ECSA was calculated with steady-state CV using H-adsorption characteristic of the Ir metal surface. The charge density required for the desorption of the H-upd layer at polycrystalline Ir metal was assumed to be 218 μC cm<sup>-2</sup> [34].

### 2.2.3. Performance Measurements

A single cell device was assembled by placing the MEA between two current collectors. Titanium and graphite plates were used as current collector, respectively. A serpentine flow channel was engraved in the current collector plate. The torque of the cell assembly was 80 lb·in to secure the MEA without gas and electrolyte leakage. The URFC operation temperature was 80°C. In FC operation, oxygen and hydrogen fuel gas were supplied at a flow rate of 400 ccm. The fuel gas temperature was 70°C. In WE operation, DI-water was provided to the oxygen electrode at a flow rate of 15 ml min<sup>-1</sup>. The current-voltage relationship (IV-curve) and electrochemical impedance spectroscopy (EIS) were measured using a high current potentiostat (HCP-803, Bio-Logic). In WE operation, the IV-curve was obtained by averaging

the current density at each applied voltage for 1 min, while the cell voltage was varied from 1.25 to 2.0  $V_{\text{Cell}}$  at a 50 mV interval. In FC operation, the IV-curve was measured from OCV to 0.2  $V_{\text{Cell}}$  at a scan rate of 10  $\text{mV s}^{-1}$ . In long term tests, both FC and WE operations were performed at a static current of 0.4  $\text{A cm}^{-2}$  for 20 h in each cycle. Before each FC operation, the electrode was treated in CV with a voltage controlled from 0.05 to 0.6  $V_{\text{Cell}}$  and then 0.05 to 1.1  $V_{\text{cell}}$  under  $\text{H}_2$  and  $\text{N}_2$  gas atmosphere for Pt/C electrode and electrodeposited electrode, respectively.

## 2.3. Results and Discussion

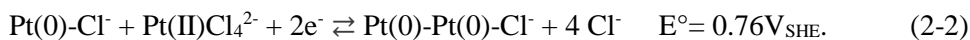
### 2.3.1. Formation of Catalyst Layers

The fabrication of e- $\text{IrO}_2$  and e-Pt@ $\text{IrO}_2$  electrodes by sequential electrodeposition of Pt and  $\text{IrO}_2$  on Ti-felt is described in the schematic illustration of procedure (Figure 2.1). Electrodeposition is a facile and highly-controllable process used to deposit catalysts on the active substrate [27-33]. Here, Ir oxide, which is a state-of-the-art OER catalyst in both its activity and stability, was electrodeposited at 0.7  $V_{\text{SCE}}$  throughout the Ti electrode using the electrochemical reaction:  $[\text{Ir}(\text{COO})_2(\text{OH})_4]^{2-} \rightarrow \text{IrO}_2 + 2 \text{CO}_2 + 2 \text{H}_2\text{O} + 2 \text{e}^-$  [33]. Chloride ligands of  $\text{IrCl}_4^-$  in aqueous solution are substituted with oxalate ligands in the presence of oxalic acid and hydrogen peroxide, and then further oxidize to  $\text{IrO}_2$  and  $\text{CO}_2$  on the Ti PTL electrode [35]. In CV tests in iridium precursor solution, oxidation current to form  $\text{IrO}_2$  was observed at 0.96  $V_{\text{RHE}}$ , and oxygen evolution reaction (OER) started at 1.41  $V_{\text{RHE}}$  (Figure 2.2). The exact onset potential for iridium oxidation was

difficult to determine through CV due to simultaneous oxidation reactions of the aqueous electrolyte, but the applied potential was 1.56 V<sub>RHE</sub>, which is sufficiently positive in order to form the IrO<sub>2</sub> [32, 36] as shown by SEM (Figure 2.2, 2.3(a), 2.3(b)).

The oxidative deposition of IrO<sub>2</sub> on Ti PTL (e-IrO<sub>2</sub>), which consists of Ti fibers with 20 μm diameter, resulted in a metal oxide of uniform thickness on Ti-fiber (e-IrO<sub>2</sub>, Figure 2.1, 2a, 2b). The thickness of IrO<sub>2</sub> on Ti fibers was approximately 170–180 nm after ED for 10 min at a constant potential of 0.7 V<sub>SCE</sub> (Figure 2.3(b)). Under these deposition conditions, the amount of IrO<sub>2</sub> layered onto Ti PTL was 0.15 mg cm<sup>-2</sup> as confirmed by ICP-OES analysis.

The electrochemical reaction rate is directly controlled by the catalyst active surface area, so the catalyst utilization and the mass activity can be enhanced by roughening the catalytic interface to the electrolyte solution. Herein, a stable metal particle is introduced as the catalyst support to enhance the active area of e-IrO<sub>2</sub>. Briefly, Pt particles were electrodeposited as the catalyst support onto Ti PTL (e-Pt) before IrO<sub>2</sub> film formation. Electrodeposition of Pt on Ti using H<sub>2</sub>PtCl<sub>6</sub> in 0.5 M H<sub>2</sub>SO<sub>4</sub> solution was conducted at -10 mA cm<sup>-2</sup> with varying electrodeposition times from 0.5 to 10 min. The electrochemical reactions during electrodeposition are shown in equation (2-1) and (2-2). Pt(IV)Cl<sub>6</sub><sup>2-</sup> complexes were reduced to metallic Pt with Pt(II)Cl<sub>4</sub><sup>2-</sup> complexes as the intermediate product [37].



As demonstrated in the SEM images in Figure 2.4, each agglomerate of Pt reveals

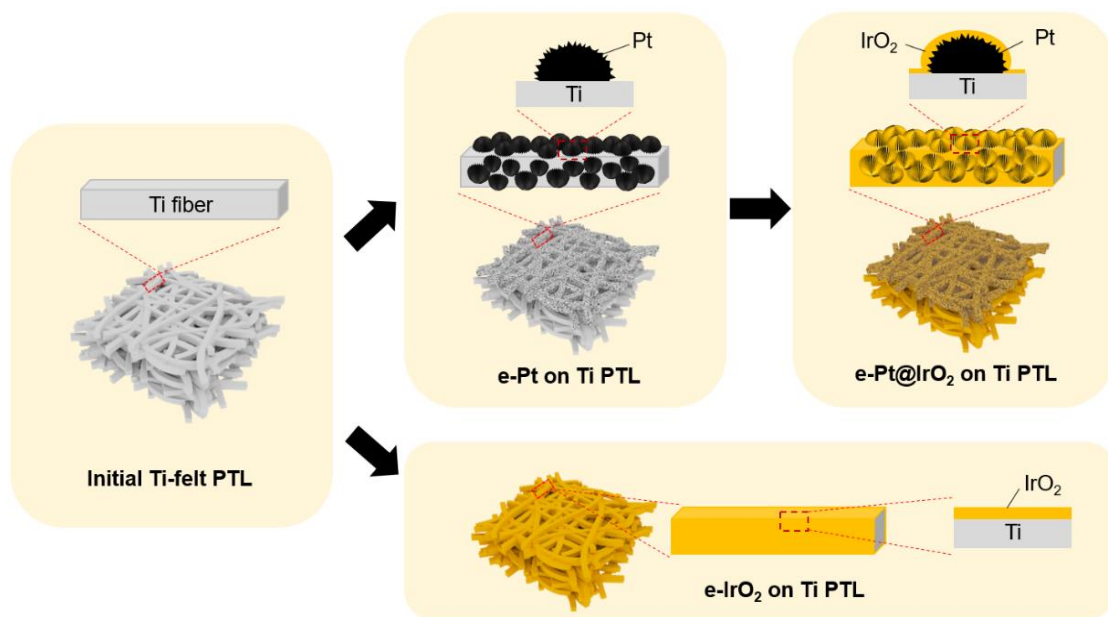


**Figure 2.1.** Schematic procedure of fabrication of e-Pt@IrO<sub>2</sub> and e-IrO<sub>2</sub>.

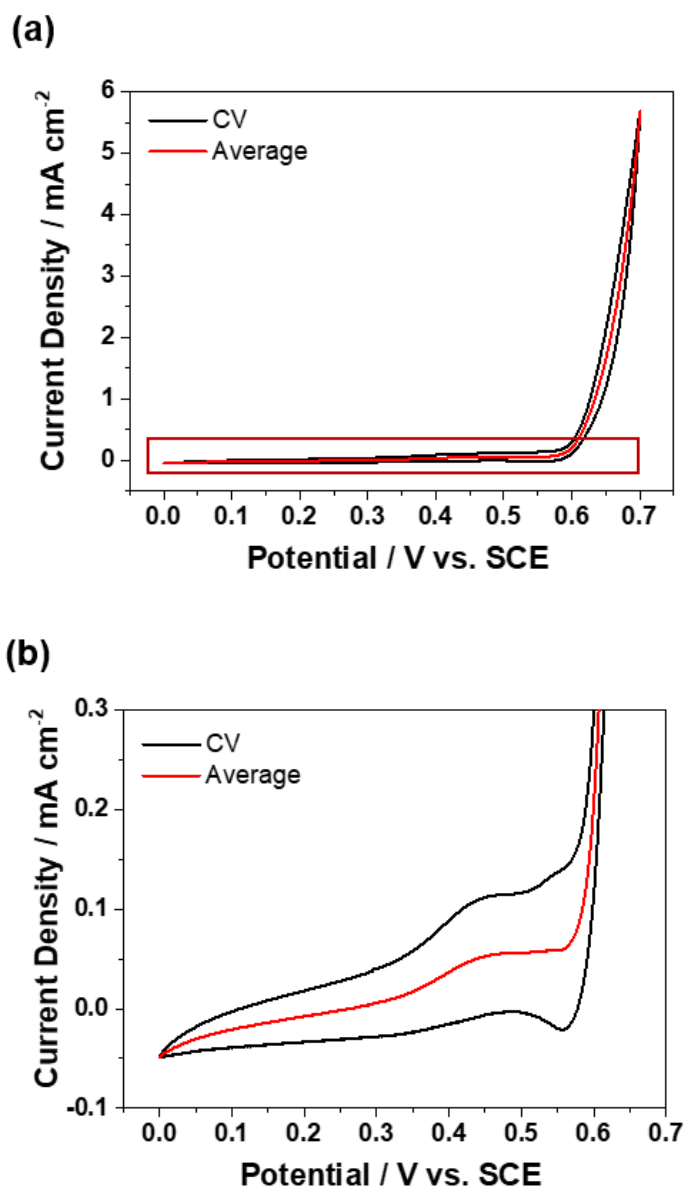


**Figure 2.2.** Electrochemical analysis in iridium oxide electrodeposition. (a) Cyclic voltammetry in precursor solution (pH 10.5) of Iridium oxide electrodeposition using rotating disk electrode without rpm at  $5 \text{ mV s}^{-1}$  and its average current density vs. potential. (b) Enlarged image of (a).

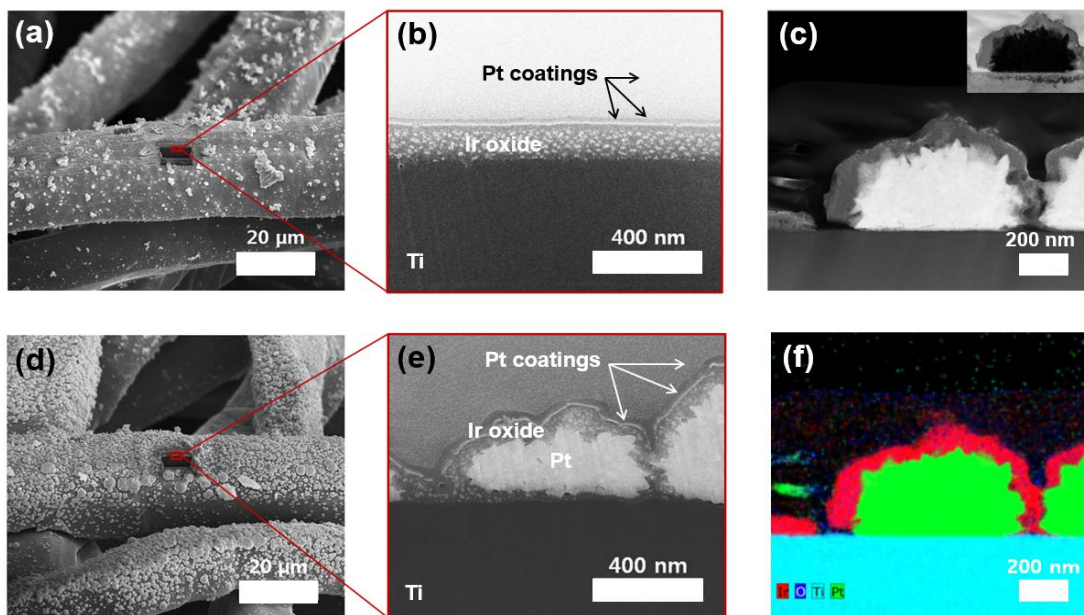


**Figure 2.3.** SEM and TEM Image of e-IrO<sub>2</sub> and e-Pt@IrO<sub>2</sub>. (a) Top and (b) cross-section FIB-SEM images of e-IrO<sub>2</sub> on each fiber in Ti felt. (c) STEM image of sequential e-Pt@IrO<sub>2</sub> (inserted; HAADF-STEM TEM image). (d) Top and (e) cross-section FIB-SEM images of sequential e-Pt@IrO<sub>2</sub>. Surface Pt coatings were done for surface protection during straight cutting using ion-beam. (f) Quantitative EDX elemental maps image of sequential e-Pt@IrO<sub>2</sub> (red:Ir, sky blue: Ti, green: Pt).

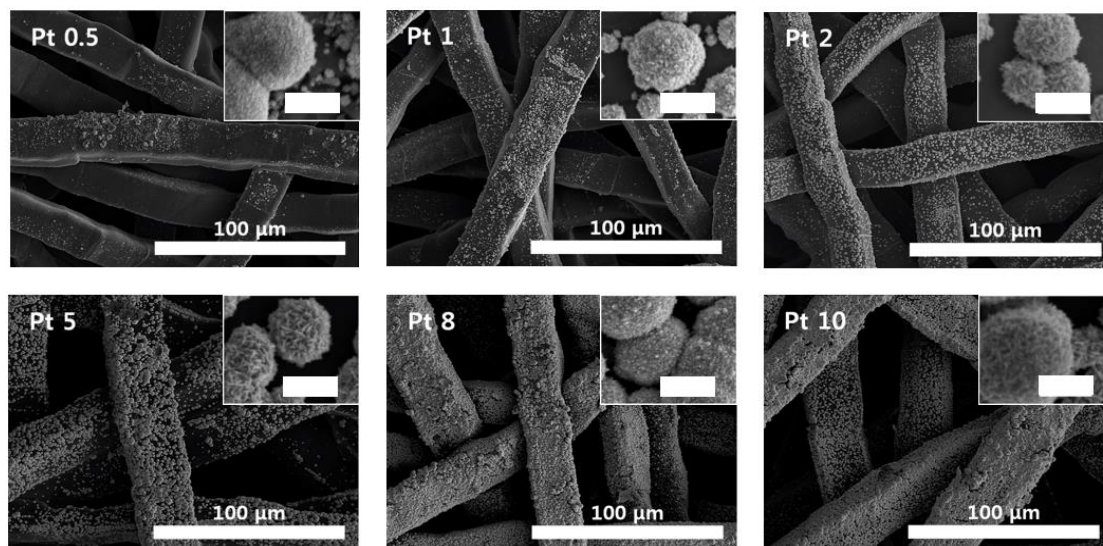


**Figure 2.4.** Image of Pt electrodeposited electrodes. SEM images of e-Pt/Ti. Pt deposition time was varied from 0.5 min to 10 min from top-left to bottom-right (scale bar in inserted figures: 1  $\mu\text{m}$ ).

clusters of a petal-shape crystal with an approximate size of 0.5–1.5  $\mu\text{m}$  (Figure 2.3(c)–(f) and 2.5) [38]. The coverage of these Pt particles increased on Ti-felt as the electrodeposition time increased from 0.5 to 10 min, but the size of the Pt agglomerates remained constant regardless of deposition time (Figure 2.4). Mass transport of metal complex ions, concentration distribution of the reactants at the electrode-electrolyte interface, and local electrode potentials control the structure of particles generated during electrodeposition [39]. Growth of larger-sized Pt agglomerates in a short period can be explained by preferred adsorption and reduction of Pt ions on the Pt cluster surfaces rather than on the bare Ti substrate. Growth on the Pt cluster is continued until the deposition kinetics favors a new nucleation on the Ti substrate. Factors, such as increased electric resistance and/or ineffective radial diffusion over larger agglomerates compared to smaller nuclei, lead to the halt of further growth [38]. As a result, the Pt particle size was limited to 0.5–1.5  $\mu\text{m}$  in this study (Figure 2.5). The total amount of Pt loaded on Ti PTL was consequently increased from 0.09 to 0.66  $\text{mg cm}^{-2}$  with the increase in deposition time from 0.5 to 10 min (Table 2.1). The Pt agglomerates were primarily produced at the top-most Ti PTL-electrolyte interface, and fewer deposits were observed in the bulk porous electrode (Figure 2.6). The localized deposition of Pt is ascribed to the limited aqueous electrolyte flow through the hydrophobic pores of Ti PTL during electrodeposition (Figure 2.6 and 2.7) [40].

In order to increase the  $\text{IrO}_2$  surface area, e- $\text{IrO}_2$  nanoparticles were uniformly produced on both Pt islands and bare Ti surfaces following the e-Pt (Figure 2.6 and 2.8). The process results in  $\text{IrO}_2$  supported on Pt (e-Pt@ $\text{IrO}_2$ ) that is mainly produced on the upmost layer of Ti PTL, in addition to the small amount of unsupported e-

IrO<sub>2</sub> on the bare Ti surface in the bulk Ti PTL (Figure 2.1 and 2.6). The outmost surface of PTL, i.e. the e-Pt@IrO<sub>2</sub> layer, is in a direct contact with the ion-conducting polymer when the membrane electrode is constructed and is the central reaction site for the URFC.

In the discussions below, the electrode fabricated with a deposition time of 5 and 10 min for Pt and IrO<sub>2</sub>, respectively, was selected based upon performance (e-Pt5@IrO<sub>2</sub> in Figure 2.9 and Table 1). The number named next to Pt in Pt#@IrO<sub>2</sub> is the time of Pt electrodeposition. 5 min Pt electrodeposition was chosen as optimized electrode as no more enhancement of performance was observed with the increased time of Pt support than 5 min. This comes from limited increase of surface area by stacking Pt agglomerates (Figure 2.4), results in optimized IrO<sub>2</sub> surface area in e-Pt@IrO<sub>2</sub>, e.g. 30.9 m<sup>2</sup> g<sub>Ir</sub><sup>-1</sup> and 31.1 m<sup>2</sup> g<sub>Ir</sub><sup>-1</sup> for e-Pt5@IrO<sub>2</sub> and e-Pt8@IrO<sub>2</sub>. For the chosen electrode, the film thickness of IrO<sub>2</sub> in the e-Pt@IrO<sub>2</sub> electrode was approximately 80 nm, which is approximately 55% thinner than that in e-IrO<sub>2</sub> electrodes (~180 nm on bare Ti PTL) with a similar amount of IrO<sub>2</sub> for the unsupported catalysts (FIB-SEM, TEM, HAADF-STEM, and EDX analysis in Figure 2.3). The decreased IrO<sub>2</sub> thickness of e-Pt@IrO<sub>2</sub> compared to e-IrO<sub>2</sub> implies an increased catalyst surface area, which further indicates a higher material utilization for catalysis. Further, XPS measurements revealed that the surface of e-Pt@IrO<sub>2</sub> was fully covered by IrO<sub>2</sub> with no Pt signal detection both before and after the URFC operation (Figure 2.10(a)). In XPS, the electronic structure of Ir layered onto e-Pt or Ti PTL was identical to that of bulk IrO<sub>2</sub>, and the deposition did not alter the electron binding energy of IrO<sub>2</sub> (Figure 2.10(b)).

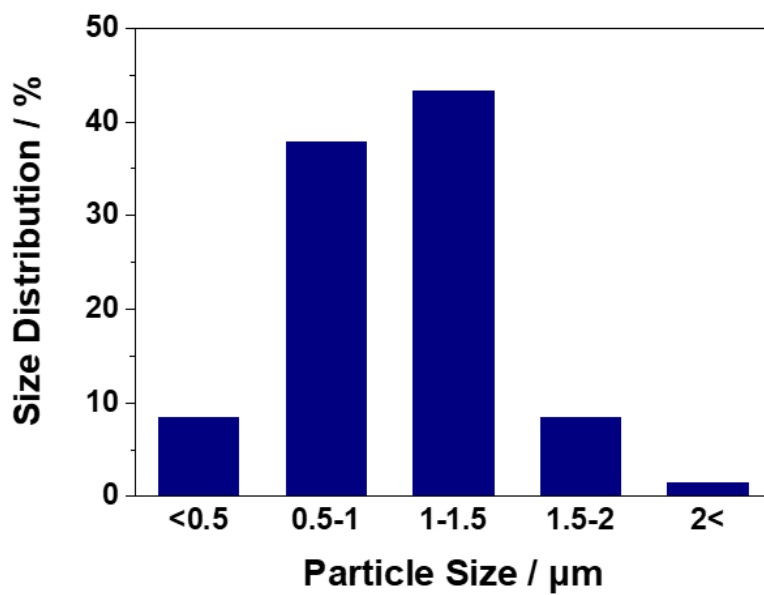


**Figure 2.5.** Particle size distribution of electrodeposited Pt (5 min).

**Table 2.1.** PEMWE current density at 1.9 V, PEMWE current density at 0.5 V, amount of catalysts on the oxygen electrode with different electrodeposition time of Pt from 0 to 10 min. The catalyst loading was determined by ICP-OES.

	<b>J at 1.9 V</b> / A cm <sup>-2</sup>	<b>J at 0.5 V</b> / A cm <sup>-2</sup>	<b>Pt<sub>avg.</sub></b> / mg cm <sup>-2</sup>	<b>Ir<sub>avg.</sub></b> / mg cm <sup>-2</sup>	<b>Total</b> / mg cm <sup>-2</sup>
<b>e-IrO<sub>2</sub></b>	2.29	0.023	0	0.15	0.15
<b>e-Pt 0.5 @IrO<sub>2</sub></b>	3.22	0.0057	0.090	0.104	0.204
<b>e-Pt 1@IrO<sub>2</sub></b>	3.69	0.0097	0.142	0.090	0.232
<b>e-Pt 2@IrO<sub>2</sub></b>	5.00	0.23	0.168	0.170	0.338
<b>e-Pt 5@IrO<sub>2</sub></b>	5.57	0.47	0.277	0.157	0.434
<b>e-Pt 8@IrO<sub>2</sub></b>	5.41	0.44	0.417	0.198	0.615
<b>e-Pt 10 @IrO<sub>2</sub></b>	5.60	0.54	0.661	0.255	0.916

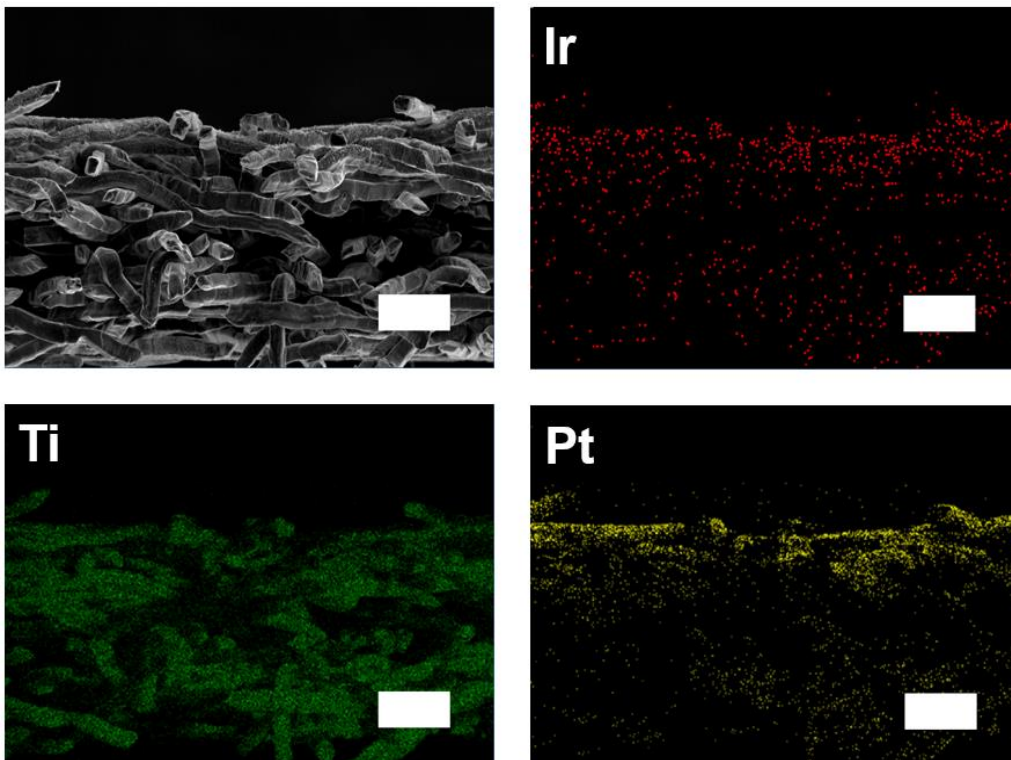


**Figure 2.6.** Elemental distribution observed in the cross-section of e-Pt@IrO<sub>2</sub> electrode. EDS mapping of cross-section of the sequential e-Pt@IrO<sub>2</sub> (0.16 mg<sub>Ir</sub> cm<sup>-2</sup>, 0.28 mg<sub>Pt</sub> cm<sup>-2</sup>)/Ti (scale bar in figures: 100 μm).

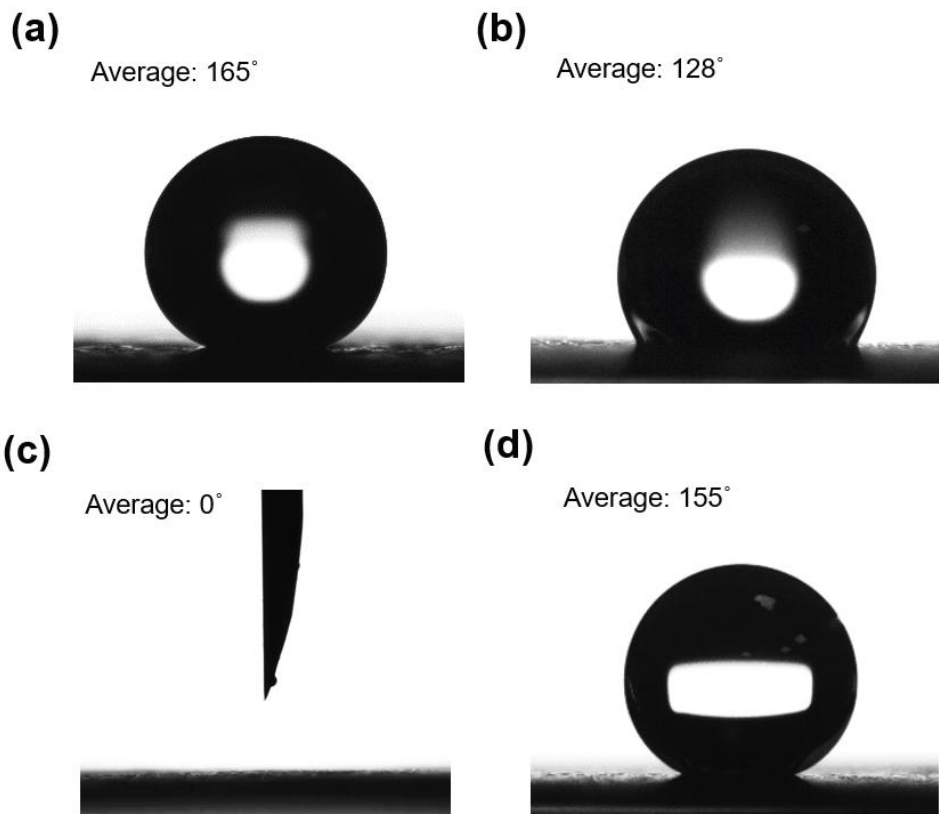


**Figure 2.7.** Hydrophobicity/hydrophilicity property of the electrodes. Water contact angle of (a) C PTL (10 BC), (b) Ti PTL, (c) IrO<sub>2</sub> electrodeposited Ti PTL and (d) sprayed IrO<sub>2</sub> on Ti PTL.

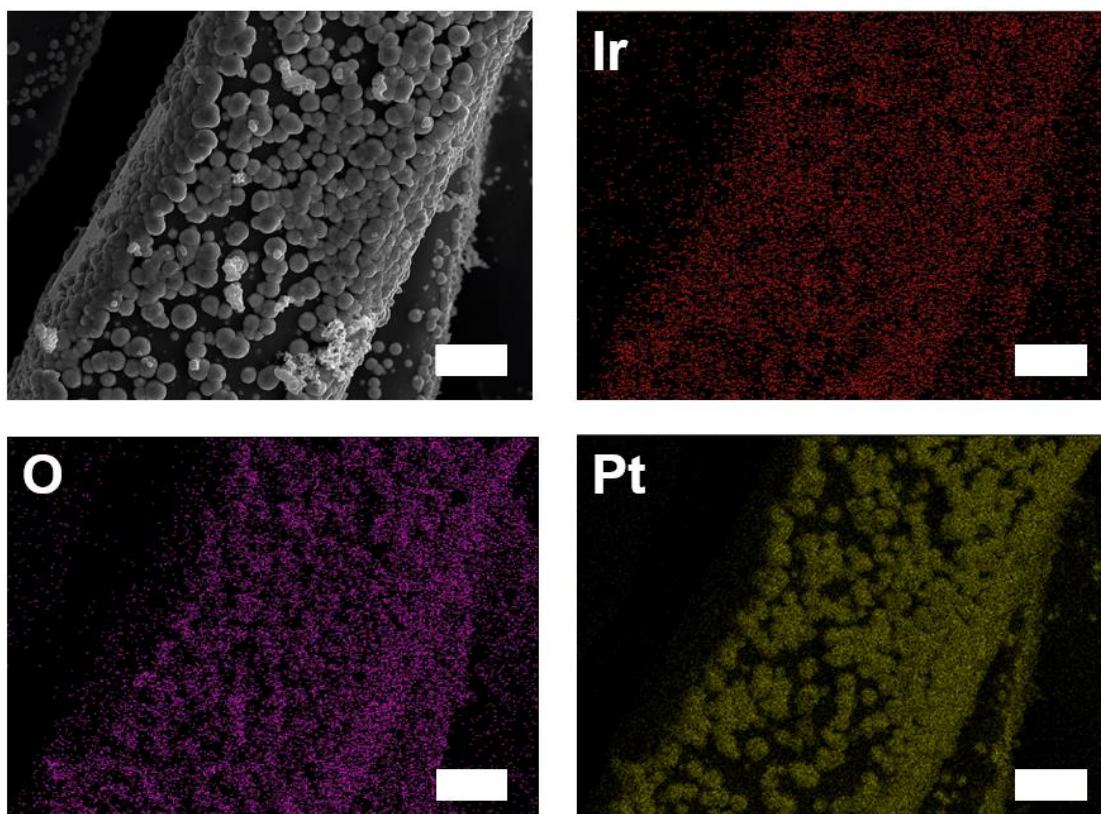


**Figure 2.8.** Elemental distribution observed in the top-surface of e-Pt@IrO<sub>2</sub> electrode. EDS mapping of surface of the sequential e-Pt@IrO<sub>2</sub> (0.16 mg<sub>Ir</sub> cm<sup>-2</sup>, 0.28 mg<sub>Pt</sub> cm<sup>-2</sup>)/Ti (scale bar in figures: 2 μm).

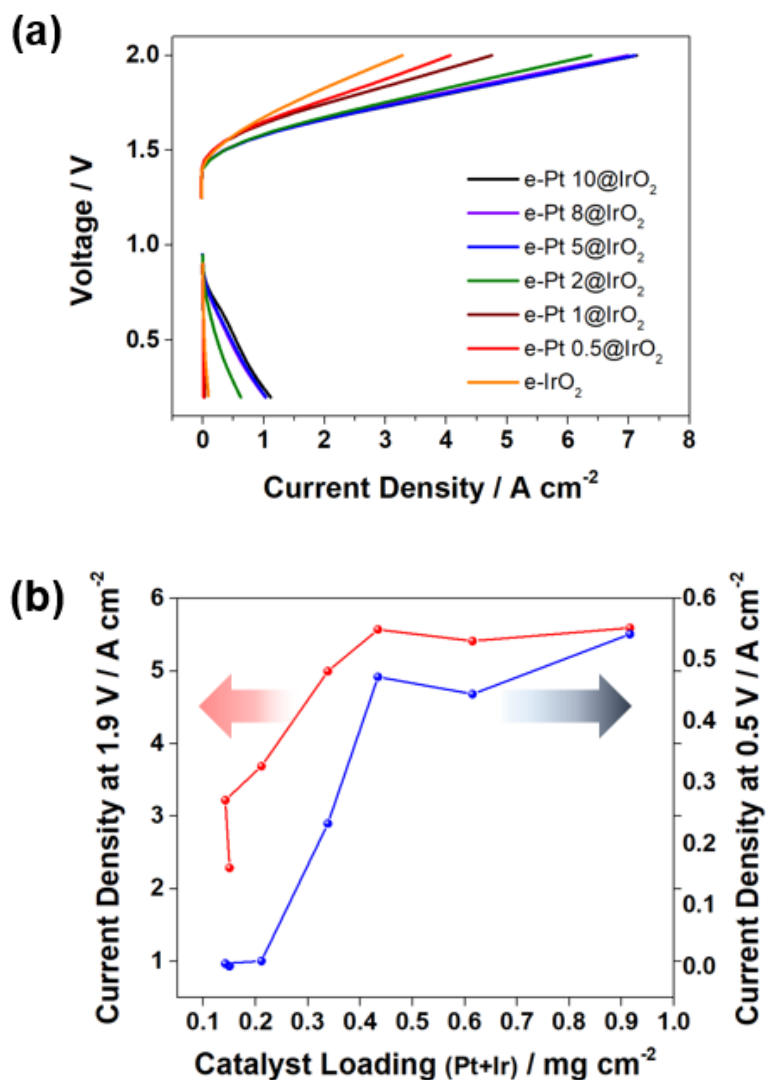


**Figure 2.9.** URFC Performance with different catalyst amounts of e-Pt@IrO<sub>2</sub>. The e-Pt@IrO<sub>2</sub> was used as oxygen electrode in both WE and FC and FC performance was measured after reduction of IrO<sub>2</sub> surface to Ir. (a) IV curve of URFC (Pt deposition time controlled from 0.5 min to 10 min). (b) Current density at 1.9 V (WE mode) and 0.5 V (FC mode) with the different amount of electrodeposited e-Pt@IrO<sub>2</sub>.

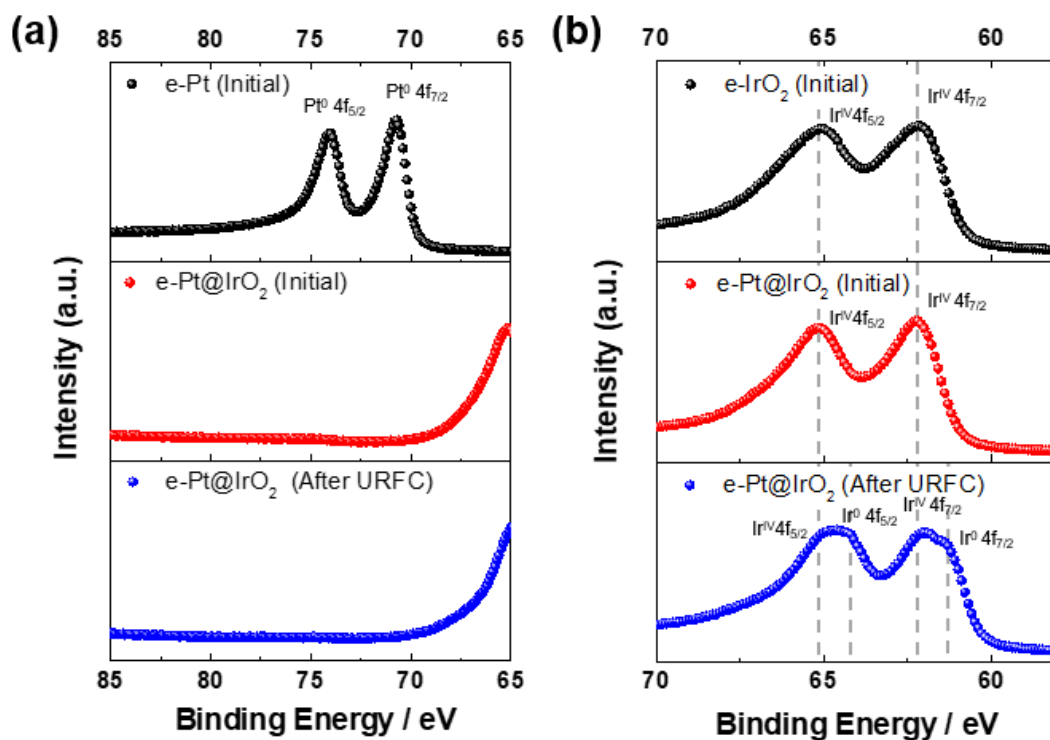


**Figure 2.10.** Surface element characterization of e-IrO<sub>2</sub> and e-Pt@IrO<sub>2</sub> by XPS. (a) Pt (4f<sub>5/2</sub> and 4f<sub>7/2</sub>) and (b) Ir (4f<sub>5/2</sub> and 4f<sub>7/2</sub>) peaks of e-Pt (black) and e-Pt@IrO<sub>2</sub> (red) in XPS.

### 2.3.2. PEM-Water Electrolysis

The water electrolysis performance of supported IrO<sub>2</sub> catalysts was investigated and compared in three different oxygen electrodes (anode): conventional sprayed IrO<sub>2</sub> (s-IrO<sub>2</sub>), e-IrO<sub>2</sub>, and e-Pt@IrO<sub>2</sub> on Ti PTL. The s-IrO<sub>2</sub> electrode was chosen to represent a conventional WE electrode containing powdery IrO<sub>2</sub> of approximately 6.5 nm in diameter sprayed onto Ti PTL (Figure 2.11(a) and 2.11(b)). The e-IrO<sub>2</sub> electrode was chosen to investigate the effects of catalyst size and distribution of electrodeposited catalysts on WE (Figure 2.11(c) and 2.11(d)), and e-Pt@IrO<sub>2</sub> was chosen to investigate the effects of Pt supports on the catalysis (Figure 2.3 and 2.10).

The single cell using s-IrO<sub>2</sub> showed an insignificant water splitting current with less than 0.2 mg cm<sup>-2</sup> of IrO<sub>2</sub> loading; more than 3 mg<sub>Ir</sub> cm<sup>-2</sup> of catalyst was required to achieve a practical WE current of approximately 3 A cm<sup>-2</sup> at 2 V<sub>cell</sub> (Figure 2.12(a)). However, the e-IrO<sub>2</sub> cell containing only 0.15 mg<sub>Ir</sub> cm<sup>-2</sup> displayed a current of 3 A cm<sup>-2</sup> at 2V<sub>cell</sub>. This result indicates a 20x higher mass activity of e-IrO<sub>2</sub> compared to s-IrO<sub>2</sub>. The significant increase in mass activity and catalyst utilization of e-IrO<sub>2</sub> can be explained by the appropriate distribution of smaller catalyst particles with enhanced surface area and improved pore distribution for facile mass transport in WE. It is clear that the electrodeposition process selectively produces deposits at electrically conducting sites on the porous bulk PTL. Thus, the electrocatalysts contacted with the aqueous electrolyte solution act as active sites for WE. In contrast to catalysts of e-IrO<sub>2</sub>, nanoparticles of s-IrO<sub>2</sub> are agglomerated with Nafion ionomer, which is an inevitable component as the binder material securing the nanoparticles in the electrode. However, it blocks the active sites of catalysts and electrically disconnects catalyst particles from the current collector, resulting in the reduction of

electrode activity. Furthermore, the size of IrO<sub>2</sub> nanoparticles produced in e-IrO<sub>2</sub> was smaller and more uniform ( $1.5 \pm 0.2$  nm) compared to the commercial IrO<sub>2</sub> nanoparticles used in s-IrO<sub>2</sub> ( $7 \pm 1$  nm), which increases the catalyst utilization (Figure 2.11(a) and 2.11(c)). Thus, e-IrO<sub>2</sub> presents a meaningful WE performance with significantly smaller amount of catalysts than that used in s-IrO<sub>2</sub>.

The pore structure of e-IrO<sub>2</sub> is also different than that of s-IrO<sub>2</sub>. The void volume between IrO<sub>2</sub> particles or its agglomerates and its surface properties dominates the mass transportation of water and gas bubbles in WE. e-IrO<sub>2</sub> preserves the pore structure of bare Ti PTL, ranging from 10 to 100  $\mu\text{m}$ , while s-IrO<sub>2</sub> with  $3.5 \text{ mg}_{\text{Ir}} \text{ cm}^{-2}$  was comprised of small-sized pores (in the size range of 0.5 to 2  $\mu\text{m}$ ) in the thick, porous, catalyst layer ( $> 10 \mu\text{m}$ ), which exerts a mass limitation due to sluggish mass transportation of water and gas bubbles during electrolysis (Figure 2.12(b)). When the pore size is less than 2  $\mu\text{m}$ , the pore is vulnerable to becoming clogged by water, which then requires a pressure of more than 3 bar to open the pore in WE [41].

In addition, a higher water contact angle is seen with s-IrO<sub>2</sub> compared to bare Ti PTL—155 and 128°, respectively—due to the hydrophobic sprayed IrO<sub>2</sub> catalysts layers with the Nafion binder (Figure 2.7). However, the highly dispersed e-IrO<sub>2</sub> particle modifies the hydrophobic Ti PTL surfaces to become super hydrophilic, displaying a contact angle of 0°. The hydrophilic nature of e-IrO<sub>2</sub> facilitates water transportation through PTL, whereas the hydrophobicity of s-IrO<sub>2</sub> mitigates the material transport required for efficient WE.

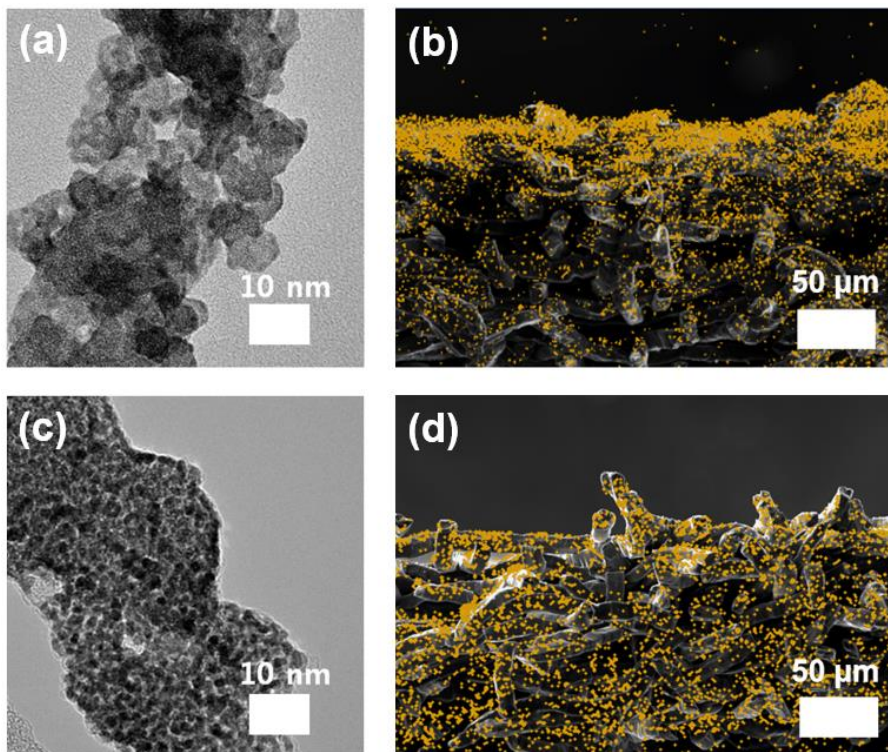


**Figure 2.11.** Comparison of IrO<sub>2</sub> nanoparticles on Ti PTL fabricated by spray and electrodeposition method. (a) TEM images of commercial IrO<sub>2</sub> nanoparticles used in s-IrO<sub>2</sub>. (b) Cross-section SEM images of s-IrO<sub>2</sub> (3.5 mg<sub>Ir</sub> cm<sup>-2</sup>) showing Ti and IrO<sub>2</sub> nanoparticle (yellow dots) distribution from EDS mapping. (c) TEM images of IrO<sub>2</sub> nanoparticles from e-IrO<sub>2</sub>. (d) Cross-section SEM images of e-IrO<sub>2</sub> (0.15 mg<sub>Ir</sub> cm<sup>-2</sup>) showing Ti and IrO<sub>2</sub> nanoparticle (yellow dots) distribution from EDS mapping.

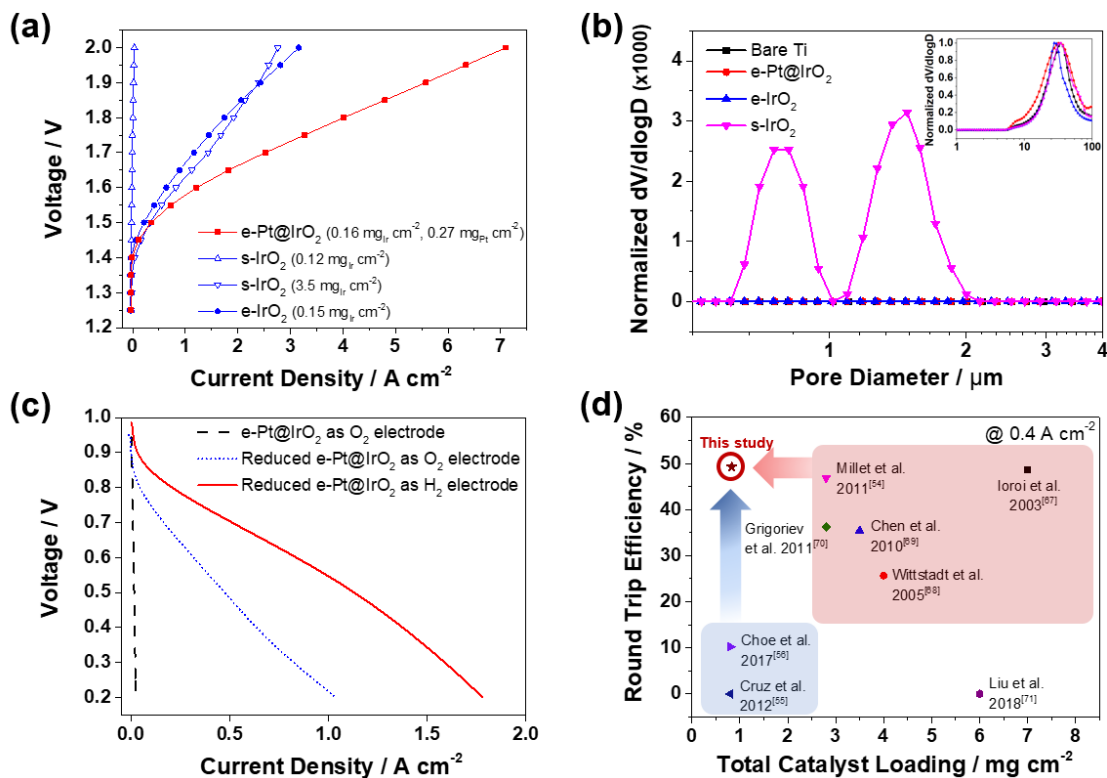


**Figure 2.12.** Comparison of IV performance of UR-PEMFC, porosity of the electrodes and round trip efficiency. (a) IV curve of PEMWE operation. (closed symbol: electrodeposited-catalysts electrode, open symbol: spray-catalysts electrode, red: Ir oxide and Pt, blue: only Ir oxide) (b) Pore distribution of electrodes measured by mercury porosimetry in 0.5 – 4 μm range (inserted; 0.5 - 100 μm range). (c) IV curve of PEMFC operation ( $T_{\text{cell}}$ : 80°C). In the device using e-Pt@IrO<sub>2</sub> or reduced e-Pt@IrO<sub>2</sub> operates as the FC oxygen electrode (cathode). H<sub>2</sub> and O<sub>2</sub> temperature was at 70°C (black dash and blue dot line). When reduced e-Pt@IrO<sub>2</sub> is used as the FC hydrogen electrode (anode), H<sub>2</sub> and O<sub>2</sub> temperature was held at 70 and 80°C, respectively (red solid line). (d) Round trip efficiency at 0.4 A cm<sup>-2</sup> versus total noble-catalysts loading in single cell.

As a result of the enhanced surface area, catalyst utilization, appropriate pore structure, and hydrophilic characteristics, e-IrO<sub>2</sub> displays a comparable performance to s-IrO<sub>2</sub> using 23x less precious metal oxide catalysts. s-IrO<sub>2</sub> displayed mass limited I-V characteristics near 2 V<sub>Cell</sub>, as indicated by the 34% decrease in the slope of the I-V curve—5.5 to 3.6 A V<sup>-1</sup> cm<sup>2</sup> at 1.70 and 1.95 V<sub>Cell</sub>, respectively (down-triangle open symbols in Figure 2.12(a)). In contrast, e-IrO<sub>2</sub> presented an increased slope of the I-V curve from 1.70 to 1.95 V<sub>Cell</sub>, suggesting that mass transport resistance is insignificant (closed symbols in Figure 2.12(a)). EIS analysis further supports that the effective mass transportation in e-IrO<sub>2</sub> occurs as the voltage loss from mass transport polarization decreased 8.7x from s-IrO<sub>2</sub> to e-IrO<sub>2</sub>, was approximately 170 and 19 mV, respectively (Figure 2.13).

More importantly, the WE performance and mass activity of IrO<sub>2</sub> were further improved when the catalyst support for the OER electrode was employed (closed symbols in Figure 2.12(a)). The e-Pt@IrO<sub>2</sub> electrode clearly demonstrates the greater current density, 1.2 and 7.1 A cm<sup>-2</sup> at 1.6 and 2.0 V<sub>Cell</sub>, respectively, with 0.16 mg<sub>Ir</sub> cm<sup>-2</sup> (closed red symbols in Figure 2.12(a)). Compared to s-IrO<sub>2</sub> and e-IrO<sub>2</sub>, a 56x and 2.1x higher mass activity was achieved with e-Pt@IrO<sub>2</sub> (0.79, 21, and 44 A mg<sub>Ir</sub><sup>-1</sup> at 2 V<sub>cell</sub> for s-IrO<sub>2</sub>, e-IrO<sub>2</sub> and e-Pt@IrO<sub>2</sub>, respectively). The performance advantages of a catalyst support in addition to the advantages of an electrodeposited electrode—e.g., enlarged active area, enhanced conductivity, widely distributed catalysts on PTL, and appropriate pore structure—are realized with e-Pt@IrO<sub>2</sub>.

The additional performance improvement of e-Pt@IrO<sub>2</sub> primarily stems from the increased ECSA compared to e-IrO<sub>2</sub>. Mass normalized ECSA increased 2.5x from e-IrO<sub>2</sub> at 12.6 m<sup>2</sup> g<sub>Ir</sub><sup>-1</sup> to e-Pt@IrO<sub>2</sub> at 30.9 m<sup>2</sup> g<sub>Ir</sub><sup>-1</sup>. ECSA of IrO<sub>2</sub> electrode was

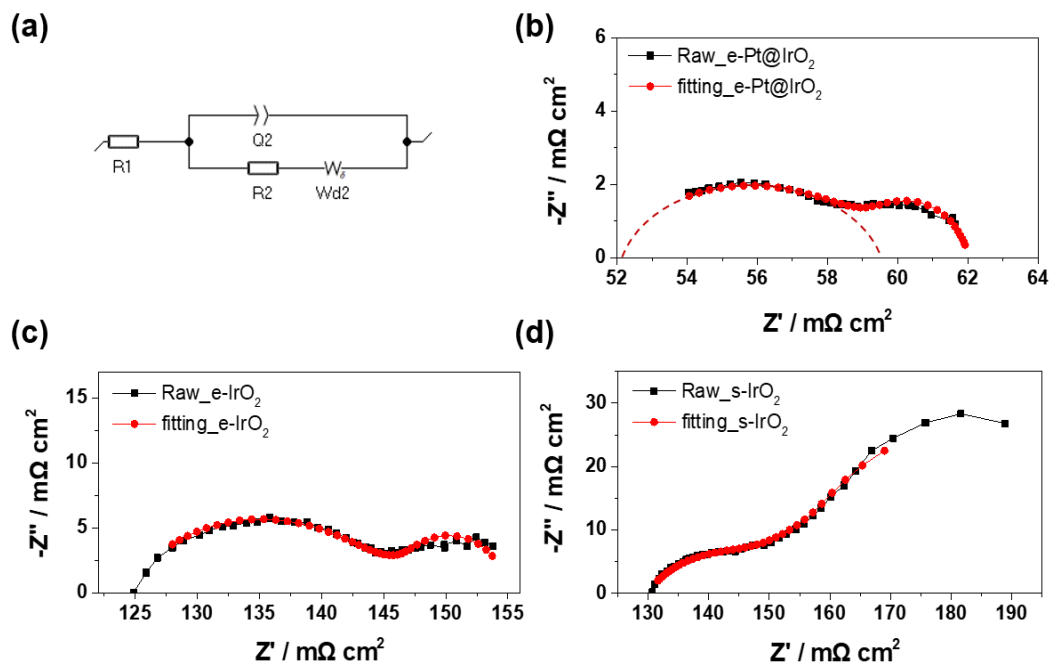


**Figure 2.13.** Potentiostatic Electrochemical Impedance Spectroscopy (PEIS) at 2.0  $V_{\text{Cell}}$  in water electrolysis for different electrodes. (a) Equivalent circuit for Impedance fitting analysis. PEIS data (black) and fitting results (red) of (b) e-Pt@IrO<sub>2</sub> (0.16 mg<sub>Ir</sub> cm<sup>-2</sup>), (c) e-IrO<sub>2</sub> (0.15 mg<sub>Ir</sub> cm<sup>-2</sup>) and (d) s-IrO<sub>2</sub> (3.5 mg<sub>Ir</sub> cm<sup>-2</sup>).

measured using the charge required for the underpotential deposition of hydrogen (H-upd) on metallic Ir surface, after IrO<sub>2</sub> surface reduction. Since IrO<sub>2</sub> has no characteristic of proton adsorption and desorption on the surface, ECSA was estimated on the reduced Ir surface using a H-upd method. CV under relative humidity (RH) 100 condition was repeated from 0.05 to 0.6 V to reduce the oxide to metallic Ir for until reach steady states, so to observe the proton adsorption and desorption current for e-IrO<sub>2</sub> and e-Pt@IrO<sub>2</sub>. In XPS, 23 % of Ir peaks were assigned to metallic phase emerging after reduction of IrO<sub>2</sub> surface (Figure S9). The result manifested that the entire surface of IrO<sub>2</sub> became metallic Ir considering the detection depth of XPS measurements. Then, hydrogen adsorption and desorption current presented in CV was used to estimate the ECSA with a capacitive charge of H-upd using equation (2-2), i.e. 218 μC cm<sup>-2</sup> [34, 42] (Figure 2.15).

$$\text{ECSA (m}^2 \text{ mg}_{\text{Ir}}^{-1}\text{)} = \frac{\int J \text{ (A cm}_{\text{geo}}^{-2}\text{)} dV}{v \left(\frac{\text{V}}{\text{s}}\right)} \div 218 \times 10^{-6} \text{ (C cm}^{-2}\text{)} \\ \times m_{\text{Ir}} \text{ (mg}_{\text{Ir}} \text{ cm}_{\text{geo}}^{-2}\text{)} \times 10^{-4} \text{ (m}^2 \text{ cm}^{-2}\text{)} \text{ ----- (2-2)}$$

The absence of Pt peaks before and after URFC in XPS for e-Pt@IrO<sub>2</sub> implies negligible exposure of Pt to the catalyst surfaces in the electrode (Figure 2.10 and 2.14). It is well known that inclusion of a catalyst support highly mediates both utilization and stability of catalysts [10, 43-47]. The positive effect of the catalyst support is also demonstrated in PEIS, as the charge transfer resistance (R<sub>ct</sub>) decreased from 21.8 to 7.61 mΩ cm<sup>2</sup> (Figure 2.13). Ohmic resistance of the electrochemical cell (R<sub>ohm</sub>), i.e. sum of ionic and electron transfer resistance, also decreased from e-Pt@IrO<sub>2</sub> at 125 mΩ cm<sup>2</sup><sub>geo</sub> to e-IrO<sub>2</sub> at 52 mΩ cm<sup>2</sup><sub>geo</sub> at 2.0 V<sub>Cell</sub>, as measured in PEIS (Figure 2.13). Both the performance increment and R<sub>ct</sub> and R<sub>ohm</sub> reduction from e-

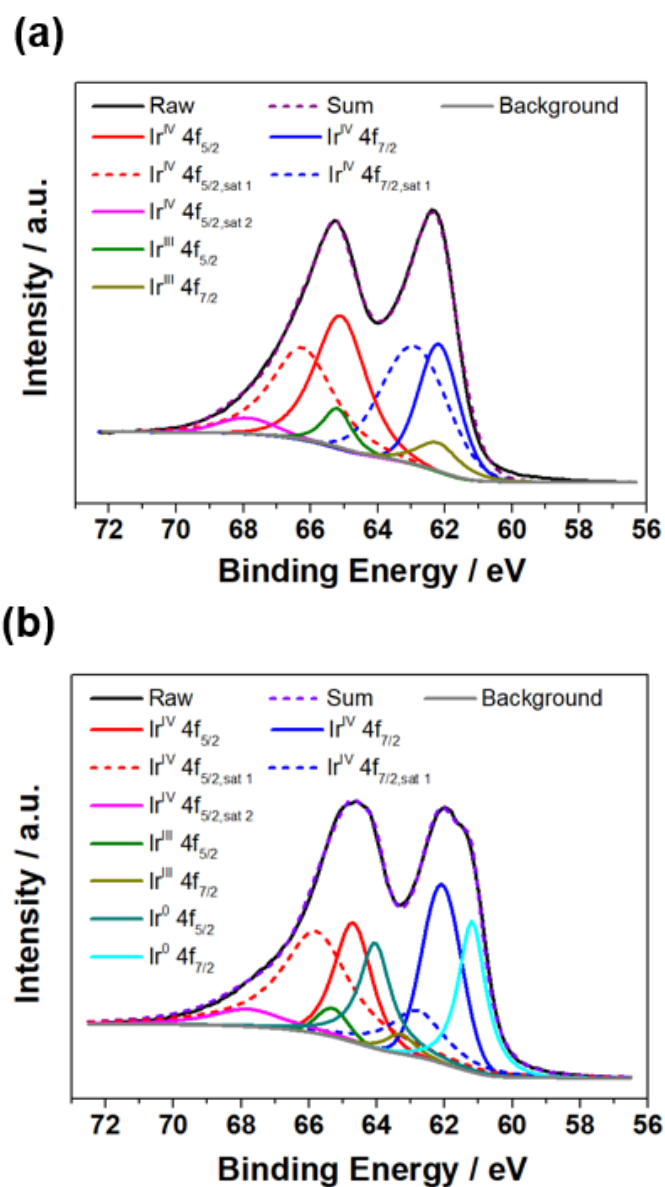


**Figure 2.14.** XPS of Ir detected in e-Pt@IrO<sub>2</sub>. XPS (a) before and (b) after electrochemical reduction process.

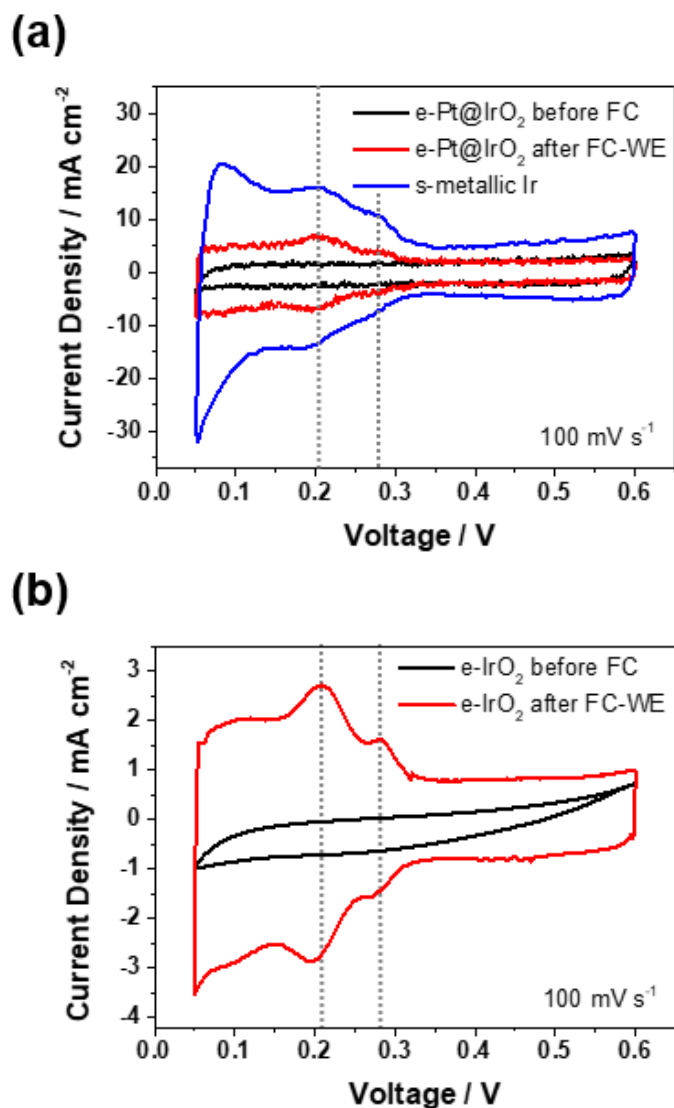


**Figure 2.15.** CVs of e-Pt@IrO<sub>2</sub> and Ir electrode ranged from 0.05 to 0.6 V (vs. pseudo RHE). CVs of e-Pt@IrO<sub>2</sub> electrode before and after electrochemical reduction process (black and red) including commercial metallic Ir electrode sprayed on Ti PTL. (a) Comparison of CVs before and after electrochemical reduction process at e-Pt@IrO<sub>2</sub> and metallic Ir electrode and (b) e-IrO<sub>2</sub> electrode.

**Table 2.2.** Resistance of bare Ti, e-IrO<sub>2</sub>, e-Pt and sequential e-Pt@IrO<sub>2</sub> obtained from 4-probe measurement using FIB-Quanta 3D. Resistivity was estimated with the assumption of cross-section area 400 μm<sup>2</sup> and probe distance 10 μm.

<b>Electrode</b>	<b>Resistance / Ω (distance: 10 μm)</b>	<b>Resistivity / Ω·m (with assumption)</b>
<b>Bare Ti</b>	2.36 x 10 <sup>-2</sup>	9.44 x 10 <sup>-7</sup>
<b>e-IrO<sub>2</sub></b>	4.74 x 10 <sup>5</sup>	1.90 x 10
<b>e-Pt</b>	7.93 x 10 <sup>-1</sup>	3.17 x 10 <sup>-5</sup>
<b>e-Pt@IrO<sub>2</sub></b>	4.63 x 10 <sup>3</sup>	1.85 x 10 <sup>-1</sup>

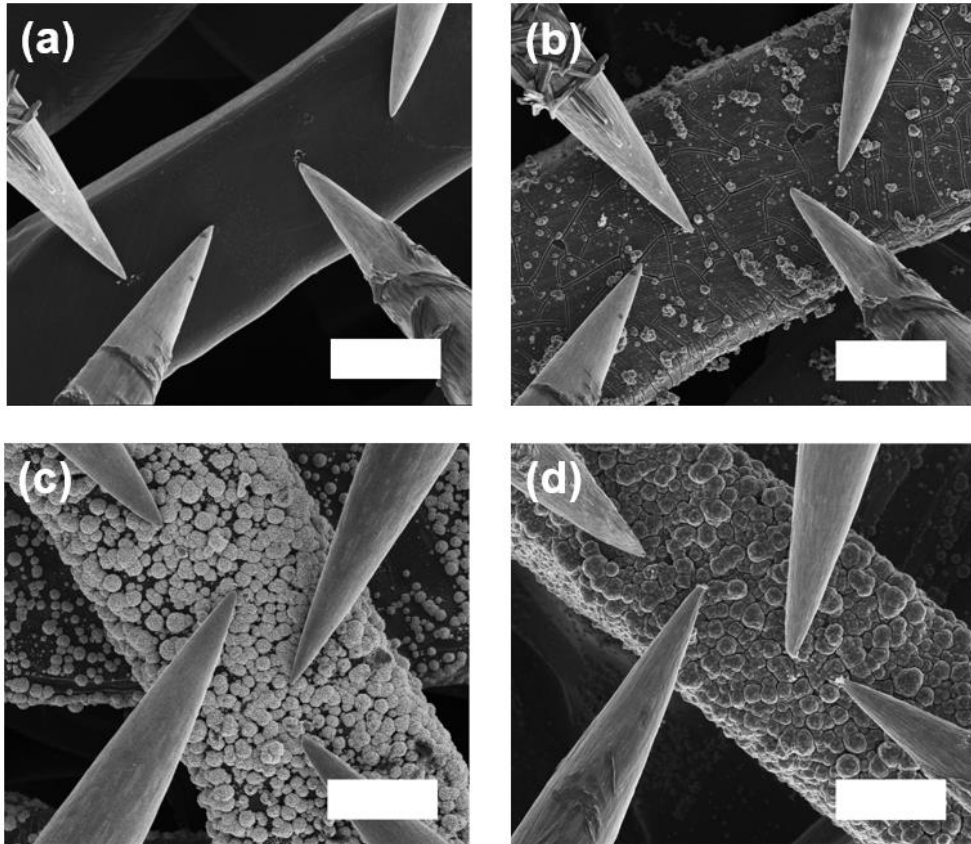


**Figure 2.16.** SEM image of 4-probe resistivity measurement in FIB-Quanta 3D. (a) Bare Ti, (b) e-IrO<sub>2</sub>/Ti, (c) e-Pt/Ti and (d) sequential e-Pt@IrO<sub>2</sub>/Ti (scale bar: 10 μm).

$\text{IrO}_2$  to e-Pt@ $\text{IrO}_2$  coincide with the ECSA increase. Since the apparent  $R_{\text{ohm}}$  and  $R_{\text{ct}}$  are inversely proportional to the actual ECSA in PEIS, the increased roughness factor of the e-Pt@ $\text{IrO}_2$  electrode clearly supports the reduction of  $R_{\text{ohm}}$  and  $R_{\text{ct}}$ , resulting in the improved performance compared to e- $\text{IrO}_2$ .

Electronic resistance, a component of  $R_{\text{ohm}}$ , is often significant when there is a considerable operation current resulting in a significant IR drop. Although the ionic resistance remains significant compared to the electronic resistance in this study, we observed reduction of two orders of magnitude in the electronic resistance at e-Pt@ $\text{IrO}_2$  compared to that of e- $\text{IrO}_2$ . The electronic resistance of bare Ti PTL, e-Pt, e- $\text{IrO}_2$ , and e-Pt@ $\text{IrO}_2$  was measured by a nanomanipulated four point-probe of SEM-FIB in vacuum (Table 2.2, Figure 2.16). For bare Ti PTL, the electronic resistance was 23.6 m $\Omega$ , (a resistivity of  $9 \times 10^{-7} \Omega \cdot \text{m}$ ), which correlates with that of metallic Ti [48]. However, by placing  $\text{IrO}_2$ , a 180 nm thickness layer of the resistive metal oxide, on the Ti PTL, the resistance increased 7 orders of magnitude. Conductivity of e- $\text{IrO}_2$  was estimated to be approximately  $5 \times 10^{-4} \text{ S cm}^{-1}$ , which is two orders lower than the reported value of bulk  $\text{IrO}_2$  of approximately  $10^{-2} \text{ S cm}^{-1}$  [49]. This discrepancy is likely due to the resistive oxide formed at the interfaces between  $\text{IrO}_2$  nanoparticles and the Ti surface during the electrodeposition of  $\text{IrO}_2$ . However, when the Pt layer is introduced between the  $\text{IrO}_2$  and Ti layers, a reduction in resistance of two orders of magnitude from e-Pt@ $\text{IrO}_2$  to e- $\text{IrO}_2$  was observed. The decreased resistance is due to two factors: the thickness decrease of  $\text{IrO}_2$  and the improved contact conductivity between the layers in e-Pt@ $\text{IrO}_2$ . The four-point measurement clearly demonstrated the positive role of the Pt interlayer for electron transfer in OER electrodes. However, it was difficult to estimate the bulk electrode

resistance from the microscopic measurement and its contribution on device performance.

In brief, e-Pt@IrO<sub>2</sub> presents higher ECSA, mass activity, and lower apparent R<sub>ct</sub> and R<sub>ohm</sub>, which culminates in a 2.2 and 2.6x higher device performance at 2 V<sub>cell</sub> and a 56 and 2.1x higher mass activity of IrO<sub>2</sub> compared to the s-IrO<sub>2</sub> and e-IrO<sub>2</sub> electrodes, respectively.

### 2.3.3. PEM-Unitized Regenerative Fuel Cells

The developed electrode, e-Pt@IrO<sub>2</sub>, was then investigated as either a hydrogen electrode (anode) or oxygen electrode (cathode) of FC, coupled to a Pt/C electrode as the counter electrode for URFC applications. In order to utilize the IrO<sub>2</sub> electrode in the hydrogen oxidation reaction (HOR) or ORR for a hydrogen electrode (anode) or oxygen electrode (cathode) of FC, respectively, the surface metal oxide must be reduced to metallic Ir under voltage cyclic operations in a N<sub>2</sub> atmosphere after WE operation [50, 51]. When the reduced surface of e-Pt@IrO<sub>2</sub> was used as the oxygen electrode (cathode) of FC (ORR), noticeable FC performance (320 mA cm<sup>-2</sup> at 0.6 V<sub>Cell</sub>) was achieved (blue dot line in Figure 2.12(c)). Although the core Pt of e-Pt@IrO<sub>2</sub> is the gold standard for ORR catalysts with high activity, it was not exposed to the surface and no Pt peak was observed in XPS (Figure 2.10(a)). Only the metallic Ir surface of e-Pt@IrO<sub>2</sub> was utilized for ORR (Figure 2.14 and 2.15). The FC current was insignificant (e.g. 13 mA cm<sup>-2</sup> at 0.6 V<sub>Cell</sub>) if the oxide surface of e-Pt@IrO<sub>2</sub> was utilized without any modifications (black dash line in Figure 12(c)).

However, the performance of the FC was significantly improved when the reduced e-Pt@IrO<sub>2</sub> surface was employed for hydrogen electrode (anode) of FC (HOR). For

example, a high current density of  $840 \text{ mA cm}^{-2}$  at  $0.6 \text{ V}_{\text{Cell}}$  was achieved (red solid line in Figure 2.12(c)). It should also be noted that lower relative humidity values (RH) of feeding gas, e.g. RH 65, were necessary to reduce flooding of the super hydrophilic electrode (Figure 2.7). Severe performance reduction due to electrode flooding was observed at RH 100 (Figure 2.17) [52, 53].

Round trip efficiency (RT) is the ratio of FC operation voltage to that of WE of the URFC at a certain operation current. High RT is important to achieve the advantages of a URFC, such as a compact embodiment and lower capital cost compared to the stand-alone WE and FC. Under the optimum operation conditions, the URFC employing the e-Pt@IrO<sub>2</sub> electrode as the oxygen electrode (anode) for WE mode and hydrogen electrode (anode) for FC mode demonstrated a 55 and 49% RT at a URFC current density of 0.2 and 0.4 A cm<sup>-2</sup>, respectively. In Figure 2.12(d), RTs reported in the literature are summarized as a function of total loading amount of metal catalyst. For example, Millet et al. reported 54 and 47 % of RT at 0.2 and 0.4 A cm<sup>-2</sup>, respectively, employing 2.5 mg cm<sup>-2</sup> of noble catalysts in the cell [54]. Cruz et al. and Choe et al. reported single cell results with merely 0.8 mg cm<sup>-2</sup> of noble catalyst electrodes for a modest RT of less than 30% at 0.2 A cm<sup>-2</sup> [55, 56]. The RT of URFC reported in this study is one of the highest values reported in the literature (Figure 2.12(d), Table 2.3), which is especially remarkable considering the amount of precious metal used in both electrodes—only 0.83 mg<sub>(Pt+Ir)</sub> cm<sup>-2</sup>. It should be noted that the studies cited in Figure 2.12(d) are from those reporting single-cell experiments without the use of carbon materials in the corrosive WE oxygen electrode (anode).

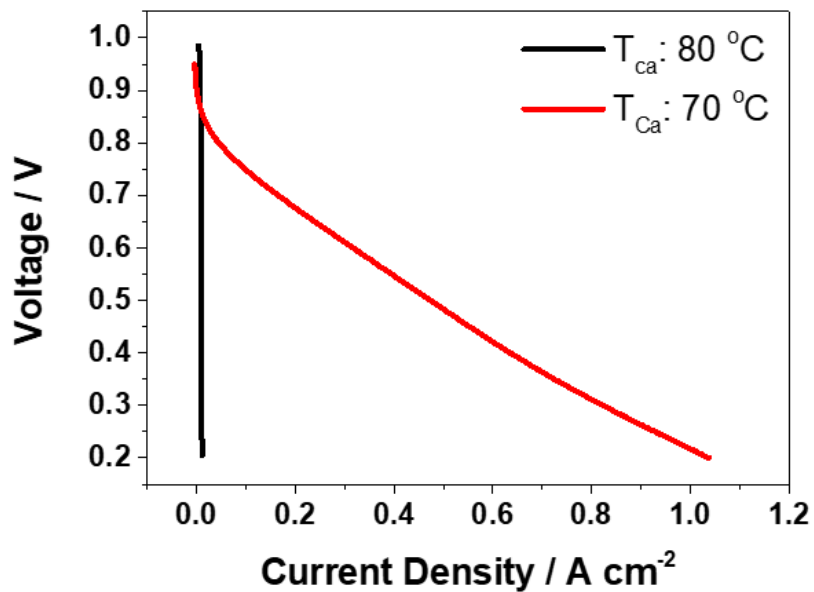


**Figure 2.17.** IV of FC mode of URFC with controlled temperature of the oxygen electrode (cathode, e-Pt@IrO<sub>2</sub> electrode). T<sub>ca</sub> indicates temperature of O<sub>2</sub> gas feeding to cathode. The temperature of fuel in the hydrogen electrode (anode, Pt/C electrode) was controlled to 70 °C.

**Table 2.3.** Literature review of round trip efficiency (RT) at 0.2 A cm<sup>-2</sup> and 0.4 A cm<sup>-2</sup> of UR-PEMFC including the catalyst loading. URFC reports shown in the table are based on non-carbon PTL for the oxygen electrode in water electrolysis. ( $m_{O_2}$ : noble-catalyst loading of oxygen electrode in fuel cell,  $m_{H_2}$ : noble-catalyst loading of hydrogen electrode in fuel cell,  $m_{tot}$  is the sum of  $m_{O_2}$  and  $m_{H_2}$ )

Author, year	Round trip efficiency at 0.2 A cm <sup>-2</sup>	Round trip efficiency at 0.4 A cm <sup>-2</sup>	$m_{O_2}$ / mg cm <sup>-2</sup>	$m_{H_2}$ / mg cm <sup>-2</sup>	$m_{tot}$ / mg cm <sup>-2</sup>
Ioroi et al., 2003 [67]	53.6	48.6	3~4	3~4	6~8
Wittstadt et al., 2005 [68]	37.8	25.7	2	2	4
Chen et al., 2010 [69]	48.0	35.4	3	0.5	3.5
Millet et al., 2011 [54]	53.7	46.8	2	0.8	2.8
Grigoriev et al., 2011 [70]	45.2	36.3	2	0.8	2.8
Cruz et al., 2012 [55]	28.5	0	0.5	0.3	0.8
Choe et al., 2017 [56]	27.0	10.3	0.4	0.4	0.8
Liu et al., 2018 [71]	41.0	0	3	3	6
Lim et al.	55.4	49.3	0.4	0.43	0.83

### 2.3.4. Stability Tests of e-Pt@IrO<sub>2</sub> Electrodes

For practical deployment of URFCs, device stability and durability should be guaranteed for more than several thousand hours [57]. However, only a limited number of the URFC studies were found in the literature reporting more than 50 h of operation [14, 58, 59]. Jung et al. used a Ti bipolar plate coated with Pt for a stable oxygen electrode, demonstrating a moderate degradation rate of 200  $\mu\text{V h}^{-1}$  at 0.3 A  $\text{cm}^{-2}$  in WE of 100 h URFC operation [60]. Lee et al. also reported a 3-layered IrO<sub>2</sub>/Pt/IrO<sub>2</sub> electrode showing a degradation rate of 645  $\mu\text{V h}^{-1}$  at 0.5 A  $\text{cm}^{-2}$  in WE of 96 h URFC operation [61].

Herein, a total of 160 h of URFC operation with sequential WE and FC modes at a device current density of 0.4 A  $\text{cm}^{-2}$  was recorded in Figure 2.18. In the first 4 cycles of FC and WE operation, the FC performance degraded rapidly after 40 h of operation (2<sup>nd</sup> cycle), so the cell voltage decreased rapidly from approximately 0.6 to 0.3 V<sub>Cell</sub> at 0.4 A  $\text{cm}^{-2}$  (Figure 2.18(a)). Studies on the stability of bifunctional Pt/IrO<sub>2</sub> catalysts report Pt dissolution is one of the important catalyst degradation mechanisms for the FC performance in repeated ORR-OER operations [62-64]. However, other factors than Pt dissolution should be considered in this study, since Pt is encapsulated by IrO<sub>2</sub> shell and effect of Pt as ORR catalysts is trivial in e-Pt@IrO<sub>2</sub> (Figure 2.10). The degradation of FC performance was greatly affected by the increased R<sub>ohm</sub> of membrane electrode assembly (MEA) (Figure 2.18(b)). The alternate operation of FC and WE of the URFC resembled the wet-dry degradation test of FCs, which has been used to mechanically accelerate degradation and stress the membrane integrity at the electrode [65]. The detachment of electrode from membrane is due to the substantial volumetric changes in membrane swelling and

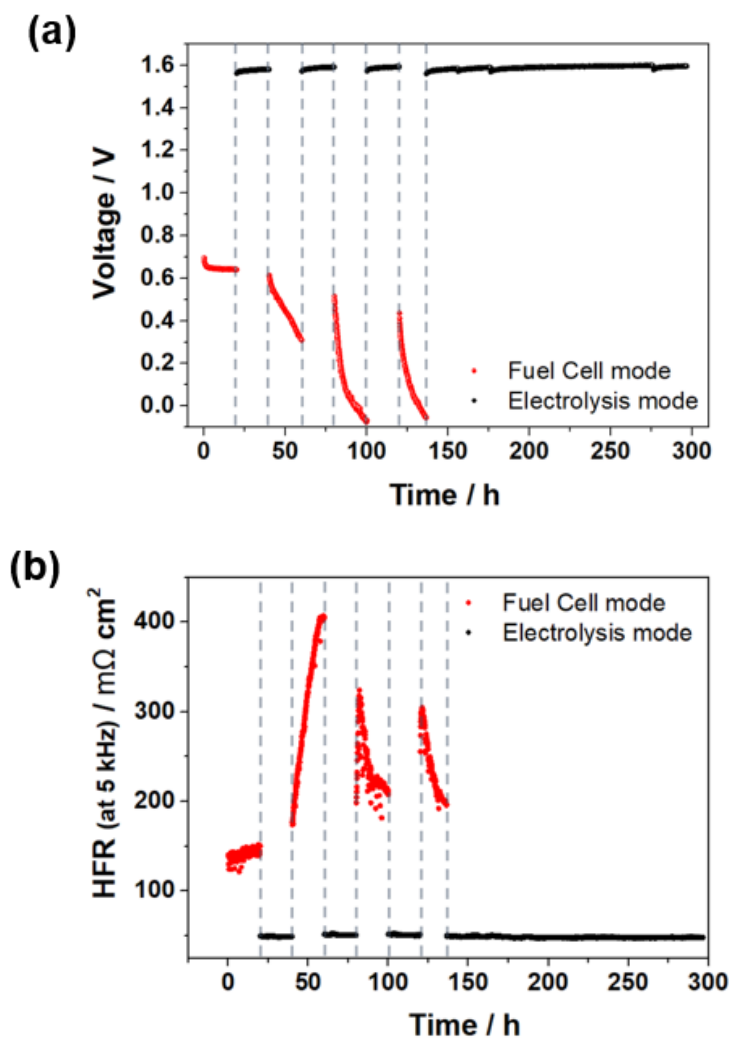


**Figure 2.18.** Long-term operation of URFC (e-Pt@IrO<sub>2</sub> as anode and Pt/C as cathode of URFC, T<sub>H2</sub>: 70°C, T<sub>O2</sub>: 80°C T<sub>cell</sub>: 80°C). (a) Cell voltage at 0.4 A cm<sup>-2</sup> and (b) high frequency resistance measured at 5 kHz in EIS during long-term operation.

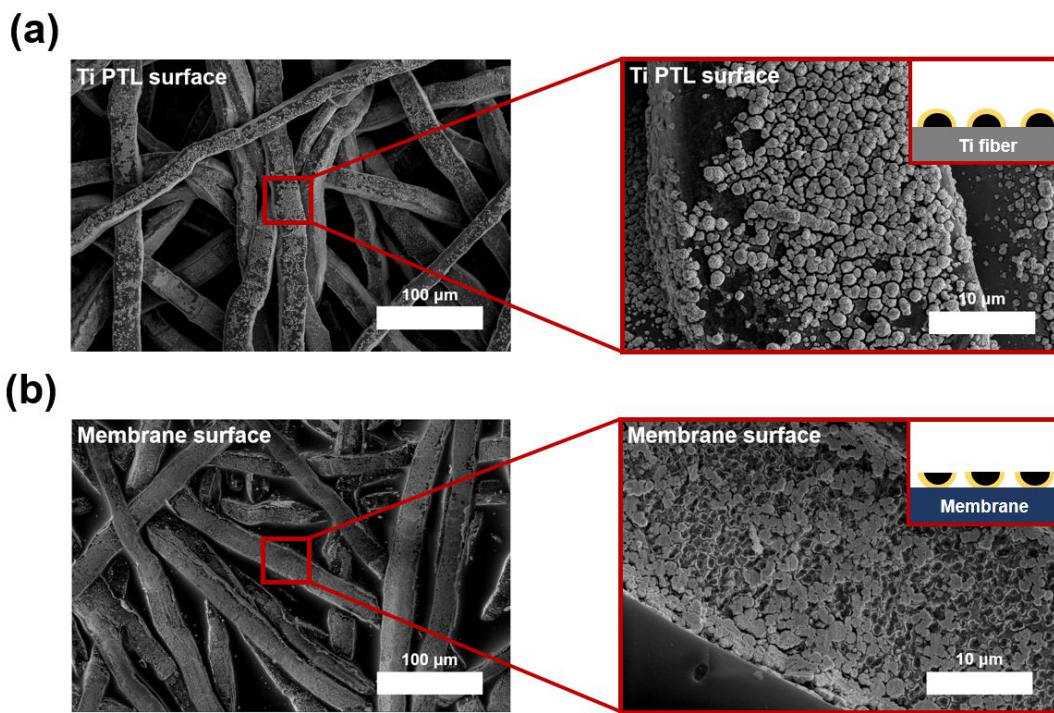


**Figure 2.19.** SEM images of surface of (a) Ti PTL and (b) membrane detached from MEA after long term tests of ED-Pt@IrO<sub>2</sub>.

drying during WE and FC operations, such that the ion transfer path is discontinued at the membrane-electrode interface.

However, WE operation using e-Pt@IrO<sub>2</sub> was stable for 220 h of operations, and the degradation rate averaged to 155  $\mu\text{V h}^{-1}$  without noticeable changes in  $R_{\text{ohm}}$  (Figure 2.18(b)).  $R_{\text{ohm}}$  measured under WE conditions was lower than that under FC operations. The different trends and magnitude of  $R_{\text{ohm}}$  for FC and WE operation imply different ion transfer mechanisms. Ionomeric transportation requires an intact polymer interface to the catalyst surfaces for the FC operation, while aqueous electrolyte ensures an easy and effective ion transfer for the WE operation. The catalysts are maintained its hemispheric structure in both sides of Ti PTL and membrane from SEM images after the long term tests, even though there are delamination of catalyst layers and transfer of Ti-felt topography to the membrane surface after detachment of the MEA (Figure 2.19). The solid WE performance and durability shown in Figure 2.18(a) also implies that the e-Pt@IrO<sub>2</sub> electrode itself is highly stable during long-term URFC operation.

Here, sequential electrodeposition as an electrode fabrication approach is used to produce e-IrO<sub>2</sub> with e-Pt support for highly efficient and stable OER in WE. The electrode using e-IrO<sub>2</sub> supported on hemispheric Pt particles possesses appropriate pore structure and catalyst distribution on the porous electrode, super-hydrophilicity for facile mass transport, enhanced electrochemically active surface, and improved electric conductivity. The electrode also provides HOR activity after reductive treatment, enabling use as a FC electrode for URFC applications. As a results, superior material utilization for the precious IrO<sub>2</sub> catalyst was obtained, which is demonstrated by significant device performance of 7.1 A cm<sup>-2</sup> at 2 V<sub>cell</sub> and the high mass activity of 44 A mg<sub>Ir</sub><sup>-1</sup> at 2 V<sub>cell</sub>, which is a 56x increase in value compared to a

conventional sprayed IrO<sub>2</sub> electrode. In addition, the electrode showed high FC performance in URFC operation.

## 2.4. Conclusions

Sequential electrodeposition of Pt and IrO<sub>2</sub> on Ti PTL was performed to achieve a highly active and stable OER electrode for PEMWE. The thin IrO<sub>2</sub> film layered on the hemispheric Pt supports has a large surface area of i.e. 30.9 m<sup>2</sup> g<sub>Ir</sub><sup>-1</sup>, which is 2.5x larger than that without the Pt support (12.6 m<sup>2</sup> g<sub>Ir</sub><sup>-1</sup>). The e-IrO<sub>2</sub> provides a super-hydrophilic surface to the OER electrode for WE. In addition, the small amount of e-IrO<sub>2</sub> catalyst is homogenously distributed without producing particle agglomerates and additional sub- $\mu$ m pores to the Ti PTL. e-Pt@IrO<sub>2</sub> results in higher WE performance (7.1 A cm<sup>-2</sup> at 2V<sub>Cell</sub>) with only 0.43 mg cm<sup>-2</sup> of total precious metal loading. The novel electrode possesses high material utilization (44 A mg<sub>Ir</sub><sup>-1</sup> at 2 V<sub>cell</sub>), displaying a 56 and 2.1x higher current per iridium used than s-IrO<sub>2</sub> or e-IrO<sub>2</sub>, respectively. e-Pt particles act as support materials of e-IrO<sub>2</sub> to enhance both the active surface area of IrO<sub>2</sub> and conductivity of the electrode, which resulted in a 2.9x and 2.4x decrease in kinetic and ohmic resistance, respectively, compared to that without Pt. The developed electrode satisfies the Ir-specific power density target of 0.01 g<sub>Ir</sub> kW<sup>-1</sup> that is required for world-wide installation of commercial water electrolyzers [66]. For URFC operation, the device using e-Pt@IrO<sub>2</sub> demonstrates 55 and 49% of RT at 0.2 and 0.4 A cm<sup>-2</sup>, respectively, with only 0.83 mg<sub>(Pt+Ir)</sub> cm<sup>-2</sup> of total noble catalysts in both electrodes. Highly-stable WE operation was also confirmed over long-term operations, demonstrating a degradation rate of 155  $\mu$ V h<sup>-1</sup>. We believe that the electrode structure and fabrication methods presented in this

study are useful for WE electrodes using other active materials. Electrodes with non-noble catalyst and support components for OER is currently under investigation in our laboratory.

## 2.5. References

- [1] T. M. Gür, Review of electrical energy storage technologies, materials and systems: challenges and prospects for large-scale grid storage, *Energ. Environ. Sci.* 11 (2018) 2696-2767.
- [2] M. T. Lawder, B. Suthar, P.W.C. Northrop, S. De, C. M. Hoff, O. Leitermann, M. L. Crow, S. Santhanagopalan, V.R. Subramanian, Battery energy storage system (BESS) and battery management system (BMS) for grid-scale applications, *Proc. IEEE* 102 (2014) 1014-1030.
- [3] P. T. Aakko-Saksa, C. Cook, J. Kiviaho, T. Repo, Liquid organic hydrogen carriers for transportation and storing of renewable energy – Review and discussion, *J. Power Sources* 396 (2018) 803-823.
- [4] A. Valera-Medina, H. Xiao, M. Owen-Jones, W.I.F. David, P. J. Bowen, Ammonia for power, *Prog. Energy Combust. Sci.* 69 (2018) 63-102.
- [5] M. Melaina, J. Eichman, Hydrogen energy storage: grid and transportation services, *National Renewable Energy Laboratory (NREL)* (2015).
- [6] F. Mitlitsky, B. Myers, A. H. Weisberg, Regenerative fuel cell systems, *Energ. Fuel.* 12 (1998) 56-71.
- [7] F. Barbir, T. Molter, L. Dalton, Efficiency and weight trade-off analysis of regenerative fuel cells as energy storage for aerospace applications, *Int. J. Hydro. Energ.* 30 (2005) 351-357.

- [8] Y. Wang, D.Y.C. Leung, J. Xuan, H. Wang, A review on unitized regenerative fuel cell technologies, part-A: Unitized regenerative proton exchange membrane fuel cells, *Renew. Sust. Energ. Rev.* 65 (2016) 961-977.
- [9] S. Sharma, B. G. Pollet, Support materials for PEMFC and DMFC electrocatalysts—A review, *J. Power Sources* 208 (2012) 96-119.
- [10] M. Darab, J.L.G.d.I. Fuente, M. S. Thomassen, S. Sunde, Pt nanoparticles dispersion influence on fuel cell performance, *ECS Trans.* 50 (2012) 1353-1367.
- [11] R. Wlodarczyk, Porous carbon materials for elements in low-temperature fuel cells, *Arch. Metall. Mater.* 60 (2015) 117-120.
- [12] M. A. Molina-García, N. V. Rees, Effect of catalyst carbon supports on the oxygen reduction reaction in alkaline media: a comparative study, *RSC Adv.* 6 (2016) 94669-94681.
- [13] J. C. Cruz, S. Rivas, D. Beltran, Y. Meas, R. Ornelas, G. Osorio-Monreal, L. Ortiz-Frade, J. Ledesma-García, L.G. Arriaga, Synthesis and evaluation of ATO as a support for Pt–IrO<sub>2</sub> in a unitized regenerative fuel cell, *Int. J. Hydro. Energ.* 37 (2012) 13522-13528.
- [14] S.-Y. Huang, P. Ganesan, H.-Y. Jung, B. N. Popov, Development of supported bifunctional oxygen electrocatalysts and corrosion-resistant gas diffusion layer for unitized regenerative fuel cell applications, *J. Power Sources* 198 (2012) 23-29.
- [15] R. E. Fuentes, H. R. Colón-Mercado, M. J. Martínez-Rodríguez, Pt-Ir/TiC electrocatalysts for PEM fuel cell/electrolyzer process, *J. Electrochem. Soc.* 161 (2013) F77-F82.
- [16] J. Polonský, I. M. Petrushina, E. Christensen, K. Bouzek, C. B. Prag, J. E. T. Andersen, N. J. Bjerrum, Tantalum carbide as a novel support material for

- anode electrocatalysts in polymer electrolyte membrane water electrolyzers, *Int. J. Hydro. Energ.* 37 (2012) 2173-2181.
- [17] V. K. Puthiyapura, M. Mamlouk, S. Pasupathi, B. G. Pollet, K. Scott, Physical and electrochemical evaluation of ATO supported IrO<sub>2</sub> catalyst for proton exchange membrane water electrolyser, *J. Power Sources* 269 (2014) 451-460.
- [18] V. K. Puthiyapura, S. Pasupathi, H. Su, X. Liu, B. Pollet, K. Scott, Investigation of supported IrO<sub>2</sub> as electrocatalyst for the oxygen evolution reaction in proton exchange membrane water electrolyser, *Int. J. Hydro. Energ.* 39 (2014) 1905-1913.
- [19] W. Yao, J. Yang, J. Wang, Y. Nuli, Chemical deposition of platinum nanoparticles on iridium oxide for oxygen electrode of unitized regenerative fuel cell, *Electrochem. Commun.* 9 (2007) 1029-1034.
- [20] F.-D. Kong, S. Zhang, G.-P. Yin, N. Zhang, Z.-B. Wang, C.-Y. Du, Pt/porous-IrO<sub>2</sub> nanocomposite as promising electrocatalyst for unitized regenerative fuel cell, *Electrochem. Commun.* 14 (2012) 63-66.
- [21] A. L. Strickler, A. Jackson, T. F. Jaramillo, Active and stable Ir@Pt core-shell catalysts for electrochemical oxygen reduction, *ACS Energy Lett.* 2 (2017) 244-249.
- [22] G. Zhang, Z.-G. Shao, W. Lu, G. Li, F. Liu, B. Yi, One-pot synthesis of Ir@Pt nanodendrites as highly active bifunctional electrocatalysts for oxygen reduction and oxygen evolution in acidic medium, *Electrochem. Commun.* 22 (2012) 145-148.
- [23] J. Zhang, M. B. Vukmirovic, K. Sasaki, A. U. Nilekar, M. Mavrikakis, R.R. Adzic, Mixed-metal Pt monolayer electrocatalysts for enhanced oxygen reduction kinetics, *Journal of American Chemical Society* 127 (2005) 12480-

12481.

- [24] T. Ioroi, N. Kitazawa, K. Yasuda, Y. Yamamoto, H. Takenaka, IrO<sub>2</sub>-deposited Pt electrocatalysts for unitized regenerative polymer electrolyte fuel cells, *J. Appl. Electrochem.* 31 (2001) 1179-1183.
- [25] T. Ioroi, N. Kitazawa, K. Yasuda, Y. Yamamoto, H. Takenaka, Iridium oxide/platinum electrocatalysts for unitized regenerative polymer electrolyte fuel cells, *J. Electrochem. Soc.* 147 (2000) 2018-2022.
- [26] J.-H. Wee, K.-Y. Lee, S. H. Kim, Fabrication methods for low-Pt-loading electrocatalysts in proton exchange membrane fuel cell systems, *J. Power Sources* 165 (2007) 667-677.
- [27] J. J. Burk, S. K. Buratto, Electrodeposition of Pt nanoparticle catalysts from H<sub>2</sub>Pt(OH)<sub>6</sub> and their application in PEM fuel cells, *The Journal of Physical Chemistry C* 117 (2013) 18957-18966.
- [28] N. Afsham, N. Fallah, B. Nassernejad, M. Javanbakht, Z. Jabbari, Fabrication of gas diffusion electrode via Pt electrodeposition on cathodic oxidized carbon paper as the anode for high-temperature polymer membrane fuel cell in the presence of CO, *Ionics* 25 (2019) 3549-3560.
- [29] F. Fouda-Onana, N. Guillet, A. M. AlMayouf, Modified pulse electrodeposition of Pt nanocatalyst as high-performance electrode for PEMFC, *J. Power Sources* 271 (2014) 401-405.
- [30] J. Choe, D. Kim, J. Shim, I. Lee, Y. Tak, Fabrication of a nanosize-Pt-embedded membrane electrode assembly to enhance the utilization of Pt in proton exchange membrane fuel cells, *J. Nanosci. Nanotechnol.* 11 (2011) 7141-7144.
- [31] H. Kim, S. Choe, H. Park, J. H. Jang, S. H. Ahn, S. K. Kim, An extremely low Pt loading cathode for a highly efficient proton exchange membrane water

- electrolyzer, *Nanoscale* 9 (2017) 19045-19049.
- [32] S. Choe, B.-S. Lee, M. K. Cho, H.-J. Kim, D. Henkensmeier, S. J. Yoo, J. Y. Kim, S. Y. Lee, H. S. Park, J. H. Jang, Electrodeposited IrO<sub>2</sub> /Ti electrodes as durable and cost-effective anodes in high-temperature polymer-membrane-electrolyte water electrolyzers, *Appl. Catal. B* 226 (2018) 289-294.
- [33] B.-S. Lee, S. H. Ahn, H.-Y. Park, I. Choi, S. J. Yoo, H.-J. Kim, D. Henkensmeier, J. Y. Kim, S. Park, S. W. Nam, K.-Y. Lee, J. H. Jang, Development of electrodeposited IrO<sub>2</sub> electrodes as anodes in polymer electrolyte membrane water electrolysis, *Appl. Catal. B* 179 (2015) 285-291.
- [34] M. Łukaszewski, M. Soszko, A. Czerwiński, Electrochemical methods of real surface area determination of noble metal electrodes – an Overview, *Int. J. Electrochem. Sci.* 11 (2016) 4442-4469.
- [35] K. Yamanaka, Anodically electrodeposited iridium oxide films (AEIROF) from alkaline solutions for electrochromic display devices, *Jpn. J. Appl. Phys.* 28 (1989) 632-637.
- [36] J. Juodkazytė, B. Šebeka, I. Valsiunas, K. Juodkasis, Iridium anodic oxidation to Ir(III) and Ir(IV) hydrous oxides, *Electroanalysis* 17 (2005) 947-952.
- [37] V. I. Kravtsov, Platinum electrodeposition mechanism during the reduction of platinum chloride complexes, *Russ. J. Electrochem.* 36 (2000) 1365-1372.
- [38] H. M. Ghartavol, R. S. Moakhar, A. Dolati, Electrochemical investigation of electrodeposited platinum nanoparticles on multi walled carbon nanotubes for methanol electro-oxidation, *J. Chem. Sci.* 129 (2017) 1399-1410.
- [39] L. B. Hunt, The mechanism of electrodeposition, *J. Electrochem. Soc.* 65 (1934) 413-427.
- [40] A. Kloke, F. von Stetten, R. Zengerle, S. Kerzenmacher, Strategies for the

- fabrication of porous platinum electrodes, *Adv. Mater.* 23 (2011) 4976-5008.
- [41] S. A. Grigoriev, P. Millet, S. A. Volobuev, V. N. Fateev, Optimization of porous current collectors for PEM water electrolyzers, *Int. J. Hydro. Energ.* 34 (2009) 4968-4973.
- [42] R. Woods, Hydrogen adsorption on platinum, Iridium and rhodium electrodes at reduced temperatures and the determination of real surface area, *J. Electroanal. Chem. Interf. Electrochem.* 49 (1974) 217-226.
- [43] Y.-C. Park, H. Tokiwa, K. Kakinuma, M. Watanabe, M. Uchida, Effects of carbon supports on Pt distribution, ionomer coverage and cathode performance for polymer electrolyte fuel cells, *J. Power Sources* 315 (2016) 179-191.
- [44] H. S. Oh, H. N. Nong, T. Reier, A. Bergmann, M. Gliech, J. Ferreira de Araujo, E. Willinger, R. Schlogl, D. Teschner, P. Strasser, Electrochemical catalyst-support effects and their stabilizing role for IrOx nanoparticle catalysts during the oxygen evolution reaction, *J. Am. Chem. Soc.* 138 (2016) 12552-12563.
- [45] P. Zhang, S.-Y. Huang, B. N. Popov, Mesoporous tin oxide as an oxidation-resistant catalyst support for proton exchange membrane fuel cells, *J. Electrochem. Soc.* 157 (2010) B1163-B1172.
- [46] S. Sui, X. Wang, X. Zhou, Y. Su, S. Riffat, C.-j. Liu, A comprehensive review of Pt electrocatalysts for the oxygen reduction reaction: Nanostructure, activity, mechanism and carbon support in PEM fuel cells, *J. Mater. Chem. A* 5 (2017) 1808-1825.
- [47] H. S. Oh, H. N. Nong, T. Reier, M. Gliech, P. Strasser, Oxide-supported Ir nanodendrites with high activity and durability for the oxygen evolution reaction in acid PEM water electrolyzers, *Chem. Sci.* 6 (2015) 3321-3328.
- [48] E. A. Bel'skaya, E. Y. Kulyamina, Electrical resistivity of titanium in the

- temperature range from 290 to 1800 K, *High Temp.* 45 (2007) 785-796.
- [49] K. F. Chow, T. M. Carducci, R. W. Murray, Electronic conductivity of films of electroflocculated 2 nm iridium oxide nanoparticles, *J. Am. Chem. Soc.* 136 (2014) 3385-3387.
- [50] E. Antolini, Iridium as catalyst and cocatalyst for oxygen evolution/reduction in acidic polymer electrolyte membrane electrolyzers and fuel cells, *ACS Catal.* 4 (2014) 1426-1440.
- [51] H. Wendt, E.V. Spinacé, A.O.N.e.M. Linardi, Electrocatalysis and electrocatalysts for low temperature fuel cells: fundamentals, state of the art, research and development, *Quim. Nova* 28 (2005) 1066-1075.
- [52] Y. A. Gandomi, M. D. Edmundson, F. C. Busby, M. M. Mench, Water management in polymer electrolyte fuel cells through asymmetric thermal and mass transport engineering of the micro-porous layers, *J. Electrochem. Soc.* 163 (2016) F933-F944.
- [53] H. Li, Y. Tang, Z. Wang, Z. Shi, S. Wu, D. Song, J. Zhang, K. Fatih, J. Zhang, H. Wang, Z. Liu, R. Abouatallah, A. Mazza, A review of water flooding issues in the proton exchange membrane fuel cell, *J. Power Sources* 178 (2008) 103-117.
- [54] P. Millet, R. Ngameni, S. A. Grigoriev, V. N. Fateev, Scientific and engineering issues related to PEM technology: Water electrolyzers, fuel cells and unitized regenerative systems, *Int. J. Hydro. Energ.* 36 (2011) 4156-4163.
- [55] J.C. Cruz, V. Baglio, S. Siracusano, R. Ornelas, L. G. Arriaga, V. Antonucci, A. S. Aricò, Nanosized Pt/IrO<sub>2</sub> electrocatalyst prepared by modified polyol method for application as dual function oxygen electrode in unitized regenerative fuel cells, *Int. J. Hydro. Energ.* 37 (2012) 5508-5517.

- [56] S. Choe, B.-S. Lee, J. H. Jang, Effects of diffusion layer (DL) and ORR catalyst (MORR) on the performance of MORR/IrO<sub>2</sub>/DL electrodes for PEM-type unitized regenerative fuel cells, *J. Electrochem. Sci. Technol.* 8 (2017) 7-14.
- [57] P. T. Moseley, J. Garche, Electrochemical energy storage for renewable sources and grid balancing, Elsevier (2014).
- [58] B.-S. Lee, H.-Y. Park, M. K. Cho, J. W. Jung, H.-J. Kim, D. Henkensmeier, S. J. Yoo, J. Y. Kim, S. Park, K.-Y. Lee, J. H. Jang, Development of porous Pt/IrO<sub>2</sub>/carbon paper electrocatalysts with enhanced mass transport as oxygen electrodes in unitized regenerative fuel cells, *Electrochem. Commun.* 64 (2016) 14-17.
- [59] S. Song, H. Zhang, X. Ma, Z.-G. Shao, Y. Zhang, B. Yi, Bifunctional oxygen electrode with corrosion-resistive gas diffusion layer for unitized regenerative fuel cell, *Electrochem. Commun.* 8 (2006) 399-405.
- [60] H.-Y. Jung, S.-Y. Huang, B. N. Popov, High-durability titanium bipolar plate modified by electrochemical deposition of platinum for unitized regenerative fuel cell (URFC), *J. Power Sources* 195 (2010) 1950-1956.
- [61] W. H. Lee, H. Kim, Optimization of electrode structure to suppress electrochemical carbon corrosion of gas diffusion layer for unitized regenerative fuel cell, *J. Electrochem. Soc.* 161 (2014) F729-F733.
- [62] G. C. da Silva, M. R. Fernandes, E. A. Ticianelli, Activity and stability of Pt/IrO<sub>2</sub> bifunctional materials as catalysts for the oxygen evolution/reduction reactions, *ACS Catal.* 8 (2018) 2081-2092.
- [63] G. C. da Silva, K. J. J. Mayrhofer, E. A. Ticianelli, S. Cherevko, Dissolution stability: The major challenge in the regenerative fuel cells bifunctional catalysis, *J. Electrochem. Soc.* 165 (2018) F1376-F1384.

- [64] G. C. da Silva, K. J. J. Mayrhofer, E. A. Ticianelli, S. Cherevko, The degradation of Pt/IrOx oxygen bifunctional catalysts, *Electrochim. Acta* 308 (2019) 400-409.
- [65] J. Kang, J. Kim, Membrane electrode assembly degradation by dry/wet gas on a PEM fuel cell, *Int. J. Hydro. Energ.* 35 (2010) 13125-13130.
- [66] M. Bernt, A. Siebel, H. A. Gasteiger, Analysis of voltage losses in PEM water electrolyzers with low platinum group metal loadings, *J. Electrochem. Soc.* 165 (2018) F305-F314.
- [67] T. Ioroi, T. Oku, K. Yasuda, N. Kumagai, Y. Miyazaki. Influence of PTFE coating on gas diffusion backing for unitized regenerative polymer electrolyte fuel cells, *J. Power Sources* 124 (2003) 385-389.
- [68] U. Wittstadt, E. Wagner, T. Jungmann, Membrane electrode assemblies for unitised regenerative polymer electrolyte fuel cells, *J. Power Sources* 145 (2005) 555-562.
- [69] G. Chen, H. Zhang, H. Zhong, H. Ma, Gas diffusion layer with titanium carbide for a unitized regenerative fuel cell, *Electrochim. Acta* 55 (2010) 8801-8807.
- [70] S. A. Grigoriev, P. Millet, V. I. Porembsky, V. N. Fateev, Development and preliminary testing of a unitized regenerative fuel cell based on PEM technology, *Int. J. Hydro. Energ.* 36 (2011) 4164-4168.
- [71] J. X. Liu, H. Guo, X. M. Yuan, F. Ye, C. F. Ma, Experimental investigation on two-phase flow in a unitized regenerative fuel cell during mode switching from water electrolyzer to fuel cell, *Int. J. Energ. Res.* 42 (2018) 2823-2834.

# **Chapter 3. Through-Plane Amphiphilic Channel Formation on Porous Transport Layer for Highly Effective Unitized Regenerative Fuel Cell (URFC)**

## **3.1. Introduction**

As the global warming caused by emission of greenhouse gases becomes serious, worldwide efforts are being made to replace fossil fuels with renewable energy. Energy storage and converting technology including large capacity is required to address seasonal power supply/demand discrepancies along with the expansion of renewable energy supplies. Hydrogen is a zero-carbon clean energy vector having high energy density of  $142 \text{ MJ kg}^{-1}$ . To this end, hydrogen energy system is received attention.

UR-PEMFC is an electrochemical device to convert and store energy by operation in both PEMFC (FC mode) and PEMWE (EC mode). PEMFC operates based on electrochemical reactions with ion conduction; i) hydrogen oxidation reaction at anode ( $\text{H}_2 \rightarrow 2 \text{H}^+ + 2 \text{e}^-$ ), ii) conduction of  $\text{H}^+$  through the membrane, and iii) oxygen reduction reaction (ORR) at cathode ( $1/2 \text{ O}_2 + 2 \text{H}^+ + 2 \text{e}^- \rightarrow \text{H}_2\text{O}$ ). Highly active HOR, ORR electrocatalysts, e.g. Pt/C, and highly conductive and stable polysulfonated membrane, e.g. Nafion<sup>®</sup>, have significantly contributed to enhance

its power density to the commercialized level. Interestingly, not only catalysts and membrane, but also, porous transport layer (PTL, or gas diffusion layer (GDL)) has done a critical role in performance enhancement of fuel cell due to importance of water management during operation. There are several requirements of PTL: i) gas and liquid permeability, ii) electronic and heat conductivity and iii) mechanical strength. Typically, porous materials based on carbon, e.g. carbon paper, are used as GDL in PEMFC. [1-3].

Membrane dehydration and water flooding is the most significant concern in water management. On the one hand, fast water emission from GDL results in increase of ohmic resistance from membrane dehydration. On the other hand, sluggish water removal blocks catalyst active sites, sudden deterioration of the FC performance. To optimize and balance the water distribution during FC operation, researches have been done for several decades in four aspects, i.e. PTFE treatment, materials of GDL, MPL and control of porosity as mentioned in Chapter 1. From tremendous studies to optimize the structure of PTLs (GDLs), the state of PTL research in PEMFC is mature and some PTLs are already commercialized, e.g. Sigracet<sup>®</sup>, Pyrofil<sup>®</sup>, etc.

However, the commercialized carbon PTLs and Pt/C catalysts in PEMFC is not applicable in UR-PEMFC because of serious carbon corrosion at high voltage more than 1.5 V in the oxygen electrode during the EC mode. Thus, Pt black catalysts and Ti based PTLs such as Ti-mesh, Ti-felt, Ti-powders instead of C supported catalysts and C PTLs are typically used in the oxygen electrode of UR-PEMFC. In addition, gas and water management in the EC mode also need to be considered along with in the FC mode. For example, PTFE coating [4-6] and Ti particles as MPL [7] have been reported to enhance water management especially in the FC mode of UR-PEMFC. However, none of researches demonstrated the enhancement of both FC and EC

performances by PTFE coating since hydrophobicity of PTFE can enhance gas approach and water removal in the FC mode, but water approach to the catalysts layer and gas removal are important in the EC mode. The PTLs of URFC still require lots of researches to satisfy facilitation of gas and water transport in both FC and EC operations.

Here, we reported fabrication of amphiphilic PTLs having distinct patterned highways of gas and water by patterning hydrophobic polymer brush on hydrophilic PTL, which upgrades the mass transport on the oxygen electrode consisting of Pt black and IrO<sub>2</sub> catalysts of UR-PEMFC. The IrO<sub>2</sub> electrodeposited Ti PTL (ED-IrO<sub>2</sub>/Ti) was used due to its hydrophilicity for water channel, stability during the EC mode from the blocking partial oxidation of Ti by the thin coated IrO<sub>2</sub> layer [8, 9] and high OER mass activity [8, 10, 11]. Interestingly, the distinct hydrophobic and hydrophilic channels achieve complimentary performance improvement of UR-PEMFC mainly in two aspects: i) reduction of the voltage loss from flooding due to hydrophilic ED-IrO<sub>2</sub>/Ti PTL in the FC mode and ii) amelioration of the mass transport resistance due to hydrophobic Pt catalysts layers in the EC mode. To the best of our knowledge, it is the first reported Ti PTL including patterning gas and water channels in UR-PEMFC.

## **3.2. Experimental Section**

### **3.2.1. Polymer Brush Coated Electrode Fabrication**

For the oxygen electrode fabrication, Iridium oxide (IrO<sub>2</sub>) was electrodeposited on Ti PTL (250 μm, Bekaert) at 0.7 V (vs. SCE) during 10 minutes in precursor

solution. Precursor solution consisting of 0.01 M Iridium(IV) chloride hydrate (99.95 %, Ir 56.5 %, Alfa-aesar), oxalic acid( $(\text{COOH})_2 \cdot 2\text{H}_2\text{O}$ : 5 g L<sup>-1</sup>), hydrogen peroxide (35 % H<sub>2</sub>O<sub>2</sub>: 10 g L<sup>-1</sup>) in deionized water (DI-water, 18 M $\Omega$ ) was stirred for 3 days before electrodeposition.

After preparation of IrO<sub>2</sub>-electrodeposited PTLs, shadow mask patterning process was performed by using hydroxyl terminated poly(dimethylsiloxane) homopolymer (PDMS brush), poly(4-vinylpyridine) (P4VP) homopolymer and metallic shadow masks with large pattern (LP, pitch = 250  $\mu\text{m}$ /width = 125  $\mu\text{m}$ ) and small pattern (SP, pitch = 75  $\mu\text{m}$ /width = 30  $\mu\text{m}$ ). The hydroxyl terminated PDMS brush with a molecular weight (MW) of 5 kg/mol was purchased from Polymer Source Inc. and P4VP homopolymer with a MW of 60 kg/mol was purchased from Sigma-Aldrich. For the patterning process, the heptane solution including the hydroxyl-terminated PDMS brush (2 wt%) and the IPA solution including P4VP homopolymer (2 wt%) were prepared respectively.

In order to prevent the PDMS brush coating on IrO<sub>2</sub>-electrodeposited catalytic surface, 150  $\mu\text{l}$  P4VP homopolymer solution was sprayed on the IrO<sub>2</sub>-electrodeposited side of PTLs. The temperature of PTLs during the spraying process was maintained at 80 °C to evaporate IPA rapidly. After passivating the surface of IrO<sub>2</sub>- electrodeposited catalysts by using P4VP homopolymer, the P4VP coated and uncoated regions were alternatively formed by spray coating of a 150  $\mu\text{l}$  P4VP homopolymer solution through the shadow mask on the opposite side. And then, the PDMS brush coating process was performed using drop casting of the heptane solution of the PDMS brush. After the surface of the micropatterned PTL was sufficiently wet with the PDMS-brush solution, it was fully dried on a hot plate at 60°C to evaporate the residual heptane solvent. Then, thermal treatment was

performed for 3 hours in a vacuum oven at 200°C to covalently link the PDMS brush to the surface of PTLs except the P4VP coated region. Lastly, the PDMS brush-coated PTLs were washed with heptane, followed with IPA to remove the unattached PDMS brush and P4VP homopolymer. The schematic illustration of the fabrication process of these amphiphilic electrodes is described in Figure 3.1.

### **3.2.2. Ex-situ and In-situ Characterization**

The surface chemical composition was analyzed by X-ray photoelectron spectroscopy (XPS, Thermo Fisher, K-alpha). The surface morphology was examined by field emission scanning electron microscopy (FE-SEM, Teneo Volume Scope) and the morphology of before and after wetting was analyzed by using optical microscopy (Carl Zeiss, Axioplan 2). The hydrophobic effect of PDMS brush coating on Ti PTL was observed by contact angle measurement (SmartDrop, Femtobiomed). Four probe measurements on the micrometer scale was done by a SEM-FIB system (Quanta-3D; FEI company, Eindhoven, Netherlands) in vacuum containing nanomanipulators (MM3A EM; Kleindiek Nanotechnik GmbH, Reutlingen, Germany) and a semiconductor device analyzer (B1500A; Agilent Technologies, Palo Alto, CA, USA). The near edge X-ray absorption fine structure (NEXAFS) analysis was performed at the soft X-ray 10D XAS KIST beamline of Pohang accelerator laboratory (PAL).

### **3.2.3. Single Cell Tests of Unitized Regenerative Fuel Cell (URFC)**

To prepare membrane electrode assembly (MEA) in a single cell, Pt black (high surface area, Alfa Aesar)  $0.6 \text{ mg}_{\text{Pt}} \text{ cm}^{-2}$  and Pt/C (46.6 wt%, Tanaka)  $0.2 \text{ mg}_{\text{Pt}} \text{ cm}^{-2}$

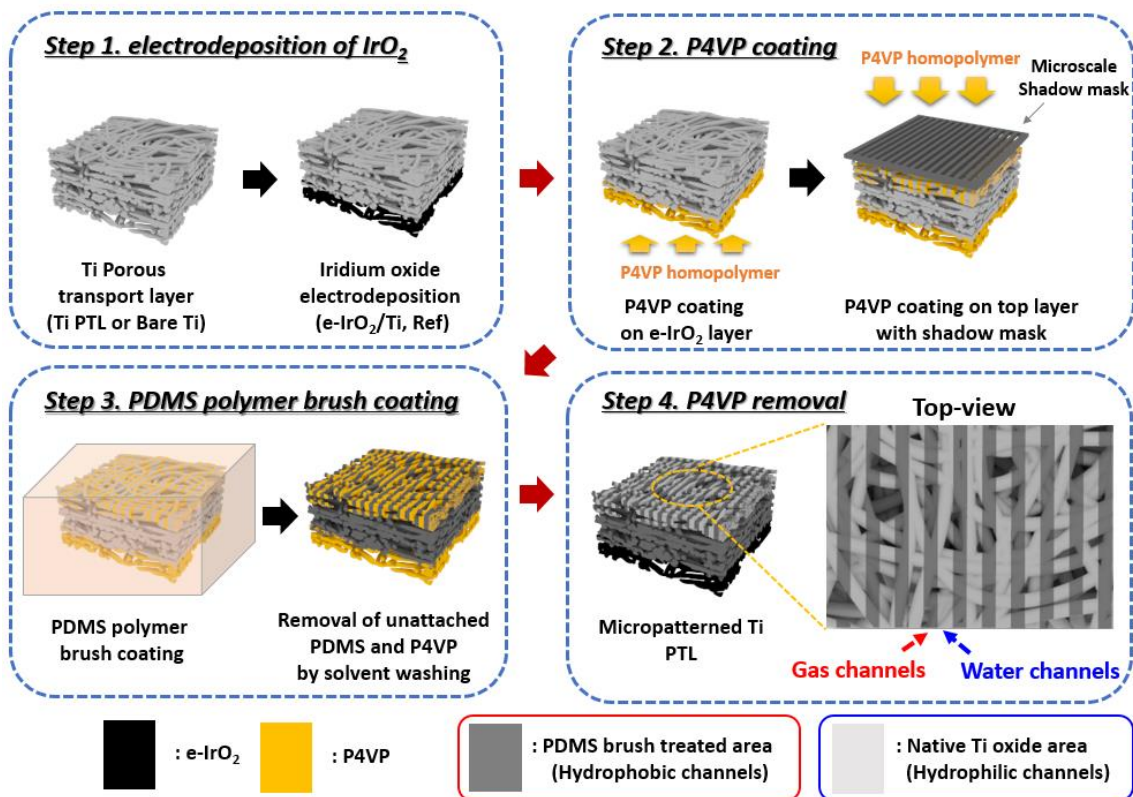


**Figure 3.1.** Schematic illustration of fabrication procedure of amphiphilic porous transport layers (PTLs).

are coated on the oxygen electrode side and the hydrogen electrode side of membrane (CCM, Nafion<sup>®</sup> 212), respectively. Catalysts are coated on each side of membrane (CCM) by spraying method. In catalysts slurry, Pt black or Pt/C, nafion ionomer solution (5 wt% nafion), isopropyl alcohol and DI water first were mixed, and then ultra-sonication for 1 hour was conducted. Ionomer contents were 15 wt% and 30 wt% for Pt black and Pt/C catalysts. MEA (2.25 cm<sup>2</sup>) comprised of a processed Ti PTL, catalysts coated N212 and a C PTL (39 BC. Sigracet<sup>®</sup>) was hot pressed at 120 °C, 43.6 Mpa for 1 minute after 2 minutes of preheating time without pressure. In a single cell assembly, MEA were assembled between a Ti bipolar plate with an end plate and a C bipolar plate with an end plate by 80 lb·in torque.

In a performance analysis, current-voltage curve (IV-curve) and electrochemical impedance spectroscopy (EIS) were determined using high current potentiostat (HCP-803, Bio-Logic). The cell temperature was 80°C during URFC operation. In fuel cell tests, the flow rate of oxygen (or air)/hydrogen gas was 200 ccm/200 ccm, and the relative humidity (RH) of supplied gas was controlled to 100% and 65%. In water electrolysis, DI water was provided to the oxygen electrode at 15 ml min<sup>-1</sup> flow rate. IVs were measured from OCV to 0.2 V for fuel cell and from 1.25 V to 2.0 V for water electrolysis with 10 mV s<sup>-1</sup> scan rate. In a long term test, 160 h operation (@ 0.5 A cm<sup>-2</sup>) was done with 16 cycles of URFC operation including 5h FC-5h EC as one cycle. The performance of FC was measured at RH 65 condition and values of impedance at 50 kHz were recorded every 2 minutes. Between each cycle, N<sub>2</sub> gases (RH 100) were purged on each side of the electrodes.

### **3.3. Results and Discussion**

### 3.3.1. Fabrication of Amphiphilic Porous Transport Layer

To create alternate hydrophilic/hydrophobic channels on the surface of Ti PTLs, patterning of hydroxyl-terminated PDMS polymer (PDMS brush) using shadow masks on the hydrophilic IrO<sub>2</sub> electrodeposited electrode was employed. In the case of microscale patterning using a shadow mask (i.e. mechanical aperture plates), it has the advantage of low costs and the simple process that enables large area fabrication. The PDMS brush, the surface modifier which has the reactive functional group at the end of polymer, could be covalently linked to the surface with very thin thickness (1~100 nm), which has the advantage of easily changing the surface polarity from hydrophilic to hydrophobic by simple thermal annealing without compromising the electrical conductivity of Ti PTLs. In order to secure the hydrophilic property of hydrophilic domains and the catalytic activity of the IrO<sub>2</sub> surface after the shadow mask patterning process, a hydrophilic P4VP homopolymer was used as a protective mask to prevent the coating of the PDMS brush. In contrast to the PDMS brush which has a reactive hydroxyl functional group at the ends of the polymer, the P4VP homopolymer does not have reactive functional groups, thus it could be easily removed by solvent washing at the end of the shadow mask patterning process.

At first, Iridium oxide (IrO<sub>2</sub>) was electrodeposited on Ti PTLs (e-IrO<sub>2</sub>/Ti) to form a thin IrO<sub>2</sub> film on Ti PTLs, which is as an efficient durable oxygen electrode for polymer electrolyte membrane water electrolyzer. The IPA solution of P4VP homopolymer was coated onto the IrO<sub>2</sub>-electrodeposited side by using the spray coating process to protect the IrO<sub>2</sub> coated surface. Due to the large difference in Hildebrand solubility parameter between P4VP ( $\delta \sim 23.0 \text{ MPa}^{1/2}$ ) and the heptane

solvent ( $\delta \sim 15.3 \text{ MPa}^{1/2}$ ) which is a good solvent for PDMS brush, the P4VP could effectively preserve IrO<sub>2</sub> surface of Ti PTLs during PDMS brush coating process. If the PDMS brush is coated on the IrO<sub>2</sub> surface, it would inhibit the catalytic reaction (OER) of IrO<sub>2</sub> by blocking the reactants on the IrO<sub>2</sub> surface. Thus, it is important to passivate the IrO<sub>2</sub> surface for preserving pure catalytic activity before the PDMS brush treatment.

On the opposite side where IrO<sub>2</sub> was not coated, the P4VP homopolymer was spray-coated through a shadow mask with large patterns (LP, pitch = 250  $\mu\text{m}$ /width = 125  $\mu\text{m}$ ) and small patterns (SP, pitch = 75  $\mu\text{m}$ /width = 30  $\mu\text{m}$ ) so that the P4VP coated and non-coated regions are formed alternately. The pitch and space of patterns in each shadow mask were observed using an optical microscopy (OM) (Figure 3.2). The space region of 125  $\mu\text{m}$  in 250  $\mu\text{m}$  of pitch was coated by the P4VP for LP, and the space region of 45  $\mu\text{m}$  in 70  $\mu\text{m}$  of pitch was coated by the P4VP for SP. Then, the PDMS brush coating process was carried out by using drop-casting, and followed thermal annealing process to covalently link the PDMS brush to the surface of Ti PTLs except for the P4VP coated region. During the thermal annealing, a reactive hydroxyl functional group at the end of the PDMS brush reacts with hydroxyl and carboxylic acid groups on the surface of the Ti PTL to be covalently linked through a condensation reaction. After thermal annealing, an unattached PDMS brush and a P4VP homopolymer were washed by using heptane and IPA solvents respectively.

### **3.3.2. Physical and Electrical Characteristics**

We prepared the Ti PTLs with pristine (Ref), PDMS brush treated without patterns (NP) and with small (SP) and large patterns (LP) for comparison through the shadow

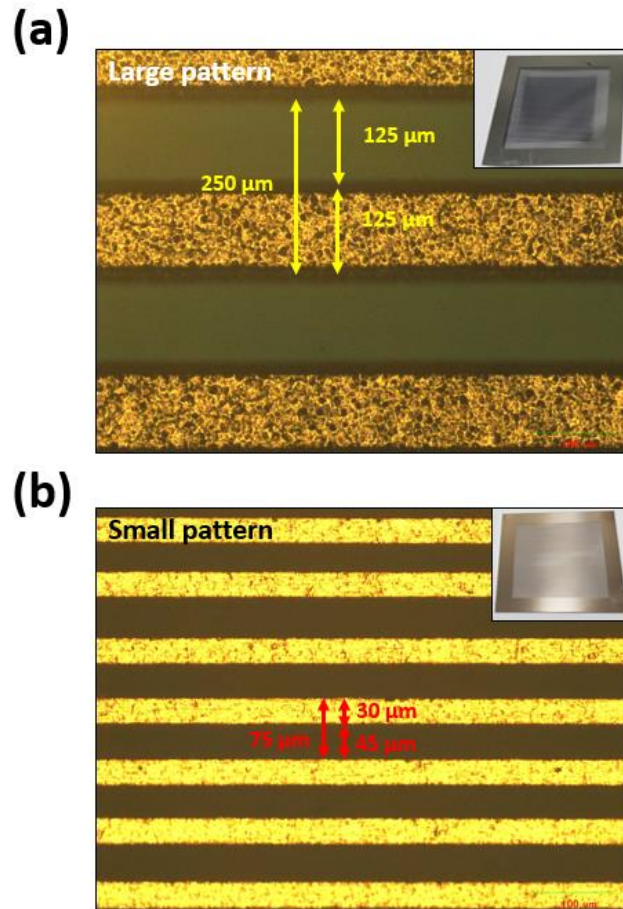


**Figure 3.2.** Optical microscope images of shadow masks of (a) LP (width: 125  $\mu\text{m}$ , space: 125  $\mu\text{m}$ , pitch: 250  $\mu\text{m}$ ) and (b) SP (width: 30  $\mu\text{m}$ , space: 45  $\mu\text{m}$ , pitch: 75  $\mu\text{m}$ ).

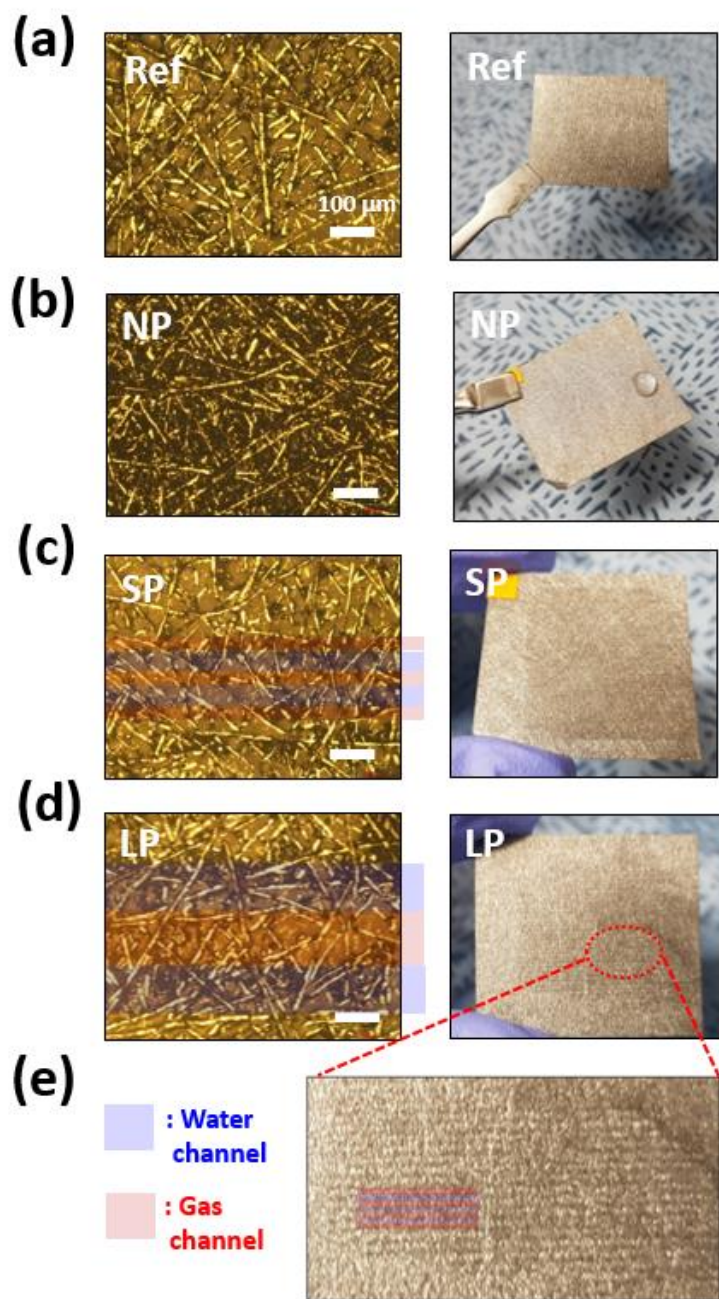


**Figure 3.3.** Optical microscope images and photographs of (a) Ref, (b) NP, (c) SP and (d) LP after dropping water. (e) The enlarged photograph of LP. (Blue indicates the region of hydrophilic channels and red indicates the region of hydrophobic channels.)

mask patterning process, and investigated the surface properties by dropping enough water droplets on the surface of Ti PTLs. In the case of the pristine Ti PTL, as soon as the water droplets fell on the surface, the water droplets rapidly disappeared due to the water absorption caused by hydrophilicity of the e-IrO<sub>2</sub>/Ti. Furthermore, the strong water accumulation in the pristine PTL layer was clearly observed by an OM image (Figure 3.3(a)). On the contrary, in the case of the NP PTL, when the water droplets fell on the surface, the water droplets were not absorbed into the NP PTL layer due to the hydrophobicity derived from surface modification with the PDMS brush (Figure 3.3(b)). Interestingly, for the micropatterned SP and LP PTLs, which have the hydrophilic/hydrophobic domains alternatively, the microscale stripe patterns are visible after the water droplets fell on the surface (Figure 3.3(c) and 3.3(d)). These stripe patterns are associated with the hydrophilic domains (marked in blue), because the water tends to accumulate in these domains and we found that the width of stripe patterns matches the size of the shadow mask patterns through OM images. On the contrary, the PDMS brush-treated region (marked in red) exhibited water-resistant properties, as described in the NP PTL earlier, due to the hydrophobicity of the PDMS brush. From the enlarged photographic image of the LP PTL, it was confirmed that the stripe patterns were more clearly visible, indicating that the formation of the amphiphilic patterns were successfully formed on the surface through the shadow mask patterning process (Figure 3.3(e)).

To investigate the change of surface properties such as electrical conductivity and chemical composition before and after the PDMS brush treatment, we carried out FE-SEM, 4-probe measurement, XPS, and NEXAFS analysis. From the SEM image, none of distinctive difference of surface was perceived (Figure 3.4(a)). With regard to electrical conductivity measured by 4-probe measurement, the bare Ti PTL and

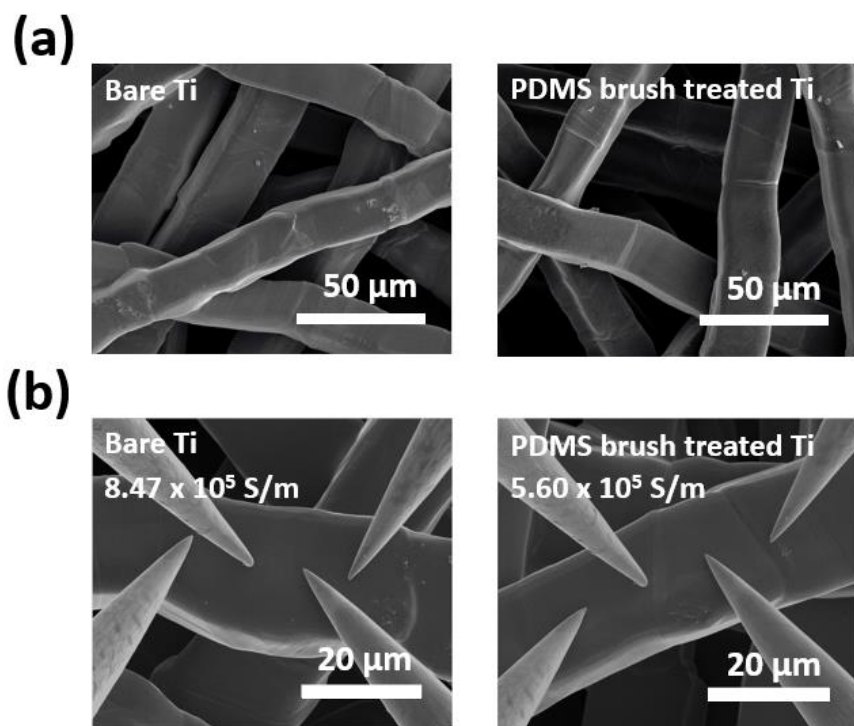


**Figure 3.4.** (a) FE-SEM images of bare Ti and PDMS brush treated Ti. (b) FE-SEM images during 4-probe measurements of bare Ti and PDMS brush treated Ti including nanomanipulators. The inserted values in images are measured conductivity.

the PDMS brush treated Ti PTL exhibited  $8.47 \times 10^5$  and  $5.60 \times 10^5$  S/m, respectively (Figure 3.4(b)). Even though the PDMS brush is an insulator, the electrical conductivity of the PDMS brush treated Ti PTL was almost similar with the bare Ti PTL due to its ultra-thin thickness. In other words, the surface modification based on the PDMS brush could change the surface hydrophobicity of Ti PTLs without significantly changing the electrical properties.

From the XPS spectra of Si 2p peaks, it was confirmed that the PDMS brush was covalently linked on the surface of Ti PTLs except for the electrodeposited-IrO<sub>2</sub> surface as we intended (Figure 3.5(a)). Since the PDMS brush contains silicon and oxygen atoms alternatively in their backbone, it is possible to confirm whether the PDMS brush treatment is successfully performed by checking the presence of Si 2p peaks. Compared to the bare Ti PTL, the high intensity of Si 2p peak for the PDMS brush treated Ti PTL was observed, indicating that the PDMS brush was coated on the surface successfully. In the case of Si 2p peak for the surface of electrodeposited-IrO<sub>2</sub>, which is the opposite side of the PDMS brush treated Ti PTL, there was no signal for Si 2p peak, which indicates that the P4VP passivation protected the surface of IrO<sub>2</sub> well during the PDMS brush treatment as intended.

Furthermore, from the NEXAFS C K-edge spectra, we found that the PDMS brush treatment was successfully occurred on the surface of Ti PTLs. In general, NEXAFS analysis is very sensitive to the detailed chemical structures, thus, polymers have a unique spectrum depending on their chemical structure. Through this, it is possible to find out the presence and the type of polymers in the samples. For the C K-edge spectra of PDMS brush,  $\sigma^*$  C-Si at 291 eV and  $\sigma^*$  C-H around 287.4 eV were clearly observed, and matched well with the values reported in literatures. For the PDMS brush treated Ti PTL, unlike the pristine Ti PTL, the C K-edge spectra clearly showed

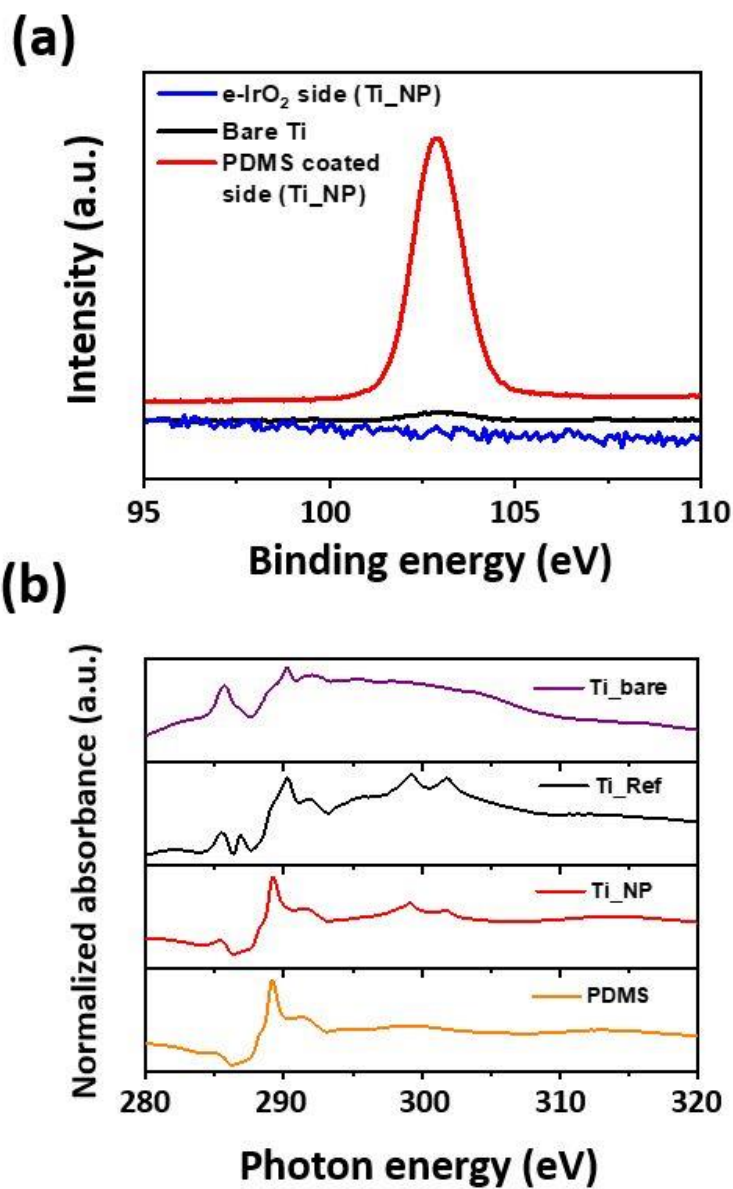


**Figure 3.5.** (a) Surface characterization by XPS of e-IrO<sub>2</sub> side of PDMS treated e-IrO<sub>2</sub>/Ti (NP), bare Ti and PDMS coated side of NP. (b) NEXAFS C K-edge spectra of bare Ti, e-IrO<sub>2</sub>/Ti (Ref), NP (PDMS coated side) and PDMS polymer brush.

the  $\sigma^*$  C-Si and  $\sigma^*$  C-H peaks arisen from the PDMS brush, indicating that the PDMS brush is linked well to the surface of the Ti PTL (Figure 3.5(b)).

### 3.3.3. Unitized Regenerative PEM-Fuel Cell

The PTLs were applied in oxygen electrode with Pt black catalysts (CCM) in single cell tests of both FC and EC modes. Since Pt is the main catalyst determines the performance, gas reactant approaches to the catalyst is significantly important in FC. However, hydrophilic electrodeposited- $\text{IrO}_2$  catalysts are directly contacted with Pt catalyst layers, which are disrupters in the aspect of ORR by blocking facile emission of water product. Performances are significantly different depending on the surface property of PTLs (Figure 3.6). In FC @ RH 65, Ref electrodes showed the poorest performance, i.e. maximum power density less than  $70 \text{ mW cm}^{-2}$  (Figure 3.6(a)). Since it is super-hydrophilic, water emission is not smooth. This results in severe flooding and voltage loss from mass transport limitation, i.e. blocking of catalysts active sites at cathode by water from electro-osmosis or produced in ORR, even at low humidity. In addition, ohmic resistance reflects the reduction of active area in the electrode by flooding since it is inversely proportional to the active area. Here, ohmic resistance in Ref cell was higher more than 2 times of other PTLs, e.g.  $0.55 \text{ } \Omega \text{ cm}^2$  for Ref and  $0.24 \text{ } \Omega \text{ cm}^2$  for LP. Hydrophobic treatment enormously ameliorates these issues. NP has many of the most hydrophobic areas of these PTLs and revealed 2.8 times higher current density @ 0.6 V compared to Ref (RH 65, Figure 3.6(c)). However, still high voltage loss from mass transport limitation is existed, mainly due to the hydrophilic  $\text{IrO}_2$  catalyst region contacted with Pt black catalysts in PTL. NP exhibited higher power density at the low current region

compared to SP, but power density of SP overtook NP in high current density more than  $0.62 \text{ A cm}^{-2}$  due to mass transport limitation. The patterning effect was more evident in the condition of providing fully hydrated gas fuels, i.e. RH 100. There was little performance for Ref and NP at RH 100 due to flooding, unlike SP and LP (Figure 3.6(b)). From the lower performance of SP and LP at RH 100 compared to RH 65 operation, some flooding still existed in SP and LP. However, amphiphilic channels facilitate transport of gas and water in discrete ways and operation of fuel cells even at fully humidified condition. The best maximum power density of  $391 \text{ mW cm}^{-2}$  was achieved in LP, which is 75 % enhancement of power density compared to NP and SP (Figure 3.6(a)). There two possible reasons: i) higher transport of gas and water due to direct channel formation from patterning compared to NP and ii) enhancement of gas approach from the wider gas transport channel due to reduced blocking by Ti fibers with  $20 \text{ }\mu\text{m}$  diameter in LP compared to SP, e.g.  $125 \text{ }\mu\text{m}$  for LP and  $30 \text{ }\mu\text{m}$  for SP.

LP also accomplished the best performance among PTLs in the EC mode. Generally, hydrophobicity of PTLs negatively affects to arrival of water to catalysts layers, resulting decrease of the current density of electrolysis [6]. However, interestingly, the worst performance was revealed in the Ref electrode without polymer coating, which is the most hydrophilic electrode. In addition, performance was enhanced in the order of NP, SP and LP (Figure 3.7(a)). This is because of highly porous Pt catalyst layers, which are disrupters between the PTL and membrane. Even though additional Pt catalysts can contribute to enhancement of OER activity, existence of Pt catalyst layers reduced the performance of EC, e.g. from  $1.7 \text{ A cm}^{-2}$  without Pt to  $0.9 \text{ A cm}^{-2}$  with Pt @  $1.8 \text{ V}$  (Figure 3.7(a)). Pt catalyst layers are composed of Pt nanoparticles and nafion ionomers which have hydrophobicity and

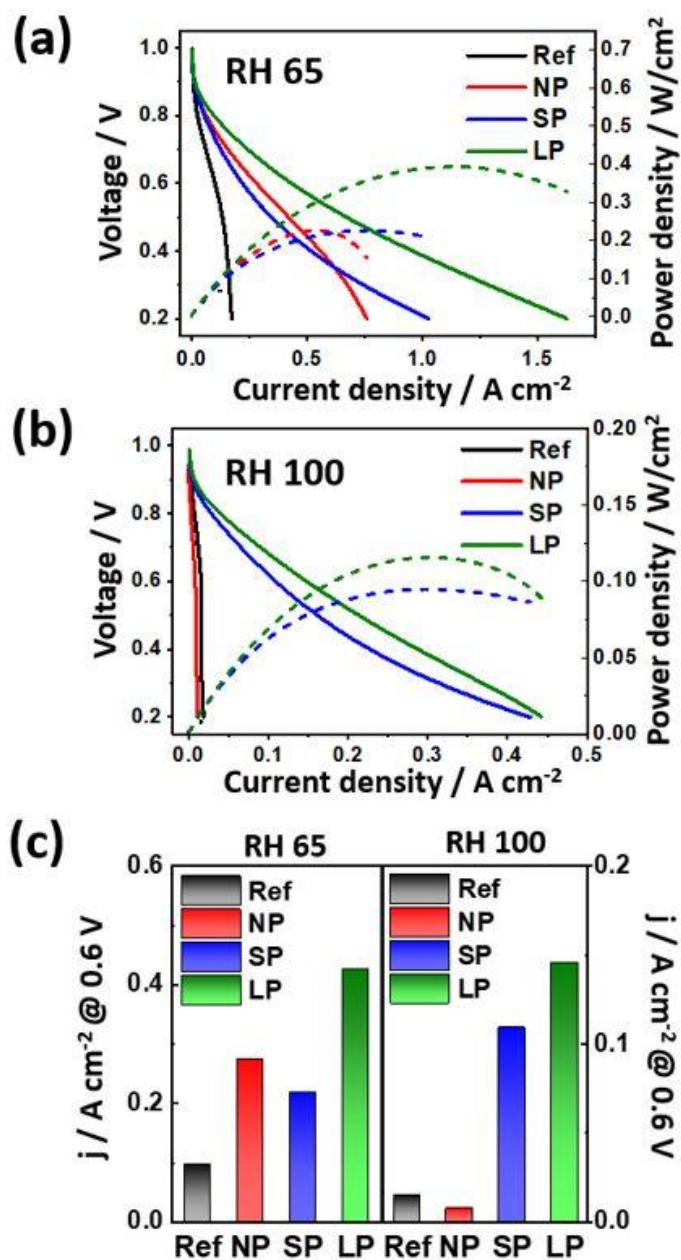


**Figure 3.6.** Comparison of IV performance and power density between Ref, NP, SP and LP in FC mode at (a) RH 65 and (b) RH 100. (c) Comparison of current density at 0.6 V at RH 65 and RH 100. Ref refers to e-IrO<sub>2</sub>/Ti, NP refers to PDMS coated e-IrO<sub>2</sub>/Ti without patterns, and SP and LP refers to PDMS coated e-IrO<sub>2</sub>/Ti with small and large patterns.

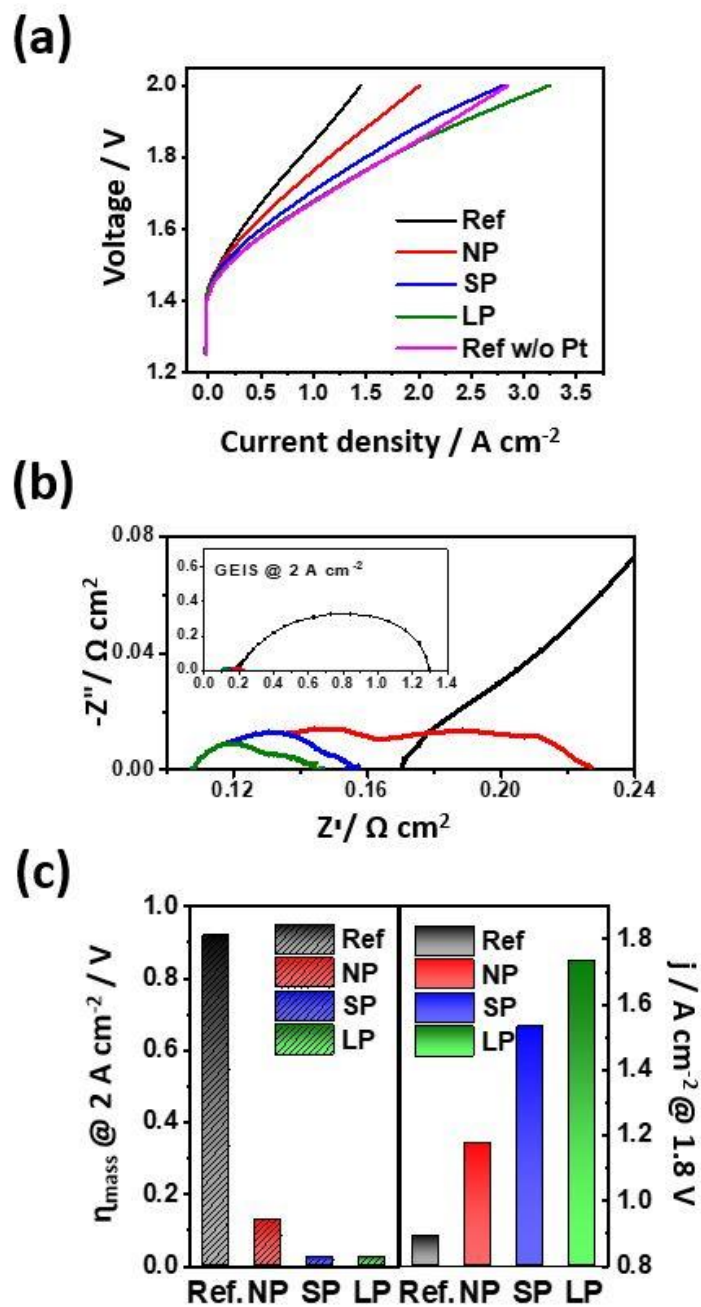


**Figure 3.7.** Comparison of (a) IV performance and (b) Nyquist plot of galvanostatic impedance spectroscopy (GEIS) at  $2 \text{ A cm}^{-2}$  between Ref, NP, SP and LP in EC mode. (c) Comparison of overvoltage from mass transport resistance at  $2 \text{ A cm}^{-2}$  and current density at  $1.8 \text{ V}$  between Ref, NP, SP and LP.

gas permeability for increase active sites on catalysts. This is indispensable property for active FC operation, but presence of Pt catalysts and its property exert negative influence during electrolysis in three main aspects compared to the case of without Pt catalysts: i) interruption of produced O<sub>2</sub> gas emission due to its hydrophobicity, ii) swelling of ionomers blocking active sites of IrO<sub>2</sub> catalysts, e.g. IrO<sub>2</sub> adjacent to Pt, and iii) increase ohmic resistance due to additional ionomer pathway from the thick Pt catalysts layer (> 10 μm). For instance, ohmic resistance was increased from 0.12 Ω cm<sup>2</sup> to 0.17 Ω cm<sup>2</sup> after addition of Pt catalyst layers, but not only from the additional proton pathway but also trapping produced O<sub>2</sub> bubbles contributed to increase of ohmic resistance.

Polymer coating on PTL ameliorates these inevitable negative effects of Pt catalyst layers. First, hydrophobicity of PTL by polymer coating promotes emission of gas bubbles, which is hindered by Pt catalyst layers. It results in reduction of mass transport resistance, which is the main reason for the enhancement of performance after polymer coating (Figure 3.7(b)). When surface is hydrophobic, water minimizes its contact with Ti PTL and unfavorable wetting property results lowering pressure of gas emission. Additionally, gas channel formation by patterning accelerates emission of gas compared to emission through random pathway. The overvoltage from mass transport resistance was decreased 7.1 times by polymer coating, and additionally 5.0 times by patterning at 2 A cm<sup>-2</sup> (Figure 3.7(c)). Reduction of blocking O<sub>2</sub> bubbles led reduction of ohmic resistance from reducing blocked proton pathways in ionomers, e.g. from 0.17 Ω cm<sup>2</sup> for Ref to 0.11 Ω cm<sup>2</sup> for LP, and also kinetic resistance from increase of active sites (Figure 3.7(b)). To verify discrete gas and water pathways through large patterning, O<sub>2</sub> emission from the backside of the Ti PTL was analyzed using scanning electrochemical microscopy

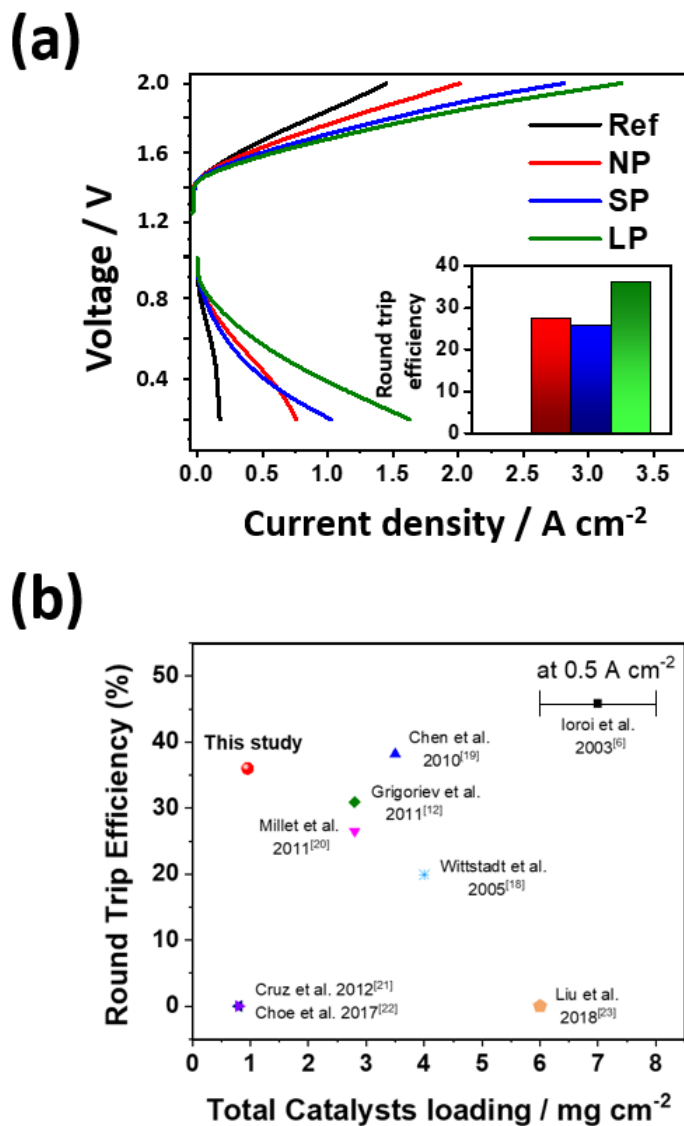


**Figure 3.8.** (a) URFC performance and round trip efficiency (RT) at 0.5 A cm<sup>-2</sup> of PTLs (Ref, NP, SP and LP). (b) Comparison of RT at 0.5 A cm<sup>-2</sup> versus total catalyst loading in URFC single cell with previous researches. The data of previous studies in the graph are limited to the case of using non-carbon PTLs in the oxygen electrode of URFC.

(SECM). The details about SECM analysis are described in chapter 4.

The performance of UR-PEMFC is summarized according to tuning of surface hydrophobicity of PTLs (Figure 3.8(a)). Round trip efficiency (RT) enhanced from 0 % to 27 % @ 0.5 A cm<sup>-2</sup> by hydrophobic treatment. SP showed 26 %, which is slightly lower than NP due to the lower voltage of FC @ 0.5 A cm<sup>-2</sup>. Among hydrophobic treated PTLs, the highest RT was achieved by LP, which is 36 % @ 0.5 A cm<sup>-2</sup> (inserted Figure in Figure 3.8(a)). To achieve high RTs, high loading more than 2.5 mg<sub>(Pt+Ir)</sub> cm<sup>-2</sup> in the cell has been required in previous reported papers when Pt black catalysts were used as ORR in the FC mode instead of Pt/C due to carbon corrosion (Figure 3.8(b)). For instance, Grigoriev et al. achieve 31 % of RT with 2.8 mg<sub>(Pt+Ir)</sub> cm<sup>-2</sup> of noble catalysts [12]. Here, higher RT only using 0.95 mg<sub>(Pt+Ir)</sub> cm<sup>-2</sup> of noble catalysts was accomplished by significant enhancement in mass transport during both FC and EC operations by introduction of the amphiphilic PTL as the oxygen electrode of the UR-PEMFC.

### **3.3.4. Stability Tests of Amphiphilic PTL in UR-PEMFC Operation**

To confirm stability of the fabricated PTL, durability test @ 0.5 A cm<sup>-2</sup> was done for LP during 160 h, i.e. 16 cycles of FC 5 h-EC 5 h. Degradation rates of 632 μV h<sup>-1</sup> and 614 μV h<sup>-1</sup> were observed for FC and EC mode operations, respectively (Figure 3.9). Although ohmic resistance was decreased from the FC to EC mode since membrane and ionomers contain higher amount of water during the EC mode, but none of increase of ohmic resistance was occurred each of the FC and EC mode operation during 160 h compared to initial ohmic resistance from measured high frequency resistance at 50 kHz during long term tests.

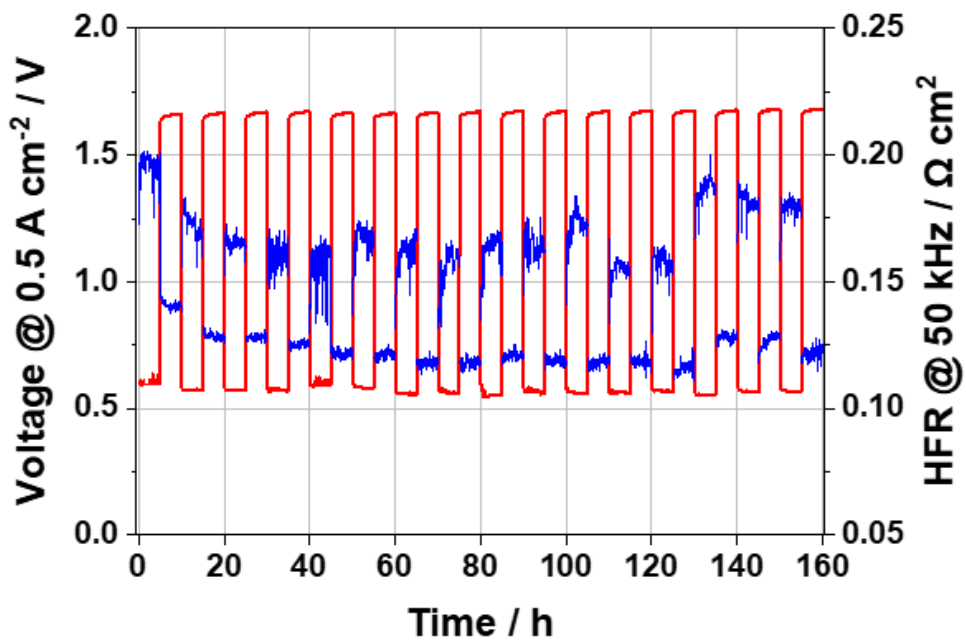


**Figure 3.9.** Long-term URFC operation of LP at  $0.5 \text{ A cm}^{-2}$  (FC:  $\text{H}_2/\text{O}_2$ , RH 65). During long-term operation, high frequency resistance at 50 kHz in GEIS (@  $0.5 \text{ A cm}^{-2}$ ) was measured every 2 minutes.

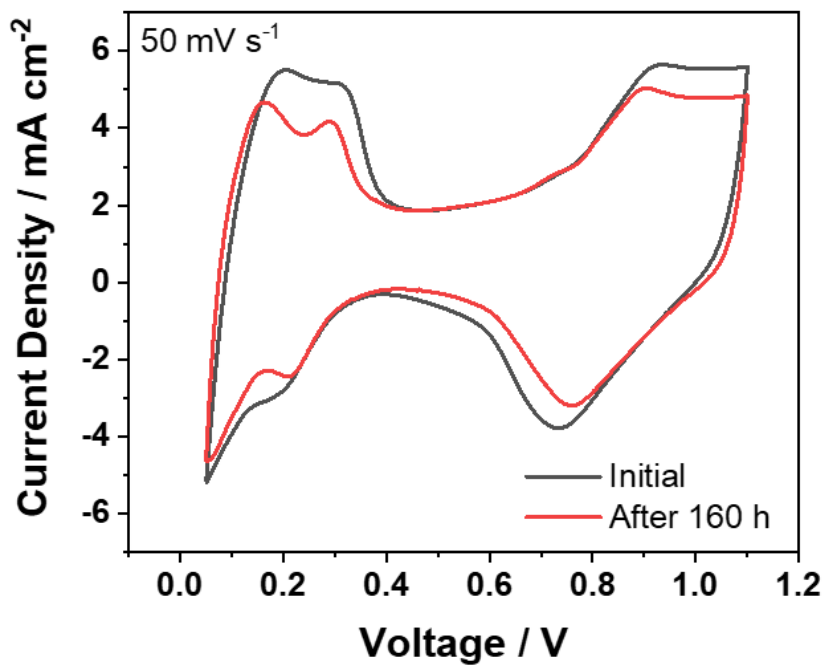


**Figure 3.10.** Cyclic voltammetry from 0.05 to 1.1 V (vs. pseudo RHE) of LP before and after the 160 h long term test. Fully humidified H<sub>2</sub> gas was purged to Pt/C catalysts on the C PTL, which acted as a pseudo reference. Fully humidified N<sub>2</sub> gas was purged to the large patterned e-IrO<sub>2</sub>/Ti PTL including Pt black catalysts.

The main cause of performance degradation in the FC mode is increase of kinetic resistance due to dissolution, migration and coalescence of Pt catalysts [13]. Reduction of Pt catalysts becomes a cause of decrease of OER current from Pt in the EC mode since Pt catalysts also have OER activity. In addition, Pt nanoparticles and ionomers getting around by dissolution or migration also can block the surface of IrO<sub>2</sub> catalysts, affecting the EC performance. Electrochemical active surface area (ECSA) of Pt calculated by Hup<sub>d</sub> was reduced 31 % from 27.2 m<sup>2</sup> g<sub>Pt</sub> to 18.7 m<sup>2</sup> g<sub>Pt</sub> after the 160 h operation (Figure 3.10). Although 31 % reduction of Pt ECSA, 33 % of RT was shown after the 160 h operation, i.e. 3 % decrease of RT. Almost none of flooding was observed in the FC mode and the influence of the amphiphilic PTL in both FC and EC was maintained during the 160 h operation. To enhance the stability of the cell, stable Pt catalysts on corrosion resistive supports, e.g. Pt/SnO<sub>2</sub> [14], Pt monolayer on CeOx [15], and reinforced membrane having good thermo-mechanical stability [16, 17] should be applied in UR-PEMFC in future.

### 3.4. Conclusions

In summary, we demonstrate that the amphiphilic patterned PTL to ameliorate issues of paradoxical requirements of PTL for water management in UR-PEMFC, i.e. hydrophobic PTL for FC and hydrophilic PTL for EC. In the oxygen electrode of UR-PEMFC, hydrophilic IrO<sub>2</sub> catalysts and hydrophobic Pt catalysts become disrupters in the FC and EC mode, respectively. However, not only mass transport limitations, e.g. 35.6 times reduction of overvoltage from mass transport resistance in EC, but also, ohmic and kinetic resistance are reduced in both FC and EC operation by active transport of reactants and products through amphiphilic channels

in the PTL. By introduction of the amphiphilic patterned PTL, enhancement of RT from 0 to 36 % was achieved using only  $0.95 \text{ mg}_{(\text{Pt+Ir})} \text{ cm}^{-2}$ . From 160 h durability tests, the stable effect of the PTL was verified although degradation rate about  $0.6 \text{ mV h}^{-1}$  was observed for both FC and EC from decrease of catalysts active area. Our amphiphilic patterned PTL suggests the solution for the paradoxical issue in UR-PEMFC and contributes to further development for commercialization of UR-PEMFC.

### 3.5. References

- [1] S. Escribano, J.-F. Blachot, J. Ethève, A. Morin, R. Mosdale, Characterization of PEMFCs gas diffusion layers properties, *J. Power Sources* 156 (2006) 8-13.
- [2] H.-K. Lee, J.-H. Park, D.-Y. Kim, T.-H. Lee, A study on the characteristics of the diffusion layer thickness and porosity of the PEMFC, *J. Power Sources* 131 (2004) 200-206.
- [3] W. Chen, F. Jiang, Impact of PTFE content and distribution on liquid–gas flow in PEMFC carbon paper gas distribution layer: 3D lattice Boltzmann simulations, *Int. J. Hydro. Energ.* 41 (2016) 8550-8562.
- [4] C. M. Hwang, M. Ishida, H. Ito, T. Maeda, A. Nakano, Y. Hasegawa, N. Yokoi, A. Kato, T. Yoshida, Influence of properties of gas diffusion layers on the performance of polymer electrolyte-based unitized reversible fuel cells, *Int. J. Hydro. Energ.* 36 (2011) 1740-1753.
- [5] C.-M. Hwang, M. Ishida, H. Ito, T. Maeda, A. Nakano, A. Kato, T. Yoshida, Effect of PTFE contents in the gas diffusion layers of polymer electrolyte-based unitized reversible fuel cells, *J. Int. Counc. Electr. Eng.* 2 (2012) 171-177.

- [6] T. Ioroi, T. Oku, K. Yasuda, N. Kumagai, Y. Miyazaki, Influence of PTFE coating on gas diffusion backing for unitized regenerative polymer electrolyte fuel cells, *J. Power Sources* 124 (2003) 385-389.
- [7] C. M. Hwang, M. Ishida, H. Ito, T. Maeda, A. Nakano, A. Kato, T. Yoshida, Effect of titanium powder loading in gas diffusion layer of a polymer electrolyte unitized reversible fuel cell, *J. Power Sources* 202 (2012) 108-113.
- [8] S. Choe, B.-S. Lee, M. K. Cho, H.-J. Kim, D. Henkensmeier, S. J. Yoo, J. Y. Kim, S. Y. Lee, H. S. Park, J. H. Jang, Electrodeposited IrO<sub>2</sub>/Ti electrodes as durable and cost-effective anodes in high-temperature polymer-membrane-electrolyte water electrolyzers, *Appl. Catal. B* 226 (2018) 289-294.
- [9] T. Hottinen, M. Mikkola, T. Mennola, P. Lund, Titanium sinter as gas diffusion backing in PEMFC, *J. Power Sources* 118 (2003) 183-188.
- [10] B.-S. Lee, S. H. Ahn, H.-Y. Park, I. Choi, S. J. Yoo, H.-J. Kim, D. Henkensmeier, J. Y. Kim, S. Park, S. W. Nam, K.-Y. Lee, J.H. Jang, Development of electrodeposited IrO<sub>2</sub> electrodes as anodes in polymer electrolyte membrane water electrolysis, *Appl. Catal. B* 179 (2015) 285-291.
- [11] B.-S. Lee, H.-Y. Park, M. K. Cho, J. W. Jung, H.-J. Kim, D. Henkensmeier, S. J. Yoo, J. Y. Kim, S. Park, K.-Y. Lee, J. H. Jang, Development of porous Pt/IrO<sub>2</sub>/carbon paper electrocatalysts with enhanced mass transport as oxygen electrodes in unitized regenerative fuel cells, *Electrochem. Commun.* 64 (2016) 14-17.
- [12] S. A. Grigoriev, P. Millet, V. I. Porembsky, V. N. Fateev, Development and preliminary testing of a unitized regenerative fuel cell based on PEM technology, *Int. J. Hydro. Energ.* 36 (2011) 4164-4168.
- [13] S. Zhang, X.-Z. Yuan, J. N. C. Hin, H. Wang, K. A. Friedrich, M. Schulze, A

- review of platinum-based catalyst layer degradation in proton exchange membrane fuel cells, *J. Power Sources* 194 (2009) 588-600.
- [14] P. Zhang, S.-Y. Huang, B.N. Popov, Mesoporous tin oxide as an oxidation-resistant catalyst support for proton exchange membrane fuel cells, *J. Electrochem. Soc.* 157 (2010) B1163-B1172.
- [15] D. Kunwar, S. Zhou, A. DeLaRiva, E. J. Peterson, H. Xiong, X. I. Pereira-Hernández, S. C. Purdy, R. ter Veen, H.H. Brongersma, J. T. Miller, H. Hashiguchi, L. Kovarik, S. Lin, H. Guo, Y. Wang, A. K. Datye, Stabilizing high metal loadings of thermally stable platinum single atoms on an industrial catalyst support, *ACS Catal.* 9 (2019) 3978-3990.
- [16] J. Miyake, M. Kusakabe, A. Tsutsumida, K. Miyatake, Remarkable reinforcement effect in sulfonated aromatic polymers as fuel cell membrane, *ACS Appl. Energ. Mater.* 1 (2018) 1233-1238.
- [17] S. Giancola, M. Zatoń, Á. Reyes-Carmona, M. Dupont, A. Donnadio, S. Cavaliere, J. Rozière, D.J. Jones, Composite short side chain PFSA membranes for PEM water electrolysis, *J. Membr. Sci.* 570-571 (2019) 69-76.
- [18] U. Wittstadt, E. Wagner, T. Jungmann, Membrane electrode assemblies for unitised regenerative polymer electrolyte fuel cells, *J. Power Sources* 145 (2005) 555-562.
- [19] G. Chen, H. Zhang, H. Zhong, H. Ma, Gas diffusion layer with titanium carbide for a unitized regenerative fuel cell, *Electrochim. Acta* 55 (2010) 8801-8807.
- [20] P. Millet, R. Ngameni, S. A. Grigoriev, V.N. Fateev, Scientific and engineering issues related to PEM technology: Water electrolyzers, fuel cells and unitized regenerative systems, *Int. J. Hydro. Energ.* 36 (2011) 4156-4163.
- [21] J. C. Cruz, V. Baglio, S. Siracusano, R. Ornelas, L. G. Arriaga, V. Antonucci, A.

- S. Aricò, Nanosized Pt/IrO<sub>2</sub> electrocatalyst prepared by modified polyol method for application as dual function oxygen electrode in unitized regenerative fuel cells, *Int. J. Hydro. Energ.* 37 (2012) 5508-5517.
- [22] S. Choe, B.-S. Lee, J. H. Jang, Effects of diffusion Layer (DL) and ORR catalyst (MORR) on the performance of MORR/IrO<sub>2</sub>/DL electrodes for PEM-type unitized regenerative fuel cells, *J. Electrochem. Sci. Technol.* 8 (2017) 7-14.
- [23] J. X. Liu, H. Guo, X. M. Yuan, F. Ye, C. F. Ma, Experimental investigation on two-phase flow in a unitized regenerative fuel cell during mode switching from water electrolyzer to fuel cell, *Int. J. Energ. Res.* 42 (2018) 2823-2834.

# Chapter 4. Scanning Electrochemical

## Microscopy (SECM)

### 4.1. Introduction

Scanning electrochemical microscopy (SECM) is a technique which measures local electrochemical behavior using an ultramicroelectrode (UME) in liquid solution. UMEs are working electrodes which have smaller size than the diffusion layer in the experiment, e.g. less than 25  $\mu\text{m}$  enclosed by glass, developed in early 1980s [1]. UMEs reveal different phenomena from that of conventional disk electrodes [2]; i) reaching steady-state very rapidly, e.g. 10  $\mu\text{m}$  electrodes exhibited 1000,000 times faster than 1 cm electrodes, ii) high steady-state current density, which is inversely proportional to the size of electrode, with small overall current, iii) high ratio of faradic current to capacitive current at low scan rate due to high ratio of diffusion layer volume to the UME surface area and iv) availability of scan rate up to  $10^6$  V/s due to significantly decreased current and insignificant IR effect on the UME. As diameter of the UME decreases, transport rate of electroactive species to the UME increases as fast or even faster than charge transfer rate, which makes possible to analyze kinetics in electrochemical reactions.

The SECM is a four electrodes system consisting of the UME tip connected to a 3D piezo positioner and a substrate as working electrodes, a counter electrode and a reference electrode in solution. The electrochemical reactions in the SECM is

controlled by a bipotentiostat (Figure 4.1). A 3D piezo positioner controls the position of the tip and sends 3D location data of the UME tip to the computer. The initial introduction of the SECM technique was done by Allen. J. Bard (a professor in the University of Texas at Austin) in 1989 [3]. From the distinguished characteristics of the UME, the SECM can provide the information of surface topography, electrochemical kinetics, surface property such as electrical conductivity, distribution of reactive sites, etc., based on feedback modes and generation/collection modes [4]. Thus, there are lots of application fields for SECM, e.g. analysis of metals, polymers, biomolecules, catalyst, enzymes, living cells, corrosion mechanisms, battery, solar cells, etc [5]. The detail explanation of fundamentals on each analysis mode is discussed based on the basic experiments using ferricyanide and ferrocyanide redox couples, first. Then, application of analysis of surface electrical property and geometry of Ti PTLs, and the study of effect of the polymer patterned PTL on O<sub>2</sub> emission through the backside of the PTLs using SECM are discussed.

## **4.2. Experimental Section**

### **4.2.1. Basic Experiments**

In basic experiments, solution composed of 5 mM of Potassium ferricyanide (III) ( $\text{K}_3\text{Fe}(\text{CN})_6$ , 99 %, Sigma-Aldrich), 5 mM potassium hexacyanoferrate (II) trihydrate ( $\text{K}_4\text{Fe}(\text{CN})_6 \cdot 3\text{H}_2\text{O}$ ,  $\geq 99.95$  %, Sigma-Aldrich) and 1 M potassium chloride ( $\text{KCl}$ ,  $\geq 99$  %, Sigma-Aldrich) in deionized water was prepared to observe the characteristics of UMEs in SECM. The UMEs (25 m Pt SECM probes, BioLogic)

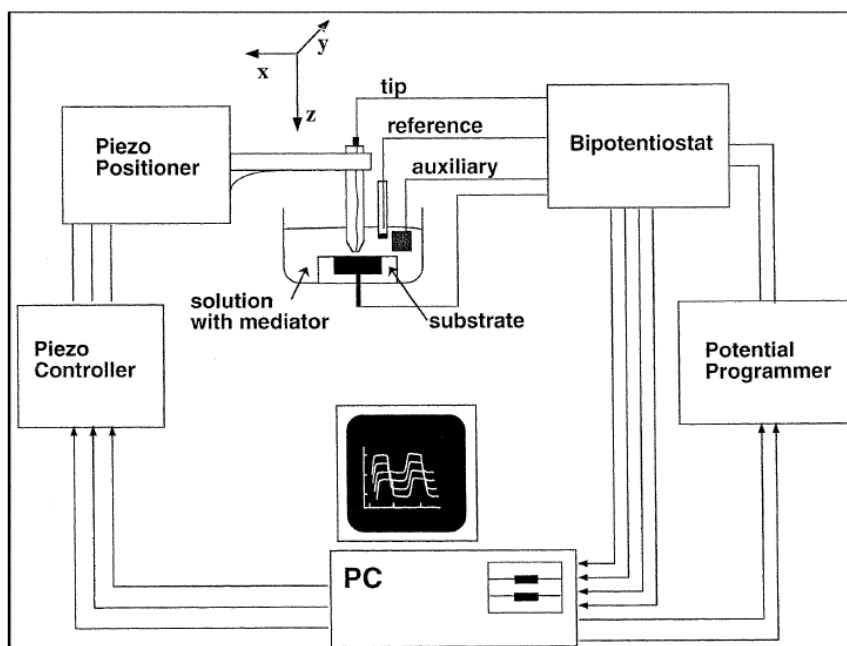


**Figure 4.1.** Structure illustration of the SECM. (Adapted from P. Sun et al., *Phys.*

*Chem. Chem. Phys.* 9 (2007) 802-823.)

were purchased and polished before tests. The diameter of the tip and the RG ratio (ratio of radius of the Pt tip to radius of the glass insulating sheath) were observed by the optical microscope (HMSZMN45T-MST1, SUNNY). SECM experiments were implemented using the modular instrument for SECM (M470, BioLogic) combined with the Potentiostat (SP-300, BioLogic). The Pt and Ag/AgCl electrode were used as the counter and the reference electrode, respectively.

#### **4.2.2. Preparation of Ti Porous Transport Layer Substrate (PTL) in SECM**

To analyze topography of the Ti PTL, same solution and electrodes were utilized with basic experiments, but 0.5 M sodium persulfate ( $\text{Na}_2\text{SO}_4$ ,  $\geq 99.0\%$ , Sigma-Aldrich) in deionized water was used for OER-ORR experiments due to prevention of  $\text{Cl}_2$  generation instead of  $\text{O}_2$  generation in KCl solution. To prepare the Ti PTL substrate in SECM, iridium oxide electrodeposited electrodes with and without polymer bush patterning (detail preparation methods of electrodes are described in chapter 3) were electrically connected with copper wires by silver paste and the conductive exposed region except for the electrode was sealed with epoxy to block any chemical reactions. Then, the Kapton tape was attached to prepared substrate except for the region of active area for the experiment. Since the Ti PTL has the randomly porous structure, it is hard to define the distance between the tip of and the Ti PTL using approach curves. Instead, approach curves were done on the Kapton tape attached on the electrodes to know the distance between the substrate and the tip,  $d$ , of the UME. Then the tip was horizontally moved to the active area region of the electrode and lowered  $73\ \mu\text{m}$  vertically since the thickness of Kapton tape is

about 73  $\mu\text{m}$ . The detail explanation of experiments and results will be discussed in results and discussion.

## 4.3. Results and Discussion

### 4.3.1. Basic Experiments

First, cyclic voltammetry in  $[\text{Fe}(\text{CN})_6]^{4-}/[\text{Fe}(\text{CN})_6]^{3-}$  reversible redox couple is observed. If the electrochemical reaction is fast enough, the current is determined by the rate of reactant diffusion to the electrode. Since redox reaction of ferricyanide and ferrocyanide solution is a simple and fast one order electron transfer reaction which is highly reversible, the current is determined by diffusion of reactant in this redox reaction, generally. In the conventional disk electrode, the size of electrode is much larger than the thickness of diffusion layer which is from 1  $\mu\text{m}$  to 100  $\mu\text{m}$ . In this case, linear diffusion of reactants to the electrode surface is dominant. However, if the size of the electrode is smaller than the thickness of diffusion layer such as the case of the UME, spherical diffusion is dominant as time goes by due to extremely small reactive area. Since spherical diffusion to the UME has higher flux of reactant per unit area than that of planer diffusion to the conventional electrode, absolute current density of the UME shows higher value than that of the conventional disk electrode, e.g.  $-0.19 \text{ mA cm}^{-2}$  (Disk electrode) and  $-4.2 \text{ mA cm}^{-2}$  (UME) at  $-0.25 \text{ V}_{\text{Ag}/\text{AgCl}}$  ( $5 \text{ mV s}^{-1}$ ) (Figure 4.2). The current on the planer electrode is expressed by following equation from this phenomena (4-1).

$$i_d = \frac{nFAD_o^{1/2}C_o^*}{\sqrt{\pi t}} + \frac{nFAD_oC_o^*}{r} \quad (4-1)$$

The first part of the equation describes linear diffusion, which is called the Cottrell

equation. When the size of electrode is large enough, e.g. larger than 1 mm, the value of the second part goes to zero and the first part of the equation becomes dominant. The peak current follows the Cottrell equation which is inversely proportional to  $t^{1/2}$ , i.e. proportional to (scan rate)<sup>1/2</sup>, due to limitation of diffusion rate of reactants to the electrode surface. Thus, the peak currents in CVs increase as scan rates increase as shown in Figure 4.2(a). In addition, each CV has a duck shape due to decrease of current after the peak current as time goes on in the disk electrode (Figure 4.2(a)). Unlike the conventional disk electrode, the second part of the equation (4-1), which describes spherical diffusion, becomes dominant due to the extremely small radius of the UME, less than 50  $\mu\text{m}$ . As the scan rate increases, the current value of the Cottrell equation increases but not significantly affect to the total current until 100  $\text{mV s}^{-1}$  due to the high value of the current from the second part of the equation (Figure 4.2(b)). Thus, the scan rate has almost no influence on the CV of the UME. It reveals the steady state current instead of the duck shape CV in the disk electrode. From this steady state current, the diffusion rate of reactants can be calculated by the UME without knowing the time value, i.e. without controlling various scan rate, if the size of the UME and the bulk concentration of reactants are known.

The basic experiments were done with the substrate composed of gold (conductor) in the middle surround by Teflon (insulator) (Figure 4.3(a)). The schematic illustration of the experiment condition is shown in Figure 4.3(b). The 25  $\mu\text{m}$  Pt UME approaches to the substrate to  $-z$  direction until the  $d$  reaches within 200  $\mu\text{m}$  and the motion of the approach of the tip is monitored by the video microscope to prevent crushing of the UME to the substrate. Then, the change of the current was recorded as the UME becomes close to the substrate, which is called 'approach curve', in the 5 mM  $[\text{Fe}(\text{CN})_6]^{4-}/[\text{Fe}(\text{CN})_6]^{3-}$  solution. Approach curves are observed

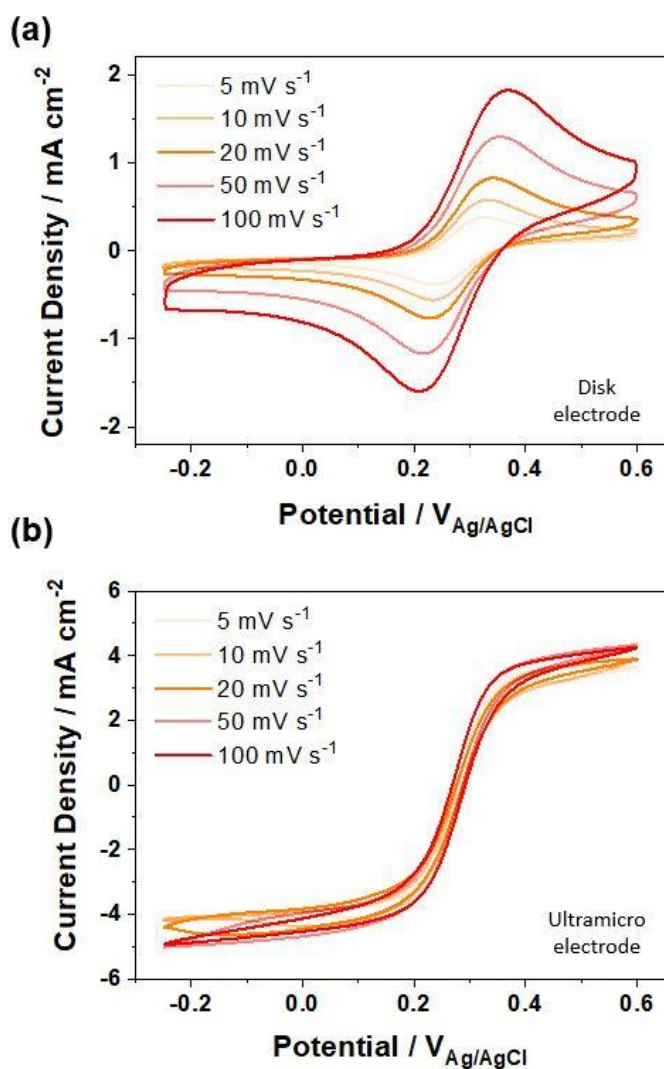


**Figure 4.2.** Cyclic voltammetry of (a) 5 mm glassy carbon disk electrode and (b) 25 μm ultramicroelectrode (UME) in ferricyanide/ferrocyanide redox couple solution through the scan rate from 5 mV s<sup>-1</sup> to 100 mV s<sup>-1</sup>.

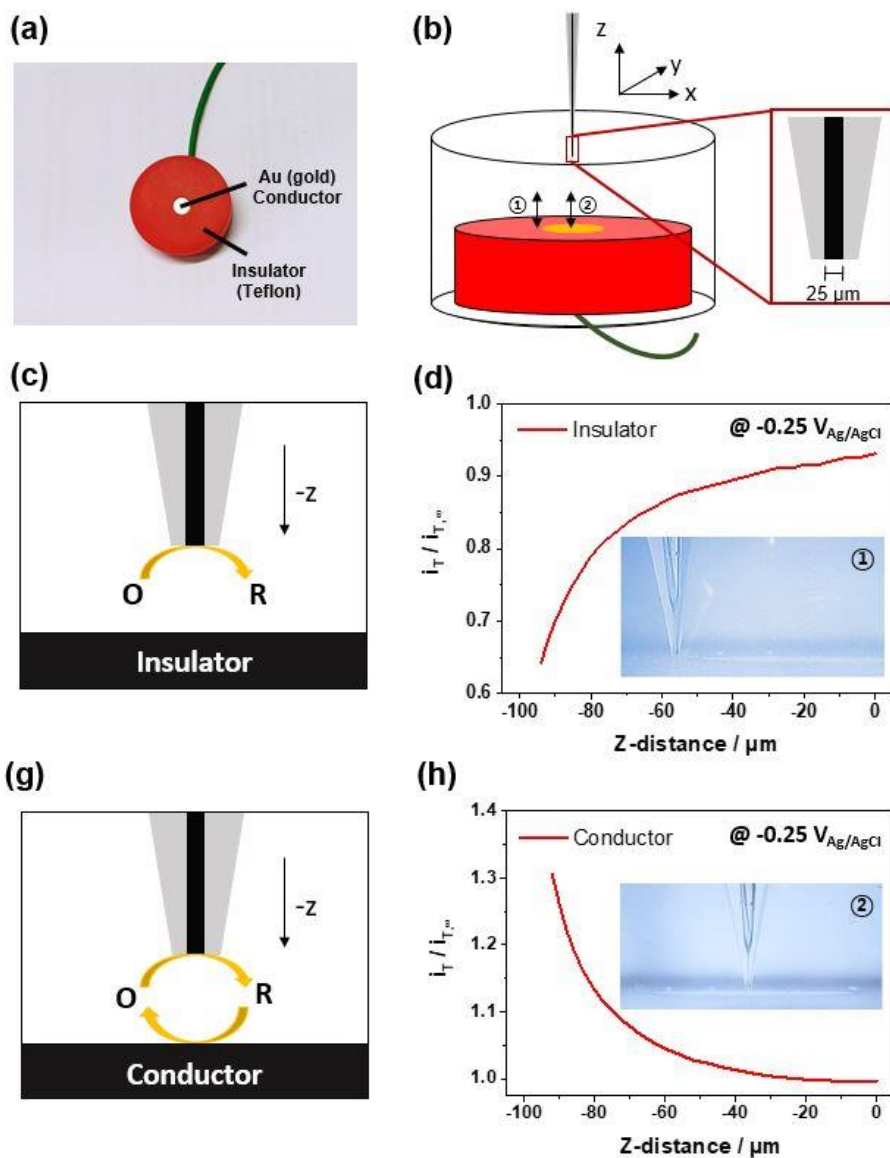


**Figure 4.3.** Setting of basic experiments including feedback modes. (a) The photo of the substrate and (b) the schematic diagram of the test system with the UME in SECM used in basic experiments. (c) The schematic illustration of a negative feedback mode of the UME on insulator. (d) Decrease of the tip current as approach of the UME tip to the insulating substrate. (g) The schematic illustration of a positive feedback mode of the UME on conductor. (h) Increase of the tip current as approach of the UME tip to the conductive substrate.

in two points, i.e. on the insulating substrate (Teflon) and on the conductive substrate (gold). The applied potential on the tip was  $-0.25 \text{ V}_{\text{Ag}/\text{AgCl}}$ , which is reduction of  $[\text{Fe}(\text{CN})_6]^{3-}$  (Oxidized form (III), O) to  $[\text{Fe}(\text{CN})_6]^{4-}$  (Reduced form (II), R) is occurred ( $\text{O} + \text{e}^- \rightarrow \text{R}$ ). When, the UME approaches to the substrate, two different tendencies of approach curves are observed depending on the electrical property of the substrate, called feedback modes. First, if the substrate has an insulating property, reactants (R) are diffused to the UME, but this insulating substrate blocks the diffusion of R, results in decrease of reductive current in the UME when the  $d$  decreases, which is called ‘negative feedback’ (Figure 4.3(c), 4.3(d)). Here, the  $i_{\text{T}}/i_{\text{T},\infty}$  indicates the tip current divided by the tip current at infinite distance, i.e. steady state current at  $d = \infty$ . Figure 4.3(d) reveals decrease of  $i_{\text{T}}/i_{\text{T},\infty}$  when the UME approaches to the Teflon insulating substrate. The inserted image is from the video microscope during measuring of the approach curve on the Teflon insulating substrate (① in Figure 4.3(b)). Second,  $i_{\text{T}}/i_{\text{T},\infty}$  increases as  $d$  decreases on the conductive substrate, called ‘positive feedback’ (Figure 4.3(g), 4.3(h)). During the reductive reaction on the tip, the concentration of R increases and the concentration of O decreases near the tip. Then, the local electrochemical formal potential near the tip decreases from the Nernst equation (4-2).

$$E = E^\circ + \frac{RT}{nF} \ln \frac{C_{\text{O}}}{C_{\text{R}}} \quad (4-2)$$

As the tip close to the conductive substrate, the local fermi level of the solution compared to equilibrium potential of the conductive substrate near the tip becomes strongly negative ( $E - E^\circ \ll 0$ ) since  $C_{\text{O}}$  goes to zero. In other words, the local potential of the conductive substrate becomes much positive compared to fermi level

of the solution. Then, the oxidative reaction ( $R \rightarrow O + e^-$ ) tends to occur spontaneously at the conductive surface near the tip. Circulation of the reductive reaction on the tip and the oxidative reaction on the substrate becomes highly active as decrease of  $d$ , results in positive feedback on the conductive substrate (Figure 4.3(g)). Here, an increase of  $i_T/i_{T,\infty}$  is observed as the UME approaches to the gold conductive substrate (Figure 4.3(h)).

When the UME is used in SECM, the radius-ratio of the tip to the insulating sheath (RG ratio) is important. Usually, the RG ratio is less than 10. If the RG ratio is too high, slight slope of the tip can result in crushing of the UME during approach of the tip to the substrate although  $d$  is not zero from approach curve due to contact of the insulating sheath to the substrate. In addition, collision of the UME can occur during scanning if the substrate is not levelled. Thus, before the start of the line or area scan in SECM, leveling is required to maintain same  $d$  in all spots during scan. Figure 4.4 (a) portrays the leveling process for the flat substrate in SECM. There are three leveling screws in the SECM device below the substrate. First, three positions on the substrate, e.g. P1 (-750, 0, z), P2 (1500, 1299, z), P3 (1500, -1299, z), are designated. Second, approach curves on three positions are measured (Figure 4.4(b)). From the approach curves, the leveling state of the substrate can be apprehended. For example, the  $d$  is  $P1 < P3 < P2$  from the approach curves in Figure 4.4(b). From the data, leveling is achieved by lowering P1, P3 or elevating P2, P3 properly using leveling screws. After leveling, all points (P1, P2, P3) show similar approach curves with deviation less than 1  $\mu\text{m}$  (Figure 4.4(c)).

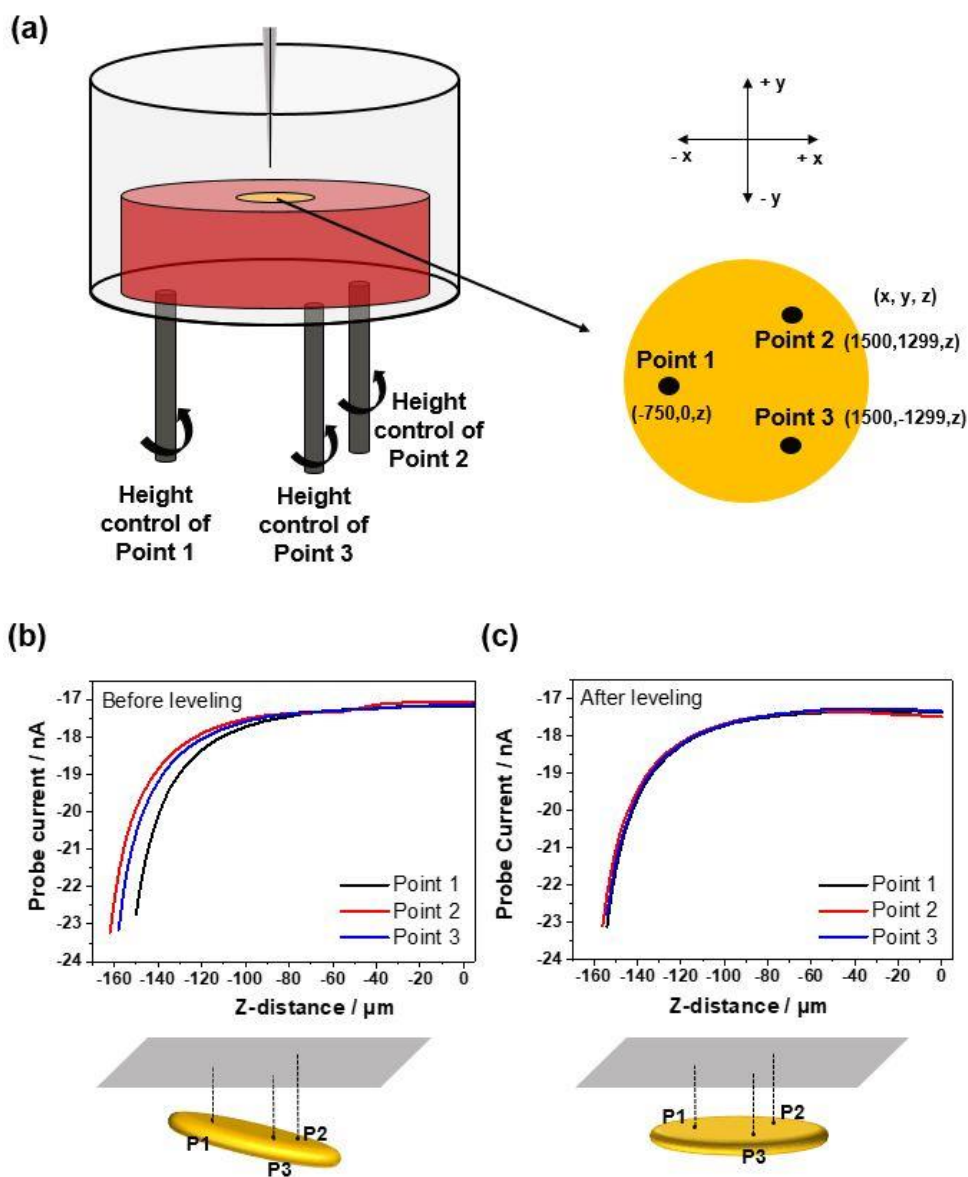


**Figure 4.4.** Leveling of the substrate in ferricyanide/ferrocyanide redox couple solution with approach curves. (a) Schematic method of leveling by controlling the height of the substrate. Approach curves at three points (UNE tip:  $-0.25 V_{\text{Ag}/\text{AgCl}}$ ) (b) before and (c) after leveling.

### 4.3.2. Analysis of Ti Porous Transport Layers (PTLs)

The Ti-felt PTL consisting of 20  $\mu\text{m}$  diameter Ti fibers is one of the materials used as the electrode in PEMWEs and UR-PEMFCs. Since the PTL takes a role of passageway of reactants and products which has the gas or liquid phase, it has the highly porous structure as shown in the example of the SEM image (Figure 4.5). Since the diameter of the UME tip is about 25  $\mu\text{m}$ , the ratio of the radius of Ti fibers to that of the Pt UME tip ( $h$  ratio) is less than 1. When the  $h$  ratio is less than 2.5, approach curves are different from the case of infinite substrates [6]. Additionally, the significant deviation of the approach curves through the  $h$  ratio is observed if  $h$  value is less than 1 (Figure 4.6). Thus, the approach curve of the UME to the Ti PTL does not follow general approach curves in the case of the infinite substrate even though the Ti PTL itself can be assumed almost infinite to the UME tip. Therefore,  $d$  was determined by approach curve on the flat Kapton tape (insulator,  $\sim 73$   $\mu\text{m}$  thickness) attached on the Ti PTL instead of directly on the porous Ti PTL. Leveling of the substrate was done on the Kapton tape first, and then the tip was moved to the Ti PTL region horizontally and moved down 73  $\mu\text{m}$  before the line or area scan in the SECM (Figure 4.5).

There are theoretical approach curves depending on RG values in the case of the conductive or insulating substrate [4]. Some examples of theoretical approach curves are shown in Figure 4.7(a). Before the SECM, the RG ratio of the UME is measured by the optical microscope and  $d$  is determined from fitting of approach curves (Figure 4.7(b)). For example, if 8.13 of RG ratio and 12.5  $\mu\text{m}$  of the tip radius on insulating substrate,  $d/a$  is 1.28 at 60 % ( $i_T/i_{T,\infty} = 0.6$ ) approach, i.e.  $d = 1.28 \times 12.5 =$

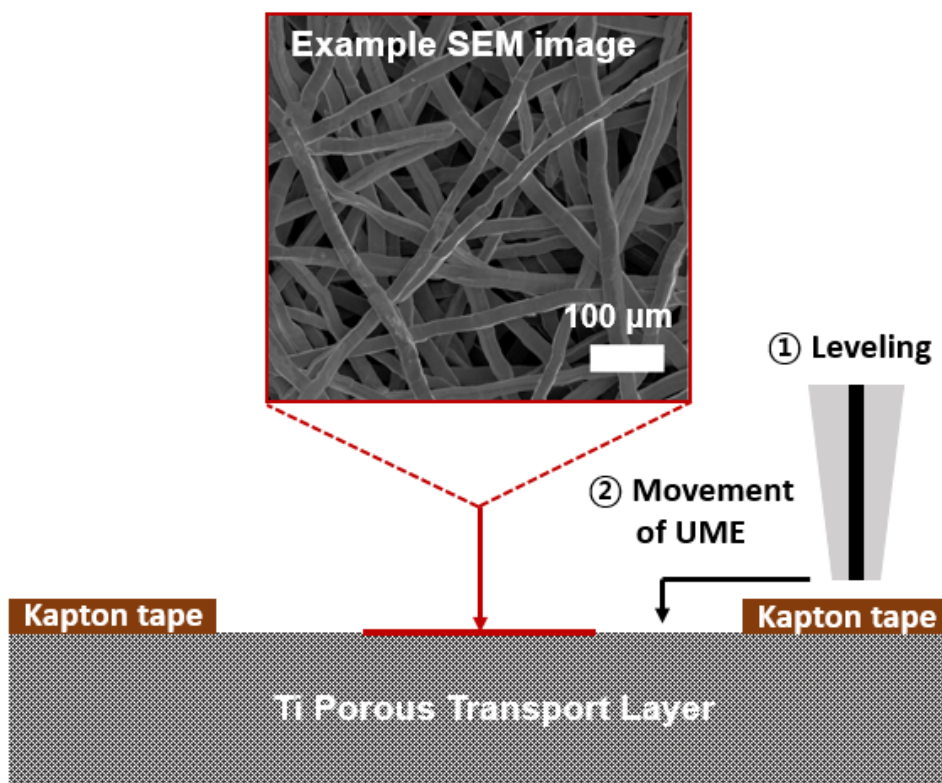


**Figure 4.5.** Schematic diagram of setting of Ti substrates for line mapping, area mapping, etc. in SECM. Inserted SEM image is the Ti porous transport layer used in the experiments.

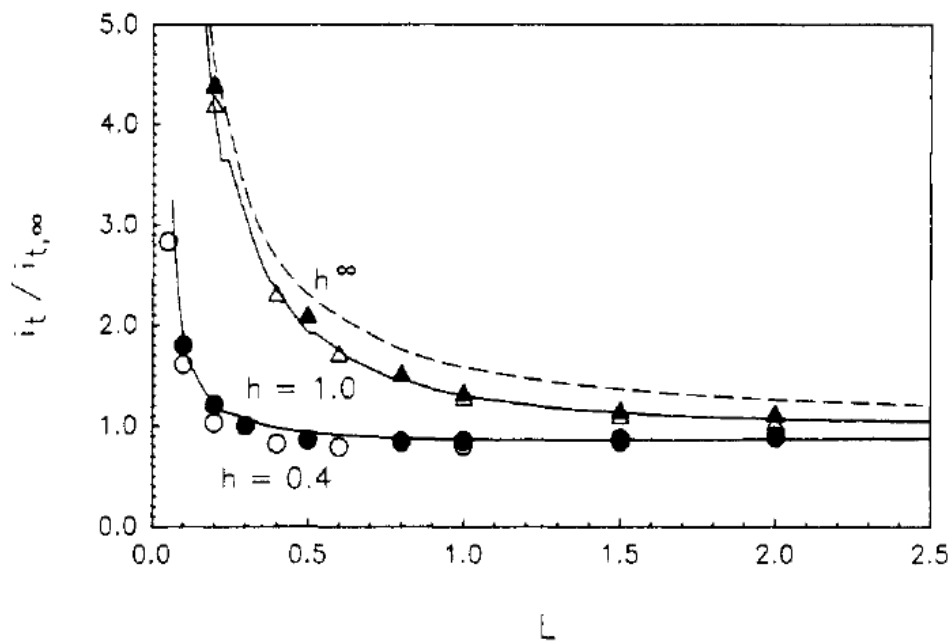


**Figure 4.6.** Experimental and simulated approach curves.  $h$  is the ratio of radius of substrate to that of UME tip. ( $L=d/a$ ,  $d$ : distance between the tip and the substrate,  $a$ : radius of the UME tip). (Adapted from A. Bard et al., *J. Phys. Chem.* 96 (1992) 1861-1868.)

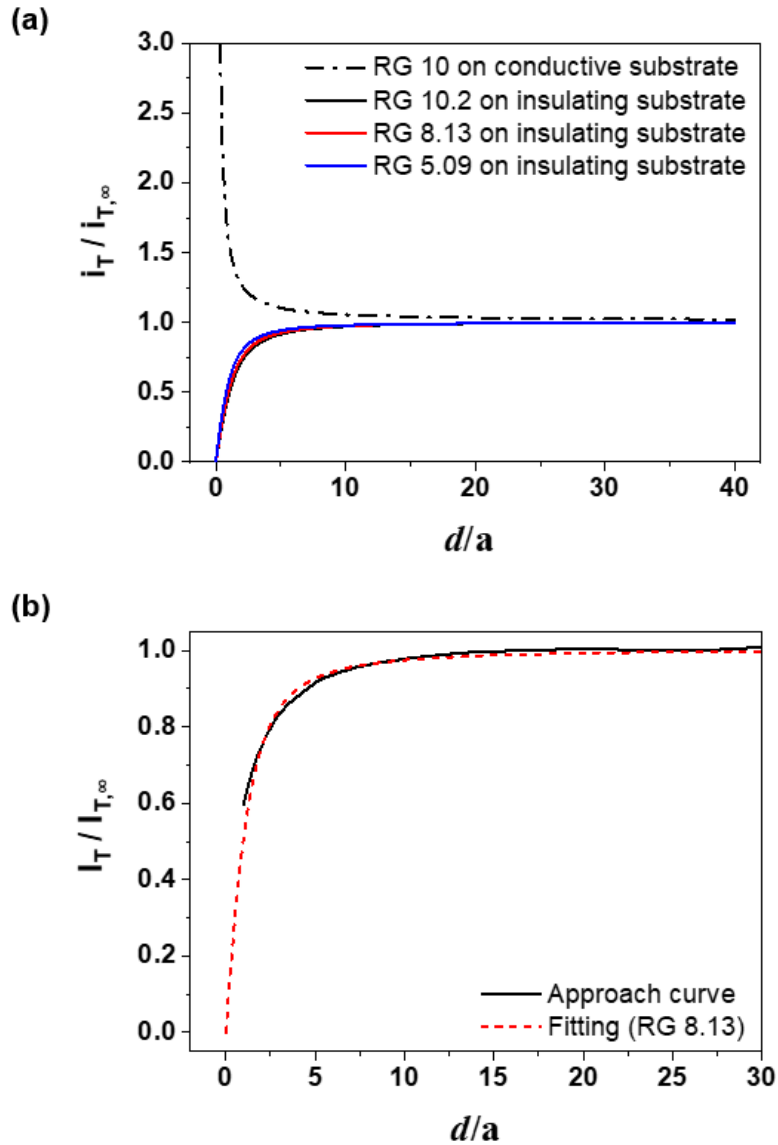


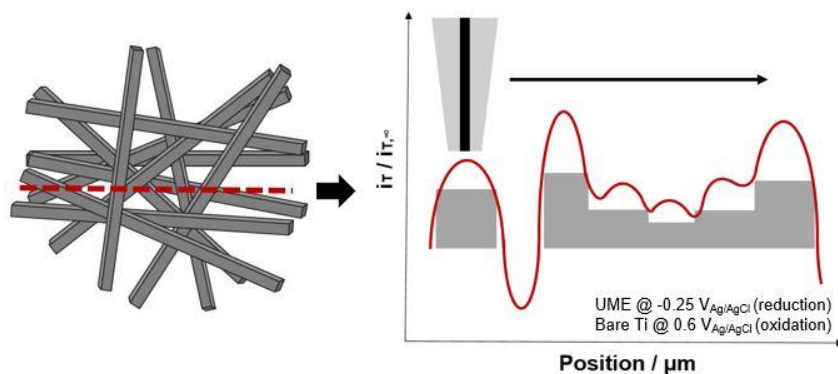
**Figure 4.7.** (a) Theoretical approach curves on the conductive substrate and the insulating substrate for some RG values, e.g. 10, 8, 5. The theoretical values are obtained from ref. [4]. (b) The example of fitting of the approach curve on the Kapton tape (the insulating substrate).

16.0  $\mu\text{m}$ ,

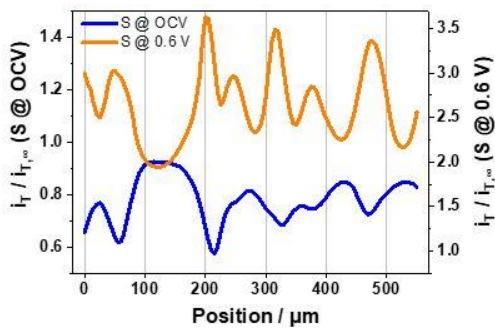
From characteristics of UMEs in SECM described previously, properties of the Ti PTL can be analyzed, e.g. the surface electrical property and geometry, etc. Here, line scans on the Ti PTL were done with  $d=17\ \mu\text{m}$ , at which reveals the feedback mode. When the negative potential, e.g.  $-0.25\ \text{V}_{\text{Ag}/\text{AgCl}}$ , is applied to the UME and the positive potential, e.g.  $0.6\ \text{V}_{\text{Ag}/\text{AgCl}}$ , is applied to the Ti PTL, the UME reveals the positive feedback on the Ti substrate. Thus,  $i_{\text{T}}/i_{\text{T},\infty}$  decreases if the tip is on the pore region and  $i_{\text{T}}/i_{\text{T},\infty}$  increases if the tip is on the protruded Ti fiber. Fluctuation of the tip current from the change of  $d$  during the scan discloses surface geometry of the substrate (Figure 4.8(a)). When the line scan was done on the backside of the iridium oxide electrodeposited Ti PTL without applying potential (S@ OCV), it shows the negative feedback in contrast to the case of applying  $0.6\ \text{V}_{\text{Ag}/\text{AgCl}}$  (S@  $0.6\ \text{V}_{\text{Ag}/\text{AgCl}}$ ). Thus, the graphs of S@ OCV and S@  $0.6\ \text{V}_{\text{Ag}/\text{AgCl}}$  form the symmetrical shape (Figure 4.8(b)). From the line scan, not only the geometry, but also the surface electrical properties are ascertained. The surface property of the electrode is insulating without any applied potential, but applying potential changes its property to conductive. If polymer is coated on the backside of the Ti PTL, both S@ OCV and S@  $0.6\ \text{V}$  show the negative feedback, i.e. the insulating surface property (Figure 4.8(c)).

Area mapping of the Ti PTL ( $500\ \mu\text{m} \times 500\ \mu\text{m}$ ) was done in the positive feedback mode (Tip @  $-0.25\ \text{V}_{\text{Ag}/\text{AgCl}}$ , S@  $0.6\ \text{V}_{\text{Ag}/\text{AgCl}}$ ) at  $d=24.5\ \mu\text{m}$  (Figure 4.9). Fluctuation of the tip current compared to the steady-state current ( $i_{\text{T},\infty}$ ) due to change of  $d$  during scanning depicts the topography of the Ti PTL. For example, the

(a)



(b) Ti w/o surface polymer coating



(c) Ti w/ surface polymer coating

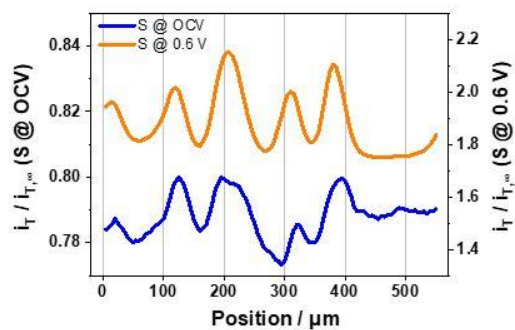


**Figure 4.8.** (a) Schematic example of line-mapping of Ti PTL using SECM in  $[\text{Fe}(\text{CN})_6]^{4-}/[\text{Fe}(\text{CN})_6]^{3-}$  redox couple solution. Line mapping of Ti PTL (b) without and (b) with surface polymer coating in two cases, i.e. Ti substrate at OCV and  $0.6 \text{ V}_{\text{Ag}/\text{AgCl}}$ .

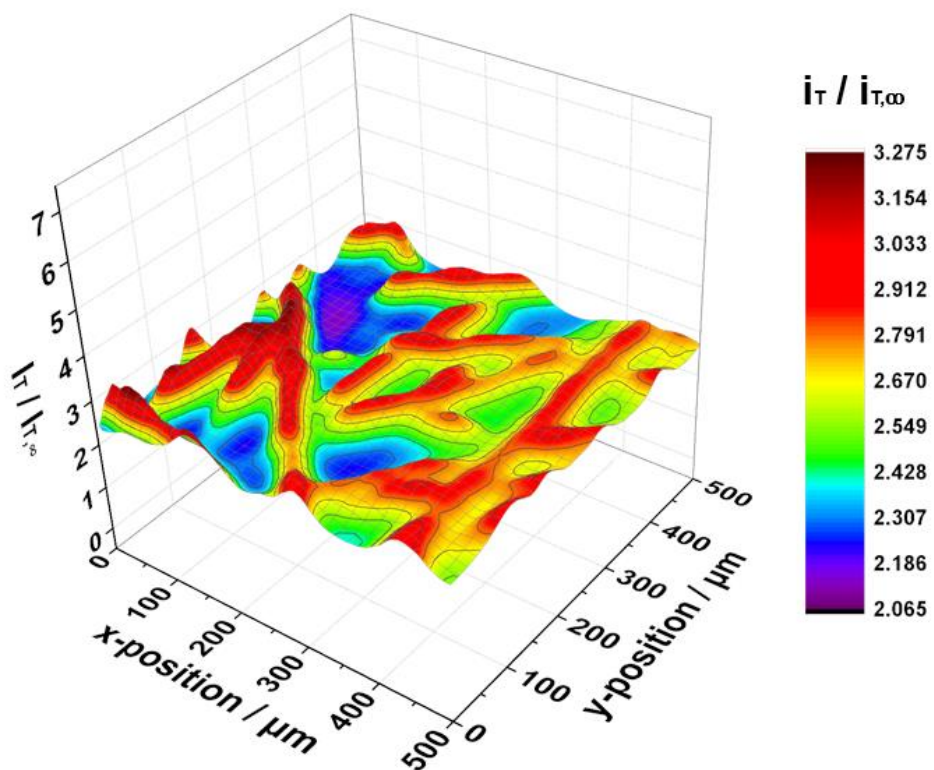


**Figure 4.9.** Area mapping of Ti porous transport layer without polymer coating (500  $\mu\text{m}$  x 500  $\mu\text{m}$ ) using SECM. (Pt tip:  $-0.25 V_{\text{Ag}/\text{AgCl}}$ , Ti substrate:  $0.6 V_{\text{Ag}/\text{AgCl}}$ )

thickness of red region ( $i_T/i_{T,\infty} > 2.9$ ) is about 20  $\mu\text{m}$ , which is the fiber diameter of the Ti PTL observed in the SEM. Here, mapping of the Ti PTL with 5  $\mu\text{m}$  resolution using the 29  $\mu\text{m}$  UME tip. From the ratio of the tip current density at the local point to substrate current density, it is possible to analyze electrochemical activity at local position. However, it is not appropriate in this case since the tip current reveals geometrical effect due to larger the tip diameter than the fiber diameter in this mapping, i.e.  $h$  ratio is less than 1 in this area mapping. If the tip size less than 5  $\mu\text{m}$  is used, comparison of local electrochemical reactions at certain positions on the Ti fiber is also possible. Fabrication of nanometer sized tips was developed and is commercialized state nowadays. From the advances in the SECM technique, mapping of the nanoparticle was also reported. For instance, Takahashi et al. studied  $\text{MoS}_2$  nanosheets as HER catalysts and visualized the active sites of catalysts with the mapping image by the SECM, i.e. the edge of  $\text{MoS}_2$  nanosheets shows the highest activity in HER [7].

### **4.3.3. Application on Polymer Patterned Ti PTL Research**

In PEMWE, absorption of water and emission of  $\text{O}_2$  occur through the Ti PTL. From the single cell tests, the generated  $\text{O}_2$  from water electrolysis in the cell can be measured, but local phenomena in the Ti PTL cannot be analyzed. Here,  $\text{O}_2$  emissions from the backside of the Ti PTL was analyzed using SECM (Figure 4.10(a)). Iridium oxide is electrodeposited as OER electrocatalysts throughout the Ti PTL but not on top of the backside of the Ti PTL, which means generation of  $\text{O}_2$  is occurred inside of the Ti PTL (detail description of distribution of iridium oxide electrocatalysts is explained in chapter 2).

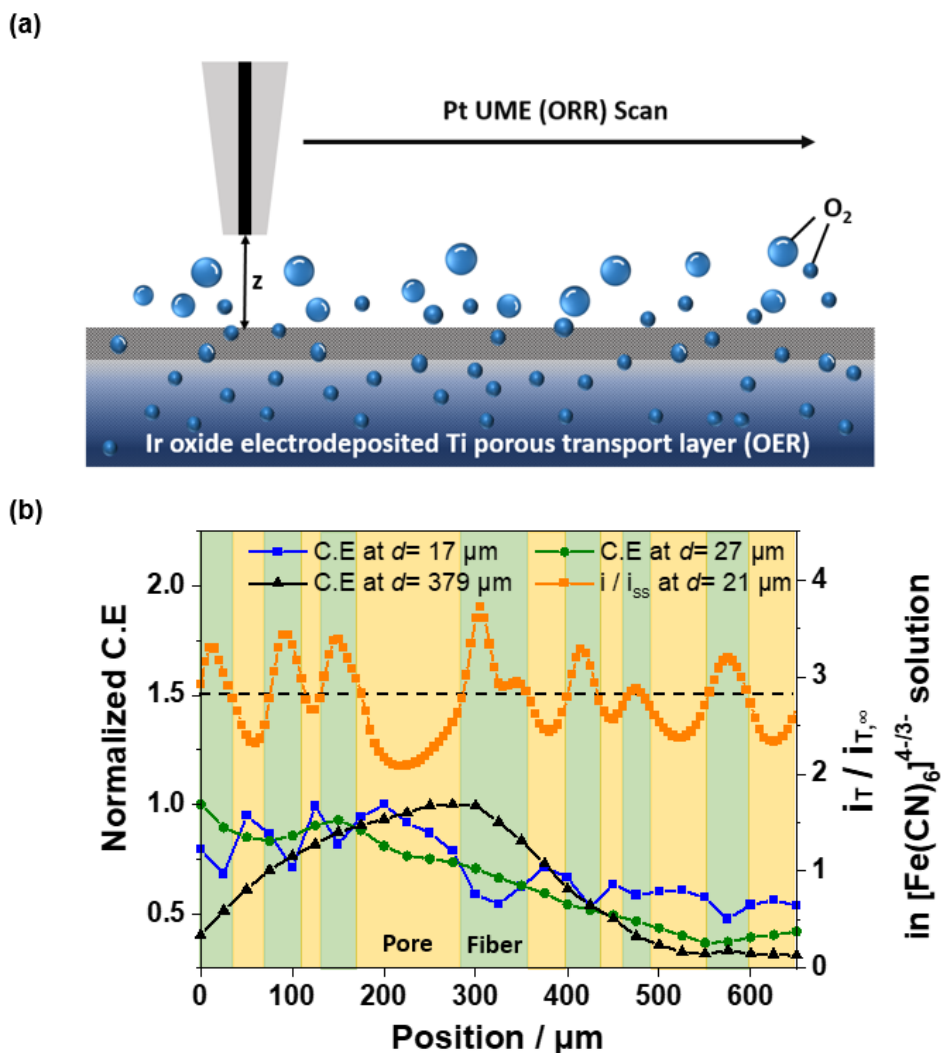


**Figure 4.10.** (a) Schematic illustration of line scan of the OER-ORR (SG-TC) mode of a UME on the back side of the iridium oxide electrodeposited Ti PTL without polymer coating. (b) Comparison of normalized collection efficiency (C.E) of line scans of the OER-ORR (SG-TC) mode on the back side of the iridium oxide electrodeposited Ti PTL through the distance of the UME tip on the substrate and  $i_T/i_{T,\infty}$  of the positive feedback mode in line scan using  $[\text{Fe}(\text{CN})_6]^{4-}/[\text{Fe}(\text{CN})_6]^{3-}$  redox solution. Potentials of the substrate and the tip were 1.15 and 0  $V_{\text{Ag}/\text{AgCl}}$  in the OER-ORR (SG-TC) mode and 0.6 and -0.25 0  $V_{\text{Ag}/\text{AgCl}}$  in the positive feedback mode.

The Ti substrate generates O<sub>2</sub> bubbles (OER@ 1.15 V<sub>Ag/AgCl</sub>) and the Pt UME tip detects O<sub>2</sub>, generated from the substrate, by ORR@ 0 V<sub>Ag/AgCl</sub>. This kind of operation in SECM is called substrate generation/tip collection (SG/TC) mode. When the tip is too close to the Ti PTL, ORR current on the tip is affected by surface geometry. For example, if the tip is too close to Ti fibers, e.g. distance within 20 μm, diffusion of O<sub>2</sub> bubbles to the tip is blocked by Ti fibers, which results in decrease of the ORR current. On the other hand, if the tip is above pores, ORR current increases compared to the case of above the Ti fiber. Collection efficiency is the percentage of ratio of detected amounts of electroactive species on the tip to that of electroactive species produced in the substrate. The geometry of a line scan range was analyzed using [Fe(CN)<sub>6</sub>]<sup>4-</sup>/[Fe(CN)<sub>6</sub>]<sup>3-</sup> redox couple at  $d= 21 \mu\text{m}$ , then it was compared with OER/ORR (SG/TC) operation through  $d$  (Figure 4.10(b)). Interestingly, fluctuation of normalized collection efficiency at  $d= 17 \mu\text{m}$  through the line scan exactly coincided with the geometry of the Ti PTL surface as expected, i.e. increase above pores and decrease above fibers. However, when the tip was far enough, e.g. at  $d= 27 \mu\text{m}$  and  $d= 379 \mu\text{m}$ , the ORR current was not affected by the surface geometry anymore.

In chapter 3, application of the polymer brush patterned Ti PTL on UR-PEMFC is reported for the creation of discrete pathways of gas and water to enhance mass transport during cell operation. To verify the effect of patterning, two approaches in SECM were done, line scan and points detection (Figure 4.11(a)). ORR signals become too weak and randomized due to diffusion if  $d$  is too long and ORR signals include the effect of Ti geometry if  $d$  is too short. Considering the results of  $d$  effect on the ORR signal above the Ti PTL previously, ORR current was measured at  $d= 32 \mu\text{m}$  (line scan) and  $30 \mu\text{m}$  (points detection) to analyze the effect of patterning

with minimizing the effect of the surface topography.

In line scan, the UME was moved from 0 to 500  $\mu\text{m}$  and detected and generated  $\text{O}_2$  through the position was calculated from the ORR current (Figure 4.11(b)). When the tip moves, the substrate keeps generating  $\text{O}_2$  bubbles, resulting the background ORR current from diffusion regardless of the effect of patterning, e.g. at least 50  $\text{pmol cm}^{-2} \text{s}^{-1}$  from Figure 4.11(b). Since it is hard to define the exact position of patterning, 125  $\mu\text{m}$  width of polymer brush pattern with 250  $\mu\text{m}$  period, the region of hydrophobic and hydrophilic sections was divided by designating the maximum point (116  $\text{pmol cm}^{-2} \text{s}^{-1}$  at 150  $\mu\text{m}$ ) and the minimum point (65.9  $\text{pmol cm}^{-2} \text{s}^{-1}$  at 275  $\mu\text{m}$ ) as the middle of the hydrophobic and hydrophilic area. Interestingly, the distance between two maximum points (at 150  $\mu\text{m}$  and 400  $\mu\text{m}$ ) and the minimum point (at 275  $\mu\text{m}$ ) in hydrophobic and hydrophilic region is exactly 125  $\mu\text{m}$ , which is the width of patterning. As time goes on, some of generated  $\text{O}_2$  bubbles in the Ti PTL can block the active sites, i.e. mass transport limitation, results in decrease of  $\text{O}_2$  generation during line scan from 0 to 500  $\mu\text{m}$ , i.e. generated  $\text{O}_2$  moles from 1.65 to 1.34  $\text{nmol cm}^{-2} \text{s}^{-1}$ . Thus, value of detected  $\text{O}_2$  moles itself has deviation, e.g. 90-110  $\text{pmol cm}^{-2} \text{s}^{-1}$  and 65-90  $\text{pmol cm}^{-2} \text{s}^{-1}$  in the 0-87.5  $\mu\text{m}$  and 212.5-275  $\mu\text{m}$  hydrophobic region, respectively. However, the change of detected  $\text{O}_2$  from the hypothetical boundary to the middle of each region shows increase of 15-20  $\text{pmol cm}^{-2} \text{s}^{-1}$  in hydrophobic regions and decrease of 15-20  $\text{pmol cm}^{-2} \text{s}^{-1}$  in hydrophilic regions.

In points detection,  $\text{O}_2$  detection from the tip was done for 70 seconds at fixed positions and  $\text{O}_2$  generation from the substrate was done for 10 seconds in the middle of  $\text{O}_2$  detection from the tip. Before starting the tests at each point, agitation of solution was done to remove residue of  $\text{O}_2$  bubbles in the Ti PTL from the previous

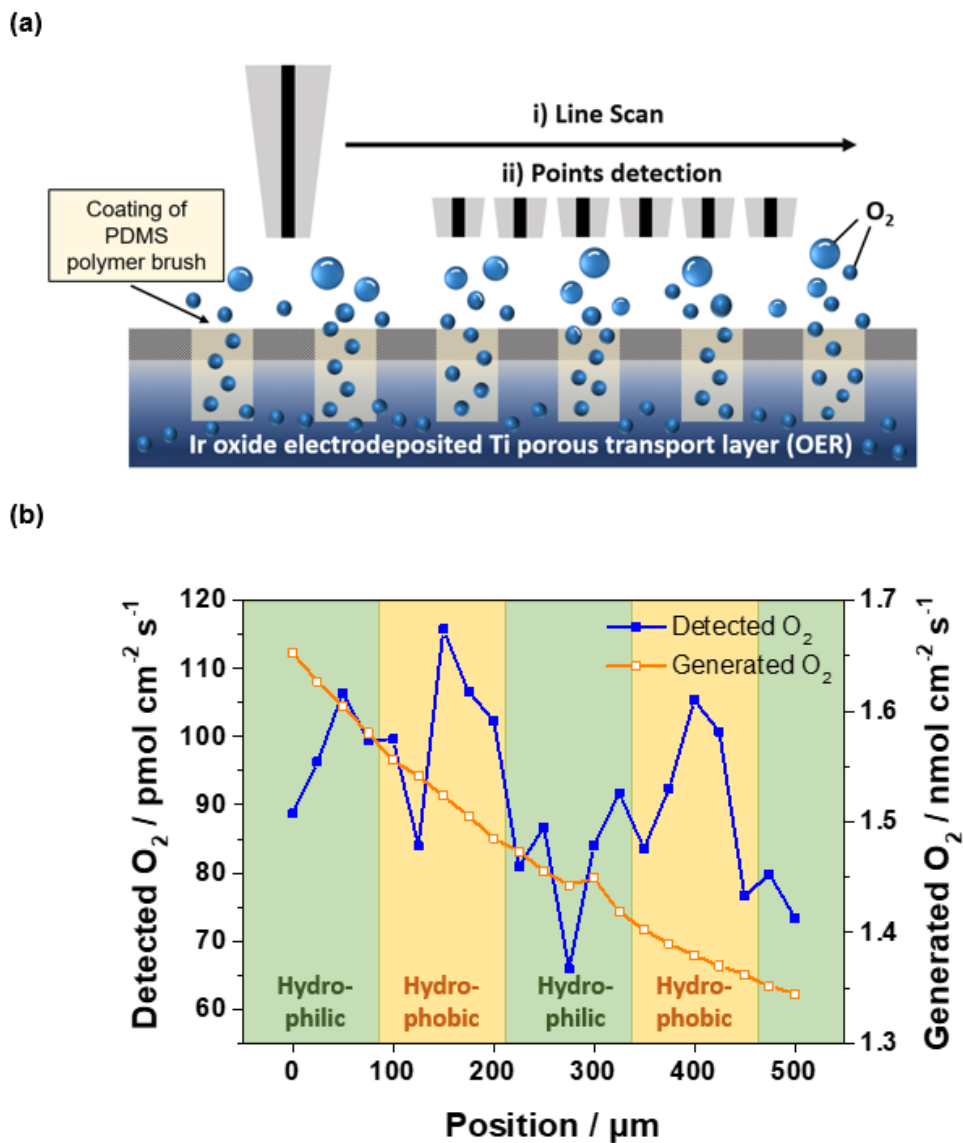
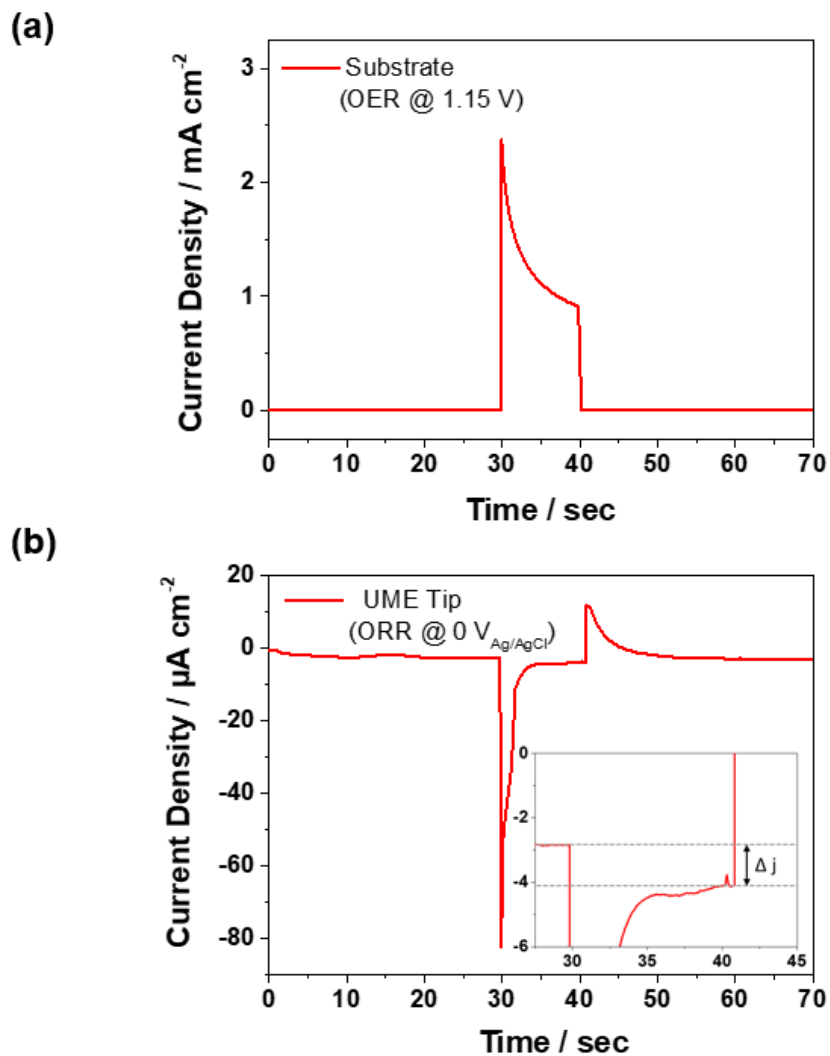


**Figure 4.11.** (a) Schematic illustration of line scan of the OER-ORR (SG-TC) mode of a UME on the back side of hydrophobic polymer patterned Ti PTL. (b) Generated  $\text{O}_2$  and detected  $\text{O}_2$  through line scan on the back side of the hydrophobic polymer patterned Ti PTL. Potentials of the substrate and the tip were  $1.15 V_{\text{Ag}/\text{AgCl}}$  and  $0 V_{\text{Ag}/\text{AgCl}}$  in the OER-ORR (SG-TC) mode.

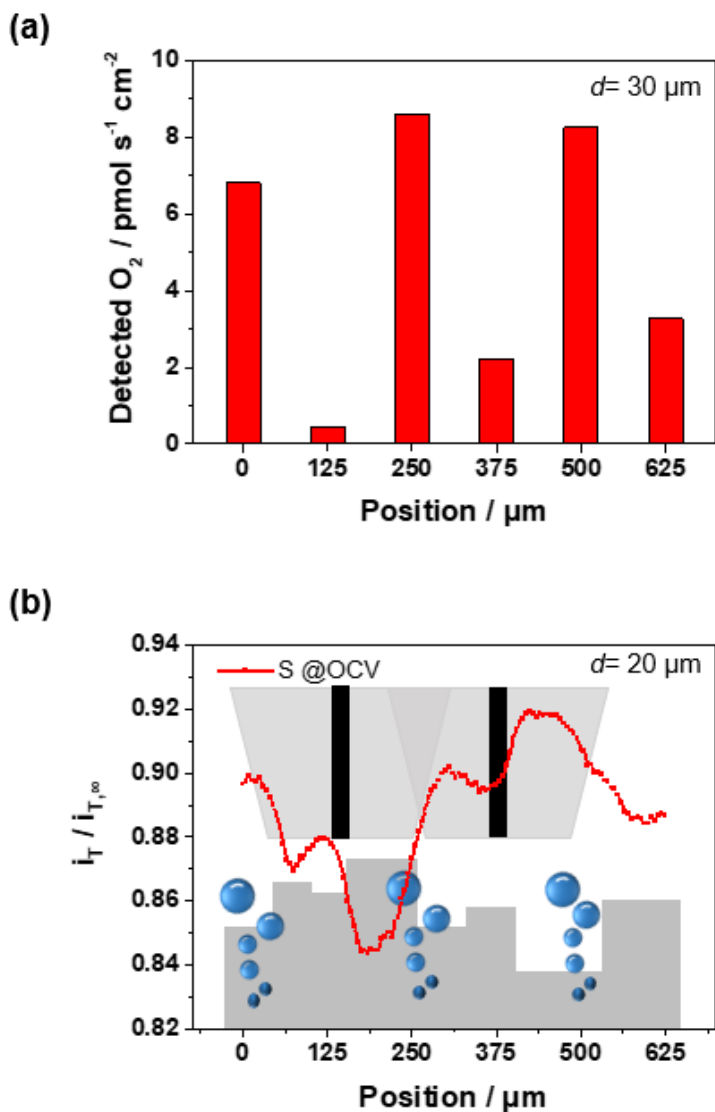
test. Line scan is a useful way to figure out the tendency of O<sub>2</sub> emission through the direction. However, points detection has some advantages compared to line scan: i) availability of calculation of detected O<sub>2</sub> with background correction, ii) amelioration of blocking issue of the tip or pores in the Ti PTL from big O<sub>2</sub> bubbles, which are generated by agglomeration of O<sub>2</sub> in the solution as time goes on, due to short time of OER (10 seconds) compared to line scan (more than 30 seconds), iii) prevention of the effect of roiling the solution in line scan due to fixed position of the tip.

Figure 4.12 shows the example of the current density of the substrate and the UME tip through time in points detection. Since OER of the substrate is diffusion controlled, OER current decreases as time goes on during 10 seconds (Figure 4.12(a)). To calculate detected O<sub>2</sub> in points detection, the ORR current at 40 second ( $\Delta j$ , the inserted figure in Figure 4.12(b)) was analyzed with calibration of the background ORR current which comes from existed O<sub>2</sub> in the solution before OER at the substrate. The positive current peak around 40 seconds of the tip seems to be happened from the systematic error of the device in a 4-electrode system by sharing same reference and counter electrode of two working electrodes (tip and substrate) rather than from somewhat oxidative reaction at 0 V<sub>Ag/AgCl</sub> on the UME tip after stopping the OER (Figure 4.12(b)).

The O<sub>2</sub> detection was measured in the range of 625  $\mu\text{m}$  with 125  $\mu\text{m}$  intervals (Figure 4.13(a)). Detected O<sub>2</sub> above in region of the hydrophobic channels was 6.80-8.61  $\text{pmol cm}^{-2} \text{s}^{-1}$ , which reveals 2.1 to 19 times higher value than the amount of O<sub>2</sub> on the above the hydrophobic channels. Compared to hydrophobic region, O<sub>2</sub> detection has high relative deviation, 0.45-3.26  $\text{pmol cm}^{-2} \text{s}^{-1}$ , above the hydrophilic channels. One possible reason is difference of diffusion of O<sub>2</sub> reactant on the tip due



**Figure 4.12.** The example of current density through time on (a) the substrate and (b) the tip from OER and ORR (at 625  $\mu\text{m}$ ). The inserted figure in (b) is the magnified graph in the region of 27.5 to 45.0 second.



**Figure 4.13.** (a) Detected amount of oxygen estimated by UME tip current on each position of the backside of patterned Ti PTL at 40 sec ( $d=30 \mu\text{m}$ ). (b) Line-mapping of the region of points detection in  $[\text{Fe}(\text{CN})_6]^{4-}/[\text{Fe}(\text{CN})_6]^{3-}$  redox couple solution at  $d=20 \mu\text{m}$ .

to surface geometry if we assumed most of O<sub>2</sub> detected above hydrophilic regions comes from diffusion of O<sub>2</sub> passed through the hydrophobic channels. If the O<sub>2</sub> pass through all region randomly, detected amount of O<sub>2</sub> does not reflect the effect of surface geometry at  $d=30\ \mu\text{m}$  as shown in Figure 4.10. However, if the O<sub>2</sub> diffuses to the UME tip from side directions after passing the hydrophobic channels, diffusion is blocked by the small space between the tip and the substrate. This geometrical effect is described in Figure 4.13(b) with the simplified bubble and geometrical illustration from overlapping results of points detection and the line scan data at OCV state of the substrate (negative feedback). For instance, the space is too narrow to facilitate side diffusion around the  $125\ \mu\text{m}$  region due to protruded fibers, resulting lower O<sub>2</sub> detection, in contrast to other hydrophilic regions including larger space to diffuse. The results in line scan and points detection verify that emission of generated gas bubbles through the patterned hydrophobic channels fabricated by coating of PDMS polymer brush.

## 4.4. Conclusions

In this chapter, the SECM from the fundamental experiments for understanding the basic principle of analysis to the application in the Ti PTLs research was studied. From the unique properties of the UME, Ti PTLs, which are the main components in PEMWE and UR-PEMFC, were characterized as follows: i) topography of the Ti PTL, ii) electrical properties of the substrate, iii) behavior of gas emission in the backside of Ti PTLs through its surface geometry, and iv) verification of the effect of fabrication of gas channels in the Ti PTL by patterned polymer brush coating (in chapter 3). This study demonstrates that the SECM is the useful and powerful device

for analysis of the local phenomena in PTLs of PEMWE (or PEMFC) in addition to the bulk phenomena data from other electrochemical analyses such as IV and impedance.

## 4.5. References

- [1] R. M. Wightman, Microvoltammetric electrodes, *Anal. Chem.* 53 (1981) 1125-1134.
- [2] j. Heinze, Ultramicroelectrodes in electrochemistry, *Angew. Chem. Int. Ed. Engl.* 32 (1993) 1268-1288.
- [3] A. J. Bard, F.-R.F. Fan, J. Kwak, O. Lev, Scanning electrochemical microscopy. Introduction and principles, *Anal. Chem.* 61 (1989) 132-138.
- [4] P. Sun, F.O. Laforge, M.V. Mirkin, Scanning electrochemical microscopy in the 21st century, *Phys. Chem. Chem. Phys.* 9 (2007) 802-823.
- [5] D. Polcari, P. Dauphin-Ducharme, J. Mauzeroll, Scanning electrochemical microscopy: A comprehensive review of experimental parameters from 1989 to 2015, *Chem Rev* 116 (2016) 13234-13278.
- [6] A. J. Bard, M.V. Mirkin, P.R. Unwin, D.O. Wipf, Scanning electrochemical microscopy. 12. Theory and experiment of the feedback mode with finite heterogeneous electron-transfer kinetics and arbitrary substrate size *J. Phys. Chem.* 96 (1992) 1861-1868.
- [7] Y. Takahashi, Y. Kobayashi, Z. Wang, Y. Ito, M. Ota, H. Ida, A. Kumatani, K. Miyazawa, T. Fujita, H. Shiku, Y.E. Korchev, Y. Miyata, T. Fukuma, M. Chen, T. Matsue, High-resolution electrochemical mapping of the hydrogen evolution reaction on transition-metal dichalcogenide nanosheets, *Angew. Chem. Int. Ed.*

59 (2020) 3601-3608.

# **Chapter 5. Highly Efficient Operation of Unitized Regenerative Fuel Cell with Amphiphilic Membrane-Electrode Assembly**

## **5.1. Introduction**

As an effort to reduce the greenhouse gas emission from fossil fuels, electricity generated from renewable sources such as wind, solar and hydroelectric powers has been rapidly growing in energy system. Almost 2.3% of growth rate of renewables and 31% of world energy by renewables with 3.7 TW of installed capacity are expected until 2040 [1]. To store GW to TW scale electricity, unitized regenerative fuel cell (URFC), i.e. a combined system of electrolysis cell (EC) producing hydrogen fuels from water in providing electricity and fuel cell (FC) producing electricity in providing hydrogen fuels, is considered as a great potential technology due to high specific energy, e.g. 3660 Wh/kg which is 5.2 times higher than that of Li-ion battery [2]. However, polymer electrolyte membrane based URFC (UR-PEMFC) has several issues; i) lower round trip efficiency compared to discrete RFC, ii) high costs of system (UR-PEMFC: \$1400-1500 kWh<sup>-1</sup> [3], PEMEC: \$1860-2320 kWh<sup>-1</sup> [4], PEMFC: \$40-50 kW<sup>-1</sup>), especially, high loading of noble catalysts from sluggish oxygen reactions and iii) hydrogen storage (\$18 /kW h) [3].

UR-PEMFC has an advantage of a compact system, but each of EC and FC operations in UR-PEMFC has a task to reach the state of performance as much as discrete RFC, i.e. PEMEC and PEMFC. Nowadays, PEMFC is highly mature enough to be commercialized as a result of ardent and enthusiastic researches over the past decades. In widespread commercialization of fuel cell, development of three components of membrane electrode assembly (MEA) played major roles; i) highly dispersive Pt catalysts on carbon supports having high surface area and electric conductivity, i.e. Pt/C [5, 6], ii) sulfonated tetrafluoroethylene based highly proton conductive polymer [7] and iii) efficient carbon gas diffusion layer (GDL or PTL (porous transport layer)) containing microporous layer (MPL) [8]. However, URFC is more complicated than FC and the optimized system of FC is not appropriate anymore in URFC because of carbon corrosion. In addition to the FC mode composed of hydrogen oxidation reaction (HOR) and oxygen reduction reaction (ORR), hydrogen evolution reaction (HER) and oxygen evolution reaction (OER) are required in the EC mode. It gives rise to two critical issues. First, carbon materials such as C GDL and C support of catalysts are not appropriate and need to be replaced to other non-corrosive materials in the oxygen electrode side of EC due to severe carbon corrosion ( $\text{CO}_2 + 4\text{H}^+ + 4\text{e}^- \rightleftharpoons \text{C} + 2\text{H}_2\text{O}$ ,  $E^0 = 0.206 \text{ V}_{\text{RHE}}$ ) in high voltage, e.g. more than 1.5 V. Second, optimized hydrophobic PTLs (or GDLs) containing MPL in fuel cell are required to be ameliorated since not only gas approach to ORR catalysts in FC mode, but water approach to the catalysts in EC mode become also important.

Researches to replace carbon materials in catalyst supports or PTLs were done to enhance stability in PEMEC and UR-PEMFC. In the aspect of catalysts, mixtures of Pt black as ORR catalysts and  $\text{IrO}_2$  (or Ir black) as OER catalysts with high noble-

metal (platinum group metal, PGM) loading more than  $2 \text{ mg cm}^{-2}$  have been widely reported in URFC researches [9]. In other ways, instead of mixture structure of Pt and  $\text{IrO}_2$  catalysts,  $\text{IrO}_2$  supported on Pt ( $\text{IrO}_2/\text{Pt}$ ) [10] or Pt supported on  $\text{IrO}_2$  ( $\text{Pt}/\text{IrO}_2$ ) [11] catalysts are synthesized, which the one catalyst acts as both the catalyst and the support of the other catalyst. Not only higher dispersion, but also creation of electrical connection between particles result in higher FC performance compared to mixed catalysts in  $\text{IrO}_2/\text{Pt}$  [10]. For researches of non-corrosive support materials especially for EC, which is severely corrosive condition from high voltage ( $>1.6 \text{ V}$ ), catalysts on TiC [12-14], TiN [13, 15], TiCN [13], ATO [16, 17], TaC [18], ITO [19],  $\text{TiO}_2$  [20, 21] were introduced. Rozain et al. reported EC operation using  $\text{IrO}_2/\text{Ti}$   $0.1 \text{ mg cm}^{-2}$  as anode catalysts reveals high mass activity and stable performance, e.g.  $1 \text{ A cm}^{-2}$  @  $1.73 \text{ V}$  with  $20 \mu\text{Vh}^{-1}$  degradation rate [22]. Choe. et al. informed low loading of noble catalysts without support materials ( $0.4 \text{ mg cm}^{-2}$ ,  $0.96 \text{ A cm}^{-2}$  @  $1.6 \text{ V}$ ,  $120 \text{ }^\circ\text{C}$ ) by direct electrodeposition of  $\text{IrO}_2$  on Ti mesh, which enhances electrical conductivity between catalysts layer and Ti substrate and reduce Ti corrosion by  $\text{IrO}_2$  coating [23].

Incessant studies of PTLs, e.g. its porosity, materials, MPL, etc., have been done in FC since water management is critical as much as catalysts [24]. Especially, when water (from inlet gas, electro-osmotic flow and products of ORR) is not effectively removed in the cathode side of FC, significant performance loss is accompanied by blocking of gas supply to the catalysts layer, called flooding. To remove water efficiently, hydrophobic treated bulk carbon PTLs and additional MPLs comprised of carbon particles and PTFE binders consist the cathode of FC with catalysts layers. In URFC, PTFE coating [25-28] or MPL of Ti particles [29] on Ti PTL were studied. Ioroi et al. reported increase of PTFE coating has opposite influence on FC

(enhancement) and EC (aggregation) performance [25], but Hwang et al. mentioned PTFE content is not critical to EC [27]. However, unlike the matured state of researches with hundreds of papers related to PTLs of FC, the state of PTL research in URFC is in the early stage [9, 30].

Change of the conventional operation mode of URFC provides highway to solve the two issues in URFC above. There are two possible operation configurations in URFC, i.e. hydrogen and oxygen electrode configuration (HOEC) and reduction and oxidation electrode configuration (ROEC) (Figure 5.1). HOEC, which same gas is supplied (FC) and produced (EC) in the same electrode, is generally studied in UR-PEMFC researches. Since each of O<sub>2</sub> and H<sub>2</sub> gases penetrates the one side of electrodes, it is possible to change operation mode at once, i.e. FC to EC or EC to FC. However, it has a huge bottleneck to fabricate the efficient oxygen electrode since both of ORR and OER at the oxygen electrode are sluggish reactions compared to HER and HOR. As a results, most of papers in URFC including more than 2 mg cm<sup>-2</sup> of noble catalysts in the oxygen electrode with Pt and IrO<sub>2</sub> catalysts due to absence of appropriate commercialized materials of catalysts supports like carbon supports in FC [9]. On the other hand, reduction reactions (HER, ORR) and oxidation reactions (OER, HOR) are occurred in the same electrode, respectively in ROEC. This configuration has two main advantages. First, the commercialized PTL structure of oxygen electrode in FC is applicable since it is operated as hydrogen electrode in EC mode, in which applied potential marginally affects carbon corrosion. Second, it is easy to reduce the amount of Pt black catalysts in the cell because HOR does not require noble catalyst as much as ORR [31, 32] and Pt/C as ORR catalysts is applicable without compromising stability. However, there are a few studies about effects of operation modes of URFC and papers reported ROEC operation in URFC

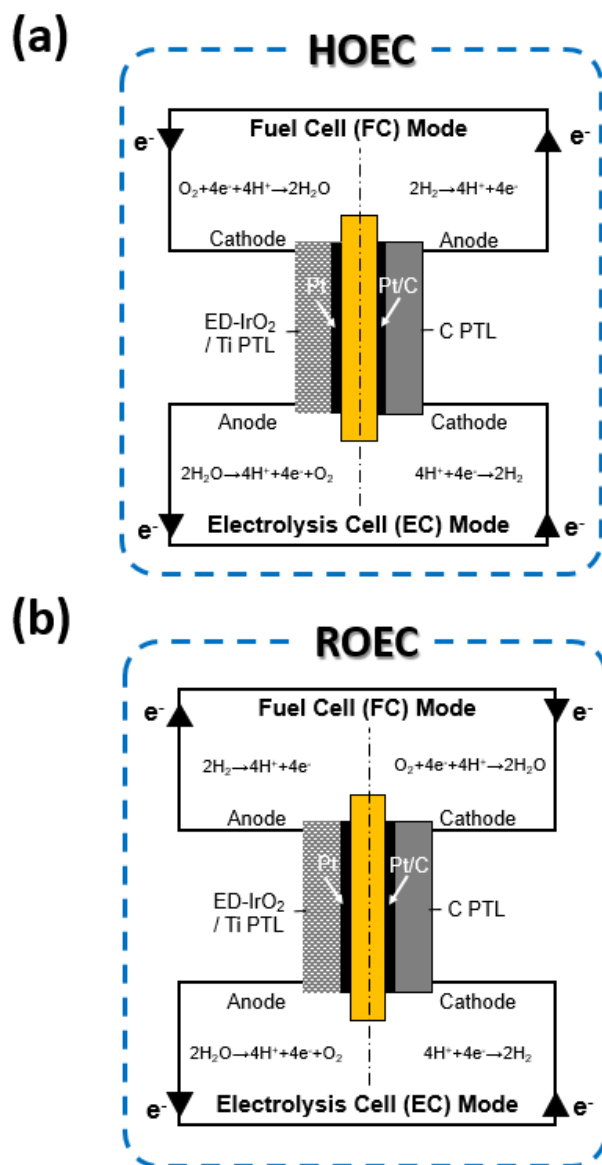


**Figure 5.1.** Schematic illustration of two operation configurations in unitized regenerative fuel cell (URFC). (a) hydrogen and oxygen electrode configuration (HOEC) and (b) reduction and oxidation electrode configuration (ROEC).

**Table 5.1.** Definition of abbreviations in manuscripts.

<b>Abbreviations</b>	<b>Definition</b>
URFC	Unitized Regenerative Fuel Cell
EC	Electrolysis Cell
FC	Fuel cell
PTL	Porous Transport Layer
MPL	Microporous Layer
HOR	Hydrogen Oxidation Reaction
HER	Hydrogen Evolution Reaction
ORR	Oxygen Reduction Reaction
OER	Oxygen Evolution Reaction
PGM	Platinum Group Metal
e-IrO <sub>2</sub>	Electrodeposited-Iridium Oxide
s-IrO <sub>2</sub>	Spray coated-Iridium Oxide
HOEC	Hydrogen and Oxygen Electrode Configuration
ROEC	Reduction and Oxidation Electrode Configuration
MWF	Membrane Water Flux
CWF/AWF/TWF	Cathode/Anode/Total Water out-Flux

[3, 14, 33-36]. In order to get a highly efficient URFC system, not only development of materials, e.g. porous transport layer and superior catalysts, but also understanding of the cell are important.

Here, we introduced a hydrophilic electrodeposited IrO<sub>2</sub> electrode (e-IrO<sub>2</sub>/Ti), i.e. 0.15 mg cm<sup>-2</sup> of IrO<sub>2</sub> coating acts as both catalysts and protective layer of Ti PTL, since material degradation and high PGM catalysts loading are serious issues in UR-PEMFC, and fabricated the amphiphilic MEA. In this research, we analyzed the water distribution and its influence on operation conditions, i.e. operation mode (ROEC and HOEC) and relative humidity (RH), in FC mode of URFC. By application of amphiphilic MEA in ROEC based on understanding of water distribution effect on the cell through RH, UR-PEMFC achieved high round trip efficiency, 49% @ 0.5 A cm<sup>-2</sup>, with only 0.65 mg cm<sup>-2</sup> of noble catalysts in the cell which is similar amount of catalyst loading in PEMFCs.

## 5.2. Experimental Section

### 5.2.1. Electrode Preparation

To prepare MEA (2.25 cm<sup>2</sup>), electrodeposition on PTL and catalyst coated on membrane (CCM) method were used. One side of electrode was electrodeposited IrO<sub>2</sub> on a Ti PTL (250 μm, Bekaert). Electrodeposition was conducted at 0.7 V (vs. SCE) for 10 minutes in Ir precursor solution consisting of 0.01 M Iridium(IV) chloride hydrate (99.95%, Ir 56.5%, Alfa-aesar), oxalic acid((COOH)<sub>2</sub>·2H<sub>2</sub>O: 5 g L<sup>-1</sup>), hydrogen peroxide (35% H<sub>2</sub>O<sub>2</sub>: 10 g L<sup>-1</sup>) dissolved in deionized water (DI water). Ir precursor solution was stirred for 3 days before using in electrodeposition. In the

Ti PTL side of electrode, Pt black (high surface area, Alfa Aesar) was sprayed on the Nafion<sup>®</sup> 212 membrane. The amount of Pt catalyst loading was controlled from 0.1 to 0.6 mg cm<sup>-2</sup>. The other side of electrode, Pt/C (46.2 wt%, Tanaka K.K) 0.4 mg cm<sup>-2</sup> was sprayed on the Nafion<sup>®</sup> 212 membrane combined with a carbon PTL (39 BC, SIGRACET<sup>®</sup>). Pt slurry, i.e. mixture of Pt black or Pt/C, nafion ionomer, isopropyl alcohol (IPA) and DI water, was ultra-sonicated before spraying. For spray coated IrO<sub>2</sub>, slurry composition was almost same except for using IrO<sub>2</sub> (Iridium(IV) oxide, 99.99% (metals basis), Alfa-Aesar) instead of Pt. The ionomer content in catalyst layers were 30 wt% for Pt (Pt black and Pt/C) and 20 wt% for IrO<sub>2</sub>.

### **5.2.2. Physical and Electrochemical Characterization**

Field emission scanning electron microscopy (FE-SEM, Teneo Volume Scope) and energy dispersive spectrometer (EDS) were utilized to observe catalysts distribution on surface and cross section of PTLs. Hydrophilicity of PTLs is analyzed by contact angle measurement (SmartDrop, Femtobiomed). Inductively coupled plasma-optical emission spectroscopy (ICP-OES, iCAP6500 Duo, Thermo) was used to analyze the amount of Ir in electrodeposited electrode.

### **5.2.3. Single Cell Tests**

The single cell components (end plate, titanium flow field, MEA, graphite flow field and end plate) were assembled with 80 lb·in torque. The operation temperature of the cell was 80°C in both of EC and FC. In EC, the electrode side of IrO<sub>2</sub>-electrodeposited Ti PTL with Pt black catalysts on membrane was operated as anode, and the C electrode with Pt/C catalysts was operated as cathode. DI-water was

provided to anode with a flow rate of 15 ml min<sup>-1</sup>. IV curve was obtained by averaging measured current during constant voltage mode for 1.2 min at each voltage from 1.25 to 2.0 V with the interval of 0.05 V. In FC operation, a feeding rate of fuel (H<sub>2</sub>/O<sub>2</sub> or air) was 400 ccm for both electrodes. Two operation modes were conducted by changing the side of anode and cathode electrodes. RH of fuel providing each side of electrode was controlled from 30 to 100. Both IV and impedance results of EC and FC tests were obtained using high current potentiostat (HCP-803, Bio-Logic). For 80 h long term tests, 2 cycles of 20 h FC-20 h EC were conducted at 0.4 A cm<sup>-2</sup>. Between operation modes (FC to EC or EC to FC), N<sub>2</sub> was purged at each electrode until OCV becomes less than 0.1 V.

## 5.3. Results and Discussion

### 5.3.1. Background Physical Characteristics of Electrodes

Here, e-IrO<sub>2</sub>/Ti was introduced in UR-PEMFC operation due to three main reasons: i) low loading of IrO<sub>2</sub> with high performance in the EC operation [37] and ii) stability from the IrO<sub>2</sub> coating effect [23], iii) simplicity of the process (formation and loading of catalysts on PTLs at the same time). The distribution of catalysts is significantly different for the electrodeposited electrode compared to the spray-coated electrode. As Figure 5.2 and 5.3 shows, catalysts are evenly and thinly coated for e-IrO<sub>2</sub> but, s-IrO<sub>2</sub> are distributed irregularly and roughly with ionomers on Ti fibers. On the top surface, both of electrodeposited and spray coated catalysts dispersed on the almost all region of Ti fibers. However, electrodeposition was conducted on the whole conductive Ti felt resulting the wider dispersion of catalysts (Figure 5.4 (a))

compared to s-IrO<sub>2</sub>, which is top concentrated (Figure 5.4 (b)).

Not only dispersion of catalysts, but also surface hydrophobicity are different between e-IrO<sub>2</sub> and s-IrO<sub>2</sub>. Since hydrophobicity of PTLs is critical in water management of the FC operation, water contact angle of PTLs was measured to understand the surface property of hydrophobicity/hydrophilicity before application of PTLs in single cells (Figure 5.5). The IrO<sub>2</sub> electrodeposited-Ti PTL rapidly absorbs water drop, which is super-hydrophilic. This super-hydrophilic property of the electrodeposited-PTL comes from each Ti fiber surrounded uniformly by electrodeposited IrO<sub>2</sub>, which is electrochemically connected with nanoparticles without using binders (Figure 5.2 and 5.4(a)). From penetration pressure equation (5-1), Ti-felt pore repels water droplets when IrO<sub>2</sub> surface water contact angle  $\theta > 90^\circ$  because  $P_r$  becomes negative and higher  $P_p$  than  $P_r$  is required pore to adsorb water. Where  $\gamma$  is the surface tension (mM/m) of water,  $\theta$  is water contact angle ( $^\circ$ ),  $r_p$  is the radius (m) of the pore in PTL,  $P_r$  is the pressure (mPa) on water droplets,  $P_p$  is penetration pressure or wetting pressure (mPa) [38]. On the other hand, it is spontaneous to absorb water when  $\theta < 90^\circ$ . Since water contact angle of IrO<sub>2</sub> is less than  $90^\circ$  [39-41], water droplet rapidly adsorbed to pore of e-IrO<sub>2</sub>/Ti (Figure 5.5).

$$P_p = -P_r = -\frac{2\gamma\cos(\theta)}{r_p} \quad (5-1)$$

Interestingly, for the catalysts coated PTL by spraying, hydrophobic property is maintained even though IrO<sub>2</sub> nanoparticles are coated on the surface of Ti or C PTL (Figure 5.3 and 5.5). This is because of inclusion of hydrophobic nafion ionomers in the catalyst layer, which makes s-IrO<sub>2</sub> itself hydrophobic. Therefore, application of e-IrO<sub>2</sub>/Ti in URFC has advantages in EC mode, but disadvantages in FC mode in

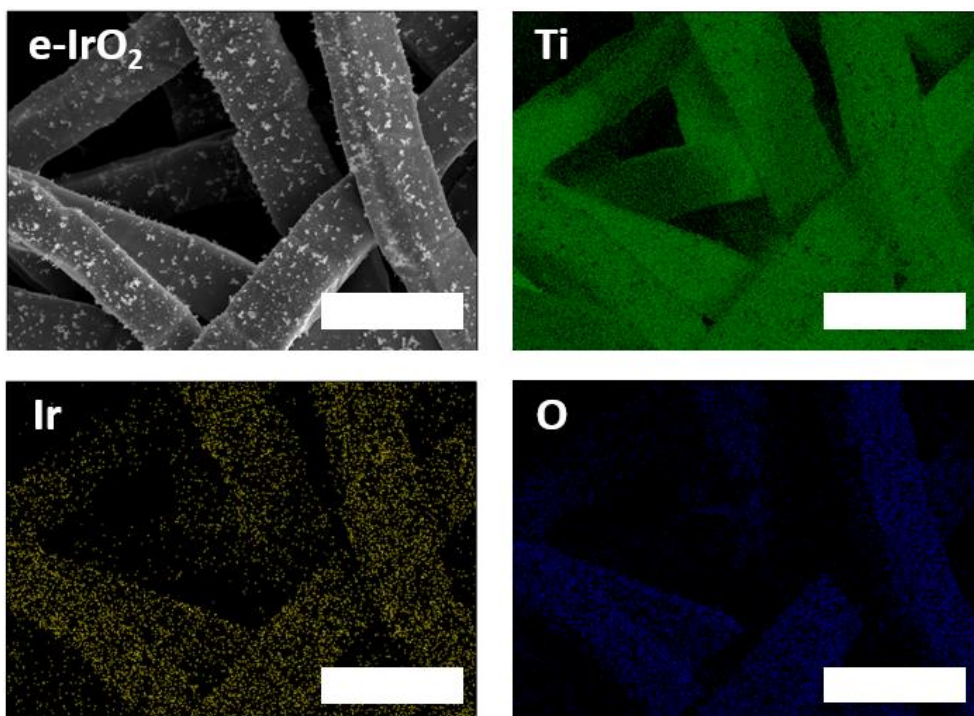


**Figure 5.2.** SEM and EDS mapping of top surface of e-IrO<sub>2</sub>/Ti (0.15 mg<sub>Ir</sub> cm<sup>-2</sup>).

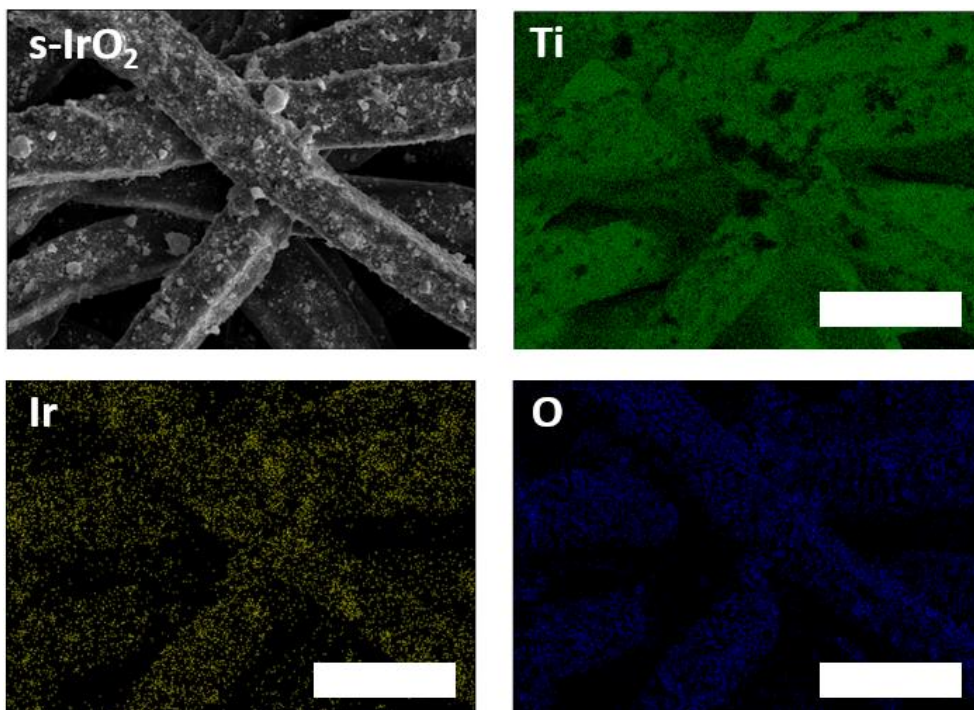


**Figure 5.3.** SEM and EDS mapping of top surface of s-IrO<sub>2</sub>/Ti (0.15 mg<sub>Ir</sub> cm<sup>-2</sup>).

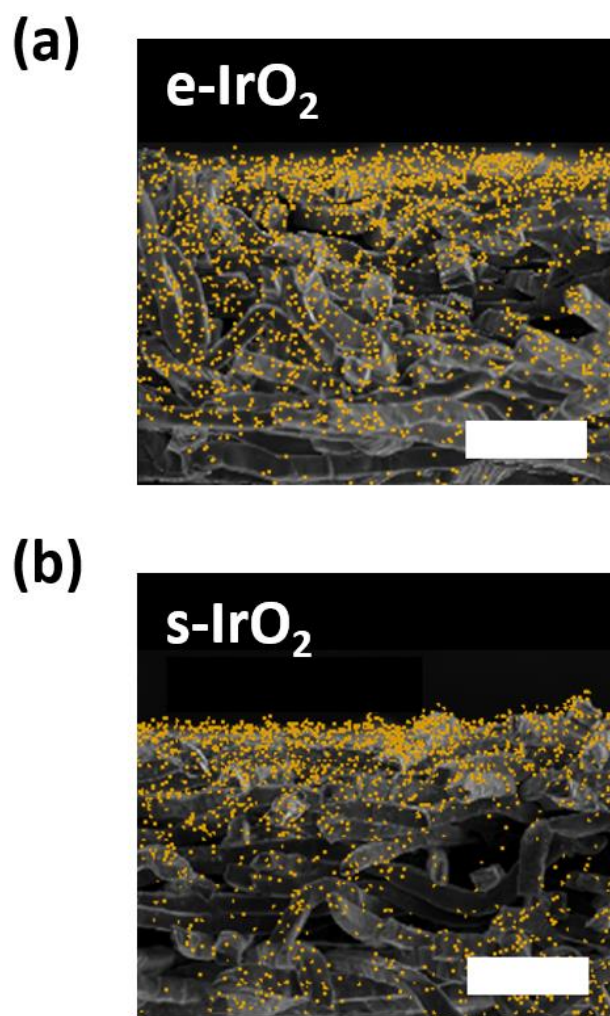


**Figure 5.4.** Overlapping SEM and EDS images of cross-section of (a) e-IrO<sub>2</sub>/Ti and (b) s-IrO<sub>2</sub>/Ti (inserted bar: 50  $\mu$ m).

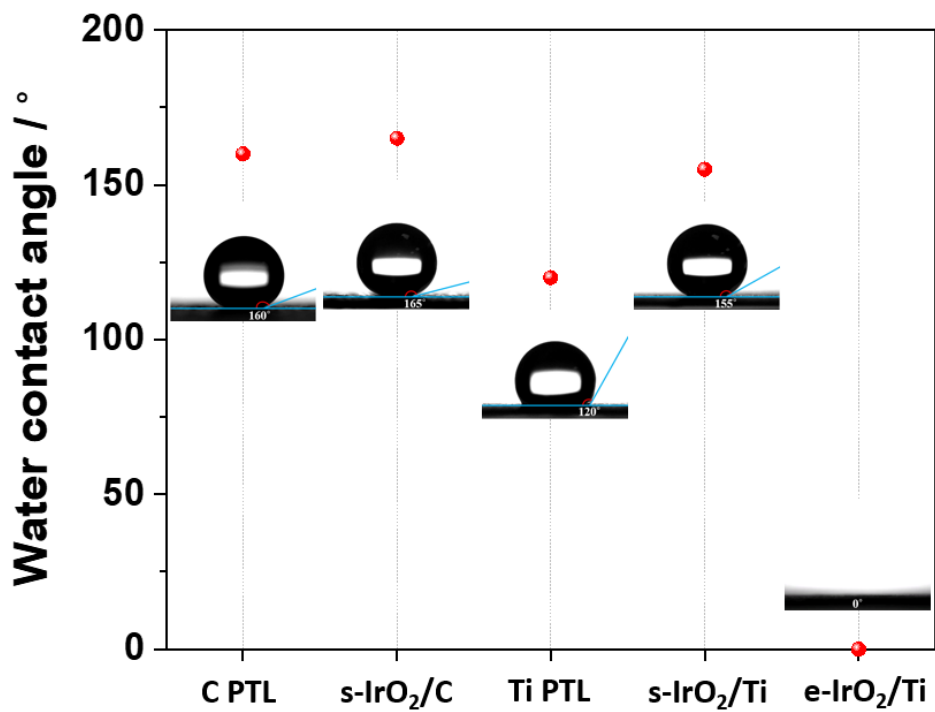


**Figure 5.5.** Water contact angle of pristine C PTL, IrO<sub>2</sub> spray coated C PTL, pristine Ti PTL, IrO<sub>2</sub> spray coated Ti PTL and IrO<sub>2</sub> electrodeposited Ti PTL.

terms of water management. Since it is vulnerable to water flooding when e-IrO<sub>2</sub>/Ti is used as cathode in FC mode, operation configuration (ROEC or HOEC) is more critical. However, if operation conditions are controlled with understanding of water management in the system, e-IrO<sub>2</sub>/Ti can be greatly utilized in URFC to get superior performance with maintaining its advantages such as low loading of noble catalysts and electrochemical stability of the electrode.

### 5.3.2. Analysis of URFC Single Cell Operation

The cell was operated in two variables: i) operation configuration (ROEC and HOEC), ii) RH of each fuel on anode and cathode (RH 100, 65 and 30). To understand the phenomena observed in IV curves through RH control, water distribution at each RH was estimated based on current density and water content in providing fuel. The cell basically consists of i) end plate; holding up the cell, ii) flow field plate; flow gas and water along with electrical connection with power supply and iii) MEA composed of PTLs, catalysts and a membrane (Figure 5.6). Fuels and products are provided and emitted from end plates to the catalysts and vice versa. Based on this principle of flow, water flux in each side of electrodes can be explained as Figure 5.6. In membrane, water flows accompanied with proton conduction (assumed this direction as positive direction) and back diffusion from the water concentration gradient (5-2). The anode side of water out-flux includes water content in providing fuels and water flux through membrane (5-3). Cathode also includes these two factors and additionally, water generation at catalysts by ORR (5-4).

$$\begin{aligned} & \text{Membrane water flux (MWF, } \dot{n}_{H_2O,m}) \\ & = \text{electro-osmotic drag } (\dot{n}_{H_2O,m,osmotic}) - \text{back diffusion } (\dot{n}_{H_2O,m,backdiff}) \quad (5-2) \end{aligned}$$

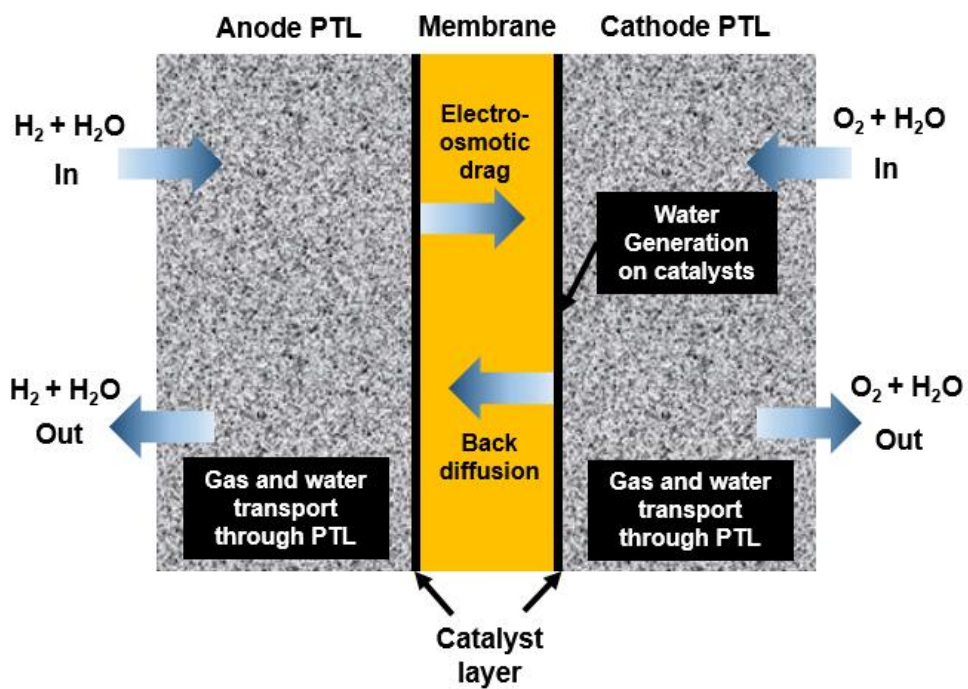


**Figure 5.6.** Schematic illustration of water distribution inside of membrane electrode assembly (MEA) during operation of fuel cell.

$$\text{Anode water out-flux (AWF)} = \text{water in-flux} - \text{MWF} (\dot{n}_{H_2O,m}) \quad (5-3)$$

$$\begin{aligned} \text{Cathode water out-flux (CWF)} &= \text{MWF} (\dot{n}_{H_2O,m}) + \text{water production} \\ &+ \text{water in-flux} \end{aligned} \quad (5-4)$$

Electro-osmotic drag is proportional to proton conduction, which can be expressed as (5-5).  $i$  is current,  $F$  is faraday constant (96485 C/mol) and  $n_d$  is electro-osmotic drag coefficient.  $n_d$  can be expressed as (5-6) from Dutta et al. [42].  $\lambda_m$  is the term of moles of H<sub>2</sub>O per equivalent polymer. It will be discussed in the explanation of back diffusion.

$$\dot{n}_{H_2O,m,osmotic} = n_d \frac{i}{F} \quad (5-5)$$

$$n_d = 0.0029 \cdot \lambda_m^2 + 0.05 \cdot \lambda_m - 3.4 \times 10^{-19} \quad (5-6)$$

Back diffusion generally refers water flux from cathode to anode, which is originated from the concentration gradient of water between anode and cathode with a membrane in between. It is expressed as a similar equation to Fick's law (5-7).

$$\dot{n}_{H_2O,m,backdiff} \simeq D_w \frac{c_w^{ca} - c_w^{an}}{t_{mem}} \quad (5-7)$$

$t_{mem}$  is thickness of the membrane,  $D_w$  (cm<sup>2</sup>/s) is diffusion coefficient and  $c_w^{ca} - c_w^{an}$  (mol/cm<sup>3</sup>) indicates water concentration gradient. Each side of water concentration ( $c_w^i$ , mol/cm<sup>3</sup>), i.e. the number of moles of water per 1 cm<sup>3</sup> of membrane, can be calculated by (5-8).  $M_{m,dry}$  (g/mol) is equivalent weight of dry membrane and  $\rho_{m,dry}$  (g/cm<sup>3</sup>) is density of dry membrane.

$$c_w^i = \frac{\rho_{m,dry}}{M_{m,dry}} \lambda_{equi,i} \quad (5-8)$$

The important factor in water concentration is  $\lambda_{equi,i}$ , which refers to the number of water molecules per -SO<sub>3</sub> in polymer membrane. This factor was experimentally measured and expressed as (5-9) using water vapor activity ( $a_i$ ) at each side of

electrode by Zawodzinski et al [43]. Water vapor activity can be calculated by relative humidity (5-10).

$$\lambda_{equi,i} = \begin{cases} 0.043 + 17.81a_i - 39.85a_i^2 + 36.0a_i^3 & , (0 \leq a_i \leq 1) \\ 14 + 1.4(a_i - 1) & , (1 < a_i \leq 3) \end{cases} \quad (5-9)$$

$$a_i = \frac{y_{w,i}P_i}{p_{sat,i}} = \frac{p_{w,i}}{p_{sat,i}} \quad (5-10)$$

Water diffusion coefficient ( $D_w$ ) in (5-7) is critically dependent on water content and temperature, which is expressed as modified form of the Arrhenius equation from experimental measurements with polymer electrolyte between 30° and 80° (5-11) [44]. Diffusion coefficient ( $D_\lambda$ ) is calculated by (5-12), measured by Dutta et al [42].  $\lambda_m$  is average of  $\lambda_{equi,i}$  at anode and cathode (5-13), which means water diffusion coefficient ( $D_w$ ) is also determined by relative humidity.

$$D_w = D_\lambda \cdot \exp\left(2416 \cdot \left(\frac{1}{303} - \frac{1}{T_{fuel\ cell}}\right)\right) \quad (5-11)$$

$$D_\lambda = \begin{cases} 10^{-6} & , \lambda_m < 2 \\ 10^{-6}(1 + 2(\lambda_m - 2)) & , 2 \leq \lambda_m \leq 3 \\ 10^{-6}(3 - 1.67(\lambda_m - 3)) & , 3 < \lambda_m < 4.5 \\ 1.25 \times 10^{-6} & , \lambda_m \geq 4.5 \end{cases} \quad (5-12)$$

$$\lambda_m = \frac{\lambda_{equi,ca} + \lambda_{equi,an}}{2} \quad (5-13)$$

From these calculated factors, we can estimate MWF ( $\dot{n}_{H_2O,m}$ ). Additionally, water in-flux is obtained from ideal gas law using saturated vapor pressure at certain temperature (5-14) and vapor pressure from relative humidity conditions. Water flux from ORR at cathode can be calculated using current density (5-15).

$$P = 0.61078 \exp\left(\frac{17.27T}{T+237.3}\right) \quad (5-14)$$

$$\dot{n}_{H_2O,gen} = \frac{I}{2F} \quad (5-15)$$

In Figure 5.7(a), the estimated MWF versus current density is disclosed through relative humidity. Water flux by diffusion is dominated at the state of OCV (at zero

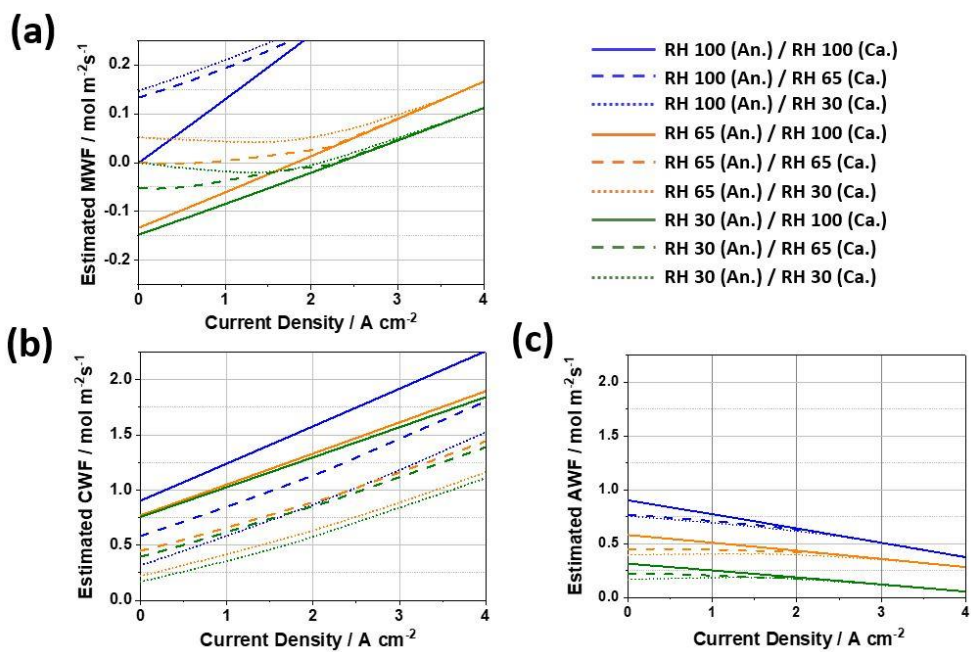


**Figure 5.7.** Estimated (a) membrane water flux (MWF), (b) cathode water out-flux (CWF) and (c) anode water out-flux (AWF) versus current density according to conditions of gas humidification.

current density) since none of water flux from electro-osmosis is occurred. Thus, the estimated values of MWF are positive or zero or negative when RH of cathode are lower or same or higher than RH of anode, respectively. Also, estimated MWF increases in the positive direction as current density increases because effects of water flux rising from electro-osmosis is greater than water flux from back diffusion as increase of current density. CWF includes water from membrane, water generation at cathode and inlet water which is related to RH of fuel. CWF is proportional to current density because electro-osmosis and ORR are increased (Figure 5.7(b)). AWF includes MWF and water inflow at the anode side. It decreases as current density increases since loss of water from electro-osmosis is dominant as current density increases (Figure 5.7(c)).

The estimated water flux assists explanation of the phenomena in FC performance. None of flooding was observed at RH 100 (An.) / RH 100 (Ca.) in ROEC, which means produced water was being discharged smoothly through C PTLs, but severe flooding was exhibited at the same RH in HOEC, which was alleviated as RH of anode or cathode becomes 65 (or less than 65) (Figure 5.8). In the HOEC operation, performance was much lower than the case of ROEC mainly due to Pt black catalysts without C support and the hydrophilic Ti PTL in the oxygen electrode, which revealed less than  $0.8 \text{ A cm}^{-2}$  @  $0.6 \text{ V}$  (Figure 5.8). Estimated MWF ( $\dot{n}_{H_2O,m}$ ) is positive at RH 100 (An.) / RH100 (Ca.), but negative at RH 65 (An.) / RH 100 (Ca.) and RH 30 (An.) / RH 100 (Ca.) when current density is less than  $1.5 \text{ A cm}^{-2}$  (Figure 5.7(a)). In other words, produced water tends to flow to the direction from the cathode to anode side at RH 65 (An.) / RH 100 (Ca.) and RH 30 (An.) / RH 100 (Ca.) in HOEC operation. This backward water flow induces alleviation blocking of catalysts by produced water at cathode, unlike the condition at RH 100 (An.) /

RH100 (Ca.), i.e. positive  $\dot{n}_{H_2O,m}$  in addition to saturated vapor pressure at the cathode side. It resulted in sudden recovery of performance, e.g. 0 to 0.67 A cm<sup>-2</sup> (@ 0.6 V) at anode RH 100 to 65, even though RH of cathode is still 100 at RH 65 (An.) / RH 100 (Ca.) and RH 30 (An.) / RH 100 (Ca.) in HOEC. Although  $\dot{n}_{H_2O,m}$  is also positive for RH 100 (An.) / RH65 (Ca.) and RH 100 (An.) / RH 30 (Ca.), flooding did not happened due to the dry condition of cathode.

The effect of relative humidity is also different between ROEC and HOEC (Figure 5.8). For instance, current density was higher at RH 100 (An.) / RH 30 (Ca.) than RH 65 (An.) / RH 100 (Ca.) for ROEC but reverse in HOEC. To simplify the explanation, the main determination factors on the performance are assumed as membrane and the electrode side composed of Pt black catalysts and electrodeposited Ti PTL, since Pt/C and C PTLs in the other side of the electrode are the optimized state materials in fuel cell compared to Pt black or Ti PTLs [6, 30, 45]. Since protons conduct from the anode to cathode side, the ohmic resistance from membrane decreases as AWF increases [46, 47]. In ROEC, the ohmic resistance comes from ionomer in Pt black catalysts (anode) and the membrane, which was decreased as the estimated AWF increases (Figure 5.9(a)). Thus, the tendency of the ohmic resistance followed the estimated AWF through RH control and also for the current density @ 0.6 V. In HOEC, ionomers on Pt black catalysts are distributed on the cathode side. Both of AWF (for H<sup>+</sup> transport through membrane) and CWF (for H<sup>+</sup> transport through cathode ionomers) contribute significantly to the ohmic resistance. Therefore, the ohmic resistance was reduced as TWF (=AWF+CWF) increases in HOEC (Figure 5.9(b)). In Figure 5.10, R<sub>ct</sub> and CWF through RH is described since ORR is more critical in performance. Both configurations revealed similar tendency, i.e. R<sub>ct</sub> decreased as decrease of CWF due to reduction of blocked

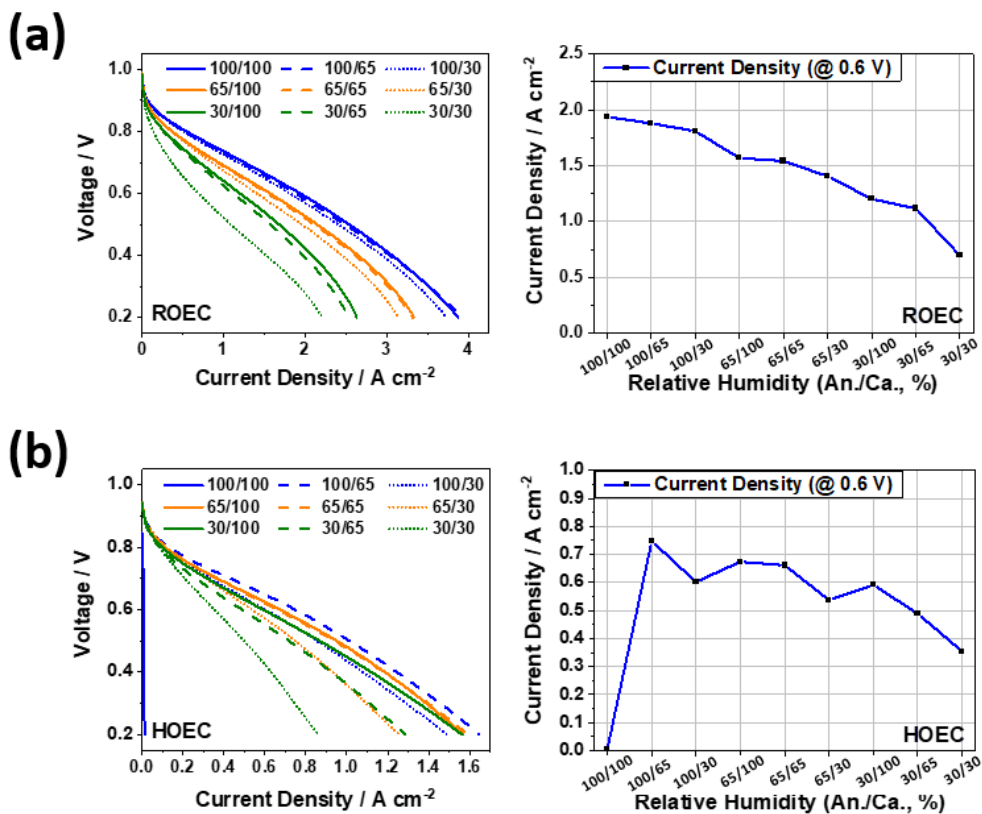


**Figure 5.8.** IV performance and current density at 0.6 V through control of relative humidity (RH) in (a) ROEC and (b) HOEC operation. In RH A/B, A and B indicate RH value of anode and cathode, respectively.

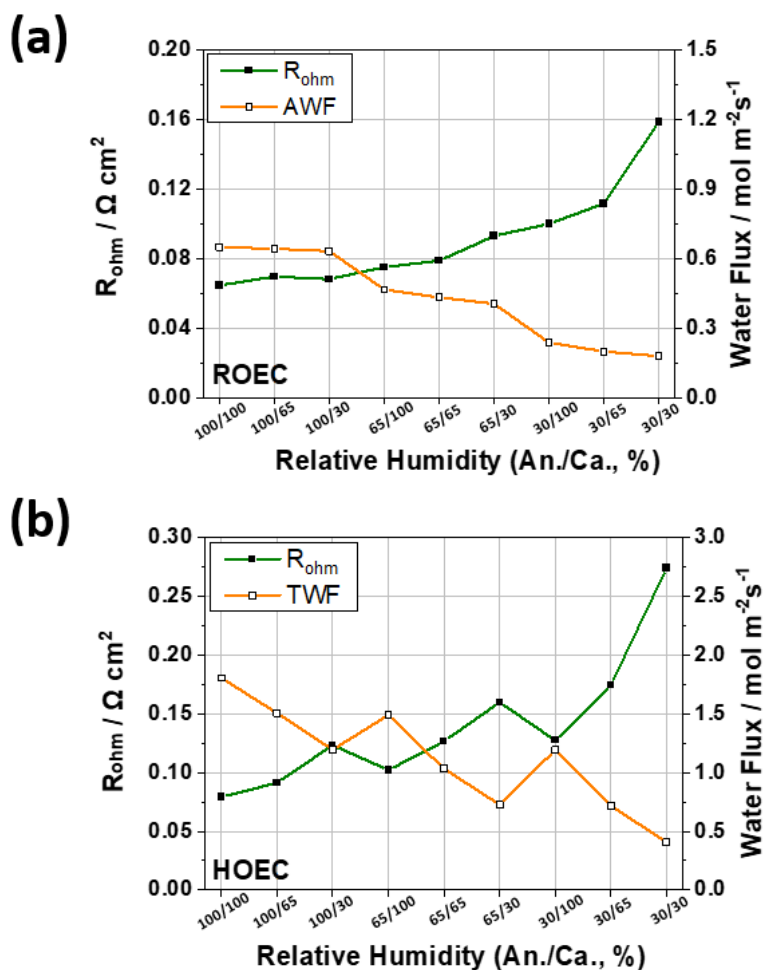


**Figure 5.9.** Comparison of ohmic resistance ( $R_{ohm}$ ) and estimated water out-flux based on current density and impedance measurements at 0.6 V of FC. (a) Ohmic resistance and estimated anode water out-flux (AWF) according to RH conditions in ROEC operation. (b) Ohmic resistance and estimated total water out-flux (TWF) according to RH conditions in HOEC operation.

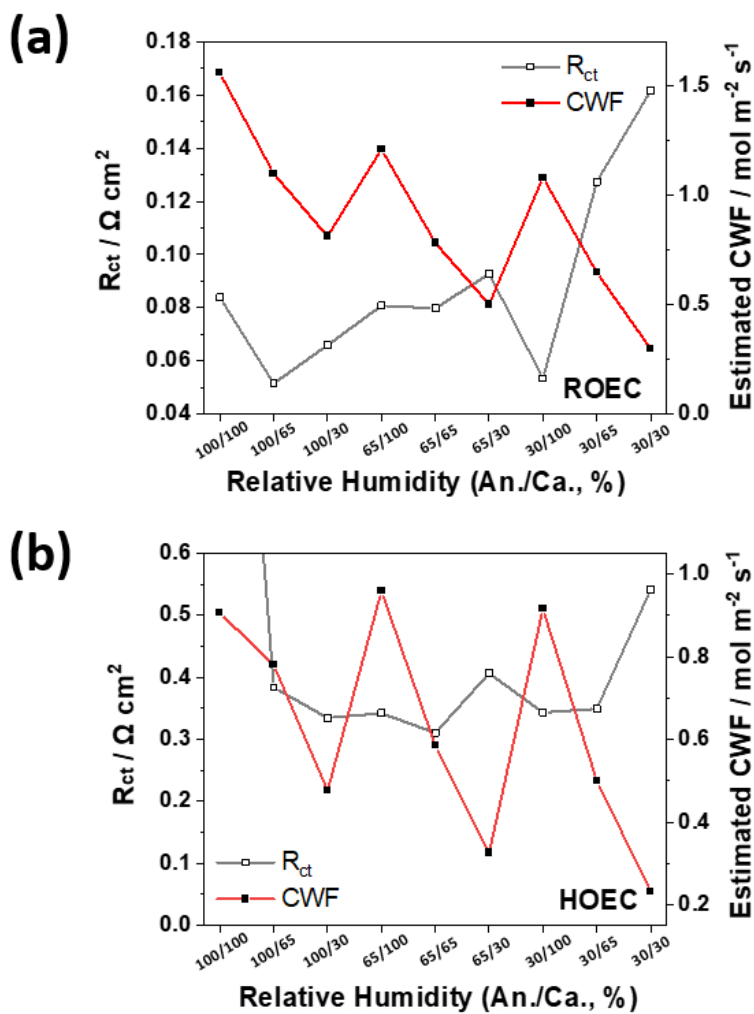


**Figure 5.10.** Comparison of charge transfer resistance ( $R_{ct}$ ) and estimated cathode water out-flux (CWF) according to RH conditions based on current density and impedance measurements at 0.6 V of FC in (a) ROEC and (b) HOEC operation.

active sites by ionomer swelling in higher RH compared to RH 65 (An.) / RH 65 (Ca.), but  $R_{ct}$  increased as decrease of CWF in low RH because proton transport through hydrated ionomers for ORR is more significant in low RH.

### 5.3.3. Control of Pt Catalysts Loading

To reduce loading of catalysts in the cell, Pt black catalysts loading was tried to control from 0.6 to 0.1 mg cm<sup>-2</sup> with maintaining Pt/C catalysts loading as 0.4 mg<sub>Pt</sub> cm<sup>-2</sup>. Since HOR is a fast reaction compared to ORR, reduction of Pt loading at anode until 0.1 mg cm<sup>-2</sup> does not significantly affect FC performance in ROEC [48]. However, since Pt black having low activity per area compared to Pt/C was used due to the carbon corrosion issue, current density @ 0.6 V was decreased about 29 % by reduction of Pt catalysts, e.g. 1.90 A cm<sup>-2</sup> (Pt 0.6 mg cm<sup>-2</sup>) to 1.34 A cm<sup>-2</sup> (Pt 0.1 mg cm<sup>-2</sup>) @ 0.6 V, but still maintained higher performance even than the case of HOEC using Pt 0.6 mg cm<sup>-2</sup>, i.e. 0.75 A cm<sup>-2</sup> @ 0.6 V (Figure 5.11). In addition, the influence of reduction of Pt loading was much severe in HOEC compared to ROEC, e.g. 78% decrease of current density @ 0.6 V from Pt 0.6 to Pt 0.1 mg cm<sup>-2</sup> in HOEC (Figure 5.11(b)).

Additional Pt catalysts on e-IrO<sub>2</sub> electrode has some positive and negative influence on WE; i) enhancement of OER from Pt, ii) increase of ohmic resistance from additional proton pathways in ionomers of Pt catalyst layers and iii) increase of overvoltage from mass transport limitation due to porous and hydrophobic Pt catalysts layers. Because of some negative effects from Pt catalyst layers, increase Pt loading did not reveal linear improvement in WE performance although Pt also can act as OER catalysts. Rather, change of Pt loading from 0.6 to 0.1 mg cm<sup>-2</sup> was

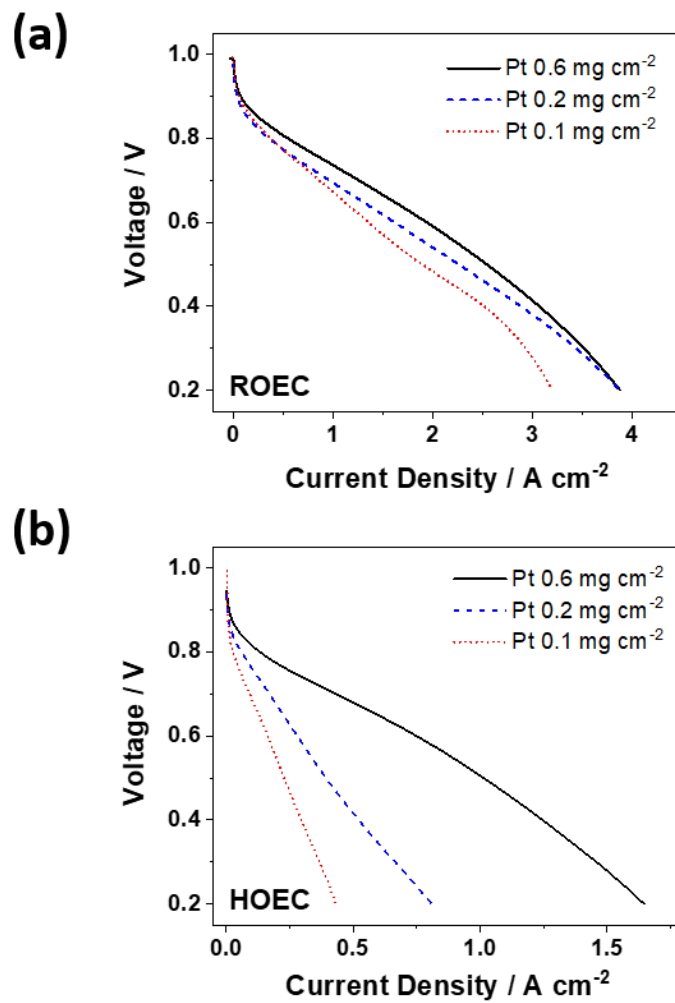


**Figure 5.11.** Comparison of IV performance of FC according to the amount of Pt black catalysts (0.6, 0.2 and 0.1 mg cm<sup>-2</sup>) in (a) ROEC (RH100(Ca.)/RH100(An.)) and (b) HOEC (RH100(Ca.)/RH65(An.)) operation

not critical in WE performance (Figure 5.12(a)).

Round trip efficiency (RT) represents the ratio of power generation by H<sub>2</sub> and required power to generate the same amount of H<sub>2</sub> in URFC. Here, RT was almost same even though Pt loading was decreased, i.e. 53, 51 and 51% @ 0.4 A cm<sup>-2</sup> for 0.6, 0.2 and 0.1 mg cm<sup>-2</sup> of Pt black loading. The reported RT according to catalyst loading in the cell is summarized for the case of using non-carbon PTL as oxygen electrode in WE (Figure 5.12(b)). Most of previous researches reported HOEC operation, but it required high loading (> 2 mg<sub>(Pt+Ir)</sub> cm<sup>-2</sup>) of noble catalysts to obtain RT higher than 40% @ 0.4 A cm<sup>-2</sup>. For instance, Choe. et al. reported 10% @ 0.4 A cm<sup>-2</sup> employing 0.8 mg cm<sup>-2</sup> of noble catalysts in the cell [49]. Ioroi. et al. reported high RT, i.e. 49% @ 0.4 A cm<sup>-2</sup>, but more than 6.0 mg cm<sup>-2</sup> of catalysts was utilized [25]. Recently, Kus. et al. demonstrated high RT, i.e. 47% @ 0.4 A cm<sup>-2</sup>, using only 0.72 mg cm<sup>-2</sup> of catalysts including sandwich-like structure of Ir/TiC/Pt by ROEC operation [14]. However, it did not mention the stability of electrodes.

### 5.3.4. Stability Tests

Durability tests are indispensable for commercialization of URFC, but a few papers reported long term durability tests in UR-PEMFC [20, 37, 50-53]. Here, a long term test of 80 h was done by 2 cycles of 40 h per each cycle using 0.65 mg<sub>(Pt+Ir)</sub> cm<sup>-2</sup> of PGM catalysts in the cell (Figure 5.13). Average degradation rate was 1.08 mV h<sup>-1</sup> for FC and 0.80 mV h<sup>-1</sup> for WE. However, the voltages at the end of each WE cycle (at 40 h and at 80 h) were both 1.58 V, which are the same overvoltage. In other words, the loss in WE performance was from the inside mass transport issue during 20 h operation rather than from degradation of the electrode. For degradation of FC,

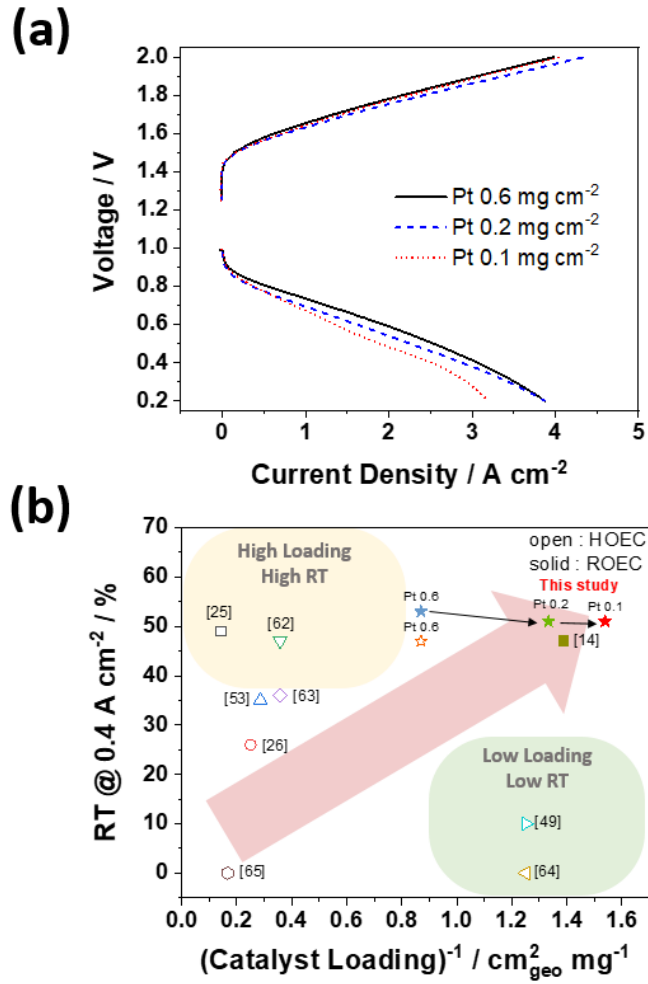


**Figure 5.12.** Comparison of (a) IV performance of URFC in ROEC according to the amount of Pt black catalysts ( $0.6$ ,  $0.2$  and  $0.1 \text{ mg cm}^{-2}$ ) and (b) Round trip efficiency at  $0.4 \text{ A cm}^{-2}$  versus reciprocal values of catalyst loading.

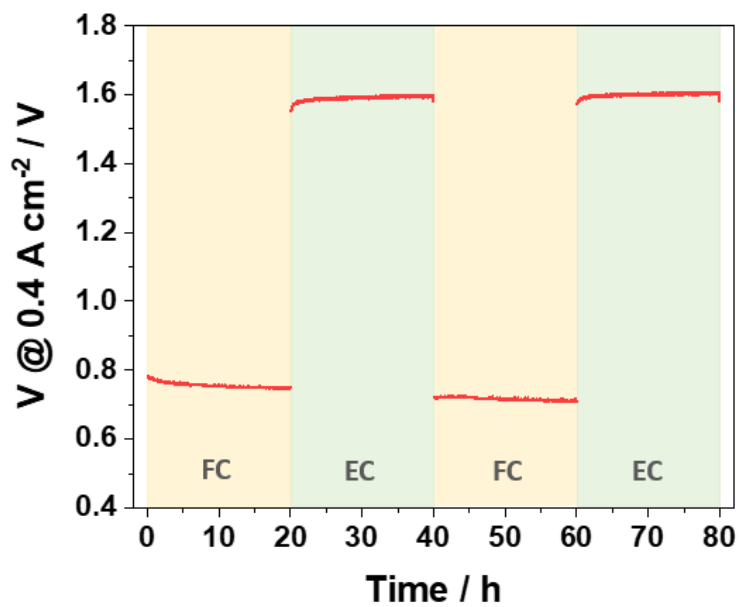


**Figure 5.13.** Long-term operation of URFC at  $0.4 \text{ A cm}^{-2}$  during 80 h (ROEC: Pt(CCM),e-IrO<sub>2</sub>/Ti electrode as anode and Pt/C(CCM) C electrode as cathode of URFC). Cell temperature of both FC (RH 65) and EC is  $80^\circ \text{ C}$ . Amount of Pt black catalysts loading is  $0.1 \text{ mg cm}^{-2}$ .

dissolution of Pt catalysts from repetition of OER-ORR along with agglomeration of catalysts is one of the main factors [54, 55]. In addition, the long term FC operation was done at RH 65 for observing the performance without the occurrence of flooding in case. However, it can accelerate the degradation of FC during operation due to the wet-dry condition when it changes the operation mode between WE and FC [56]. Not only catalysts, e.g. agglomeration, pinholes and cracks, but also increase of contact resistance between electrodes and membrane from wet-dry cycles affect the FC [56, 57]. To enhance the stability of a URFC system, more stable catalyst structures in wet-dry cycles and reinforced membranes having less volume expansion/contraction change from water content are required to be introduced in a URFC system [58-61].

## 5.4. Conclusions

To achieve highly efficient URFC with low noble catalysts loading, ROEC with the e-IrO<sub>2</sub>/Ti electrode was applied and water distribution effects on the URFC performance according to change of operation modes and RH were analyzed. Outstanding performance, e.g. 4.0 A cm<sup>-2</sup> @ 2.0 V with only 0.15 mg<sub>Ir</sub> cm<sup>-2</sup>, was attained in EC from highly dispersive catalysts in super-hydrophilic e-IrO<sub>2</sub> electrode. When RH control in FC of ROEC, ohmic resistance is critically affected by AWF due to nafion ionomers in Pt black catalysts and electro-osmosis. The performance was the best at RH100 (An.) / RH100 (Ca.) including the highest AWF in ROEC, in contrast to the worst performance due to flooding in HOEC, e.g. 1.9 A cm<sup>-2</sup> (ROEC) and 0 A cm<sup>-2</sup> (HOEC) @ 0.6 V. By taking both advantages of electrodes in ROEC, the hydrophobic electrode in the FC mode and the hydrophilic electrode in the EC

mode as the oxygen electrode, 51% round trip efficiency @ 0.4 A cm<sup>-2</sup> with 0.65 mg cm<sup>-2</sup> is accomplished. Stability tests was done for 80 h, reveals degradation rate of 1.08 mV h<sup>-1</sup> and 0.80 mV h<sup>-1</sup> for FC and EC. To enhance stability of the cell, reinforced membrane having high thermo-mechanical and chemical stability during long term of wet-dry cycles (EC-FC) should be introduced in future research.

## 5.5. References

- [1] T. M. Gür, Review of electrical energy storage technologies, materials and systems: challenges and prospects for large-scale grid storage, *Energy Environ. Sci.* 11 (2018) 2696-2767.
- [2] F. Mitlitsky, B. Myers, A.H. Weisberg, Regenerative fuel cell systems, *Energ. Fuel.* 12 (1998) 56-71.
- [3] Y. N. Regmi, X. Peng, J. C. Fornaciari, M. Wei, D. J. Myers, A. Z. Weber, N. Danilovic, A low temperature unitized regenerative fuel cell realizing 60% round trip efficiency and 10 000 cycles of durability for energy storage applications, *Energy Environ. Sci.* (2020) Advance Article.
- [4] O. Schmidt, A. Gambhir, I. Staffell, A. Hawkes, J. Nelson, S. Few, Future cost and performance of water electrolysis: An expert elicitation study, *Int. J. Hydro. Energ.* 42 (2017) 30470-30492.
- [5] E. Auer, A. Freund, J. Pietsch, T. Tacke, Carbons as supports for industrial precious metal catalysts, *Appl. Catal. A* 173 (1998) 259-271.
- [6] E. Antolini, Carbon supports for low-temperature fuel cell catalysts, *Appl. Catal. B* 88 (2009) 1-24.
- [7] S. Banerjee, D. E. Curtin, Nafion® perfluorinated membranes in fuel cells, *J.*

- Fluor. Chem.* 125 (2004) 1211-1216.
- [8] S. Park, J.-W. Lee, B. N. Popov, A review of gas diffusion layer in PEM fuel cells: Materials and designs, *Int. J. Hydro. Energ.* 37 (2012) 5850-5865.
- [9] Y. Wang, D. Y. C. Leung, J. Xuan, H. Wang, A review on unitized regenerative fuel cell technologies, part-A: Unitized regenerative proton exchange membrane fuel cells, *Renew. Sust. Energ. Rev.* 65 (2016) 961-977.
- [10] T. Ioroi, N. Kitazawa, K. Yasuda, Y. Yamamoto, H. Takenaka, IrO<sub>2</sub>-deposited Pt electrocatalysts for unitized regenerative polymer electrolyte fuel cells, *J. Appl. Electrochem.* 31 (2001) 1179-1183.
- [11] W. Yao, J. Yang, J. Wang, Y. Nuli, Chemical deposition of platinum nanoparticles on iridium oxide for oxygen electrode of unitized regenerative fuel cell, *Electrochem. Comm.* 9 (2007) 1029-1034.
- [12] R. E. Fuentes, H. R. Colón-Mercado, M. J. Martínez-Rodríguez, Pt-Ir/TiC electrocatalysts for PEM fuel cell/electrolyzer process, *J. Electrochem. Soc.* 161 (2013) F77-F82.
- [13] M. Roca-Ayats, G. García, J. L. Galante, M. A. Peña, M. V. Martínez-Huerta, Electrocatalytic stability of Ti based-supported Pt<sub>3</sub>Ir nanoparticles for unitized regenerative fuel cells, *Int. J. Hydro. Energ.* 39 (2014) 5477-5484.
- [14] P. Kúš, A. Ostroverkh, I. Khalakhan, R. Fiala, Y. Kosto, B. Šmíd, Y. Lobko, Y. Yakovlev, J. Nováková, I. Matolínová, V. Matolín, Magnetron sputtered thin-film vertically segmented Pt-Ir catalyst supported on TiC for anode side of proton exchange membrane unitized regenerative fuel cells, *Int. J. Hydro. Energ.* 44 (2019) 16087-16098.
- [15] G. Li, K. Li, L. Yang, J. Chang, R. Ma, Z. Wu, J. Ge, C. Liu, W. Xing, Boosted performance of Ir species by employing TiN as the support toward oxygen

- evolution reaction, *ACS Appl. Mater. Interfaces* 10 (2018) 38117-38124.
- [16] V. K. Puthiyapura, M. Mamlouk, S. Pasupathi, B. G. Pollet, K. Scott, Physical and electrochemical evaluation of ATO supported IrO<sub>2</sub> catalyst for proton exchange membrane water electrolyser, *J. Power Sources* 269 (2014) 451-460.
- [17] H.S. Oh, H.N. Nong, T. Reier, A. Bergmann, M. Gliech, J. Ferreira de Araujo, E. Willinger, R. Schlogl, D. Teschner, P. Strasser, Electrochemical catalyst-support effects and their stabilizing role for IrO<sub>x</sub> nanoparticle catalysts during the oxygen evolution reaction, *J. Am. Chem. Soc.* 138 (2016) 12552-12563.
- [18] J. Polonský, I. M. Petrushina, E. Christensen, K. Bouzek, C. B. Prag, J. E. T. Andersen, N. J. Bjerrum, Tantalum carbide as a novel support material for anode electrocatalysts in polymer electrolyte membrane water electrolyzers, *Int. J. Hydro. Energ.* 37 (2012) 2173-2181.
- [19] V. K. Puthiyapura, S. Pasupathi, H. Su, X. Liu, B. Pollet, K. Scott, Investigation of supported IrO<sub>2</sub> as electrocatalyst for the oxygen evolution reaction in proton exchange membrane water electrolyser, *Int. J. Hydro. Energ.* 39 (2014) 1905-1913.
- [20] S.-Y. Huang, P. Ganesan, H.-Y. Jung, B. N. Popov, Development of supported bifunctional oxygen electrocatalysts and corrosion-resistant gas diffusion layer for unitized regenerative fuel cell applications, *J. Power Sources* 198 (2012) 23-29.
- [21] P. Mazúr, J. Polonský, M. Paidar, K. Bouzek, Non-conductive TiO<sub>2</sub> as the anode catalyst support for PEM water electrolysis, *Int. J. Hydro. Energ.* 37 (2012) 12081-12088.
- [22] C. Rozain, E. Mayousse, N. Guillet, P. Millet, Influence of iridium oxide loadings on the performance of PEM water electrolysis cells: Part II –

- Advanced oxygen electrodes, *Appl. Catal. B* 182 (2016) 123-131.
- [23] S. Choe, B.-S. Lee, M. K. Cho, H.-J. Kim, D. Henkensmeier, S. J. Yoo, J. Y. Kim, S. Y. Lee, H. S. Park, J. H. Jang, Electrodeposited IrO<sub>2</sub>/Ti electrodes as durable and cost-effective anodes in high-temperature polymer-membrane-electrolyte water electrolyzers, *Appl. Catal. B* 226 (2018) 289-294.
- [24] H. Li, Y. Tang, Z. Wang, Z. Shi, S. Wu, D. Song, J. Zhang, K. Fatih, J. Zhang, H. Wang, Z. Liu, R. Abouatallah, A. Mazza, A review of water flooding issues in the proton exchange membrane fuel cell, *J. Power Sources* 178 (2008) 103-117.
- [25] T. Ioroi, T. Oku, K. Yasuda, N. Kumagai, Y. Miyazaki, Influence of PTFE coating on gas diffusion backing for unitized regenerative polymer electrolyte fuel cells, *J. Power Sources* 124 (2003) 385-389.
- [26] U. Wittstadt, E. Wagner, T. Jungmann, Membrane electrode assemblies for unitised regenerative polymer electrolyte fuel cells, *J. Power Sources* 145 (2005) 555-562.
- [27] C. M. Hwang, M. Ishida, H. Ito, T. Maeda, A. Nakano, Y. Hasegawa, N. Yokoi, A. Kato, T. Yoshida, Influence of properties of gas diffusion layers on the performance of polymer electrolyte-based unitized reversible fuel cells, *Int. J. Hydro. Energ.* 36 (2011) 1740-1753.
- [28] C.-M. Hwang, M. Ishida, H. Ito, T. Maeda, A. Nakano, A. Kato, T. Yoshida, Effect of PTFE contents in the gas diffusion layers of polymer electrolyte-based unitized reversible fuel cells, *J. Int. Counc. Electr. Eng.* 2 (2014) 171-177.
- [29] C. M. Hwang, M. Ishida, H. Ito, T. Maeda, A. Nakano, A. Kato, T. Yoshida, Effect of titanium powder loading in gas diffusion layer of a polymer electrolyte unitized reversible fuel cell, *J. Power Sources* 202 (2012) 108-113.

- [30] R. Omrani, B. Shabani, Review of gas diffusion layer for proton exchange membrane-based technologies with a focus on unitised regenerative fuel cells, *Int. J. Hydro. Energ.* 44 (2019) 3834-3860.
- [31] K. Karan, Assessment of transport-limited catalyst utilization for engineering of ultra-low Pt loading polymer electrolyte fuel cell anode, *Electrochem. Comm.* 9 (2007) 747-753.
- [32] Z. Song, M. Norouzi Banis, H. Liu, L. Zhang, Y. Zhao, J. Li, K. Doyle-Davis, R. Li, S. Knights, S. Ye, G. A. Botton, P. He, X. Sun, Ultralow loading and high-performing Pt catalyst for a polymer electrolyte membrane fuel cell anode achieved by atomic layer deposition, *ACS Catal.* 9 (2019) 5365-5374.
- [33] J. Ahn, R. Holze, Bifunctional electrodes for an integrated water electrolysis and hydrogen-oxygen fuel cell with a solid polymer electrolyte, *J. Appl. Electrochem.* 22 (1992) 1167-1174.
- [34] K. Ledjeff, F. Mahlendorf, V. Peinecke, A. Heinzl, Development of electrode/membrane units for the reversible solid polymer fuel cell (RSPFC), *Electrochim. Acta* 40 (1995) 315-319.
- [35] M. A. Tsytkin, E. K. Lyutikova, V. N. Fateev, V. D. Rusanov, Catalytic layers in a reversible system comprising an electrolyzing cell and a fuel cell based on solid polymer electrolyte, *Russ. J. Electrochem.* 36 (2000) 545-548.
- [36] S. A. Grigoriev, P. Millet, K. A. Dzhus, H. Middleton, T. O. Saetre, V. N. Fateev, Design and characterization of bi-functional electrocatalytic layers for application in PEM unitized regenerative fuel cells, *Int. J. Hydro. Energ.* 35 (2010) 5070-5076.
- [37] B.-S. Lee, H.-Y. Park, M. K. Cho, J. W. Jung, H.-J. Kim, D. Henkensmeier, S. J. Yoo, J. Y. Kim, S. Park, K.-Y. Lee, J. H. Jang, Development of porous

- Pt/IrO<sub>2</sub>/carbon paper electrocatalysts with enhanced mass transport as oxygen electrodes in unitized regenerative fuel cells, *Electrochem. Comm.* 64 (2016) 14-17.
- [38] J. S. Lee, J. A. Seo, H. H. Lee, B. R. Min, Salt rejection characterization of PA/PVDF composite membranes prepared by pressurization method, *Chem. Lett.* 44 (2015) 1404-1406.
- [39] K. Gobbels, T. Kuenzel, A. van Ooyen, W. Baumgartner, U. Schnakenberg, P. Braunig, Neuronal cell growth on iridium oxide, *Biomaterials* 31 (2010) 1055-1067.
- [40] Y.-M. Chen, T.-W. Chung, P.-W. Wu, P.-C. Chen, A cost-effective fabrication of iridium oxide films as biocompatible electrostimulation electrodes for neural interface applications, *J. Alloys Compd.* 692 (2017) 339-345.
- [41] T.-W. Chung, C.-N. Huang, P.-C. Chen, T. Noda, T. Tokuda, J. Ohta, Fabrication of iridium oxide/platinum composite film on titanium substrate for high-performance neurostimulation electrodes, *Coatings* 8 (2018) 420-427.
- [42] S. Dutta, S. Shimpalee, J.W.V. Zee, Numerical prediction of mass-exchange between cathode and anode channels in a PEM fuel cell, *Int. J. Heat. Mass. Tran.* 44 (2001) 2029-2042.
- [43] T. A. Zawodzinski, Jr, C. Derouin, S. Radzinski, R. J. Sherman, V.T. Smith, T. E. Springer, S. Gottesfeld, Water uptake by and transport through nafion 117 Membranes, *J. Electrochem. Soc.* 140 (1993) 1041-1047.
- [44] V. Liso, S. Simon Araya, A. C. Olesen, M. P. Nielsen, S.K. Kær, Modeling and experimental validation of water mass balance in a PEM fuel cell stack, *Int. J. Hydro. Energ.* 41 (2016) 3079-3092.
- [45] A. Jayakumar, S. P. Sethu, M. Ramos, J. Robertson, A. Al-Jumaily, A technical

- review on gas diffusion, mechanism and medium of PEM fuel cell, *Ionics* 21 (2015) 1-18.
- [46] P. Antonacci, S. Chevalier, J. Lee, N. Ge, J. Hinebaugh, R. Yip, Y. Tabuchi, T. Kotaka, A. Bazylak, Balancing mass transport resistance and membrane resistance when tailoring microporous layer thickness for polymer electrolyte membrane fuel cells operating at high current densities, *Electrochim. Acta* 188 (2016) 888-897.
- [47] T. V. Reshetenko, G. Bender, K. Bethune, R. Rocheleau, Systematic studies of the gas humidification effects on spatial PEMFC performance distributions, *Electrochim. Acta* 69 (2012) 220-229.
- [48] K. Eom, G. Kim, E. Cho, J. H. Jang, H.-J. Kim, S. J. Yoo, S.-K. Kim, B. K. Hong, Effects of Pt loading in the anode on the durability of a membrane–electrode assembly for polymer electrolyte membrane fuel cells during startup/shutdown cycling, *Int. J. Hydro. Energ.* 37 (2012) 18455-18462.
- [49] S. Choe, B.-S. Lee, J. H. Jang, Effects of diffusion layer (DL) and ORR catalyst (MORR) on the performance of MORR/IrO<sub>2</sub>/DL electrodes for PEM-type unitized regenerative fuel cells, *J. Electrochem. Sci. Technol.* 8 (2017) 7-14.
- [50] S. Song, H. Zhang, X. Ma, Z.-G. Shao, Y. Zhang, B. Yi, Bifunctional oxygen electrode with corrosion-resistive gas diffusion layer for unitized regenerative fuel cell, *Electrochem. Comm.* 8 (2006) 399-405.
- [51] W. H. Lee, H. Kim, Optimization of electrode structure to suppress electrochemical carbon corrosion of gas diffusion layer for unitized regenerative fuel cell, *J. Electrochem. Soc.* 161 (2014) F729-F733.
- [52] H.-Y. Jung, S.-Y. Huang, B.N. Popov, High-durability titanium bipolar plate modified by electrochemical deposition of platinum for unitized regenerative

- fuel cell (URFC), *J. Power Sources* 195 (2010) 1950-1956.
- [53] G. Chen, H. Zhang, H. Zhong, H. Ma, Gas diffusion layer with titanium carbide for a unitized regenerative fuel cell, *Electrochim. Acta* 55 (2010) 8801-8807.
- [54] G. C. da Silva, K. J. J. Mayrhofer, E. A. Ticianelli, S. Cherevko, Dissolution stability: The major challenge in the regenerative fuel cells bifunctional catalysis, *J. Electrochem. Soc.* 165 (2018) F1376-F1384.
- [55] G. C. da Silva, M. R. Fernandes, E. A. Ticianelli, Activity and stability of Pt/IrO<sub>2</sub> bifunctional materials as catalysts for the oxygen evolution/reduction reactions, *ACS Catal.* 8 (2018) 2081-2092.
- [56] J. Zhao, S. Shahgaldi, X. Li, Z. Liu, Experimental observations of microstructure changes in the catalyst layers of proton exchange membrane fuel cells under wet-dry cycles, *J. Electrochem. Soc.* 165 (2018) F3337-F3345.
- [57] J. Kang, J. Kim, Membrane electrode assembly degradation by dry/wet gas on a PEM fuel cell, *Int. J. Hydro. Energ.* 35 (2010) 13125-13130.
- [58] Y. Tang, A. Kusoglu, A.M. Karlsson, M. H. Santare, S. Cleghorn, W. B. Johnson, Mechanical properties of a reinforced composite polymer electrolyte membrane and its simulated performance in PEM fuel cells, *J. Power Sources* 175 (2008) 817-825.
- [59] S. Giancola, M. Zatoń, Á. Reyes-Carmona, M. Dupont, A. Donnadio, S. Cavaliere, J. Rozière, D.J. Jones, Composite short side chain PFSA membranes for PEM water electrolysis, *J. Membr. Sci.* 570-571 (2019) 69-76.
- [60] D. J. Kim, M. J. Jo, S. Y. Nam, A review of polymer–nanocomposite electrolyte membranes for fuel cell application, *J. Ind. Eng. Chem.* 21 (2015) 36-52.
- [61] L. Wang, B. L. Yi, H. M. Zhang, Y. H. Liu, D. M. Xing, Z. G. Shao, Y. H. Cai, Sulfonated polyimide/PTFE reinforced membrane for PEMFCs, *J. Power*

*Sources* 167 (2007) 47-52.

- [62] P. Millet, R. Ngameni, S. A. Grigoriev, V. N. Fateev, Scientific and engineering issues related to PEM technology: Water electrolyzers, fuel cells and unitized regenerative systems, *Int. J. Hydro. Energ.* 36 (2011) 4156-4163.
- [63] S. A. Grigoriev, P. Millet, V. I. Porembsky, V. N. Fateev, Development and preliminary testing of a unitized regenerative fuel cell based on PEM technology, *Int. J. Hydro. Energ.* 36 (2011) 4164-4168.
- [64] J. C. Cruz, V. Baglio, S. Siracusano, R. Ornelas, L. G. Arriaga, V. Antonucci, A. S. Aricò, Nanosized Pt/IrO<sub>2</sub> electrocatalyst prepared by modified polyol method for application as dual function oxygen electrode in unitized regenerative fuel cells, *Int. J. Hydro. Energ.* 37 (2012) 5508-5517.
- [65] J. X. Liu, H. Guo, X. M. Yuan, F. Ye, C. F. Ma, Experimental investigation on two-phase flow in a unitized regenerative fuel cell during mode switching from water electrolyzer to fuel cell, *Int. J. Energ. Res.* 42 (2018) 2823-2834.

# **Chapter 6. A Study on Electrode Fabrication and Operation Variables Affecting the Performance of Anion Exchange Membrane Water Electrolysis**

## **6.1. Introduction**

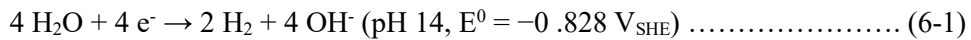
The impacts of global warming and climate change due to increased greenhouse gas emissions have become a serious issue in recent decades [1, 2]. In order to mitigate the effects of climate change, environmentally clean and economically efficient non-carbon fuel should be produced and used to reduce the carbon emissions from fossil fuel consumption [3]. Hydrogen is considered an ideal energy storage medium, converting energy from renewable power sources into chemical bonds with a high energy density, i.e. 33.3 kWh kg<sup>-1</sup> for pressurized hydrogen (200 bar) or for liquid hydrogen (-253 °C) [4, 5]. The use of hydrogen in fuel cell technology is mature and has already been commercialized for large stationary and mobile applications [6]. However, environmentally sustainable production of hydrogen should also be implemented to form complete hydrogen-based energy cycles.

Hydrogen can be generated by different technologies including hydrocarbon steam reforming, gas-shift reaction, biomass gasification, and water splitting through pyrolysis, plasma reforming, and electrolysis. Steam reforming of natural gas by a gas-shift reaction is the most commonly used industrial process for large-scale hydrogen production due to its high thermal efficiency (> 85 %) and low production cost [7]. However, it generates carbon monoxide or dioxide as byproducts from the natural gas decomposition. Biomass gasification can play a significant role in the steady production of hydrogen; however, the non-combustion process still produces a low level of carbon dioxide [8]. Water electrolysis has zero carbon footprint if the process is operated by renewable power sources, e.g. wind, geothermal, or solar energy, opening the door to the possibility of carbon-free and eco-friendly energy cycles.

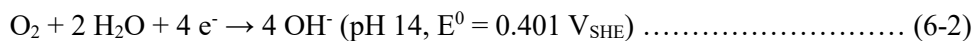
Water electrolysis is categorized into different methods based on the type of electrolyte, operation temperature, and pressure [9]. For example, alkaline water electrolysis (AWE) using diaphragm separators is operated in basic aqueous solutions at low temperature (<80 °C). It is a mature technology and has been industrially implemented for hydrogen production more than 50 years. However, AWE operates in low current densities compared to those using polymer electrolyte membranes [10]. Water electrolysis based on a polymer electrolyte membrane makes the process more energy-efficient and easy to operate for pressurized hydrogen production compared to that using liquid electrolytes, where the membrane separates the hydrogen and oxygen evolution reactors [11]. There are two types of polymer-based water electrolysis; proton exchange membrane based water electrolysis (PEMWE) and anion exchange membrane based water electrolysis (AEMWE).

PEMWE has high operational efficiency from the high ionic conductivity ( $100 \pm 20$  mS cm<sup>-1</sup>), and high current density above 2 A cm<sup>-2</sup>, and high operation pressure up to 700 bar on the prototype level [12]. However, the materials used in PEMWE must sustain its property in highly corrosive condition, i.e. low pH, leading cost issue of using noble catalysts such as Ir and Ru [13]. By contrast, AEMWE alleviates the cost problem as inexpensive hydrocarbon-based membrane and non-noble catalysts can be employed in the alkaline medium. However, AEMWE generally presents low performance compared to PEMWE due to low thermal stability of anion conducting membranes and low activities of non-noble catalysts. In other words, AEMWE has much room to improve the performance. The basic principles of polymer membrane based water electrolysis are described below.

Cathode half-reaction:



Anode half-reaction:



A schematic structure of the membrane reactor comprising the cathode and anode on both sides of the ion-conducting membrane is shown in Figure 6.1, where the proton reduction and water oxidation reactions occur at the cathode and anode, respectively (equation 6-1 and 6-2). In the device operation, a basic aqueous solution is provided to the anode, with a voltage larger than 1.23 V applied between the two electrodes. At the anode, water is oxidized to produce oxygen molecules and electrons. Ionic charge balance of the two electrodes is maintained by hydroxide ion

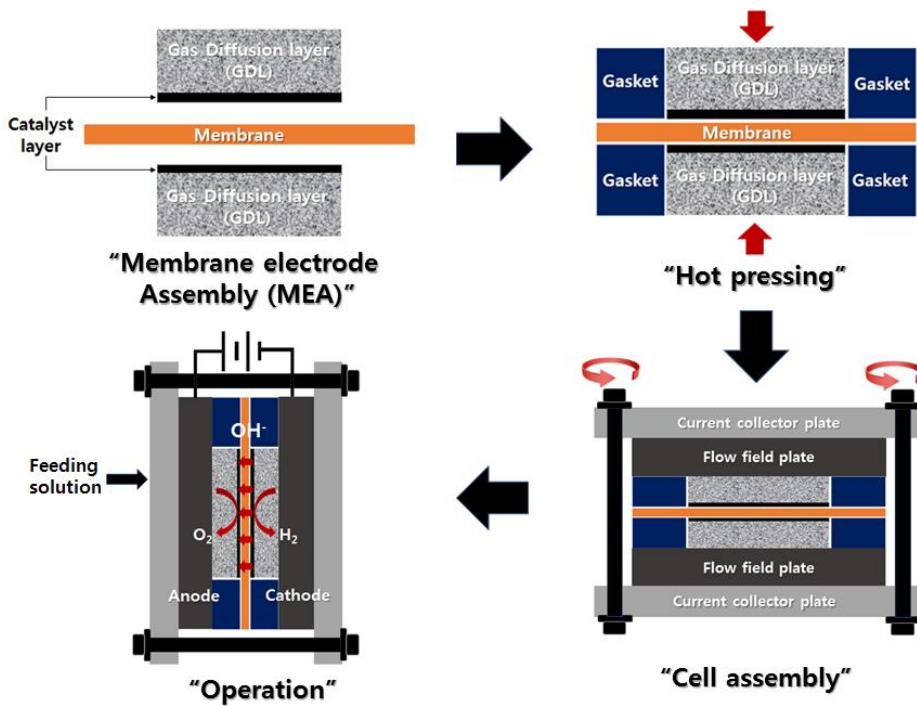


**Figure 6.1.** Schematic procedure of fabrication and operation of the anion exchange membrane water electrolysis cell.

diffusion through the polymer membrane while the proton is reduced at the cathode. Efficient electrochemical reactions require that the kinetics at the catalyst surfaces, ionic transport through the membrane and catalyst layers, and the mass transport of water and gases through the diffusion and catalyst layers be optimized [11, 14].

Inexpensive and efficient device components for alkaline water electrolysis have been widely studied for decades with the goal of improved hydrogen and oxygen evolution reaction (HER and OER) kinetics [15]. In particular, extensive research has been conducted on the development of non-noble catalysts and ion-conducting membranes in alkaline conditions. For non-noble catalysts for HER in alkaline conditions, Ni-based alloy metals or metal oxides, e.g. Ni-Mo, Ni-Zn, Ni-Co, NiFeO<sub>x</sub>, and Ni-based composites have been rigorously studied, showing promising electrocatalytic activity and stability [16, 17]. As examples of promising OER non-noble catalysts, metal oxides such as MnO<sub>x</sub>, CoO<sub>x</sub>, Cu<sub>0.81</sub>Co<sub>2.19</sub>O<sub>4</sub> and NiO<sub>x</sub> [18-21], FeOOH [22] and NiFe-OS [23] are reported, e.g. 10 mA cm<sup>-2</sup> at overpotentials of less than 0.5 V in alkali media. In addition to the catalysts, alkaline-exchange membranes have also been developed, demonstrating high anionic conductivity ranging from 7 to 100 mS cm<sup>-1</sup>, which is comparable to the proton conductivity of Nafion [24-32]. However, the state of operation performance of AEMWE is still significantly lower than that in PEMWE. Despite the large amounts of catalysts used with the developed anion-conducting polymer electrolytes, AEMWE is often reported to have performances less than 20% of those of PEMWE [14, 24, 33]. One of the reasons for low performance is the instability of AEM at high temperature and pressure compared to PEM (e.g. Nafion), which obstructs to scale up AEMWE to commercial level [28].

In addition to material research, determining the proper electrode structures and operation factors of AEMWE to obtain high electrolysis efficiency is nontrivial [10, 11, 18, 29, 34]. To understand the electrochemical behavior of AEMWE in conjunction of complex mass and ionic transport, mathematical modeling was employed to describe experimental results including exchange current density, membrane thickness and the liquid saturation [35]. Many aspects of the electrode structures, e.g. catalyst layer porosity, polymer binder amount and distribution, and exposed active surface area of catalyst, and operation factors, e.g. electrolyte acidity, solution feed methods, or temperature, should be optimized in the device fabrication and operation for efficient production of hydrogen by water splitting hydrogen. For example, the content of a non-ionomeric polytetrafluoroethylene (PTFE) binder in the anode catalyst layer was studied for the efficient and stable operation of AEMWE. The amount and distribution of PTFE in the catalyst layer is one of the essential factors determining the catalyst layer structure. Cell assembly methods, e.g. hot press conditions, were investigated to improve the performance in AEMWE [14]. Hot press conditions (pressure, temperature, process duration) in the electrode fabrication process can alter the electrode structure and pore distribution of the catalyst layer so to change the exposed catalyst area and mass transfer resistances. Further, a few studies reported the effects of device operation factors on the performance of AEMWE, including temperature [36], pH and concentration of the electrolyte solution [24, 37], and electrolyte supply method [11]. The significant dependency of electrolysis performance on various electrode fabrication and operation factors shown in several previous reports indicates that the device performance is determined by complex ensemble effects of many different aspects of cell construction and operation. Therefore, concurrent optimization of different

process components from electrode fabrication to device operation is important to understand the effect of each item on the resulting AEMWE performance.

In this work, we focused to study the influence of cell fabrication and operation parameters with the standard catalysts, iridium oxide and platinum at anode and cathode. We selected four factors, i.e. fabrication pressing conditions for (i) electrode and (ii) cell assembly; (iii) electrolyte pre-feed methods; and (iv) operation temperatures, to clarify the different effect of each items on the AEMWE performance. By the combinatorial controls of the fabrication and operation variable of AEMWE, the impact of each factor on device performance is revealed, resulting in significant improvement of the AEMWE device activity.

## **6.2. Experimental Section**

### **6.2.1. Electrode Preparation**

The membrane electrode assembly (MEA) was fabricated by the catalyst-coated substrate (CCS) method. Iridium oxide ( $\text{IrO}_2$ , Premion®, Alfa Aesar) and platinum on carbon (Pt/C, Pt 46.5 wt%, Tanaka K.K) were used as OER and HER catalysts, respectively. In this study, a metal oxide and precious metal were used, since they are the standard water splitting catalysts, while other electrode fabrication and operational factors were investigated. Carbon paper (TGP-H-120, Toray) and Titanium paper (250  $\mu\text{m}$ , Bekaert) were utilized as the conducting substrates supporting the catalysts for the cathode and anode, respectively. The catalyst ink suspension containing catalyst powder, PTFE (60 wt% PTFE dispersion in  $\text{H}_2\text{O}$ ,

Aldrich), distilled water, and isopropyl alcohol was sprayed onto the GDL and Ti paper to form the catalyst layer. Before spraying, the catalyst suspension was homogenized in an ultrasonic bath for 1 h. The content of PTFE binder was 20 and 9.1 wt.% for the anode and cathode catalyst layers, respectively. Then, the electrodes were sintered at 350 °C in Ar gas. Finally, an anion exchange membrane (FAA-3-PK-75) was sandwiched, or hot-pressed, between two sintered electrodes to form the MEA of 6.25 cm<sup>2</sup> in the electrolytic cell. Hot pressing was performed at 50 °C and 395 psi. The temperature and pressure were not controlled to higher value because of the degradation problem of anion exchange membrane. For the electrochemical measurement, Au-coated Ti and graphite bipolar plates were used as the current collectors on the anode and cathode sides of the cell, respectively. The assembly torque used to construct the cell was controlled as shown in Table 1. A pressure measurement film (Prescale LLLW, Fujifilm) was utilized to measure the contact pressure applied between the electrode and current collector under different cell assembly torques.

### **6.2.2. Electrochemistry and Physical Characterization**

The electrolysis performance of AEMWE was measured using a high-current potentiostat (HCP-803, Bio-Logic). The device was operated at 50 °C unless otherwise stated. The current and voltage relationship of the AEMWE was obtained during the voltage cycling, which ranged from 1.5 to 2.2 V<sub>cell</sub> at a scan rate of 20 mV s<sup>-1</sup>. Before the water splitting operation, the electrolyte solution was pre-fed to the anode for 24 h, if necessary (Table 1). During electrolysis, 0.5 M KOH aqueous electrolyte solution was fed to the anode with a 1 mL min<sup>-1</sup> flow rate. In between

electrolysis operations, electrochemical impedance spectroscopy (EIS) was conducted at 1.8 V<sub>cell</sub> with an AC frequency ranging from 10 kHz to 30 mHz and an alternating voltage amplitude of 10 mV. The surface morphology of the electrodes was observed by scanning electron microscopy (SEM, Teneo VS<sup>TM</sup>). The porosity of the catalyst layer coated on the gas diffusion layer was studied by mercury porosimetry (Mercury intrusion porosimetry, Autopore 9600).

### 6.3. Results and Discussion

Effects of the electrode fabrication and operation factors on the hydrogen production performance by AEMWE were studied and are summarized in Table 6.1 and Figure 6.2. Three main parameters—the apparent electron transfer kinetics, mass transport, and ion conductivity—considerably determine the performance of electrolytic devices. However, the key factors of AEMWE mentioned are greatly affected by the electrode fabrication methods and operation variables as shown below. For example, the apparent electron transfer rate of electrocatalysis is directly proportional to the electrochemically active surface area (ECSA) of the catalyst layer [38]. The ion conductivity and chemical mass transport including the ECSA are also determined by the catalyst layer structure including the distribution of ionomeric binder and pores in the catalyst layer [14, 33, 39]. The ionic conductivity of the polymeric binder and membrane electrolyte is strongly influenced by humidity or chemical environments constructed under specific operation conditions. As shown in Table 6.1 and Figure 6.2, the AEMWE performance varied by more than three times from 293 to 983 mA cm<sup>-2</sup> at approximately 1.8 V<sub>cell</sub> when conducting

**Table 6.1.** AEMWE current density at 1.8 V with different variables employed in the cell fabrication and operation. The electrolysis current was obtained at 50<sup>th</sup> cycle in voltage cycle operation from 1.5 to 2.2 V except the measurements at different operation temperatures. For the temperature controlled operations, current density at 1.8 V was averaged during 60 min of chronoamperometry.

Sample #	Controlled Variable		MEA Press Time (min)	Cell Assemble Torque (Nm)	Pre-feed Time (h)	Operation Temp. (°C)	j at 1.8 V (mA/cm <sup>2</sup> )
1	Fabrication	MEA Press Time	0	4	24	50	478
2			1				457
3			3				293
4		Cell Assemble Torque	0	3	24	50	242
5				4			478
6				5			356
7	Operation	Pre-feed Time	0	4	0	50	303
8					24		478
9		Temp.	0	4	24	50	460
10						60	607
11						70	625
12						80	870
13						90	983

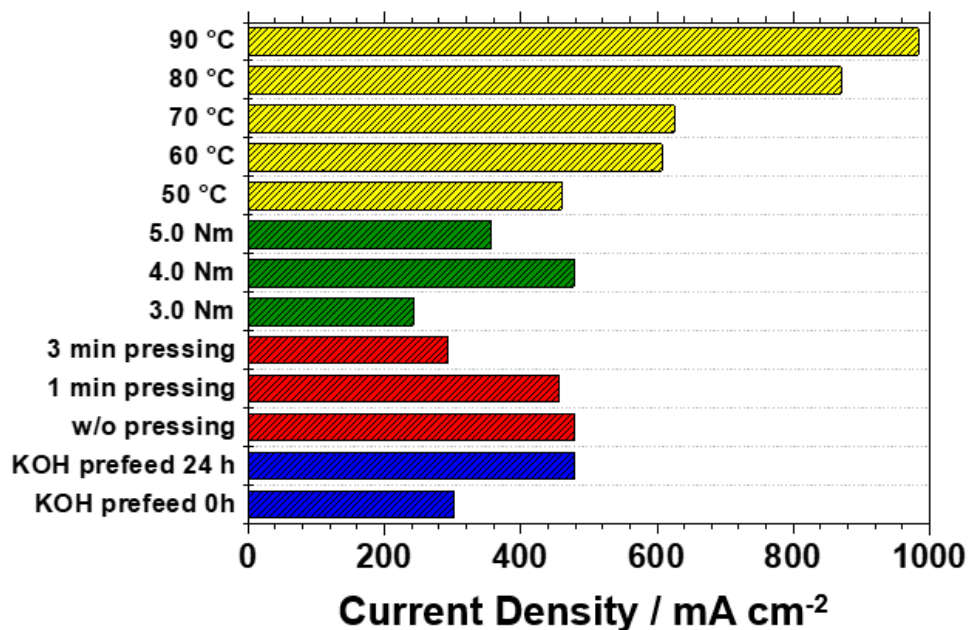


**Figure 6.2.** Performance summary of AEMWE cells with different fabrication and operation variables. The displayed performance is the current density at 1.8 V measured at 50<sup>th</sup> cycle in voltage cycle operation from 1.5 to 2.2 V. However, for the temperature controlled operation, current density at 1.8 V was averaged during 60 min of chronoamperometry. Factors of the AEMWE fabrication and operation are summarized in Table 1.

combinatorial control of the catalyst layer and MEA construction methods and operation variables. The effects of each variable on the cell performance are discussed below in detail.

### **6.3.1 Effect of Membrane Electrode and Device Assembly Method**

Previous reports of single-cell tests of AEMWE have shown MEAs fabricated both using hot pressing [14, 40-42] and without heating or pressing [11, 43-47]. In the previous study investigating the MEA pressing process, hot pressing (395 psi of applied pressure at 25, 50, and 80 °C for 1 min) was performed to enhance the performance by reducing the interface resistance between the GDL and the membrane [14]. Cho et al. reported that the higher pressing temperature has a positive effect on polarization resistance, but ohmic resistance is increased due to membrane degradation if the process is conducted above a certain temperature; the optimum hot press temperature was 50 °C [13].

In this study, the pressing time was controlled (0, 1, and 3 min) at 50 °C and 395 psi. The highest water electrolysis performance was shown in the case of MEA without pressing (Figure 6.3(a)), which differed from previous studies where the press process was advantageous for the water splitting, probably due to different membrane properties, i.e., the thickness, mechanical strength, etc., employed in MEA (see below). In this work, the MEAs were constructed either without or with 1 or 3 min of hot pressing (see Experimental section and Table 1). In the lower cell voltage region, the current densities of MEAs formed by 1 and 3 min pressing were similar but were lower than the current density of the MEA constructed without pressing. For example, the electrolysis current densities were 118, 118, and 161 mA

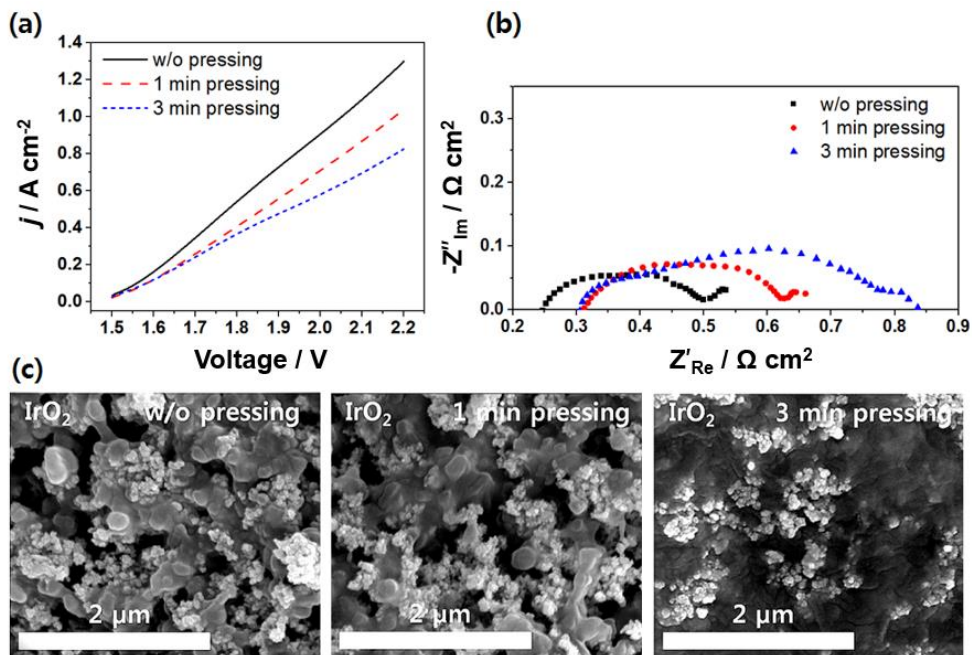


**Figure 6.3.** (a) Current-voltage relationship, (b) Nyquist plot, and (c) SEM images of the anode catalyst layer surface of AEMWE cells with different press time used in the electrode fabrication (0, 1, and 3 min.). PEIS was measured at 500<sup>th</sup> cycle at 1.8 V.

$\text{cm}^{-2}$  at  $1.6 V_{\text{cell}}$  for the cell fabricated with 3, 1, and 0 min of pressing, respectively. The decreased performance of MEA assembled with hot pressing can be explained by the reduced active surface area of the catalysts by increase PTFE coverage of catalytic active sites and structural deformation of the catalyst layers after the press process (Figure 6.3). The electrolysis performance at low overpotentials, or low current densities, is largely determined by the reaction kinetics and catalyst activity rather than the ionic conductivity or mass transport. In other words, the ohmic drop ( $iR$ ) is smaller in the low current region, and mass transport hindrance is also negligible when the reaction rate is low. The water splitting current in MEAs with 1 and 3 min hot pressing was identical at the voltages smaller than  $1.7 V_{\text{cell}}$ , but the MEA with 1 min pressing shows an approximately 20 % higher electrolysis current compared to that with 3 min pressing. As the press time increases, pores in catalysts becomes smaller by agglomeration of PTFE surrounded catalysts (Figure 6.3(c)). In addition, the binder, i.e. PTFE, is hydrophobic and non-ion conducting. It induces harsher condition for reactant water and ion approaching to catalysts. The mass limitation or ohmic voltage drop issue becomes more serious in high current operation. IV curve also reveals that larger current differences at a higher cell voltage, which implies a longer pressing time leads to increased mass transport resistance in addition to reduced catalyst surfaces.

The electrochemical and structural impacts of the hot press process on the catalyst layer are revealed in EIS plots and SEM images (Figure 6.3(b) and 6.3(c)). The high frequency x-axis intercept of the Nyquist plot in EIS spectra indicates that the hot press process induces an increase in ohmic resistance of approximately 0.25 and 0.31  $\Omega \text{ cm}^2$  without and with the hot press process, respectively (Figure 6.3(b)). The hot

press process also noticeably changed the porous composite of catalyst and polymeric binder seen at the catalyst layer surface (porosity shown in Figure 6.4) and the PTFE binder penetrated the interparticle spaces and blocked the anode catalyst surface (Figure 6.3(c)). However, the effect of pressing was not clear in the cathode surfaces under SEM measurements (Figure 6.5). As the anode and cathode catalyst are layered on carbon and metallic supports with different mechanical properties, e.g. structural rigidity, the press process results in the increased ohmic, charge, and mass transport resistances of each electrode differently. The structural deformation of the catalyst layer by hot pressing is the main reason behind the performance degradation as no change in membrane conductivity and thickness was observed after the pressing process (see below).

To further understand the effect of pressing on the structural deformation of MEA, the pore volume distribution of the electrodes was measured through mercury porosimetry (Figure 6.4). The primary pores between the catalysts and polymer composites in the electrodes were small, with a diameter of a few tens to hundreds of nanometers (Figure 6.4(a)). The peak pore volume of the cathode catalyst layer decreased from approximately 0.18 to 0.13 mL g<sup>-1</sup> at a pore diameter of 0.038 to 0.034 μm in the cathodes after the hot press. However, the effect of hot press duration was negligible in the primary pore distribution and no meaningful difference was detected between cathodes with 1 and 3 min pressing. The reduced primary pore volume and distribution changes in the porosimetry clearly demonstrate that the press process decreases the electrocatalytic active surface area and causes severe electrode agglomeration. As shown in Figure 6.4(b), the peak volume of the larger secondary pores of the cathode also decreased by approximately 30 % from 5 to 3.5

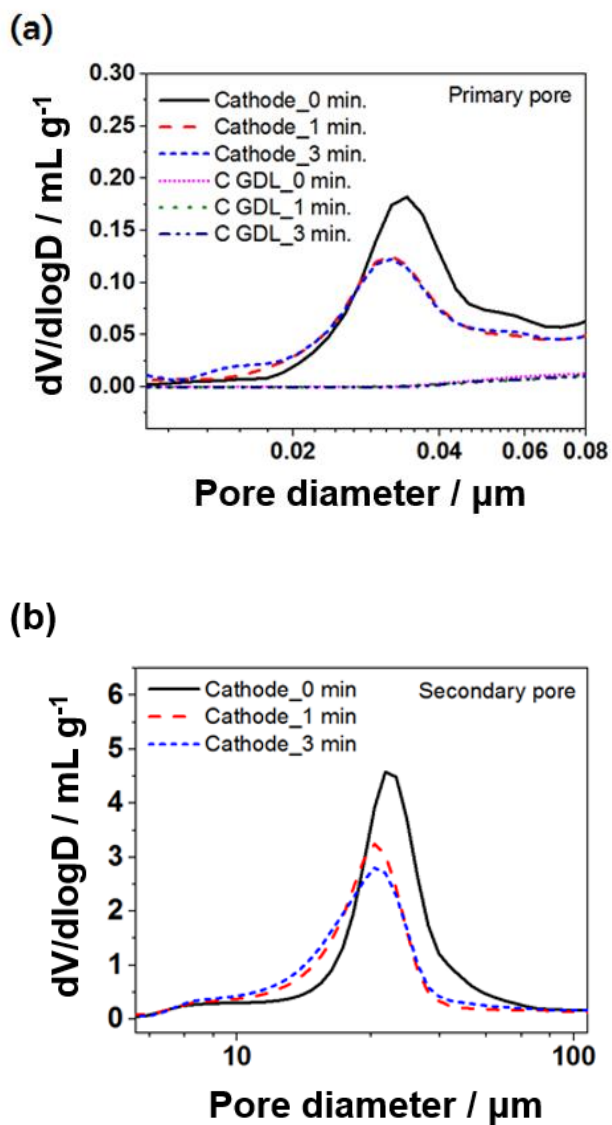


**Figure 6.4.** (a) Primary pore and (b) secondary pore distribution of cathode with different press time used in the electrode fabrication (0, 1, and 3 min.). The pore distribution is measured by mercury porosimetry.

mL g<sup>-1</sup> due to the press process. Along with the volume changes, the press process decreases the peak secondary pore diameter from 27.58 to 25.62 μm. The secondary pores exist mainly in the GDL since the catalyst layer is thinner (1.96 μm) than the secondary pore size, so the changes in the secondary pores imply that deformation occurred in the GDL and impacted the mass transport of produced H<sub>2</sub>, O<sub>2</sub> and water through the diffusion medium. Similarly, the pore structure of the anode was clearly deformed by the hot press process, as shown in the supporting information (Figures 6.5 and 6.6). However, the weight-averaged pore volume of the anode coated on the titanium GDL is an order smaller than that of those on the carbon GDL.

In addition to the electrode fabrication method, one of the assembly variables in the device construction step—the torque applied to the cell assembly—was controlled which affects the electric contact resistance of the MEA. Using carbon and titanium GDLs with thicknesses of 370 and 250 μm, respectively, the surface pressure applied between the GDL and current collector was measured at different cell assembly torques. As water electrolysis forms liquid and gaseous reactants and products, the device must be airtight to prevent fluid leakage. The contact between the electrode and current collector should also be intact and allow electric conductivity through the end-plate to the catalyst surface. However, when the assembly torque is too high, the cell components, specifically the catalyst layer, GDL, and membrane electrolyte, would be mechanically damaged between the two metal end-plates. Any non-ideal deformation of the cell components induces performance degradation because it hinders the electronic, ionic, and mass transportation through the devices. For the device components used in this study, we found that 3 Nm of cell assembly torque was not high enough to prevent fluid leakage through the gaps

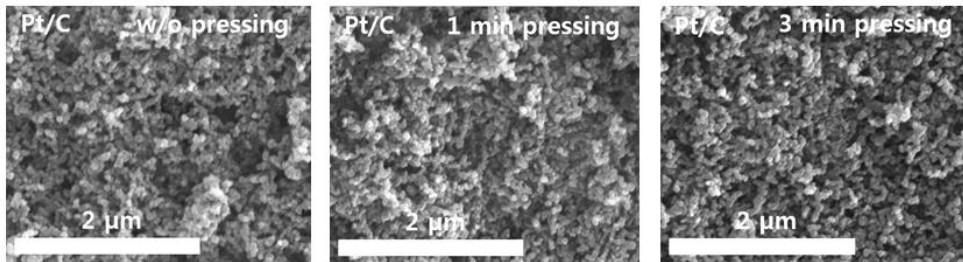


**Figure 6.5.** SEM images of the cathode catalyst layer surface of AEMWE cells with different press time used in the electrode fabrication (0, 1, and 3 min.).

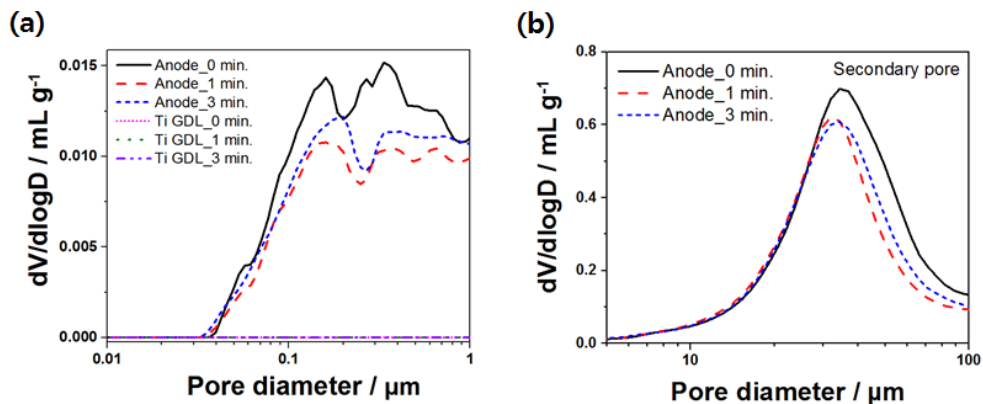


**Figure 6.6.** (a) Primary pore and (b) secondary pore distribution of anode electrodes with different press time used in the electrode fabrication (0, 1, and 3 min.). The pore distribution is measured by mercury porosimetry.

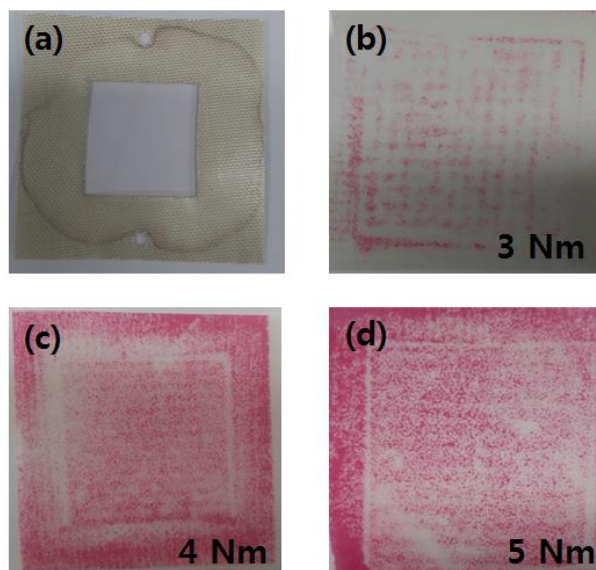


**Figure 6.7.** (a) The picture of gasket with contamination after the operation in the case of 3 Nm cell assembly. The results of pressure-film after application of (b) 3Nm, (c) 4Nm, (d) 5 Nm assemble torque on the cell.

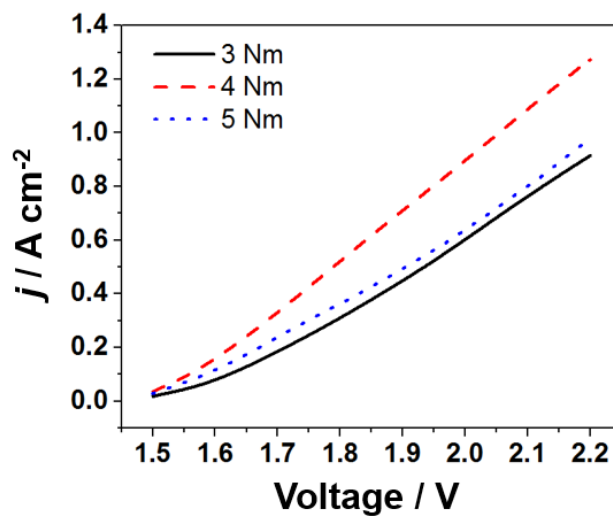


**Figure 6.8.** Linear sweep voltammetry with different torque of cell assembly.

between the electrodes and gaskets (Figure 6.7(a) and 6.7(b)). When the assembly torque increased from 3 to 4 Nm and 5 Nm, a uniform pressure applied to the electrode was observed using the pressure measurement film (Figure 6.7(c) and 6.7(d)). The water splitting performance was also improved with the increased assembly torque (Figure 6.8). However, if the assembly torque was too large, e.g. 5 Nm, the performance was decreased compared to the case of 4 Nm presumably by the mechanical deformation that occurred under the high pressure. Thus, we found the optimized torque of cell assembly to be 4 Nm in this study, which resulted in an electrolysis current density of  $478 \text{ mA cm}^{-2}$  at  $1.8 \text{ V}_{\text{cell}}$  (Figure 6.8).

### **6.3.2 Effect of Electrolyte Solution Feed Method and Operation Temperature**

The membrane in the AEMWE is the core component, separating the gas product and transporting ions to complete the electrochemical reaction of the cell. High ionic conductivity of the membrane is essential for high performance of water electrolysis with low ohmic loss. The hydroxide ion conduction in the AEM are mainly through the Grotthuss mechanism as in water [48, 49]. In the Grotthuss mechanism, hydroxide ions are diffused via hydrogen bonded water molecules. Thus, ion diffusion occurs along with the water in the membrane and the ionic conductivity of the electrolyte membrane is a significant function of the water content.

In order to ensure facile ion transport through the membrane from the beginning of electrolysis operation, the electrolyte membrane should be sufficiently wetted. The polymer functional group in the membrane should possess  $\text{OH}^-$  rather than other anions such as  $\text{Br}^-$ , since ion conduction in the membranes significantly relies not

only on the mobility but also on the concentration of hydroxide ions. This anion substitution process is called OH<sup>-</sup> doping in the anion exchange electrolyte membrane. Luo et al. reported that ion conductivity in an anion exchange membrane is significantly affected by alkali doping, which decreases the conductivity activation energy with increased doping until reaching saturation [50].

In this study, the ohmic resistance, i.e. the ion transfer resistance, was measured at an open-circuit voltage by EIS. The ohmic resistances showed a sharp decrease in the first 5 h of the OH<sup>-</sup> doping process using a 0.5 M KOH solution with a flow rate of 1 mL min<sup>-1</sup> (Figure 6.9(a)). The decrease in ohmic resistance was smaller after the 5 h pre-feeding process, then decreased more gradually for up to approximately 24 h.

The water splitting performance measured after different pre-feeding durations indicates that the MEA activation, or OH<sup>-</sup> doping, requires a longer time to reach a level of doping that ensures its maximum current (Figure 6.10). The results show that the MEA requires additional time to stabilize, as demonstrated in the comparison between the case of 8 and 24 h feeding times (Figure 6.10). The initial electrolysis performance was higher and showed a lower ohmic resistance with 24 h of pre-feeding compared to those without or with only 8 h of pre-feeding. The activation step is related to the fluid flow through the catalyst layer, and insignificant performance enhancement or ohmic resistance drop occurs if the AEM is simply immersed in a 1 M KOH aqueous solution for 24 h (Figure 6.10). Since the ionic transport limitation becomes important given the large current flows, the performance differences become larger with the applied cell voltage increase between the devices with different pre-feeding methods. The electrolysis current

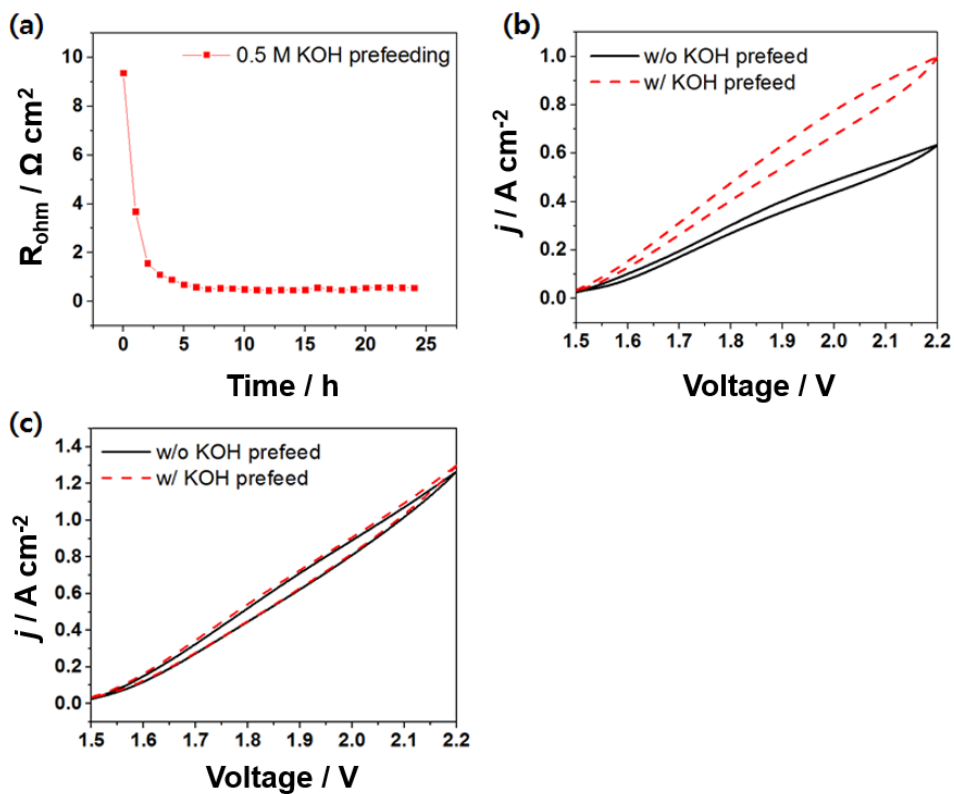


**Figure 6.9.** (a) Ohmic resistance change in the continuous solution feed of 0.5 M KOH electrolyte solution to AEMWE single cell. CVs at (b) 50<sup>th</sup> and (c) 500<sup>th</sup> cycle with and without 24 h of electrolyte pre-feed to AEMWE cell. The ohmic resistance was measured in EIS at open circuit voltage. CVs were measured at a scan rate of 20 mV/s.

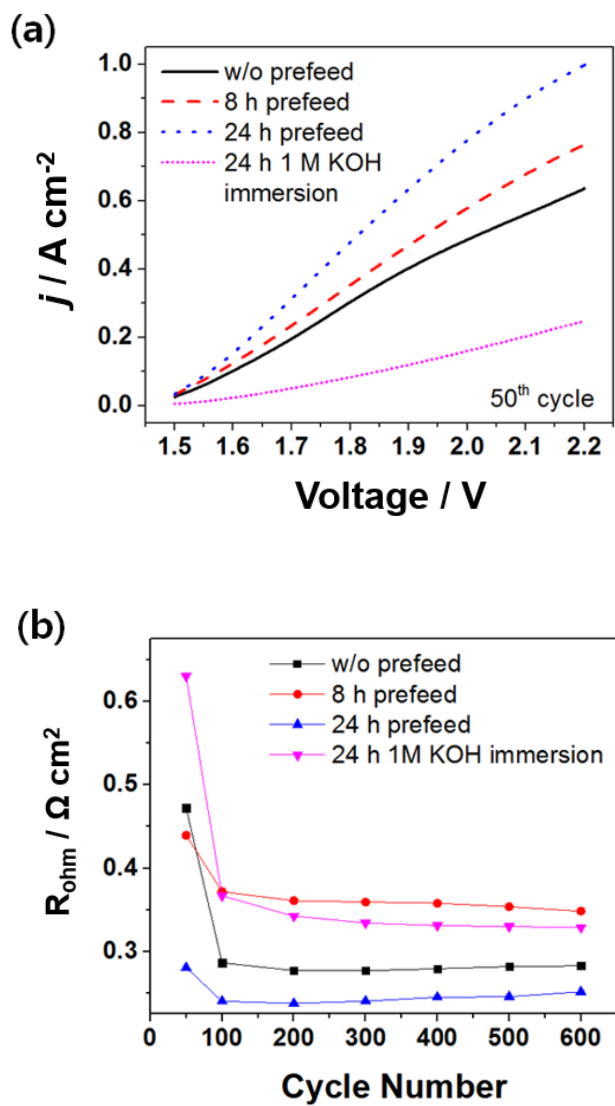


**Figure 6.10.** (a) Linear sweep voltammetry and (b) ohmic resistance with different solution.

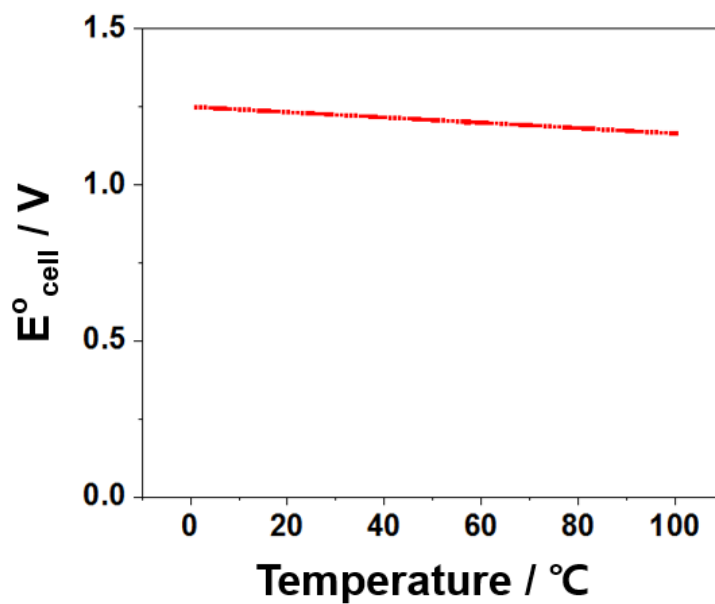


**Figure 6.11.** Calculated open circuit voltage of water electrolysis versus temperature from 0 to 100  $^{\circ}\text{C}$ .

density differences were 53 and 361 mA cm<sup>-2</sup> at 1.6 and 2.2 V<sub>cell</sub> respectively, between MEA with 0 and 24 h of pre-feeding operation at the beginning of the cell operation. However, the performance difference caused by the pre-feeding process disappears when the electrolysis cell is operated for a few hours (Figures 6.9(b) and 6.9(c)). It is highly likely that electrolysis does what the pre-soak is doing in the initial AEMWE operation. The gradual performance enhancement of AEMWE in continuous operation without the pre-feed process implies that the catalyst layer and electrolyte membrane is doped by OH<sup>-</sup> during the water splitting operation and the pre-feeding is only effective at the initial stage of AEMWE cell operation (Figure 6.9(c)).

Lastly, the effect of temperature was investigated by controlling the cell operation temperature from 50 to 90 °C. The enhancement of electrolysis performance with temperature increase was also briefly reported elsewhere. [36, 51] In general, the cell voltage considering different voltage loss terms is expressed by equation (6-3),

$$E_{\text{Cell}} = E^{\circ} + \eta_{\text{Ca.}} + \eta_{\text{An.}} + iR_{\text{Ohm}} + iR' \dots\dots\dots(6-3)$$

where the open-circuit voltage ( $E^{\circ}$ ) of water electrolysis is the thermodynamic value and a function of the temperature (Figure 6.11). The variation of  $E^{\circ}$  can be described by equation (6-4), where ( $d E^{\circ}/dT$ ) is the temperature coefficient of the electrochemical reactions.

$$E^{\circ}(T_2) = E^{\circ}(T_1) + (d E^{\circ}/dT)(T_2-T_1) \dots\dots\dots(6-4)$$

In this equation, the isothermal temperature coefficient, ( $d E^{\circ}/dT$ ), for the OER reaction is calculated as  $-0.846 \text{ mV deg}^{-1}$  considering the entropy changes near room temperature given that HER is  $0.000 \text{ mV deg}^{-1}$  [52]. Thus, chronoamperometry was used to consider the onset of potential changes in water electrolysis at different

temperatures (Figure 6.12(a)). The overvoltage applied to the cell at each temperature is the same, 0.591 V, and the increase in current density was approximately 50 mA cm<sup>-2</sup> per 10 °C. This result implies that the ionic conductivity (Figure 6.13) and catalytic activity increase at higher temperatures. In addition to the improved kinetics of electrochemical reactions, the higher ionic conductivity through the Grotthuss mechanism in the range of 0–100 °C at a higher temperature is likely the reason for the performance improvements [53]. Though the hydrogen bonding strength decreases with increased temperature, the ionic conductivity by ionic hopping conduction reportedly improves in this temperature range [53].

In order to elucidate the enhanced ionic conduction and electron transfer kinetics with increased temperature, electrochemical impedance spectroscopy was conducted on the AEMWE at the different operational temperatures. As the Nyquist plot shows, both ohmic resistance and polarization resistance decrease consistently as temperature increases (Figures 6.12(b) and 6.13). For example, when the cell temperature increases from 50 °C to 90 °C, reduction ratios are 22.6 % (0.239 Ω cm<sup>2</sup> → 0.185 Ω cm<sup>2</sup>) for the ohmic resistance and 21.9% (0.219 Ω cm<sup>2</sup> → 0.171 Ω cm<sup>2</sup>) for the polarization resistance. The current obtained at 90 °C, averaged 0.983 A cm<sup>-2</sup> at 1.8 V<sub>cell</sub>, is approximately twice of that at 50 °C and is one of the high performance among the reported values of the AEMWE (Figures 6.14 and 6.15).

In summary, we examined the effect of cell operation variables on solid-state alkaline water electrolysis. Pre-feeding the electrolyte 24 h before cell operation accelerates ionic transport through membrane activation. For pressing of MEA, the negative effects due to the change in the structure of the catalyst layer is greater than the reduction in contact resistance from pressing. Since cell assembly torque influences the pressure of contact between the electrodes and membrane, cell

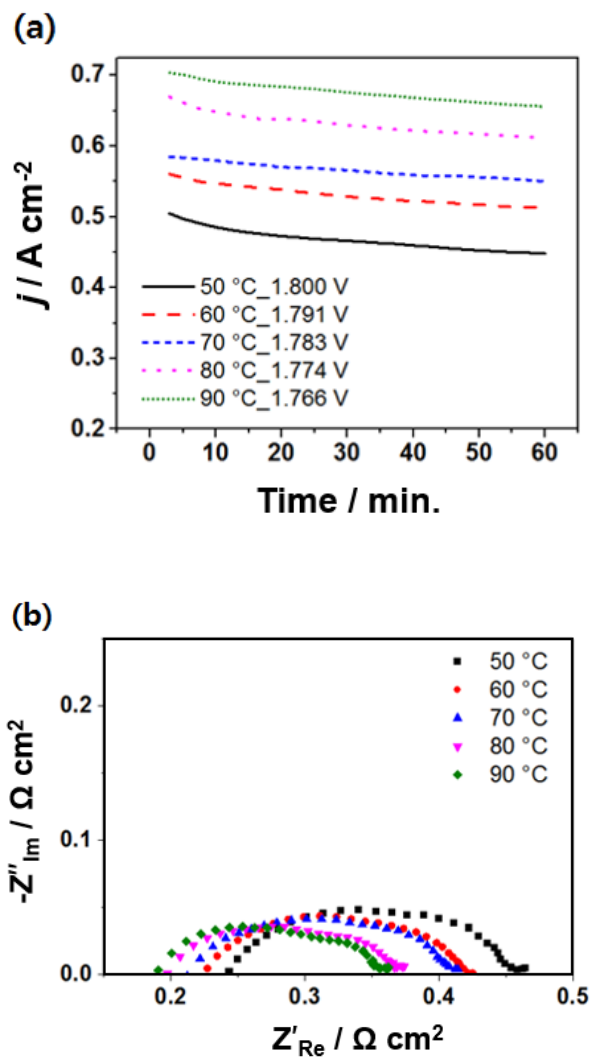


**Figure 6.12.** (a) Chronoamperograms and (b) EIS Nyquist plots of the AEMWE cell operated at different temperatures from 50 to 90 °C. The chronoamperometry and EIS was performed at the identical overvoltage of 0.59 V at different operational temperatures.

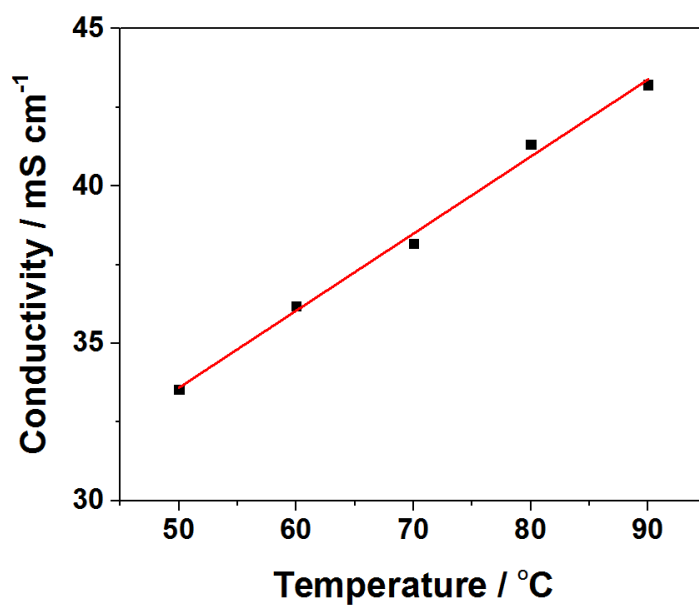


**Figure 6.13.** Conductivity of electrolysis cell based on ohmic resistance measured by impedance spectroscopy during cell-operation. (Assume ion transport resistance in the membrane dominates the ohmic resistance during the operation of the electrolysis cell.)

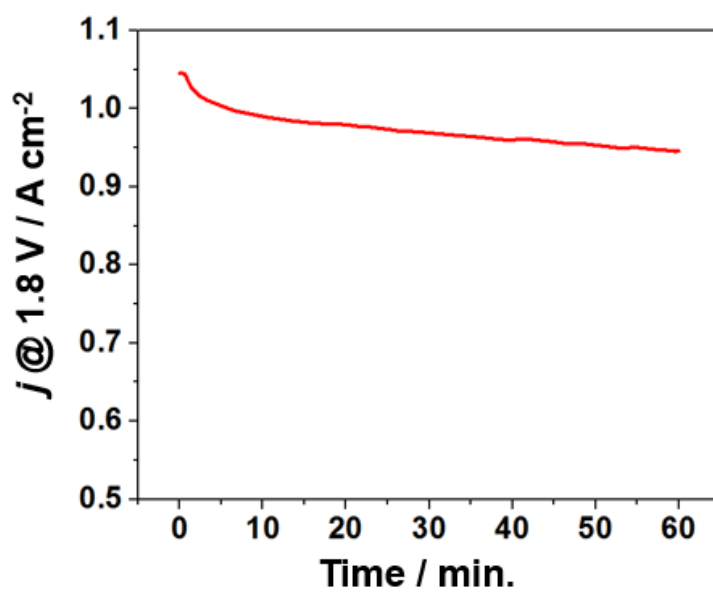


**Figure 6.14.** Chronoamperometry of 90 °C operation at 1.8 V (w/o pressing, 4 Nm torque of cell assembly, 24 h 0.5 M KOH prefeed) for 1 hour.

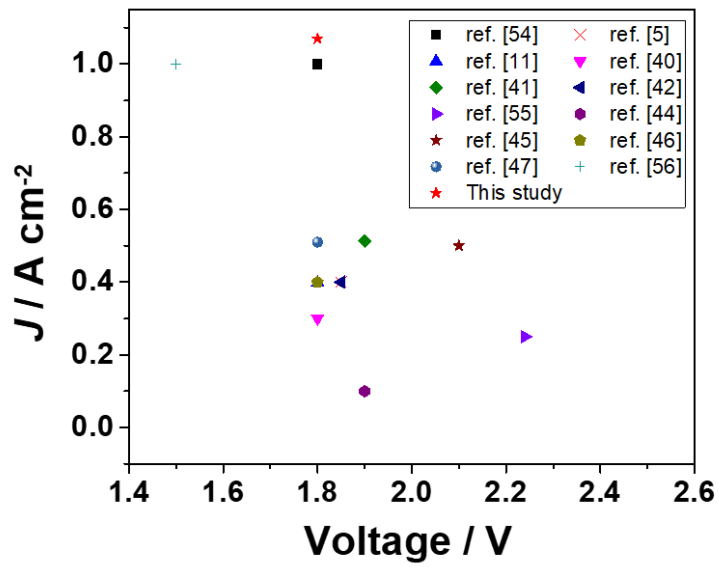


**Figure 6.15.** Comparison of AEMWE performance with other research.

integration, gas leakage, chemical mass transport, and mechanical deformation of the electrode, an optimum value of 4 Nm was found in this study. Lastly, the higher cell temperature significantly activates both ionic conduction and catalyst activity so to enhance the water electrolysis performance. This study provides insights to reduce the gap between the developed material properties and device performance in electrolysis, showing meaningful performance enhancement by solely controlling the electrode fabrication and operation factors when utilizing standard materials.

## 6.4. Conclusions

In this study, electrode fabrication and operation factors including 1) the pressing process during electrode-electrolyte membrane assembly, 2) the cell assembly torque, 3) the electrolyte solution pre-feeding method, and 4) the operating temperature were studied to determine the effects on water electrolysis. The best performance of AEMWE with FAA-3 membranes was approximately  $1 \text{ A cm}^{-2}$  at 1.8 V (average of 1 h operation) when the optimum fabrication methods, i.e. no MEA press and 4 Nm cell assembly torque, and operational factors, i.e. 24 h of electrolyte pre-feed and 90 °C operation temperature, were applied. The engineering factors affect the electrolysis performance in numerous ways, and ion conductivity in the membrane and catalyst layers, gas permeability, and catalytic activity are largely determined by the fabrication and operation variables. Herein, the crucial effect of external parameters on the performance of AEMWE was revealed by physical and electrochemical analysis on the cell, leading to a current density more than three times higher at 1.8 V following parameter optimization. Although this study used

standard noble catalysts, the principles presented in this research can also be applied to AEMWE using non-noble catalysts to achieve high performance, which contributes to commercialization of AEMWE.

## 6.5. References

- [1] E. Kintisch, New push focuses on quick ways to curb global warming, *Science* 324 (2009) 323.
- [2] B. Obama, The irreversible momentum of clean energy, *Science* 355 (2017) 126-129.
- [3] R. A. KERR, The carbon cycle and climate warming: Learning how carbon cycles through the environment, with and without human intervention, is crucial to predicting the greenhouse effect, *Science* 222 (1983) 1107-1108.
- [4] P. P. Edwards, V. L. Kuznetsov, W. I. F. David, Hydrogen energy, *Phil. Trans. R. Soc. A* 365 (2007) 1043-1056.
- [5] S. Dutta, A review on production, storage of hydrogen and its utilization as an energy resource, *J. Ind. Eng. Chem.* 20 (2014) 1148-1156.
- [6] J. Garche, L. Jörissen, Applications of fuel cell technology: Status and perspectives, *Electrochem. Soc. Interface* 24 (2015) 39-43.
- [7] J. D. Holladay, J. Hu, D.L. King, Y. Wang, An overview of hydrogen production technologies, *Catal. Today* 139 (2009) 244-260.
- [8] M. F. Demirbas, Hydrogen from various biomass species via pyrolysis and steam gasification processes, *Energy Sources* 28 (2006) 245-252.
- [9] M. Götz, J. Lefebvre, F. Mörs, A. M. Koch, F. Graf, S. Bajohr, R. Reimert, T.

- Kolb, Renewable power-to-gas: A technological and economic review, *Renew. Energy* 85 (2016) 1371-1390.
- [10] D. Pletcher, X. Li, Prospects for alkaline zero gap water electrolyzers for hydrogen production, *Int. J. Hydro. Energ.* 36 (2011) 15089-15104.
- [11] Y. Leng, G. Chen, A. J. Mendoza, T. B. Tighe, M. A. Hickner, C.-Y. Wang, Solid-state water electrolysis with an alkaline membrane, *J. Am. Chem. Soc.* 134 (2012) 9054-9057.
- [12] U. Babic, M. Suermann, F. N. B. uchi, L. Gubler, T. J. Schmidt, Review—Identifying critical gaps for polymer electrolyte water electrolysis development, *J. Electrochem. Soc.* 164 (2017) F387-F399
- [13] M. Carmo, D. L. Fritz, J. Mergel, D. Stolten, A comprehensive review on PEM water electrolysis, *Int. J. Hydro. Energ.* 38 (2013) 4901-4934.
- [14] M. K. Cho, H.-Y. Park, S. Choe, S. J. Yoo, J. Y. Kim, H.-J. Kim, D. Henkensmeier, S. Y. Lee, Y.-E. Sung, H. S. Park, J. H. Jang, Factors in electrode fabrication for performance enhancement of anion exchange membrane water electrolysis, *J. Power Sources* 347 (2017) 283-290.
- [15] H. Osgood, S. V. Devaguptapu, H. Xu, J. Cho, G. Wu, Transition metal (Fe, Co, Ni, and Mn) oxides for oxygen reduction and evolution bifunctional catalysts in alkaline media, *Nano Today* 11 (2016) 601-625.
- [16] M. Gong, D.-Y. Wang, C.-C. Chen, B.-J. Hwang, H. Dai, A mini review on nickel-based electrocatalysts for alkaline hydrogen evolution reaction, *Nano Research* 9 (2016) 28-46.
- [17] P.T. Babar, A.C. Lokhande, E. Jo, B.S. Pawar, M.G. Gang, S.M. Pawar, J.H. Kim, Facile electrosynthesis of Fe (Ni/Co) hydroxyphosphate as a bifunctional electrocatalyst for efficient water splitting, *J. Ind. Eng. Chem.* 70 (2019) 116-212

123.

- [18] S. Jung, C. C. L. McCrory, I. M. Ferrer, J. C. Peters, T. F. Jaramillo, Benchmarking nanoparticulate metal oxide electrocatalysts for the alkaline water oxidation reaction, *J. Mater. Chem. A* 4 (2016) 3068-3076.
- [19] R. Frydendal, E. A. Paoli, B. P. Knudsen, B. Wickman, P. Malacrida, I. E. L. Stephens, I. Chorkendorff, Benchmarking the stability of oxygen evolution reaction catalysts: The importance of monitoring mass losses, *ChemElectroChem* 1 (2014) 2075-2081.
- [20] P. T. Babar, A. C. Lokhande, M. G. Gang, B. S. Pawar, S. M. Pawar, J. H. Kim, Thermally oxidized porous NiO as an efficient oxygen evolution reaction (OER) electrocatalyst for electrochemical water splitting application, *J. Ind. Eng. Chem.* 60 (2018) 493-497.
- [21] W. S. Choi, M. J. Jang, Y. S. Park, K. H. Lee, J. Y. Lee, M. H. Seo, S. M. Choi, Three-dimensional honeycomb-Like  $\text{Cu}_{0.81}\text{Co}_{2.19}\text{O}_4$  nanosheet arrays supported by Ni foam and their high efficiency as oxygen evolution electrodes, *ACS Appl. Mater. Interfaces* 10 (2018) 38663-38668.
- [22] J. Lee, H. Lee, B. Lim, Chemical transformation of iron alkoxide nanosheets to  $\text{FeOOH}$  nanoparticles for highly active and stable oxygen evolution electrocatalysts, *J. Ind. Eng. Chem.* 58 (2018) 100-104.
- [23] H. Kim, J. Kim, S. H. Ahn, Monitoring oxygen-vacancy ratio in NiFe-based electrocatalysts during oxygen evolution reaction in alkaline electrolyte, *J. Ind. Eng. Chem.* 72 (2019) 273-280.
- [24] L. Zeng, T. S. Zhao, Integrated inorganic membrane electrode assembly with layered double hydroxides as ionic conductors for anion exchange membrane water electrolysis, *Nano Energy* 11 (2015) 110-118.

- [25] Q. Duan, S. Ge, C.-Y. Wang, Water uptake, ionic conductivity and swelling properties of anion-exchange membrane, *J. Power Sources* 243 (2013) 773-778.
- [26] H. Yanagi, K. Fukuta, Anion exchange membrane and ionomer for alkaline membrane fuel cells (AMFCs), *ECS trans.* 16 (2008) 257-262.
- [27] D. Aili, A. G. Wright, M. R. Kraglund, K. Jankova, S. Holdcroftb, J. O. Jensen, Towards a stable ion-solvating polymer electrolyte for advanced alkaline water electrolysis, *J. Mater. Chem. A* 5 (2017) 5055-5066.
- [28] D. Chen, M.A. Hickner, Degradation of imidazolium- and quaternary ammonium-functionalized poly(fluorenyl ether ketone sulfone) anion exchange membranes, *ACS Appl. Mater. Interfaces* 4 (2012) 5775-5781.
- [29] X. Ren, S.C. Price, A.C. Jackson, N. Pomerantz, F.L. Beyer, Highly conductive anion exchange membrane for high power density fuel-cell performance, *ACS Appl. Mater. Interfaces* 6 (2014) 13330-13333.
- [30] A. Konovalova, H. Kim, S. Kim, A. Lim, H. S. Park, M. R. Kraglund, D. Aili, J. H. Jang, H.-J. Kim, D. Henkensmeier, Blend membranes of polybenzimidazole and an anion exchange ionomer (FAA3) for alkaline water electrolysis: Improved alkaline stability and conductivity, *J. Membr. Sci.* 564 (2018) 653-662.
- [31] A. Marinkas, I. Strużyńska-Piron, Y. Lee, A. Lim, H. S. Park, J. H. Jang, H.-J. Kim, J. Kim, A. Maljusch, O. Conradi, D. Henkensmeier, Anion-conductive membranes based on 2-mesityl-benzimidazolium functionalised poly(2,6-dimethyl-1,4-phenylene oxide) and their use in alkaline water electrolysis, *Polymer* 145 (2018) 242-251.
- [32] V. Vijayakumar, S. Y. Nam, Recent advancements in applications of alkaline anion exchange membranes for polymer electrolyte fuel cells, *J. Ind. Eng. Chem.*

70 (2019) 70-86.

- [33] W. Xu, K. Scott, The effects of ionomer content on PEM water electrolyser membrane electrode assembly performance, *Int. J. Hydro. Energ.* 35 (2010) 12029-12037.
- [34] J. E. Park, S. Y. Kang, S.-H. Oh, J. K. Kim, M. S. Lim, C.-Y. Ahn, Y.-H. Cho, Y.-E. Sung, High-performance anion-exchange membrane water electrolysis, *Electrochim. Acta* 295 (2019) 99-106.
- [35] L. An, T. S. Zhao, Z. H. Chai, P. Tan, L. Zeng, Mathematical modeling of an anion-exchange membrane water electrolyzer for hydrogen production, *Int. J. Hydro. Energ.* 39 (2014) 19869-19876.
- [36] C. C. Pavel, F. Cecconi, C. Emiliani, S. Santuccioli, A. Scaffidi, S. Catanorchi, M. Comotti, Highly efficient platinum group metal free based membrane-electrode assembly for anion exchange membrane water electrolysis, *Angew. Chem. Int. Ed.* 53 (2014) 1378-1381.
- [37] H. Ito, N. Kawaguchi, S. Someya, T. Munakata, N. Miyazaki, M. Ishida, A. Nakano, Experimental investigation of electrolytic solution for anion exchange membrane water electrolysis, *Int. J. Hydro. Energ.* 43 (2018) 17030-17039.
- [38] C. Chaiburi, V. Hacker, Catalytic activity of various platinum loading in acid electrolyte at 303 K, *Energy Procedia* 138 (2017) 229-234.
- [39] G. Jeong, M. Kim, J. Han, H.-J. Kim, Y.-G. Shul, E. Cho, High-performance membrane-electrode assembly with an optimal polytetrafluoroethylene content for high-temperature polymer electrolyte membrane fuel cells, *J. Power Sources* 323 (2016) 142-146.
- [40] T. Pandiarajan, L.J. Berchmans, S. Ravichandran, Fabrication of spinel ferrite based alkaline anion exchange membrane water electrolyzers for hydrogen

- production, *RSC Adv.* 5 (2015) 34100-34108.
- [41] S. Seetharaman, R. Balaji, K. Ramya, K.S. Dhathathreyan, M. Velan, Graphene oxide modified non-noble metal electrode for alkaline anion exchange membrane water electrolyzers, *Int. J. Hydro. Energ.* 38 (2013) 14934-14942.
- [42] L. Xiao, S. Zhang, J. Pan, C. Yang, M. He, L. Zhuang, J. Lu, First implementation of alkaline polymer electrolyte water electrolysis working only with pure water, *Energ. Environ. Sci.* 5 (2012) 7869-7871.
- [43] X. Wu, K. Scott, A Li-doped Co<sub>3</sub>O<sub>4</sub> oxygen evolution catalyst for nonprecious metal alkaline anion exchange membrane water electrolyzers, *Int. J. Hydro. Energ.* 38 (2013) 3123-3129.
- [44] X. Wu, K. Scott, A polymethacrylate-based quaternary ammonium OH<sup>-</sup> ionomer binder for non-precious metal alkaline anion exchange membrane water electrolyzers, *J. Power Sources* 214 (2012) 124-129.
- [45] M. Faraj, M. Boccia, H. Miller, F. Martini, S. Borsacchi, M. Geppi, A. Pucci, New LDPE based anion-exchange membranes for alkaline solid polymeric electrolyte water electrolysis, *Int. J. Hydro. Energ.* 37 (2012) 14992-15002.
- [46] J. Parrondo, C. G. Arges, M. Niedzwiecki, E. B. Anderson, K. E. Ayers, V. Ramani, Degradation of anion exchange membranes used for hydrogen production by ultrapure water electrolysis, *RSC Adv.* 4 (2014) 9875-9879.
- [47] J. Parrondo, M. George, C. Capuano, K.E. Ayers, V. Ramani, Pyrochlore electrocatalysts for efficient alkaline water electrolysis, *J. Mater. Chem. A* 3 (2015) 10819-10828.
- [48] C. Chen, Y.-L. S. Tse, G. E. Lindberg, C. Knight, G. A. Voth, Hydroxide solvation and transport in anion exchange membranes, *J. Am. Chem. Soc.* 138 (2016) 991-1000.

- [49] S. Maurya, S.-H. Shin, Y. Kim, S.-H. Moon, A review on recent developments of anion exchange membranes for fuel cells and redox flow batteries, *RSC Adv.* 5 (2015) 37206–37230.
- [50] H. Luo, G. Vaivars, B. Agboola, S. Mu, M. Mathe, Anion exchange membrane based on alkali doped poly(2,5-benzimidazole) for fuel cell, *Solid State Ion.* 208 (2012) 52-55.
- [51] V. K. Puthiyapura, S. Pasupathi, H. Su, X. Liu, B. Pollet, K. Scott, Investigation of supported IrO<sub>2</sub> as electrocatalyst for the oxygen evolution reaction in proton exchange membrane water electrolyser, *Int. J. Hydro. Energ.* 39 (2014) 1905-1913.
- [52] A. J. deBethune, T. S. Licht, N. Swendeman, The temperature coefficients of electrode potentials, *J. Electrochem. Soc.* 106 (1959) 616-625.
- [53] E. Gileadi, E. Kirowa-Eisner, Electrolytic conductivity—the hopping mechanism of the proton and beyond, *Electrochim. Acta* 51 (2006) 6003-6011.
- [54] X. Wu, K. Scott, Cu<sub>x</sub>Co<sub>3-x</sub>O<sub>4</sub> (0 ≤ x < 1) nanoparticles for oxygen evolution in high performance alkaline exchange membrane water electrolyzers, *J. Mater. Chem.* 21 (2011) 12344-12351.
- [55] T.-C. Cao, X. Wu, K. Scott, A quaternary ammonium grafted poly vinyl benzyl chloride membrane for alkaline anion exchange membrane water electrolyzers with no-noble-metal catalysts, *Int. J. Hydro. Energ.* 37 (2012) 9524–9528.
- [56] F. Allebrod, C. Chatzichristodoulou, M. B. Mogensen, Alkaline electrolysis cell at high temperature and pressure of 250 °C and 42 bar, *J. Power Sources* 229 (2013) 22-31.

# Chapter 7. Conclusions

## 7.1. Summary

Unitized regenerative fuel cell (URFC) is one of the best eco-friendly electrochemical device for energy conversion and storage, which can operate as both fuel cell (FC) to produce power and electrolysis cell (EC) to produce fuel. It has higher specific energy, e.g. 400-1000 Wh/kg including weight of gas tanks, compared to secondary batteries [1]. Among URFC, UR-PEMFC is the most mature state as much as already applied in some area, e.g. aerospace, but low round trip efficiency (< 60 %) and a cost issue from metal components and high noble catalysts block its large-scale commercialization [2]. Especially, oxygen reactions, i.e. OER and ORR, are sluggish and determine the performance. Ir/Ir oxide and Pt are known as the best OER and ORR electrocatalysts, respectively, which are expensive due to its rareness, e.g. \$0.03/g (Co), \$0.01/g (Ni), \$55.5-56.2/g (Ir) and \$27.8/g (Pt) [3]. To overcome the issue of high loading of noble catalysts up to 4 mg cm<sup>-2</sup> in UR-PEMFC, electrodeposited IrO<sub>2</sub> on Ti (e-IrO<sub>2</sub>/Ti) was tried to be introduced in UR-PEMFC in this research, which had been previously reported as high electrolysis performance with less than 0.5 mg cm<sup>-2</sup> of noble metal in the oxygen electrode of PEMWE [4, 5]. Not only high mass activity compared to the spray-electrode, but also enhancement of stability of the electrode from IrO<sub>2</sub> coating effect on Ti PTL are expected in UR-PEMFC [4]. Here, three aspects of studies were done to maximize the efficiency of the e-IrO<sub>2</sub>/Ti electrode in UR-PEMFC: i) catalysts (chapter 2), ii)

amphiphilic treatment of Ti electrode (chapter 3,4) and iii) operation (chapter 5).

In chapter 2, sequential electrodeposition of Pt and IrO<sub>2</sub> (e-Pt@IrO<sub>2</sub>) was performed on Ti PTL to overcome the limitation of active surface area of IrO<sub>2</sub> by single electrodeposition. Catalysts composed of hemispheric Pt core and IrO<sub>2</sub> shell were formed on Ti fibers without exposure of Pt. Surface area of IrO<sub>2</sub> thin film increased 2.5x by hemispheric Pt supports from 12.6 m<sup>2</sup> gr<sup>-1</sup> to 30.9 m<sup>2</sup> gr<sup>-1</sup>. Compared to the spray coated IrO<sub>2</sub> electrode (s-IrO<sub>2</sub>), hydrophilicity of the e-Pt@IrO<sub>2</sub> electrode and higher electrochemical surface area resulted in 56x higher catalysts activity, i.e. 44 A mg<sub>Ir</sub><sup>-1</sup> @ 2.0 V. Enhanced active surface area, improved electrical conductivity and facile mass transport of e-Pt@IrO<sub>2</sub> led superior current density in EC operation, i.e. 7.1 A cm<sup>-2</sup> @ 2.0 V. In addition, e-Pt@IrO<sub>2</sub> was utilized in FC operation by reduction of surface IrO<sub>2</sub> to Ir and 49 % of round trip efficiency was achieved using only 0.83 mg<sub>(Pt+Ir)</sub> cm<sup>-2</sup> of noble catalysts in the cell. In long term tests, insignificant degradation rate of 155 μV h<sup>-1</sup> at 0.4 A cm<sup>-2</sup> was observed in the EC mode during URFC operation.

In chapter 3, the amphiphilic e-IrO<sub>2</sub>/Ti electrode was fabricated by patterning of hydrophobic PDMS polymer brush on the hydrophilic e-IrO<sub>2</sub>/Ti electrode. On one hand, hydrophobicity of PTL is critical for water management in FC due to flooding issue [6], but on the other hand, hydrophilic PTL facilitates transport of liquid water to catalysts in EC. To solve paradoxical requirements of PTL in UR-PEMFC, patterning of hydrophobic/hydrophilic ways in the oxygen electrode of e-IrO<sub>2</sub>/Ti PTL was applied. In the oxygen electrode composed of e-IrO<sub>2</sub> and s-Pt without patterning, hydrophilic IrO<sub>2</sub> catalysts induce severe flooding in FC operation and hydrophobic Pt catalysts increase overvoltage from mass transport limitation in EC operation. Interestingly, amphiphilic e-IrO<sub>2</sub>/Ti PTL enhances mass transport in both

FC and EC by formation of direct pathway of gas and water. Current density enhanced 4.3x @ 0.6 V in FC and 1.9x @ 1.8 V in EC from amphiphilic patterning on Ti PTL. In EC, overvoltage from mass transport resistance @ 2 A cm<sup>-2</sup> was decreased 35.6x by patterning of hydrophobic channels. In durability tests for 160 h, performance degradation, e.g. degradation rate about 0.6 mV h<sup>-1</sup>, was observed from loss of active surface area of Pt catalyst, but the effect of amphiphilic PTL was maintained. In other words, polymer coating on Ti PTL is thermally and chemically stable during URFC operation.

In chapter 4, the basic principle of SECM is introduced with experiments, and the effect of the amphiphilic Ti PTL is verified using OER-ORR (substrate generation-tip collection, SG-TC) mode in SECM. In basic experiments, difference of general disk electrodes and UME, characteristics of UME, and methods of leveling the substrate using UME in SECM are explained. For example, increase of  $i_T/i_{T,\infty}$  is observed as a UME tip close to conductive substrates in redox couple solution, e.g.  $[\text{Fe}(\text{CN})_6]^{4-}/[\text{Fe}(\text{CN})_6]^{3-}$ , due to change of local electrochemical formal potential from the Nernst equation. With this principle, topography of Ti PTL was analyzed using SECM and its effect on O<sub>2</sub> detection was demonstrated. When the UME tip was closer than 20 μm on Ti PTLs, higher amount of O<sub>2</sub> was detected above pores compared to above Ti fibers in Ti PTLs, but geometrical effect was negligible as the tip was far as much as 30 μm in the case of e-IrO<sub>2</sub>/Ti PTL without patterning, i.e. random O<sub>2</sub> diffusion. ORR detection of UME tip above 30 μm of backside of the amphiphilic Ti PTL during OER (SG-TC) was performed to confirm the O<sub>2</sub> emission through hydrophobic channels in the patterned amphiphilic Ti PTL in chapter 3. The effect was verified in two ways: i) line scan and ii) points detection. For instance, the distance between the highest peak O<sub>2</sub> detection points in hydrophobic region during

the line scan was exactly 250  $\mu\text{m}$ , which is the period of pattern distance.

In chapter 5, operation configuration and relative humidity (RH) of fuels are controlled in UR-PEMFC. In general configuration, gases in reactions are identical in the same electrode of UR-PEMFC, e.g. OER and ORR at the same electrode (hydrogen and oxygen electrode configuration, HOEC). However, if same reduction or oxidation reactions occur at the same electrode (reduction and oxidation electrode configuration, ROEC), the advantages of each electrode are maximized, i.e. the hydrophilic e-IrO<sub>2</sub>/Ti electrode and the hydrophobic Pt/C/C electrode as the oxygen electrode of EC and FC, respectively. From estimated calculation of water distribution through RH control in two configurations, it was figured out that the ohmic resistance and the performance of FC is significantly affected by anode water flux (AWF) in ROEC and by total water flux in HOEC. In ROEC, AWF is the highest at RH 100 (An.) / RH 100 (Ca.), results in lowest ohmic resistance. Thus, the highest performance was shown in ROEC at RH 100, e.g. 1.9 A cm<sup>-2</sup> @ 0.6 V, unlike severe flooding in FC was observed in HOEC due to the hydrophilic oxygen electrode. With understanding of water distribution effect on the performance, 51% round trip efficiency @ 0.4 A cm<sup>-2</sup> was achieved only using 0.65 mg cm<sup>-2</sup> of noble catalysts in the cell.

Additionally, the effects of electrode fabrication and operation variables on performance of AEMWE are studied in chapter 6. AEMWE has great potential, which has advantages in the aspect of cost from non-noble catalysts and inexpensive membrane, but lower performances have been reported compared to PEMWE. In addition to material researches such as catalysts and membrane, the engineering factors are significantly important in the device performance. To enhance the performance of AEMWE, the effects of electrode fabrications, i.e. MEA pressing

and cell assemble torque, and operation factors, i.e. electrolyte pre-feeding and operating temperature, were analyzed. For instance, ohmic resistance was decreased 94 % from pre-feeding of electrolyte to the cell and current density was increased 50 mA cm<sup>-2</sup>@ 0.591 V of overvoltage as 10°C increase of temperature (50-90°C) from reduction of kinetic and ohmic resistance. By optimizing factor, 1 A cm<sup>-2</sup> @ 1.8 V was accomplished in AEMWE, which is more than three times enhancement by controlling engineering factors. From the study, we explained how these engineering factors have influence on ion transport, gas permeability and catalytic activity.

From the research, highly efficient UR-PEMFCs were developed with low amount of noble catalysts less than 1 mg cm<sup>-2</sup> of noble catalysts by approaching studies in three aspects, i.e. catalyst, PTL and operation, which contribute to one step closer to wide commercialization of UR-PEMFC.

## 7.2. Perspectives

Here, stable electrodes resistant to corrosion including reduced noble catalysts were studied utilizing e-IrO<sub>2</sub>/Ti in UR-PEMFC. In addition, effects of amphiphilic PTL and operation configuration on water distribution and performance were discussed. However, still many further researches are required to solve technical challenges for development of UR-PEMFC up to wide commercialization state, e.g. heavy weight, stable MEA during repetition of FC-EC cycling, support materials for catalysts in the oxygen electrode of EC and membrane, etc.

Since the main challenge in UR-PEMFC is substitution of carbon materials in PEMFC to obtain stable electrodes during EC operation without compromising the performance of FC. To replace carbon supports in bifunctional oxygen catalysts

(OER/ORR), Pt on IrO<sub>2</sub> [7], Pt and IrO<sub>2</sub> on Sb-doped SnO<sub>2</sub> [8], Pt and Ir on TiO<sub>2</sub> [9], Pt<sub>3</sub>Ru on TiCN [10], etc. were tried. In addition to stable support materials from the oxidative condition, degradation of catalysts on supports from dissolution, agglomeration and migration of catalysts during long term electrochemical operation is the further important remaining challenge. To replace carbon PTL (C PTL), Ti-felt [11-16], Ti-mesh [17-19], PtTi screen [20-22] were generally reported since titanium (Ti) has good electric conductivity, e.g. resistivity of 42 μΩ · m, and electrochemically stable in oxidative condition compared to carbon materials. However, surface of Ti PTL is more hydrophilic than C PTL and most cases using Ti PTL did not solve the flooding issue in FC at RH 100 [11, 13-16]. To ameliorate water management, PTFE coating on Ti PTL [13-16] and Ti powder including PTFE as MPL [12] were studied, but further studies for the optimum structure of Ti PTLs including control of hydrophobicity and hydrophilic property is still required to manage water properly in UR-PEMFC. As we tried in the research, development of amphiphilic PTL and MPL can be the solution for satisfying water management in both FC and EC and the direction of further research in UR-PEMFC.

In addition, membranes are critical for stable MEA, but few researches are reported related to application of reinforced membranes in UR-PEMFC. To prevent gas crossover or electrical short during long-term operation of UR-PEMFC, a thicker membrane is needed but it increases performance loss from ohmic resistance. If swelling ratio of membrane is large, detachment of MEA during repetition of FC-EC cycling can occur due to difference of water content, which leads degradation of the cell. Development of thermo-mechanically and chemically stable and thin reinforced membranes and introduction of reinforced membranes to UR-PEMFC will play an innovative role in improving stability of MEA and purity of gas. Further, much more

complicated additional factors should be considered and optimized for commercialization of UR-PEMFC, such as auxiliary components for heat control system, water management, gas storage and pressure control.

In commercialization aspects, there are a lot of potential fields URFC can be applied, such as aerospace, aviation, transportation, portable applications, power supply and renewable energy grids (Figure 7.1). For example, URFC is one of the best electrochemical device to store and convert energy in renewable energy grids [23]. There is surplus energy produced from renewables, e.g. wind and solar energy. URFC can act as peak shaver in this case and store additional energy as hydrogen form. In addition, difference of produced renewable energy and energy demand is occurred through time (Figure 7.2). When produced energy is greater than energy demand, surplus energy can store in the form of hydrogen by electrolysis. On the other hand, when energy demand is higher than produced energy, power can be supplied using FC operation in UR-PEMFC. Although it is discrete RFCs, several RFCs connected with renewables are already reported worldwide. For instance, National Aeronautics and Space Administration (NASA) installed RFCs delivering electrical energy scale of 38-40 kWh/cycle in 2005 [24]. In 2008, the institute of Residential-scale Integrated Renewable Energy Experiment (IRENE) tested and verified the usefulness of RFCs for produced surplus H<sub>2</sub> from renewables [25]. URFCs can also be applied in transport system such as zero-emission vehicles (ZEVs) combined with the battery engine by generation of hydrogen fuels using renewables during off-peak time and operation using generated fuels [26, 27]. Unfortunately, it is economical to use URFCs in combination with battery systems due to the cost issue. However, if cost-efficient substitutes are developed in future, it would be possible to dream of a world of URFC vehicles replacing EV or FCEV.

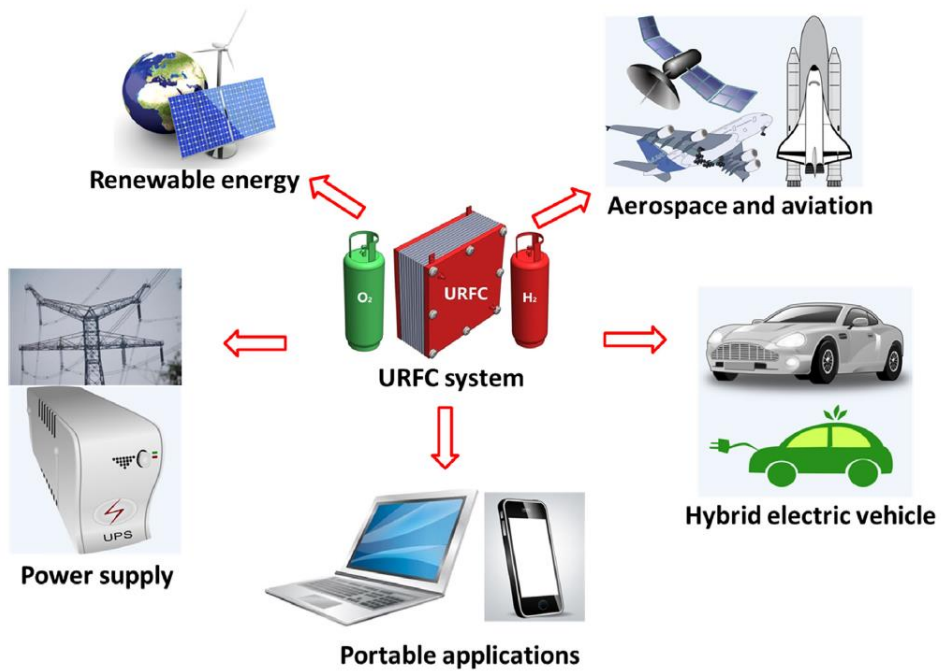


**Figure 7.1.** Schematic example fields of applications of URFC systems. (Adapted from Y. Wang et al., *Renew. Sust. Energ. Rev.* 65 (2016) 961-977.)

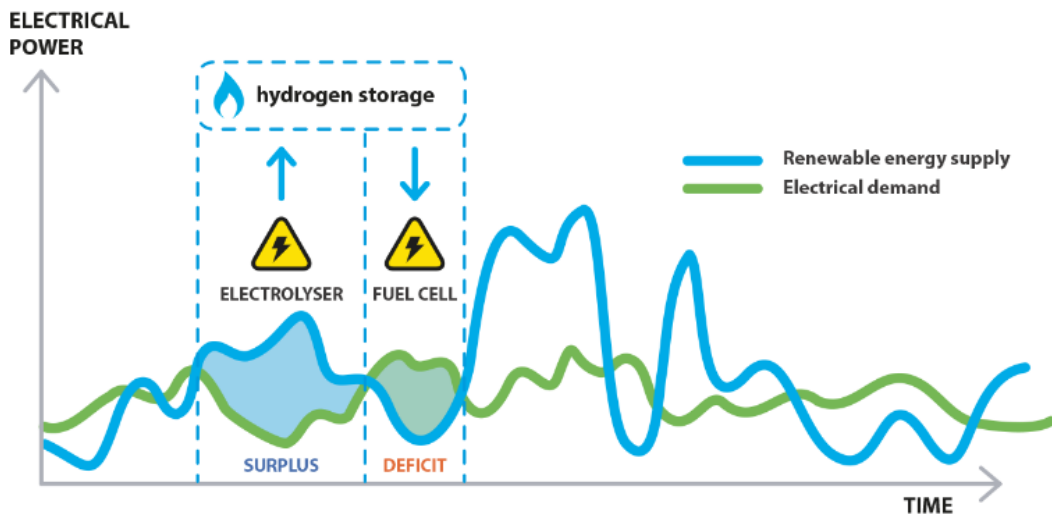


**Figure 7.2.** A schematic example of power curve of renewable energy supply and electrical demand through time. (Adapted from <https://hydron-energy.com>)

### 7.3. References

- [1] F. Mitlitsky, B. Myers, A.H. Weisberg, Regenerative fuel cell systems, *Energ. Fuel.* 12 (1998) 56-71.
- [2] Y. Wang, D. Y. C. Leung, J. Xuan, H. Wang, A review on unitized regenerative fuel cell technologies, part-A: Unitized regenerative proton exchange membrane fuel cells, *Renew. Sust. Energ. Rev.* 65 (2016) 961-977.
- [3] [https://en.wikipedia.org/wiki/Prices\\_of\\_chemical\\_elements](https://en.wikipedia.org/wiki/Prices_of_chemical_elements).
- [4] S. Choe, B.-S. Lee, M. K. Cho, H.-J. Kim, D. Henkensmeier, S. J. Yoo, J. Y. Kim, S. Y. Lee, H. S. Park, J. H. Jang, Electrodeposited IrO<sub>2</sub>/Ti electrodes as durable and cost-effective anodes in high-temperature polymer-membrane-electrolyte water electrolyzers, *Appl. Catal. B* 226 (2018) 289-294.
- [5] B.-S. Lee, S. H. Ahn, H.-Y. Park, I. Choi, S. J. Yoo, H.-J. Kim, D. Henkensmeier, J. Y. Kim, S. Park, S. W. Nam, K.-Y. Lee, J. H. Jang, Development of electrodeposited IrO<sub>2</sub> electrodes as anodes in polymer electrolyte membrane water electrolysis, *Appl. Catal. B* 179 (2015) 285-291.
- [6] H. Li, Y. Tang, Z. Wang, Z. Shi, S. Wu, D. Song, J. Zhang, K. Fatih, J. Zhang, H. Wang, Z. Liu, R. Abouatallah, A. Mazza, A review of water flooding issues in the proton exchange membrane fuel cell, *J. Power Sources* 178 (2008) 103-117.
- [7] Y. Zhang, H. Zhang, Y. Ma, J. Cheng, H. Zhong, S. Song, H. Ma, A novel bifunctional electrocatalyst for unitized regenerative fuel cell, *J. Power Sources* 195 (2010) 142-145.
- [8] J. C. Cruz, S. Rivas, D. Beltran, Y. Meas, R. Ornelas, G. Osorio-Monreal, L. Ortiz-Frade, J. Ledesma-García, L.G. Arriaga, Synthesis and evaluation of ATO

- as a support for Pt–IrO<sub>2</sub> in a unitized regenerative fuel cell, *Int. J. Hydro. Energ.* 37 (2012) 13522-13528.
- [9] S.-Y. Huang, P. Ganesan, H.-Y. Jung, B. N. Popov, Development of supported bifunctional oxygen electrocatalysts and corrosion-resistant gas diffusion layer for unitized regenerative fuel cell applications, *J. Power Sources* 198 (2012) 23-29.
- [10] M. Roca-Ayats, E. Herreros, G. García, M. A. Peña, M. V. Martínez-Huerta, Promotion of oxygen reduction and water oxidation at Pt-based electrocatalysts by titanium carbonitride, *Appl. Catal. B* 183 (2016) 53-60.
- [11] S. Choe, B.-S. Lee, J. H. Jang, Effects of diffusion layer (DL) and ORR catalyst (MORR) on the performance of MORR/IrO<sub>2</sub>/DL electrodes for PEM-type unitized regenerative fuel cells, *J. Electrochem. Sci. Technol.* 8 (2017) 7-14.
- [12] C. M. Hwang, M. Ishida, H. Ito, T. Maeda, A. Nakano, A. Kato, T. Yoshida, Effect of titanium powder loading in gas diffusion layer of a polymer electrolyte unitized reversible fuel cell, *J. Power Sources* 202 (2012) 108-113.
- [13] H. Ito, K. Abe, M. Ishida, C. M. Hwang, A. Nakano, Effect of through-plane polytetrafluoroethylene distribution in a gas diffusion layer on a polymer electrolyte unitized reversible fuel cell, *Int. J. Hydro. Energ.* 40 (2015) 16556-16565.
- [14] C.-M. Hwang, M. Ishida, H. Ito, T. Maeda, A. Nakano, A. Kato, T. Yoshida, Effect of PTFE contents in the gas diffusion layers of polymer electrolyte-based unitized reversible fuel cells, *J. Int. Counc. Electr. Eng.* 2 (2012) 171-177.
- [15] C. M. Hwang, M. Ishida, H. Ito, T. Maeda, A. Nakano, Y. Hasegawa, N. Yokoi, A. Kato, T. Yoshida, Influence of properties of gas diffusion layers on the performance of polymer electrolyte-based unitized reversible fuel cells, *Int. J.*

- Hydro. Energ.* 36 (2011) 1740-1753.
- [16] T. Ioroi, T. Oku, K. Yasuda, N. Kumagai, Y. Miyazaki, Influence of PTFE coating on gas diffusion backing for unitized regenerative polymer electrolyte fuel cells, *J. Power Sources* 124 (2003) 385-389.
- [17] H. Y. Li, H. Guo, F. Ye, C. F. Ma, Experimental investigation on voltage response to operation parameters of a unitized regenerative fuel cell during mode switching from fuel cell to electrolysis cell, *Int. J. Energ. Res.* 42 (2018) 3378-3389.
- [18] J. X. Liu, H. Guo, X. M. Yuan, F. Ye, C. F. Ma, Experimental investigation on two-phase flow in a unitized regenerative fuel cell during mode switching from water electrolyzer to fuel cell, *Int. J. Energ. Res.* 42 (2018) 2823-2834.
- [19] J. X. Liu, H. Guo, X. M. Yuan, F. Ye, C. F. Ma, Effect of mode switching on the temperature and heat flux in a unitized regenerative fuel cell, *Int. J. Hydro. Energ.* 44 (2019) 15926-15932.
- [20] X. M. Yuan, H. Guo, J. X. Liu, F. Ye, C. F. Ma, Influence of operation parameters on mode switching from electrolysis cell mode to fuel cell mode in a unitized regenerative fuel cell, *Energy* 162 (2018) 1041-1051.
- [21] X. M. Yuan, H. Guo, F. Ye, C. F. Ma, Experimental study of gas purge effect on cell voltage during mode switching from electrolyser to fuel cell mode in a unitized regenerative fuel cell, *Energ. Convers. Manage.* 186 (2019) 258-266.
- [22] X. M. Yuan, F. Ye, J. X. Liu, H. Guo, C. F. Ma, Voltage response and two-phase flow during mode switching from fuel cell to water electrolyser in a unitized regenerative fuel cell, *Int. J. Hydro. Energ.* 44 (2019) 15917-15925.
- [23] A. U. Chávez-Ramírez, J. C. Cruz, R. Espinosa-Lumbreras, J. Ledesma-García, S. M. Durón-Torres, L. G. Arriaga, Design and set up of a hybrid power system

- (PV-WT-URFC) for a stand-alone application in Mexico, *Int. J. Hydro. Energ.* 38 (2013) 12623-12633.
- [24] D. J. Bents, V. J. Scullin, B. J. Chang, D. W. Johnson, C. P. Garcia, I. J. Jakupca, Hydrogen-oxygen PEM regenerative fuel cell development at Nasa Glenn Research Center, *Fuel Cells Bull.* 2006 (2006) 12-14.
- [25] A. Bergen, L. Pitt, A. Rowe, P. Wild, N. Djilali, Experimental assessment of a residential scale renewable–regenerative energy system, *J. Power Sources* 186 (2009) 158-166.
- [26] G. Suppes, Roles of plug-in hybrid electric vehicles in the transition to the hydrogen economy, *Int. J. Hydro. Energ.* 31 (2006) 353-360.
- [27] N. Bizon, P. Thounthong, Fuel economy using the global optimization of the Fuel Cell Hybrid Power Systems, *Energ. Convers. Manage.* 173 (2018) 665-678.

## 국문 초록

# 양이온 교환막 일체형 재생 연료전지용 막-산화 이리듐 도금 전극 접합체 제조 및 운전 분석

수소 에너지는 연소하더라도 온실가스를 배출하지 않아 석유 석탄을 대체하는 친환경 미래 에너지원으로 각광받고 있다. 수소 경제가 활성화 되기 위해서는 수소의 생산과 수소에너지를 활용한 발전이 중요하다. 수소를 생산하는 방법에는 천연가스 개질, 열분해, 플라즈마 개질, 바이오메스 가스화 등과 같은 다양한 방법들이 있지만 그 중에서도 수전해는 물을 전기분해하여 수소와 산소를 생산하는 기술로 가장 친환경적인 방법으로 꼽힌다. 또한 연료전지는 수소와 산소를 통해 전력을 발생시키는 친환경 전지이다. 일체형 재생 연료전지는 수전해와 연료전지, 두 운전을 모두 할 수 있는 장비를 말한다.

효율적이고 안정적인 일체형 재생 연료전지를 제작하기 위해서는 활성이 높은 촉매와 구동환경에서 부식이 방지되며 안정적인 전극이 필요하다. 탄소 전극은 수전해의 산화환경에서 쉽게 부식되기 때문에 일체형 재생 연료전지에서는 수전해 운전에서의 산소전극으로 티타늄 전극이 주로 보고되고있다. 본 연구에서는 적은 귀금속 촉매를 사용하며 안정적이고 우수한 성능을 나타내는 일체형 재생 연료전지 전극을 제작하기 위해 산화 이리듐이 도금된 티타늄 전극을 사용하였다. 산화 이리듐 도금 전극은 적은 양의 산화 이리듐 ( $< 0.2 \text{ mg cm}^{-2}$ )으로도 좋은 수전해 성능을 낼 뿐만 아니라 전극의 표면을 산화 이리듐으로 코팅해줌으로써 티타늄

전극의 부식 또한 방지해준다. 본 학위 논문에서는 산화 이리듐이 도금된 티타늄 전극을 일체형 재생 연료전지에 도입했을 때 나타나는 문제점을 파악하고 이를 개선하기 위한 연구들을 진행하였다.

1장에서는 양이온 교환막 기반 수전해, 연료전지 및 일체형 재생 연료전지에 대한 개괄적인 설명을 하였고 도금 전극의 수전해, 연료전지 적용 사례들을 소개하였다.

제 2장에서는 산화 이리듐 도금 전극의 활성 표면적을 증가시키기 위해 백금 지지체 도금을 도입하였다. 연속적인 도금 방식을 통해 반구형 백금 코어-산화 이리듐 셸 구조의 촉매층을 형성시켰다. 백금 지지체는 산화 이리듐 도금이 일어나는 산화 반응의 환경에서 안정할 뿐만 아니라 티타늄기판과 산화 이리듐과 강한 화학적 결합을 형성하여 안정적인 촉매층을 형성시켜준다. 촉매 스프레이로 형성된 전극, 단일 도금 전극과 비교하여 수전해 운전을 실시해보았을 때 지지체가 없는 도금 전극에 비해 2.1 배, 스프레이 전극에 비해 56 배의 질량당 전류밀도 성능을 나타내었다. 이중 도금된 전극의 우수한 수전해 성능에는 도금 전극의 친수성으로 인한 물질 전달 저항의 감소, 이중 도금전극의 활성 표면적 증가, 전도성이 좋은 지지체로 인한 오믹저항 감소 등이 기여하였음을 확인하였다. 뿐만 아니라 산화 이리듐 표면을 환원시켜주면 연료전지 전극으로도 활용할 수 있으며  $0.83 \text{ mg}_{(\text{Pt}+\text{Ir})} \text{ cm}^{-2}$ 의 낮은 귀금속 담지량으로도 높은 재생연료전지의 성능을 나타냄을 확인하였다.

제 3장에서는 양친매성의 도금 전극을 제조하여 일체형 재생 연료전지에 도입하였다. 산화 이리듐 도금으로 인한 친수성은 유지하면서 소수

성의 PDMS 고분자 술을 일정 간격을 주기로 코팅하여 패터닝된 친수성 /소수성 경로를 전극에 형성시켜주었다. 일체형 재생 연료전지의 산소전극에는 도금된 산화 이리듐과 스프레이로 제작된 백금 촉매가 포함되었다. 산소전극에서 백금 촉매층은 높은 기공 구조를 가지며 소수성을 띠어서 수전해 운전시 물질전달저항을 높이는 역할을 하는 반면, 산화 이리듐 촉매는 친수성을 띠어 연료전지 운전시 가스의 원활한 이동에 악영향을 주어 심각한 플러딩(flooding) 현상을 일으킴을 확인하였다. 이에 따라 양친매성의 다공성 수송층을 일체형 재생 연료전지에 적용하였을 때 상호적인 두 악영향을 모두 개선해주어 수전해와 연료전지 운전 모두에서 성능이 크게 향상함을 확인하였다.

제 4장에서는 전기화학적 주사현미경 (SECM)의 원리 및 분석 방법을 기본적인 실험들을 통해 소개한 후 전기화학적 주사현미경 분석을 통해 제 3장에서 양친매성의 다공성 수송층의 기체 방출에서의 효과를 증명하였다. 전기화학적 주사현미경의 초미세전극에 일정한 전압을 걸어주었을 때 산화환원 중재자가 있는 용액에서 기관과의 거리에 따라 흐르는 전류의 차이가 생기는 원리를 이용하여 티타늄 다공성 수송층의 지형을 분석하였다. 또한 다공성 수송층 안에서 산소 발생 반응이 일어날 때 다공성 수송층 뒷면 위에서 초미세전극의 산소 환원 반응을 통하여 기관에서 발생한 산소를 감지하였다. 그 결과 초미세 전극이 기관 위 20  $\mu\text{m}$  거리 안에서 지나갈 때는 기공 위를 지날 경우 산소 감지량이 더 많이 발생하였다. 그러나 27  $\mu\text{m}$  이상의 거리에서는 확산에 의해 지형에 큰 영향을 받지 않았다. 또한 양친매성 다공성 수송층의 30  $\mu\text{m}$  위에서 실

험한 결과, 소수성 경로 구간을 따라 감지된 산소량이 친수성 경로 구간보다 월등히 많음을 확인하였다.

제 5장에서는 수전해 운전에서 산소 전극인 백금 촉매를 포함한 산화 이리듐 도금 전극을 일체형 재생 연료전지에 도입했을 때 운전 배치와 공급되는 연료의 상대습도가 연료전지 성능에 미치는 영향을 분석하였다. 백금은 산소환원반응과 수소산화반응의 활성이 모두 우수한 촉매이기 때문에 연료전지 운전에서 백금을 포함한 산화 이리듐 도금 전극은 산소 전극 또는 수소 전극으로 모두 사용이 가능하다. 일반적으로 보고되는 산소 전극으로가 아닌 수소 전극으로 연료 전지 운전을 할 경우 다음과 같은 장점을 가진다. 첫째, 물관리 측면에서 연료전지 운전에 최적화된 소수성의 탄소 다공성 수송층을 산소 전극에 사용함으로써 플러딩(flooding)으로 인한 성능 감소를 해결 할 수 있다. 둘째, 백금에 비해 더 넓은 전기화학적 활성면적으로 큰 질량 활성을 가지는 백금/탄소 지지체 촉매를 상대적으로 반응이 느린 산소 환원 반응이 일어나는 연료전지 운전의 산소 전극에 사용할 수 있다. 셋째, 상대적으로 빠른 수소 환원 반응에 백금 촉매를 사용함으로써 도금 전극에서의 백금 촉매 담지량을 낮출 수 있다. 친수성의 도금 전극과 소수성의 탄소 전극의 성질 차이로 인해 상대습도에 따른 연료전지 성능의 영향이 도금 전극을 산소전극으로 사용했을 때와 수소 전극으로 사용했을 때가 매우 다르다. 상대습도에 따른 전극 안에서의 물 분포의 추정값과 운전 결과를 비교해본 결과, 도금 전극을 수소 전극으로 사용했을 경우 수소 전극 안의 물의 함량이 많을수록 더 낮은 오믹 저항과 더 높은 성능을 나타냄을 확인하였다. 이

연구에서는 운전 방식과 상대 습도 조절로  $0.65 \text{ mg}_{(\text{Pt+Ir})} \text{ cm}^{-2}$ 의 낮은 귀금속 담지량으로도 우수한 수전해, 연료전지 성능을 달성하였다.

제 6장에서는 음이온 교환막 수전해의 성능 향상을 위한 전지 제조, 운전방식의 영향을 분석하는 연구를 다루었다. 음이온 교환막 수전해는 알칼리 환경에서 수전해가 일어남에 따라 비귀금속 촉매의 사용과 값싼 막의 사용으로 양이온 교환막 수전해에 비해 가격적인 면에서 이점이 있지만 성능이 낮게 보고되고 있다. 재료 외에 막-전극 접합체의 프레싱, 전지 체결압에 따라 수전해에 미치는 영향과 운전전 공급되는 전해질 여부 및 운전 온도에 따른 영향을 분석하여 음이온 교환막 수전해의 성능을 최적화하였다.

**주요어:** 일체형 재생 연료전지, 고분자 전해질 막 수전해, 도금, 전기화학적 주사현미경

**학번:** 2015-21029

## Appendix. Publication List

† indicates equal-contribution

### **Chapter 2**

**Ahyoun Lim**, Junyoung Kim, Hye Jin Lee, Hyoung-Juhn Kim, Sung Jong Yoo, Jong Hyun Jang, Hee Young Park, Yung-Eun Sung, Hyun S. Park, “Low-loading IrO<sub>2</sub> supported on Pt for catalysis of PEM water electrolysis and regenerative fuel cells” *Applied catalysis B*, 2020, 272, 118955

### **Chapter 3,4**

**Ahyoun Lim**, Hui-Yun Jeong, Jin Young Kim, Jong Hyun Jang, Yung-Eun Sung, Jong Min Kim, Hyun S. Park, “Through-plane amphiphilic channel formation on porous transport layer for effective unitized regenerative fuel cell (URFC)” (In preparation)

### **Chapter 5**

**Ahyoun Lim**<sup>†</sup>, Ju Sung Lee<sup>†</sup>, Hyoung-juhn Kim, Dirk Henkensmeier, Sung Jong Yoo, Jin Young Kim, So Young Lee, Jong Hyun Jang, Yung-Eun Sung, Hyun S. Park, “Highly efficient operation of unitized regenerative fuel cell with amphiphilic membrane-electrode assembly” (In preparation)

### **Chapter 6**

**Ahyoun Lim**, Hyoung-juhn Kim, Dirk Henkensmeier, Sung Jong Yoo, Jin Young Kim, So Young Lee, Yung-Eun Sung, Jong Hyun Jang, Hyun S. Park, “A study on electrode fabrication and operation variables affecting the performance of anion exchange membrane water electrolysis” *Journal of Industrial and Engineering Chemistry* 2019, 76, 410–418.

***Other works (as 1<sup>st</sup> Author or Co-author)***

Semin Kim<sup>†</sup>, Yohan Jang<sup>†</sup>, Minsu Jang, **Ahyoun Lim**, John G. Hardy, Hyun S. Park, Jae Young Lee, “Versatile biomimetic conductive films of polypyrrole and hyaluronic acid of different molecular weights” *Acta Biomaterialia* 2018, 80, 258-268.

Jin Kim<sup>†</sup>, Jin Soo Kang<sup>†</sup>, Juwon Jeong, Yoon Jun Son, Myeong Jae Lee, Jiho Kang, **Ahyoun Lim**, Hyun S. Park, Yung-Eun Sung, “Electrochemically synthesized nanostructured iron carbide/carbon composite as a low-cost counter electrode for dye-sensitized solar cells” *Journal of Power Sources* 2018, 396, 213-219.

Anastasiia Konovalova, Hyemi Kim, Sangwon Kim, **Ahyoun Lim**, Hyun Seo Park, Mikkel Rykær Kraglund, David Aili, Jong Hyun Jang, Hyoung-Juhn Kim, Dirk Henkensmeier, “Blend membranes of polybenzimidazole and an anion exchange ionomer (FAA3) for alkaline water electrolysis: improved alkaline stability and conductivity” *Journal of Membrane Science* 2018, 564, 653–662.

Angela Marinkas, Izabela Stru\_zy\_nska-Piron, Yona Lee, **Ahyoun Lim**, Hyun S. Park, Jong Hyun Jang, Hyoung-Juhn Kim, Jihyun Kim, Artjom Maljusch, Oliver Conradi, Dirk Henkensmeier, “Anion-conductive membranes based on 2-mesityl-benzimidazolium functionalised poly(2,6-dimethyl-1,4-phenylene oxide) and their use in alkaline water electrolysis”, *Polymer* 2018, 145, 242-251.

Min Kyung Cho, Hee-Young Park, Hye Jin Lee, Hyoung-Juhn Kim, **Ahyoun Lim**, Dirk Henkensmeier, Sung Jong Yoo, Jin Young Kim, So Young Lee, Hyun S. Park, Jong Hyun Jang, “Alkaline anion exchange membrane water electrolysis: Effects of electrolyte feed method and electrode binder content”, *Journal of Power Sources* 2018, 382, 22-29.

**Ahyoun Lim**, Min Kyung Cho, So Young Lee, Hyoung-Juhn Kim, Sung Jong Yoo, Yung-Eun Sung, Jong Hyun Jang, Hyun S. Park, “A review of industrially developed components and operation conditions for anion exchange membrane water electrolysis”, *J. Electrochem. Sci. Technol.*, 2017, 8(4) 265-273.

Min Kyung Cho, **Ahyoun Lim**, So Young Lee, Hyoung-Juhn Kim, Sung Jong Yoo, Yung-Eun Sung, Hyun S. Park, Jong Hyun Jang, “A review on membranes and catalysts for anion exchange membrane water electrolysis single cells”, *J. Electrochem. Sci. Technol.*, 2017, 8(3), 183-196.

Jimin Kong<sup>†</sup>, **Ahyoun Lim**<sup>†</sup>, Changwon Yoon, Jong Hyun Jang, Hyung Chul Ham, Jonghee Han, Sukwoo Nam, Dokyoon Kim, Yung-Eun Sung, Junhkyu Choi, Hyun S. Park, “Electrochemical synthesis of NH<sub>3</sub> at low temperature and atmospheric pressure using a  $\gamma$ -Fe<sub>2</sub>O<sub>3</sub> catalyst”, *ACS Sustainable Chem. Eng.* 2017, 5, 10986-10995.

Kyung Jin Lee, Dong Yun Shin, Ayeong Byeon, **Ahyoun Lim**, Jin Young Kim, “Hierarchical cobalt-nitride and -oxide co-doped porous carbon nanostructures for highly efficient and durable bifunctional oxygen reaction electrocatalysts”, *Nanoscale* 2017, 9, 15846-15855.

Jin Soo Kang<sup>†</sup>, Jin Kim<sup>†</sup>, Myeong Jae Lee<sup>†</sup>, Yoon Jun Son, Juwon Jeong, Dong Young Chung, **Ahyoun Lim**, Heeman Choe, Hyun S. Park, Yung-Eun Sung, “Electrochemical synthesis of nanoporous tungsten carbide and its application as electrocatalysts for photoelectrochemical cells”, *Nanoscale* 2017, 9, 5413–5424.

Segeun Jang, Jin Soo Kang, Jong-Kwon Lee, Sang Moon Kim, Yoon Jun Son, **Ahyoun Lim**, Hyesung Cho, Jin Kim, Juwon Jeong, Gunhee Lee, Yung-Eun Sung, Mansoo Choi, “Light harvesting: enhanced light harvesting in mesoscopic solar cells by pultilevel pultiscale patterned photoelectrodes with

superpositioned optical properties”, *Adv. Funct. Mater.* 2016, 26, 6584–6592.